The Equilibrium and Nonequilibrium Behaviour of Surfactant Systems

Louisa Reissig

A thesis submitted in fulfilment of the requirements
for the degree of Doctor of Philosophy
to the
University of Edinburgh
2009

Abstract

In binary systems, surfactant molecules can self-assemble into a large variety of structures depending on their chemical structure, concentration and temperature. The properties and stability of the phases, their coexistence regions and the formation of metastable structures is of great importance not only for fundamental understanding, but also for applications in many fields including industry and medicine. This thesis presents studies of the equilibrium and non-equilibrium behaviour of two widely used surfactant systems.

The understanding of the equilibrium behaviour of an aqueous surfactant system is often incomplete or partly incorrect, which is caused by experimental difficulties, long equilibration times and the occurrence of long-lived metastable states. By applying a set of complementary techniques and recording changes on different length scales, the equilibrium phase diagram of the surfactant didodecyldimethylammonium bromide (DDAB) in water has been studied and amended. Differential scanning calorimetry has been used to obtain thermodynamic parameters. The structure of phases and biphasic regions have been characterised by small angle X-ray scattering and microscopy, while the conformational properties of the surfactant molecules have been investigated using Raman spectroscopy combined with computational methods. The effects of impurities have been studied using analytical techniques and a sufficient purity of the samples could be ensured.

As a result of the studies, a new crystalline phase which exists at temperatures below 16°C was found. This phase replaces the frozen lamellar phase (L_β) in the previously reported phase diagram. The L_β phase has been found to be a long-lived metastable phase. The amended phase diagram has been tested by studying phase transitions along isoplethal and isothermal paths. All experimental results could be explained in terms of the new phase diagram.

The study of phase transition along isoplethal paths focused on the transition between

the new crystalline phase (XW_n) coexisting with a dilute monomer solution (W) and the lamellar phase (L_α). This transition was (except for a single composition ϕ_{DDAB}≈3% DDAB) a non-isothermal transition involving the phase sequence:

$$XW_n + W \longrightarrow XW_n + L_\alpha \longrightarrow L_\alpha$$

upon heating and

$$L_\alpha \longrightarrow \text{ overcooled } L_\alpha \longrightarrow XW_n + W$$

upon cooling. The structural changes within the phases and their relative ratios could be characterised using small angle X-ray scattering, microscopy and Raman spectroscopy.

During the dissolution of lamellar phases along an isothermal path, multilamellar wormlike interface instabilities (so called myelins) were found to grow from the lamellar/water interface into the water. The growth of these myelins as well as changes in the lamellar phase have been investigated using optical microscopy and direct observation. This has provided detailed quantitative information on the dynamics of myelin growth and the effect of the initial structure of the lamellar phase on the myelin growth. The dependence of the growing rate on surfactant concentration could be explained in terms of a previously reported model in which the osmotic pressure was stated to be the driving force for the myelin kinetics. It has been found that for lamellar phases in coexistence with a sufficient amount of crystals, the myelin growth could be suppressed. Preliminary measurements of a tertiary system, where the pure lamellar phase of DDAB was mixed with a crystalline phase formed by dioctadecyldimethylammonium bromide (DODAB), a DDAB analogue, were carried out.

The myelin growth has also been studied for a second system, the non-ionic surfactant triethylene glycol monododecyl ether ($C_{12}E_3$), known for its formation of myelins of great stability. The optical methods were extended to confocal microscopy, resulting in a 3D image of the myelin formation, providing detailed quantitative information on myelin growth as well as on myelin size.

Declaration

I do hereby declare that this thesis was composed by myself and that the work described within is my own, except where explicitly stated otherwise.

Louisa Reissig
October 2009

Acknowledgements

First of all, I would like to say "thank you" to all the people who supported me and believed in me during my PhD: my family, friends and fellow students.

In particular I would like to thank Andy Mount and Mike Cates for their supervision and discussions. Special thanks to Paul Clegg for his help towards the end of my PhD. Thanks to Stefan Egelhaaf for being my long-distance supervisor and his support during my stays at the Heinrich-Heine University in Düsseldorf.

I wish to express my deep gratitude to Bob Laughlin for all the discussions and meetings, for his support and encouragement and for his interest in my work.

The work could not have been done without the possibility of using different equipment in and outside the Edinburgh University and without the excellent experimental supervision of their experimental operators. I am greatly indebted to: Andy Turner (Single Molecule Calculation), Andrew Scoffield (Dyes), Alan Cooper, Margret Nutley & Joanna Jakus (Densitymetry, PPC - Glasgow University), Alan Taylor (ESI-MS), Arlene Sloan (ATR - Glasgow University), Colin Pulham (Confocal Raman Spectroscopy), David Fairhurst (Direct observation, microscopy), George Penny (X-ray diffraction - CSEC), Hugh Vass (Raman Spectroscopy), Marika DeCremoux (NMR), Peter Roloff & Walter Frank (DSC - Heinrich-Heine University, Germany), Simon Dalgleish (Recrystallisation, NMR), Wim Pyckhout-Hintzen (SAXS - Research Center Jülich, Germany) and COSMIC (Confocal Microscopy).

Many thanks to the workshop in Physics for building the temperature-controlled sample cell and to the technicians in Edinburgh, Düsseldorf and Jülich for their availability and help.

I am very grateful for the time spend by Simon Dalgleish in proof reading this thesis.

Finally I would like to thank the Marie Curie Network on Biomimetic Systems and the EPSRC for funding.

Contents

List of Figures

List of Tables

Chapter 1

Introduction

In our day to day lives we have plenty of contact with surfactant systems (i.e. surface active agents). They are found, not only in detergents, but also in drug coatings, surface coatings and in emulsions, to name but a few. Surfactant science covers a large variety of research fields, from physics and physical chemistry to biology or even pharmaceutical research groups, both in academia and industry.

Surfactants are amphiphilic molecules, where one part of the molecule likes the solvent (here water) - the head - while the other does not - the chain. Such molecules spontaneously self-organise into a variety of structures, which can be spherical, cylindrical or layered. The type of aggregate which forms depends on the relative size of the head to the tails. This size is not the geometrical size of that part of the molecule (head or chain) but the effective size, which depends not only on the chemical composition, but also on temperature and concentration, salt content or impurities. Therefore, before one can work with a surfactant molecule, a detailed knowledge of its phase diagram and the stabilities of the different phases is needed.

The study of the equilibrium phase behaviour of a surfactant/water system involves a combination of different experimental techniques and theoretical considerations (see section 2.2.2). Long equilibration times and the occurrence of metastable states can easily lead to wrong assumptions. Furthermore, changes between different colloidal states (as for example the occurrence of vesicles (see section 2.2.3.2)) within one phase, which might depend on sample preparation, have to be distinguished from real thermodynamic phase transitions. Because of these difficulties, a new phase diagram is always only a hypothesis, and the true diagram results only after further testing, often requiring the development of new experimental techniques. A number of models might have to be created and disproved before a satisfying description of the equilibrium phase behaviour is found. This has led to the occurrence of incomplete or partly wrong phase diagrams in the literature.

In general in surfactant/water systems, one can distinguish between crystalline, liquid crystalline and liquid phases. In crystalline phases (see section 2.2.3.1) the surfactant molecule is 'frozen', which means, there is only one molecular configuration possible, and the molecule is arranged in a crystal lattice. If the molecule has a thermal energy large enough to change configuration, it is in a 'liquid' state. In this configuration various aggregates can form. At higher concentrations, forces between the aggregates lead to liquid crystalline structures. The lamellar phase is the one which is of great importance to this work (see section 2.2.3.2). In this phase the surfactant molecules form bilayers and this can therefore be used as a model system for biological cell membranes. One should note that an intermediate state between a crystal and a fluid lamellar phase has been reported in the literature, the so-called L_{β}-phase (see section 2.2.3.2). In this case, the molecules are reported to be already in a frozen state, but do not form a crystal lattice, but a 'gel'.

Once the equilibrium phase behaviour of a system is well understood, this system can allow the study of kinetic and dynamic aspects of its phases and the transitions between them. The interpretation of these results within the frame of the phase diagram supports its correctness. Conversely, appropriate changes can result from the studies, leading to new hypothesis of equilibrium phase behaviour.

One of the most common parameters which can be changed to force a system to undergo a phase transition is the temperature of the system (see section 2.3.1). Different types of thermal phase transition can be distinguished, based on the type of the phases involved. A combination of theoretical, thermodynamic and kinetic laws with several experimental techniques is required to enable distinction between the different types of phase transition, but also to identify intermediate states and processes involved.

As already mentioned, changing the temperature influences the configurational state of a surfactant molecule. The melting and freezing of these molecules in lamellar phases has been of great interest in the literature. This is partly due to the biological implications, as solid-like and liquid-like domains exist in cell membranes (see Fig.1.1).

Another parameter which can be changed is the surfactant concentration (see section 2.3.2). The dissolution of surfactant systems, one of the most common processes in our daily life (e.g. detergents), is of great interest. From a practical point of view, one often requires the dissolution to be fast, homogeneous and complete. On the other hand, this field also encompasses technological issues, such as drug delivery, where total control of the dissolution process is required, along with control of kinetics. During this process

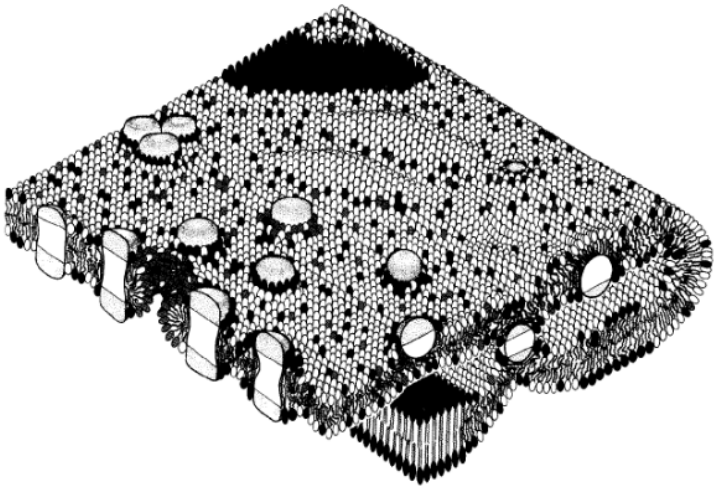

Figure 1.1: Schematic picture of a biological membrane [Israelachvili 98].

the surfactant molecules have to rearrange. There is typically variation with external conditions (such as temperature, initial surfactant concentration), and the properties of the surfactant itself. In these cases the intermediate states look different and long- or short-live metastates and instabilities may occur.

One of the most spectacular interface instabilities which might occur during the dissolution of lamellar phases is the myelin instability shown in Fig.1.2 (see section 2.3.3). The first observation of myelin figures growing from lecithin in water can be traced back to George-Luis LeClerc (Compte de Buffon, 1707-1788), who compared them to writhing eels. Although there has been interest in myelins since the 1850s when the German physician Rudolf Virchow identified the structural closeness of myelins to nerve fibres, its detailed structure was not understood and the reason for its occurrence, as well as its growth, is even now still unknown.

By the 1970s, a lot of work had been done on the myelin metastate. Among other things, the structural and kinetic properties during its growth have been studied, as well as parameters which influence its occurrence. Recently, Jacques Leng proposed a model describing the kinetics of myelin growth (see section 2.3.2) as being controlled by the osmotic pressure between the lamellar phase and the surrounding solution, as well as the water mobility between the bilayer sheets. At present it is unclear how generally applicable this model is.

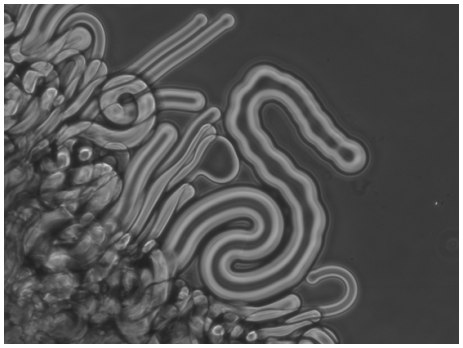

Figure 1.2: Myelins growing into water (right) out of the non-ionic surfactant $C_{12}E_3$ (left).

The content and organisation of this thesis

In this work three aqueous surfactant systems are studied: two ionic surfactants (DDAB, see section 3.2.1.1 and DODAB, see section 3.2.1.2) and a non-ionic surfactant ($C_{12}E_3$, see section 3.2.2.1). The equilibrium and/or non-equilibrium behaviour of these systems have been studied using a wide range of optical, analytical and computational techniques, which are introduced in section 3.3. This chapter also describes the way the experiments are performed, how they are calibrated and discusses the possible errors and difficulties encountered.

DDAB is one of the most commonly used cationic surfactants and has great importance in various applications. Nevertheless, this work establishes that the generally accepted phase diagram is not correct for temperatures below the chain freezing temperature. In chapter 4 a detailed study of the equilibrium phase behaviour of the surfactant is presented. It could be shown that crystalline phases form instead of the reported gel phase. These crystals were also characterised. The phase diagram was then compared to the DODAB system, which differs from DDAB only by having two 18 carbon long chains instead of 12.

In a further step, the thermal phase transition, involving the freezing of bilayers and the melting of DDAB-crystals depending on surfactant concentration, has been investigated (see chapter 5). The experimental results are explained in terms of the modified phase diagram.

Furthermore, the dissolution behaviour of the lamellar phase has been studied (see chapter 6). Myelin instabilities have been observed. The kinetic dependence on sample concentration can be explained in terms of osmotic pressure and water mobility and is

therefore consistent with the Leng-model.
An initial motivation was a comparison of the lamellar and gel phases. One of the main differences in the dissolution behaviour is the lack of myelins, when starting from a gel phase. However, due to the vanishing of the gel phase from the modified phase diagram, this could not be achieved. However, it can be shown that myelin formation is also suppressed by the existence of crystals in coexistence with the lamellar phase in the initial sample. We propose an experiment using a mixture of the DDAB and DODAB systems and therefore controlling the amount of crystals in the lamellar phase to study the influence of the crystalline phase on myelin formation (see section 6.3).

Finally, the dissolution behaviour of the non-ionic surfactant $C_{12}E_3$ has been studied. This molecule belongs to one of the most common groups of non-ionic surfactants. The measurements performed have shown that the observed kinetics vary with the droplet size. In chapter 7 it is shown that this could be explained by the assembling of the myelins on top of the water phase due to their lower density.

At the end of this thesis the most important results are summarised and their importance discussed (see chapter 8). Further possible experiments are suggested, which might help to answer question which did arise but could not been answered during this study.

Chapter 2

Theory of surfactant systems

2.1 Introduction

Surfactant molecules have been extensively studied in the past and a broad knowledge of the properties of surfactant systems and their phases can be found in the literature (see for example [Israelachvili 98,Laughlin 94,Zana 05,Rubingh 91,Jönsson 01,Evans 94, Clint 92,Everett 88]). This chapter will provide an overview of the background needed for the interpretation of the results (presented in chapters 4-7).

Many properties of phases formed in surfactant systems are caused and influenced by the amphiphilic character of the surfactant molecule (see section 2.2.1). However, a detailed knowledge of the thermodynamic and structural aspects of phase science (see section 2.2.2) is needed for a deeper understanding of the equilibrium phases (see section 2.2.3), which can be found in binary surfactant-water systems.

Based on knowledge of the equilibrium behaviour, dynamic and kinetic aspects of phases and their stabilities can be studied. It is here that the non-equilibrium behaviour induced by a change of temperature (see section 2.3.1) or by a change of concentration (see section 2.3.2) is of great interest.

2.2 Equilibrium phase behaviour

2.2.1 The amphiphilic character of a surfactant molecule

A surfactant molecule has a polar head and a non-polar tail (see Fig.2.1). The polar head can be ionic or non-ionic, but it must be hydrophilic and therefore soluble in water. The non-polar moiety contains mostly hydrocarbon chains and does not dissolve in water, thus is called the hydrophobic part of the molecule. At an air/water interface, surfactants will preferentially locate with the head group in the water and the tail in the air to minimize the energetically unfavourable tail/water contacts

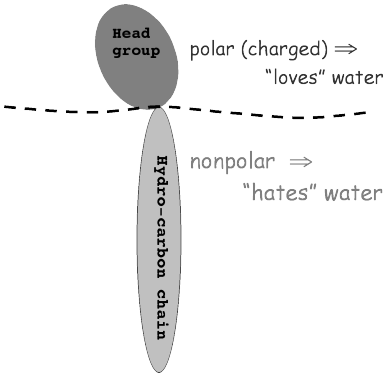

Figure 2.1: Sketch of a surfactant molecule.

[Zana 05, Clint 92, Evans 94]. The system will naturally favour an increased surface area between the air and the water, since surfactant molecules have a minimum free energy when they are at this interface. This will reduce the surface tension of an interface. [Laughlin 94, Jönsson 01, Zana 05, Clint 92].

The surfactants at the interface are in equilibrium with surfactants dissolved in the water. Above a certain concentration, the so-called *critical micelle concentration* (CMC), surfactants self-associate. Micelle formation is driven by the hydrophobic interaction that arises from the tendency of water molecules to reduce contacts with surfactant alkyl chains. Thus the head will sit at the interface between the water and the oily tails. The CMC is an important characteristic of a surfactant. [Clint 92,Zana 05]

The shape of the micelles depends on the effective relative size of the head and the tail of the surfactant molecule. In general, this is summarized in the concept of the surfactant packing parameter P given by

$$P = \frac{v}{a_0 l}, \tag{2.1}$$

where v and l are the volume[1] and length[2] of the tail and a_0 the optimal surface area occupied by the head. One should note that the packing parameter P is an effective parameter and depends on various interactions. For example P varies with ionic strength, concentration and temperature of the solution, as does therefore the optimal shape. This concept permits us to understand or predict micelle shape (see Fig.2.2) and its changes, induced by changes of experimental conditions. [Zana 05,Clint 92,Evans 94]

[1] In general: v(nm^3) = 0.0274 + 0.0269m, where m corresponds to the number of carbons [Zana 05].
[2] In general: l(nm) = 0.15 + 0.1265m, where m corresponds to the number of carbons [Zana 05].

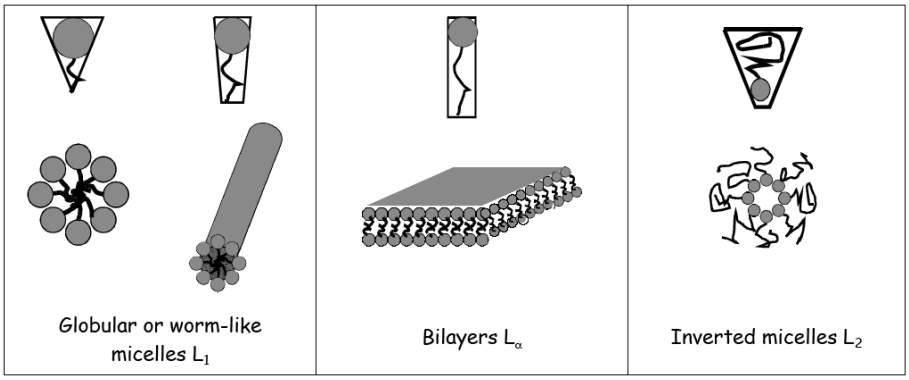

Figure 2.2: Surfactants dissolved in pure water form different types of aggregates depending on the relative size of the head and the tail of the surfactant molecule.

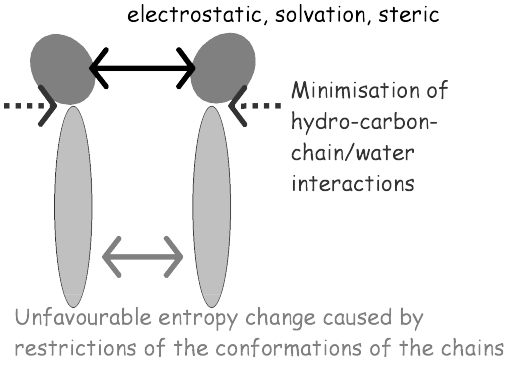

Figure 2.3: Aggregation shapes involve a balance of alkyl-chain/water repulsion and repulsion between head groups together with surface curvature and limitations due to alkyl-chain packing.

In general the situation is as follows (see Fig.2.3) [Clint 92, Mitchell 83, Evans 94]: The surfactant heads try to build an interface, which minimizes the interaction between the hydrophobic chains and the water. On the other hand there are repulsive forces, such as electrostatic forces and volume filling of the head group and associated solvent molecules. Also, for the chains, a reduction in the volume leads to unfavourable entropy changes because of the restriction of some conformations. These forces are dependent on temperature, as is therefore the shape. For example, for non-ionic surfactants, an increase in temperature is assumed to lead to a decreased surface area per molecule, because it decreases the amount of associated water [Mitchell 83]. This same effect occurs if the amount of water in the sample decreases.

So far, only intramicellar interactions i.e. forces, which are parallel to the micelle-water interface, have been considered. Thus, in concentrated aqueous solutions, where intermicellar forces come into play, surfactants give rise to lyotropic liquid crystals.

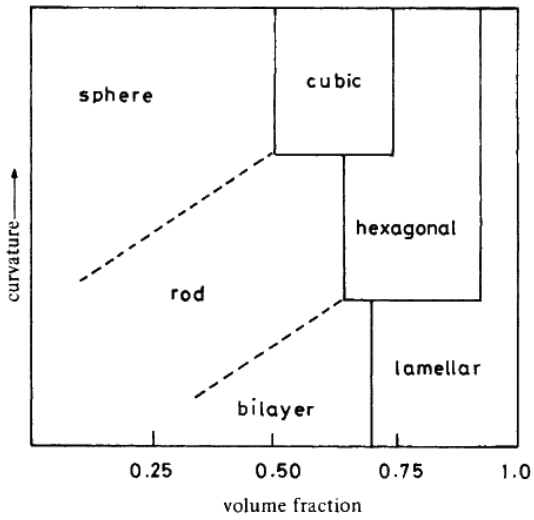

Figure 2.4: Schematic illustration of mesophase structures as a function of surfactant volume fraction and increasing curvature. The micelle shape transitions indicated in dotted lines occur over a range of volume fractions while transitions between mesophases occur at constant volume fraction. [Mitchell 83]

Intermicellar forces work perpendicular to the interface and lead to an ordering of the aggregates (*order/disorder transition*), with their symmetry depending on their shape. In order to keep the distance between micelles large, and thus to decrease the free energy of the system, the number of micelles might be reduced or the shape changed. The disordered spheres phase ceases to exist above $\phi_V \approx 0.54$ while the cubic phase ceases to exist above $\phi_V \approx 0.74$ and the equivalent composition for the hexagonal phase is $\phi_V \approx 0.91$. The rod-hexagon transition occurs at around $\phi_V \approx 0.7$ and the bilayer-lamellar transition is even less well established [Mitchell 83]. Fig.2.4 gives a schematic representation at different curvatures and as a function of the surfactant volume fraction. [Zana 05, Mitchell 83]

One should keep in mind that micelles, being thermodynamically stable, are not frozen objects. They are in equilibrium with free surfactants, which are constantly exchanged between micelles and the surrounding solution. It has been reported that in the more concentrated phases, such as liquid crystals, the exchange is much slower and therefore its structures could be considered as permanent, unless an appropriate change is brought to the system initializing transformations. [Zana 05]

The occurrences of the phases mentioned so far require the surfactants to be soluble in liquid water. This is true for many surfactants at higher temperatures, but at low temperatures surfactant molecules separate from solution as a crystal phase. The

crystal solubility boundary of such surfactants is called the *Krafft boundary.*

The next section introduces the background of phase science. This knowledge is necessary for going into more detail when discussing specific phases.

2.2.2 Phase science

Phase science provides a qualitative and quantitative description of the equilibrium phase behaviour of (surfactant) systems following the laws of the thermodynamics of mixtures, the Gibbs phase rule and conservation of mass.

In the first instance, the influence of temperature, pressure and composition on the number of phases have to be obtained, followed by a study of the composition and structure of each phase. In condensed phases at moderate pressures the phases change only slightly with pressure and therefore the influence of pressure can be neglected. Because of this, most studies involve only the change of temperature within a region of interest over the entire composition range[3]. The results of those studies are best displayed in phase diagrams.

2.2.2.1 Phase Diagrams (binary)

A phase diagram summarizes the phase behaviour of a system. In this work we will restrict our attention to binary phase diagrams. For more complex systems one can refer to e.g. chapter 12 in [Laughlin 94]. An example for the sodium chloride-water system is given in Fig.2.5. As can be seen, the phase diagram is divided into regions by solid lines - the phase boundaries. One-phase regions always exist to one side of the phase boundary and a two-phase region to the other. Horizontal lines, i.e. lines of constant temperature, display isothermal discontinuities. These discontinuities touch usually 3 one-phase regions, as shown in the figure. The following isothermal discontinuities can be distinguished:

- *eutectic*: 3 phases coexist (crystal/liquid/crystal) and the phase of intermediate composition (liquid) exists only at temperatures above the discontinuity
- *monotectic*: 3 phases coexist (liquid/liquid/crystal) and the phase of intermediate composition (liquid) exists only at temperatures above the discontinuity
- *peritectic*: 3 phases coexist (liquid/crystal/crystal) and the phase of intermediate composition (crystal) exists only at temperatures below the discontinuity

[3]Complete phase studies must span the entire composition range, defining the phase behaviour of each of the pure components as well as of all possible mixtures [Laughlin 94].

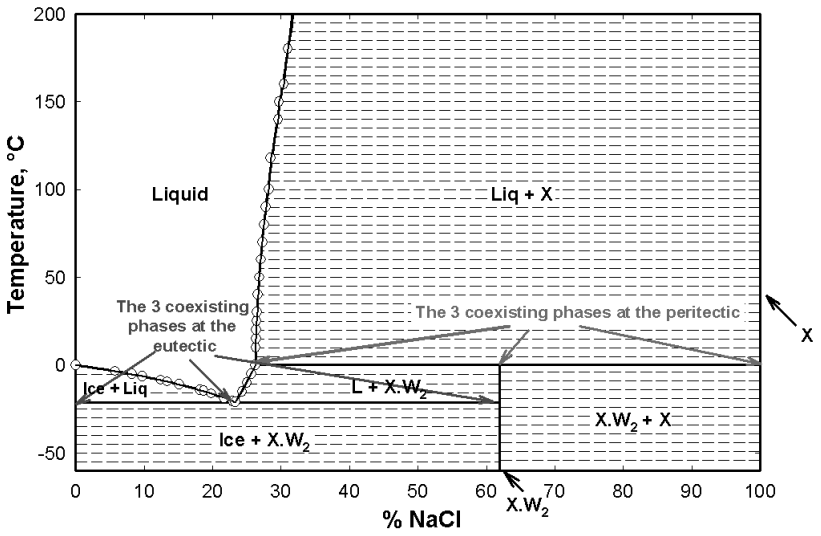

Figure 2.5: General phase diagram of the NaCl-Water system. The dashed lines are tie-lines indicating the composition of coexisting phases; the symbol X indicates the dry crystal, and $X \cdot W_2$ the dihydrate crystal. [Laughlin 94]

- *syntectic*: 3 phases coexist (liquid/crystal/liquid) and the phase of intermediate composition (crystal) exists only at temperatures below the discontinuity
- *polytectic*: 2 of the 3 coexisting phases have the same composition (e.g. crystal polymorphic transition)

These are classical 2-3-2 phase transition. In surfactant systems, liquid crystal or other phases replace the specific phases associated with the classical terms. Laughlin [Laughlin 90, Rubingh 91] suggests the use of the following terminology to describe transitions, which qualitatively resemble the classical transitions but differ in the structure of the phases involved: eutectoid (Phase of intermediate composition exists only above the discontinuity), peritectoid (Phase of intermediate composition exists only bolow the discontinuity) and polytectoid. Beside isothermal discontinuities, isoplethal ones may exist in phase diagrams, as is for example the melting of pure ice to pure water.

Crystals are usually termed as X, crystal hydrates as $X \cdot W_n$. Crystal hydrates are phase compounds, as they are stoichiometrically defined. In diagnosis of phase behaviour, these isopleths (as well as the components themselves) should be treated as phase 'regions' whose span of composition is zero.

Water is conventionally placed to the left of the phase diagram. The composition is in general expressed as the weight fraction of the solute, being insensitive to condition as

well as to the location of the experiment performed[4], thus can be easily transformed into molecular fractions.

In coexistence regions of the phase diagram, tie-lines might be displayed as dashed lines. Tie-lines indicate the composition of coexisting phases. The physical properties of the system do not change moving in the phase diagram along these lines.

2.2.2.2 Phase Rules

There are certain common rules, which every phase diagram has to follow. First of all, phase information must conform to the *Gibbs Phase Rule*, which has been experimentally proved to be valid for nonsurfactant as well as for surfactant systems: *"For a particular system, the sum of the number of phases P plus the degrees of freedom F must under all conditions of composition, temperature and pressure equal a unique constant. The value of that constant is determined by the number of components present C, and equals C plus 2."* [Laughlin 94, Rubingh 91, Evans 94].

$$P + F = C + 2 \tag{2.2}$$

The number of components C in surfactant mixtures is simply the number of chemical compounds[5] present. A system of 1 component, 2 and 3 components is called unary, binary and ternary, respectively. [Laughlin 94]

The degree of freedom F is the number of system variables (temperature, pressure or composition) that must be specified in order to define fully the state of a mixture that is held under a particular set of conditions. For a binary system the Phase Rule allows up to four phases, in which case $F = 0$ and the system is said to be invariant. If three phases exist $F = 1$ (univariant), if two phases $F = 2$ (bivariant), and if one phase exists $F = 3$ (trivariant). [Laughlin 94] The value F calculated from Eq.2.2 is the maximum value that may exist. By specifying additional system variables, F is reduced by 1. As already mentioned, most binary aqueous surfactant diagrams have no pressure dimension. For these diagrams pressure is presumed to be constant (or nearly so) over the temperature span of the diagram. In those cases only 1,2 or 3 phases can exist in a certain point of the phase diagram with $F = 2$, $F = 1$ and $F = 0$,

[4] The weight *fraction* of a system will be the same on the moon as on the earth as it is independent of gravitational forces.

[5] It is better to regard the number of components as being the number of 'compounds' present rather than the number 'molecules' to avoid confusion, which might appear in mixtures with salt. Salt is one chemical compound, but two molecules. The numbers of ions are directly related to each other and cannot be independently varied. Therefore a salt compound is only one component.

respectively. [Laughlin 94, Evans 94]

One-phase region in a binary system In a one-phase region of the phase diagram both the temperature and the composition might be varied by small increments while qualitatively preserving the phase behaviour, but every small change in either direction modifies all the properties of the phase. In other words, the temperature and composition have to be defined, to define the system and its properties. [Laughlin 94, Evans 94, DeHoff 06]

Two-phase region in a binary system In a two-phase region, only the temperature is referred to as a degree of freedom, defining the composition of the system. Changes in composition do not change the individual composition of the two phases, but the relative amount of each phase according to the lever rule (see below). In other words, only the temperature has to be defined, to define the systems and its properties. [Laughlin 94, Evans 94, DeHoff 06]

Three-phase region in a binary system In a three-phase region, the number of degrees of freedoms is zero, therefore both temperature and composition of the phases are unique. [Laughlin 94, Evans 94, DeHoff 06]

The *lever rule* can be used to calculate the relative fractions of the two coexisting phases at any point on a tie-line. If the two phases have composition c_1 and c_2 and the mixture is composition c, the fractions x_1 and x_2 of the two phases are:

$$x_1 = \frac{c - c_1}{c_2 - c_1} \tag{2.3}$$

and

$$x_2 = \frac{c_2 - c}{c_2 - c_1} \tag{2.4}$$

[Laughlin 94, DeHoff 06]

The rule of alternation One of the most important implications of the phase rule is the *rule of alternation*, which must be satisfied providing phase transitions are first order. This is the case for most phase discontinuities involving lyotropic liquid crystal phases. The rule states, that *an alternation between odd and even numbers of phases occurs (in increments of one) along isoplethal and isothermal process trajectories*[6]. This

[6]Process trajectories are paths within a phase diagram along changes in temperature and/or composition.

rule is one of the most important devices available for evaluating whether or not a particular phase diagram is consistent with the phase rule. [Laughlin 94, Rubingh 91]

2.2.2.3 Free Energy Maps

The occurrence of phases, coexistence regions and miscibility gaps can be best understood by introducing the concept of free energy maps.

In the literature both the Helmholtz free energy[7] and the Gibbs free energy[8] are used in this context. The concepts are the same for both free energies. In this work the Gibbs free energy is chosen and will be in future referred to simply as the free energy.

The free energy of a system is defined in Eq.2.5.

$$G = H - TS, \tag{2.5}$$

where H is the enthalpy and S the entropy of the system. The phase of the lowest free energy is the equilibrium phase of the system. At a phase transition between two phases the free energy of both phases are the same, and therefore the transition temperature is defined by the ratio of the difference in enthalpy and entropy of the two systems.

$$T_{tr} = \frac{H_1 - H_2}{S_1 - S_2}, \tag{2.6}$$

where the index 1 and 2 refer to phase 1 and phase 2 involved in the phase transition. The enthalpy of phase 1 is lower/higher than of phase 2 at the phase transition temperature, therefore heat flow to or from the environment is required for the transformation of one phase to the other. The relative fractions of phase 1 and phase 2 at the transition point depend therefore on the energy exchange with the environment. [Laughlin 94, DeHoff 06]

A simple model for the free energy of mixing Certain properties of the free energy curves can be displayed for the simplified case of an ideal mixture and those properties can help to understand more complex, realistic cases. To calculate the free energy of mixing the quasichemical theory of solutions is chosen [DeHoff 06]. In this theory each component is seen as being connected by a bond to a certain number of other molecules Z. In a binary system of components A and B, three of those bonds can form: A-A, B-B and A-B, with the interaction energies E_{AA}, E_{BB} and E_{AB},

[7] Used for systems under constant volume and temperature.
[8] Used for systems under constant temperature and pressure.

respectively. Calculating the relative numbers of each type being $\frac{1}{2}Nc_A^2Z$, $\frac{1}{2}Nc_B^2Z$, Nc_Ac_BZ, respectively, the internal energies before (Eq.2.7) and after (Eq.2.8) mixing can be obtained:

$$U_A + U_B = \frac{1}{2}Nc_AZE_{AA} + \frac{1}{2}Nc_BZE_{BB} \tag{2.7}$$

$$U_{mix} = \frac{1}{2}Nc_A^2ZE_{AA} + \frac{1}{2}Nc_B^2ZE_{BB} + Nc_Ac_BZE_{AB} \tag{2.8}$$

The energy obtained upon mixing is therefore:

$$\Delta U_{mix} = \frac{1}{2}Nc_Ac_BZ(2E_{AB} - E_{AA} - E_{BB}) \tag{2.9}$$

For condensed phases, the internal energy of mixing is negligibly different form the enthalpy of mixing. Furthermore it is useful to introduce the so-called interaction parameter χ, which is defined as:

$$\chi = \frac{Z}{2kT}(2E_{AB} - E_{AA} - E_{BB}) \tag{2.10}$$

The entropy of mixing can be simply calculated as:

$$S_{mix} = c_Aln(c_A) + c_Bln(c_B) \tag{2.11}$$

Therefore the free energy of mixing can be obtained from Eq.2.9 and Eq.2.11:

$$\frac{G_{mix}}{kTN} = g_{mix} = c_Aln(c_A) + c_Bln(c_B) + c_Ac_B\chi \tag{2.12}$$

The form of the dependence of free energy on composition depends on the interaction parameter and can be divided into 3 cases:

- The ideal solution case (χ=0, i.e. bonds to a molecule of the same kind is equally preferred to bonds to the molecule of the other kind): The free energy plot displays a single minimum (see Fig.2.6(a)). The lever rule can be applied to calculate the free energy of the system at composition c depending on if a homogeneous solution or a mixture of 2 phases is formed. The free energy of a mixture of phase 1 and phase 2 is simply the geometrical average of the free energies at concentrations c_1 and c_2 as shown in red in the same figure. In the case of a purely concave curve, for each composition c the minimum free energy will always be at this composition, therefore a homogeneous mixture is obtained over the entire composition range.

- Preferred mixed bonds (χ<0): The free energy plot is similar to the one in the ideal solution case, only the minimum is deeper. Also here a homogeneous mixture is obtained over the entire composition range.

- The case of low solubility (χ>0, i.e. bonds to a molecule of the same kind are preferred over the bonds to a molecule of the other kind): The free energy plot displays two local minima (see Fig.2.6(b)). In this case the common tangent rule (displayed in red in Fig.2.6(b)) has to be applied, locating the composition c_A and c_B. Those compositions are called the solubility limits of the system. In between c_A and c_B a miscibility gap forms. One has to distinguish between 2 cases.

  1. c is within the miscibility gap ($c_A<c<c_B$): the system phase separates to phase A and phase B with their concentration c_A and c_B, respectively. The relative fractions of the phases are according to the lever rule.
  2. c is outside the miscibility gap ($c<c_A$ or $c>c_B$): The situation is similar to the situation of an ideal solution. A homogeneous mixture results in the lowest free energy.

The dependence of the free energy of mixing on temperature As the parameter χ depends on temperature, so too does the free energy plot (see Fig.2.7(a)). Therefore by changing the temperature one can go from one-phase regions into two-phase regions etc, as illustrated in Fig.2.7(b). [DeHoff 06]

In Fig.2.7(b) two characteristic lines are shown. The binodal defines the two stable coexistence phases, while the spinodal separates the region of positive and negative curvature of the free energy curve, dividing it into the metastable region (above the spinodal) and the unstable region (below the spinodal). The spinodal line is important when looking at phase transitions and the occurrence of metastable phases, but is usually not displayed in phase diagrams. The main difference between the stable and metastable region is the way the free energy reacts to fluctuations in composition around composition c (see Fig.2.8). Within the spinodal, every fluctuation of c into $c+\Delta c$ and $c-\Delta c$ leads to a decrease in the free energy. Therefore phase separation is energetically favourable and a solution of concentration c is unstable. In contrast to this in the region between the binodal and the spinodal the negative curvature of the free energy curve causes every local phase separation to result in a higher free energy and therefore is not favourable. In other words a solution of concentration c can be metastable. This situation is typical for a nucleation and growth process, where a nucleation barrier has first to be overcome to govern phase separation into the two equilibrium states.

The formation of different phases of mixture As already mentioned in a binary system various phases can develop upon mixing. Each of these phases has its own free energy curve. Therefore, at a given temperature, not just one free energy plot has to

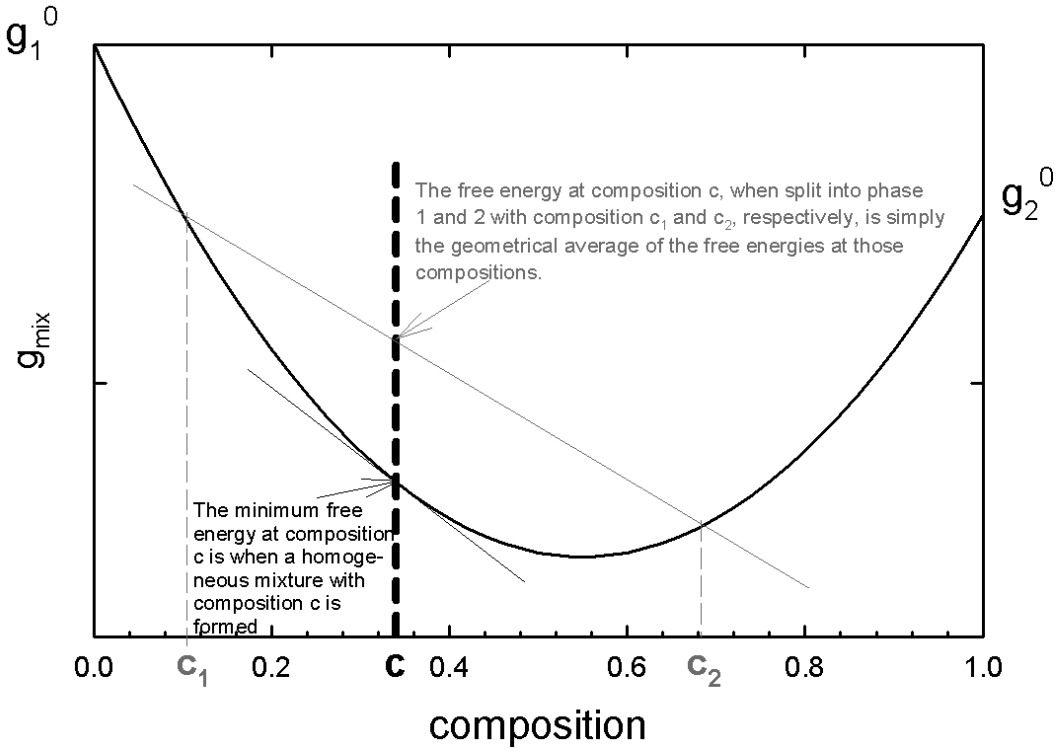

(a)

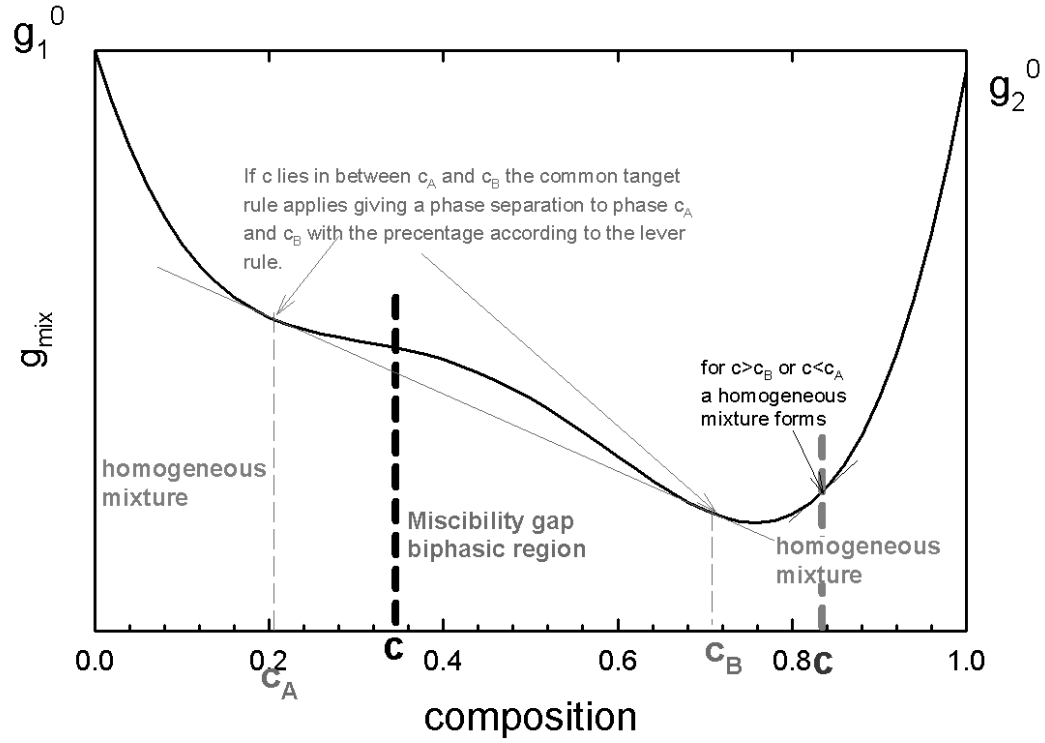

(b)

Figure 2.6: Typical free energy plots for a) an ideal solution and b) a poor solution.

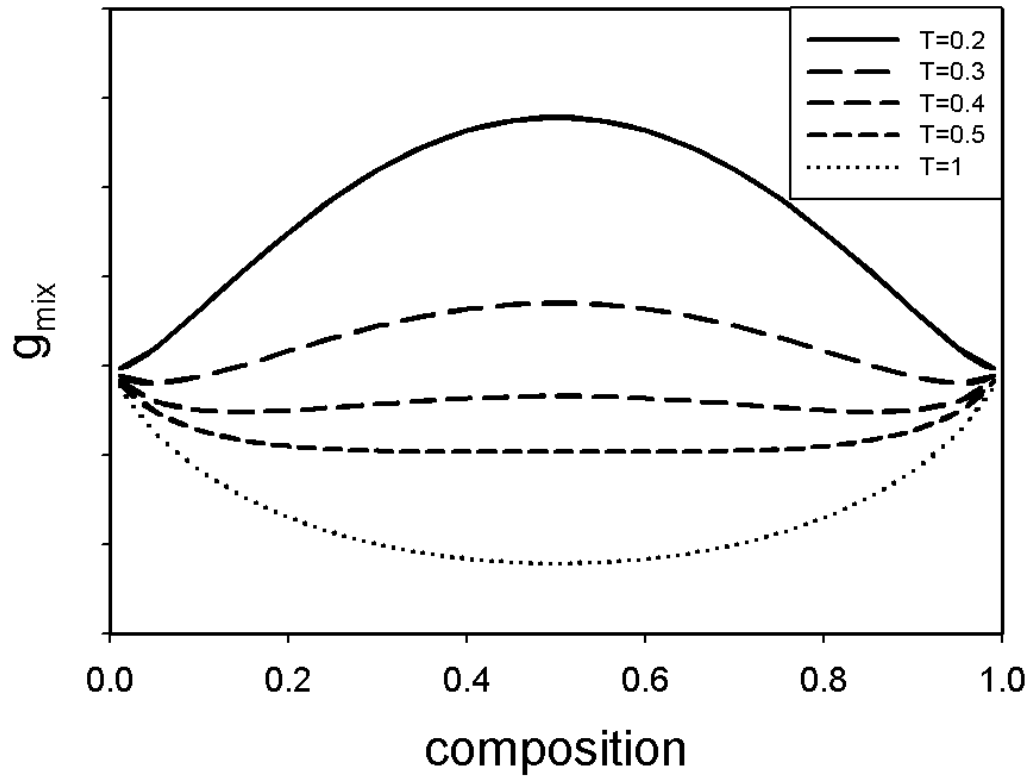

(a)

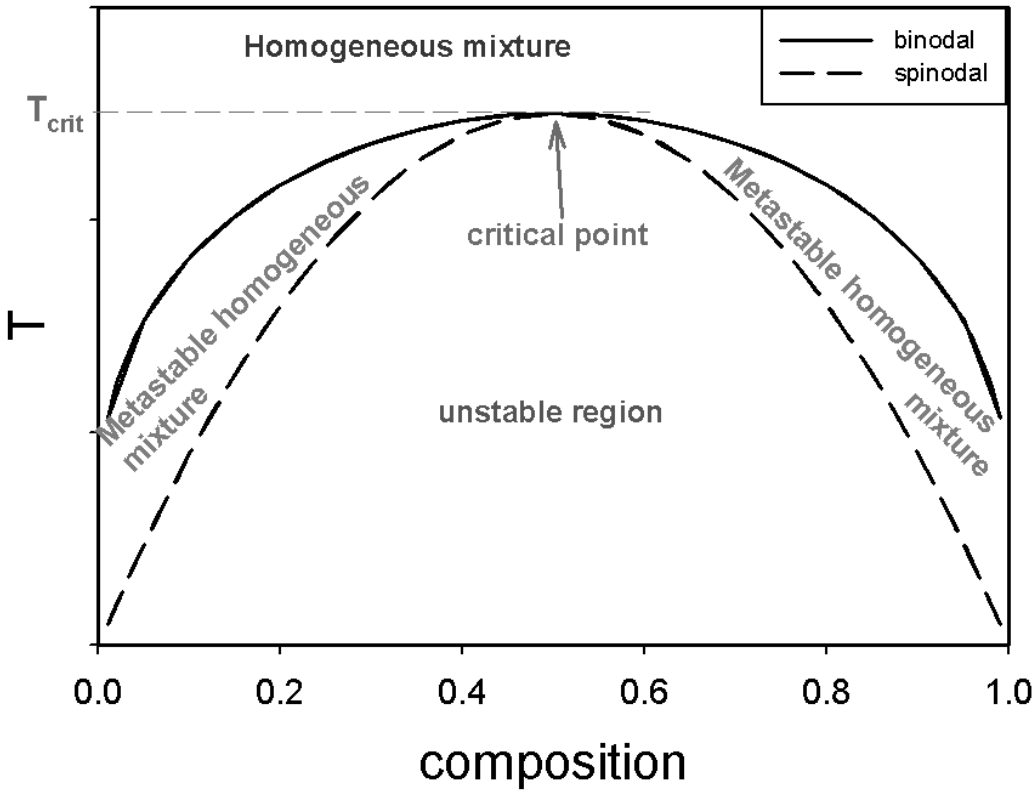

(b)

Figure 2.7: The temperature dependence of the free energy (a) leads to biphasic regions in certain parts of the phase diagram (b).

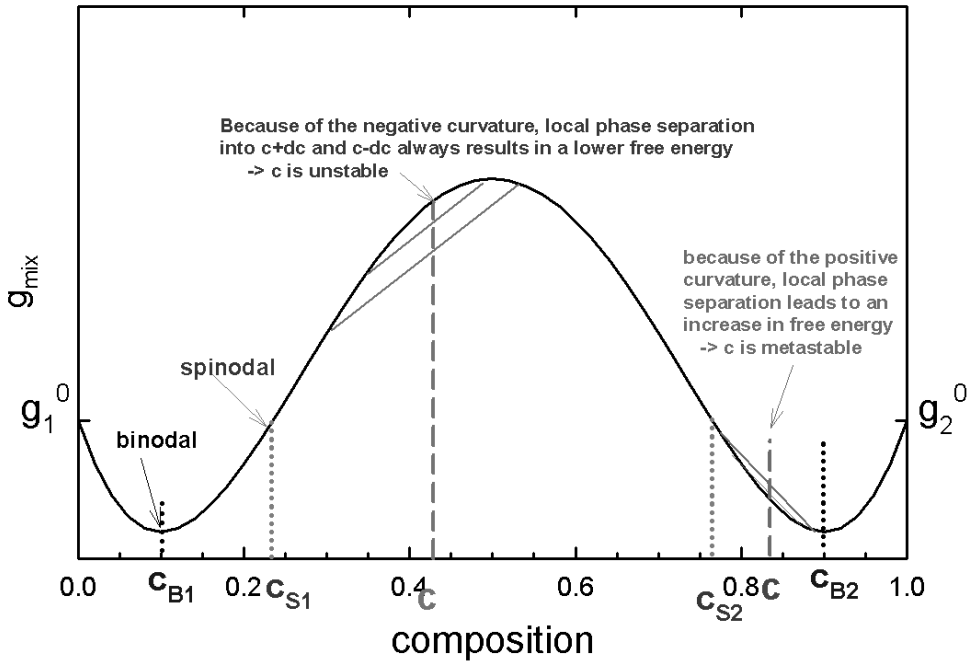

Figure 2.8: Plot illustrating the spinodal decomposition (green) and the metastability of the region between the spinodal and the binodal (red).

be taken into account, but the free energy of every phase has to be plotted separately against a certain reference state [DeHoff 06], as shown in Fig.2.9. Each of these plots refers only to one isothermal line in the corresponding phase diagram. As shown in Fig.2.9, phases can coexist with each other over a certain composition range.

As can be seen the Fig.2.9, in the case of a phase coexistence over a larger composition range, the free energy of each phase is not the same. However the slope of the free energy curve stays constant over the whole composition range of the coexistence region. This implies that the derivative of the free energy over composition, being the chemical potential, is constant within region A+B. In other words the chemical potential of component 1 in phase A at the lower phase boundary or region A+B is the same as the chemical potential of component 1 in phase B at the higher phase boundary of the coexistence region. The same is true for component 2. [Laughlin 94, DeHoff 06]

2.2.2.4 The Krafft boundary

The phase diagram is divided into a lower and higher temperature region by the Krafft eutectic, which is the upper limit of the Krafft boundary. Liquid crystal phases may exist as equilibrium phases only in the upper temperature region. Within the lower temperature region only liquid and crystalline phases occur, liquid crystalline phases

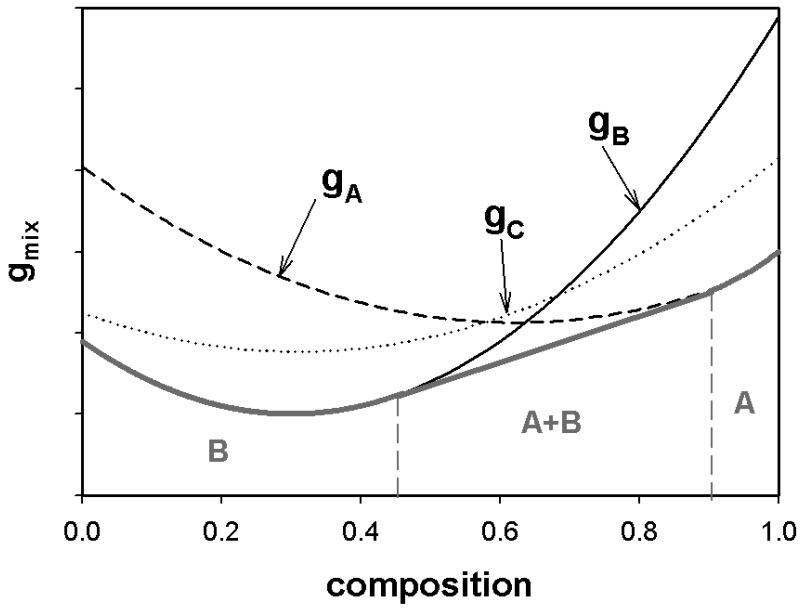

Figure 2.9: Thermodynamic behaviour generated by the interplay of three phases. Phase A is stable at low concentrations, phase B is stable at high concentration. In between is a coexistence region of phase A and phase B. Phase C does not occur as an equilibrium phase in the phase diagram, because of its comparably high free energy.

would be metastable. [Laughlin 94]

The Krafft boundary has a distinctive shape (see Fig.2.10). The slope of this boundary is very steep at low temperatures. With increasing temperature a turnover (knee) develops, above which a plateau exists. The plateau terminates at its upper limit at a eutectic discontinuity, called the Krafft discontinuity or Krafft eutectic. The shape of this boundary (including the turnover) might result simply from the necessity to smoothly connect the low temperature arm with the coexisting liquid phase at the Krafft eutectic, the temperature of which is defined by the thermodynamic properties of the coexisting liquid, liquid crystal and crystal phase at this eutectic. Another argument involves the fast changes in solution temperature associated with micellisation. This idea evolves from the fact that the CMC falls, in most cases, into the region of the knee of the Krafft boundary. Thus, below the temperature of the CMC Krafft point instead of a micellar solution a molecular solution is present in the liquid phase. [Laughlin 94]

In the region below the Krafft boundary a liquid always coexists with a crystal (dry crystal or crystal hydrate, see section 2.2.3.1). Therefore, this boundary is often defined as the crystal solubility boundary of surfactants. Consequently, changing the solubility of the surfactant molecule (e.g. by altering the length of the hydrophobic group chain

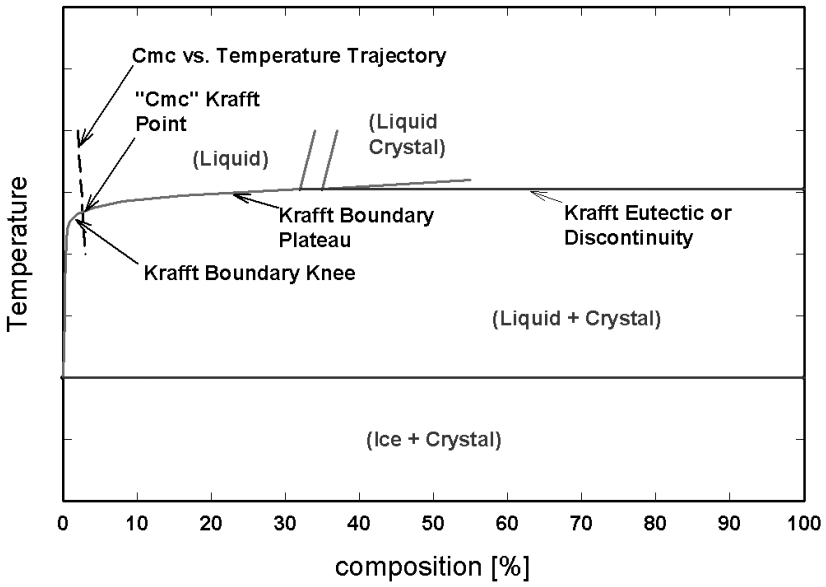

Figure 2.10: The general form of the Krafft boundary: the lower nearly vertical part, the knee, the plateau region and the Krafft eutectic, where it terminates. The CMC Krafft point is the point of intersection of the locus of the CMC versus temperature. [Laughlin 94]

length) influences the position and shape of the boundary. A decreased solubility (longer chains), usually shrinks the composition span of the Krafft plateau (until it vanishes, leaving only the low solubility arm and the Krafft eutectic) and shifts the *Krafft eutectic* to lower temperatures. In some cases it is shifted below 0°C and is therefore affected by the freezing of water. The surfactant crystal phase may persist as an equilibrium phase to temperatures above the Krafft eutectic, but the composition area, in which it is found, decreases with increasing temperature. [Laughlin 94]

2.2.2.5 The structural aspect

The structure of a system under given conditions can be described on several levels: molecular structure, conformational structure, phase structure and colloidal structure. The molecular structure is constant for nonreactive systems (the focus of this work) and depends on the connectivity of the atoms in a given molecule. This structure strongly affects the thermodynamic behaviour. Sometimes relations between the phase diagrams of molecules of similar structure can be extracted (see e.g. part 4 of [Laughlin 94]). The form of a phase diagram directly depends on the molecular structure of its components. Therefore it is crucial to ensure samples of high purity are used for studying phase diagrams and that investigations are carried out only below the thermal stability limit of the samples. [Laughlin 94]

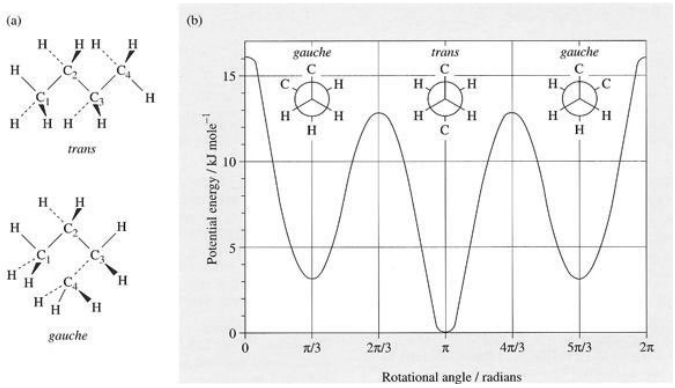

Figure 2.11: a) Trans and gauche conformations of n-butane C_4H_{10} b) potential energy for the rotational isomers of n-butane along the C-C bond [University 09].

The conformational structure can change between phases but also within one phase, depending on the energy barrier between different conformations. In surfactant systems it is predominantly rotations around carbon-carbon bonds within the hydrocarbon chains that are considered, resulting in the formation of 1 trans and 2 gauche (left- and right-handed) conformations shown in Fig.2.11. Within fluid states, only a modest energy barrier hinders the transformation of each of these conformations into another. Taking into account all the C-C bonds present in a given molecule, several million different conformations may coexist in a given fluid phase. Thus the conformational structure of a surfactant is, in general, described on an average (statistical) basis. The presence of the large amount of conformational structures in a fluid phase compared to the single conformational structure in a crystalline phase[9] results in a considerably higher entropy for the fluid phase. Furthermore, more gauche conformations increase the molecular volume of the amphiphile, but shorten the mean length of the chain. Therefore the packing parameter of surfactants depend on the conformation. [Laughlin 94]

The rate at which conformational structure changes is typically extremely fast compared to the rate at which the molecules orientate towards each other forming a specific phase. Therefore once a phase structure is defined the conformational structure (or the statistics between several conformational structures) is fixed. An exception to this are crystalline phases, where the rate at which the molecules adapt their conformation to the phase is slow and therefore the occurrence of metastable polymorphs is likely. For describing a phase (phase structure as well as phase

[9]Only rotations of the methyl groups are facile, which do not change the conformation of the molecule, but lead to an increase in entropy.

transitions) one has to take into account its macroscopic nature. None of these descriptions can be applied to isolated molecules. [Laughlin 94]

It should be mentioned that from a structural point of view, a phase does not have to look the same under all conditions, even so its phase structure should be defined. This is due to the occurrence of domain structure or, for a multiphase system, the possibility of arranging coexisting phases in various ways in space (in general, the colloidal structure of the system). Micelles are a good example of colloidal structure in a one-phase system. From a thermodynamic point of view, the dilute liquid phase does not change going from a monomer solution into a micellar solution at the CMC. However the changes in structure lead to a change in certain physical properties of the solution such as its surface tension. [Laughlin 94]

2.2.3 Surfactant Phases

Aqueous surfactant phases can be divided into 3 classes based on their structure: crystals, liquid crystals and liquids[10]. This work focuses on crystalline and lamellar phases (which fall into the class of liquid crystals). The next two sections will focus on the properties of those phases.

2.2.3.1 Crystalline phases

Surfactants in a crystalline state possess usually a bilayer structure (see Fig.2.12(a)). This is caused by the amphiphilic nature of the molecules. For a few systems other structures have also been reported as the interdigitated crystal structure, the monolayer crystal structure and the midchain monolayer crystal structure (see Fig.2.12(b), 2.12(c), 2.12(d)). A unit cell contains at least one pair of surfactants and may contain a certain number of water molecules in the case of hydrated crystals. [Laughlin 94]

The alkyl chains are generally in an all-trans configuration. Exceptions can be found amongst others in the case of dichain surfactants (see Fig.2.12(a)), which are usually bent near the middle. The unequal lengths of the straight parts of the chains lead to a tilting of the molecules relative to the bilayer plane in the crystal structure. In this case a few specific C-C bonds have to be gauche. Because the van der Waals volume and radius of methyl groups are substantially larger than are those of methylene groups, the closest lateral spacing between chains is smaller than is the closest spacing between juxtaposed planes. Both sizes must vary with temperature and pressure. [Laughlin 94]

[10]The fourth phase, the gas phase, is typically water and is therefore omitted.

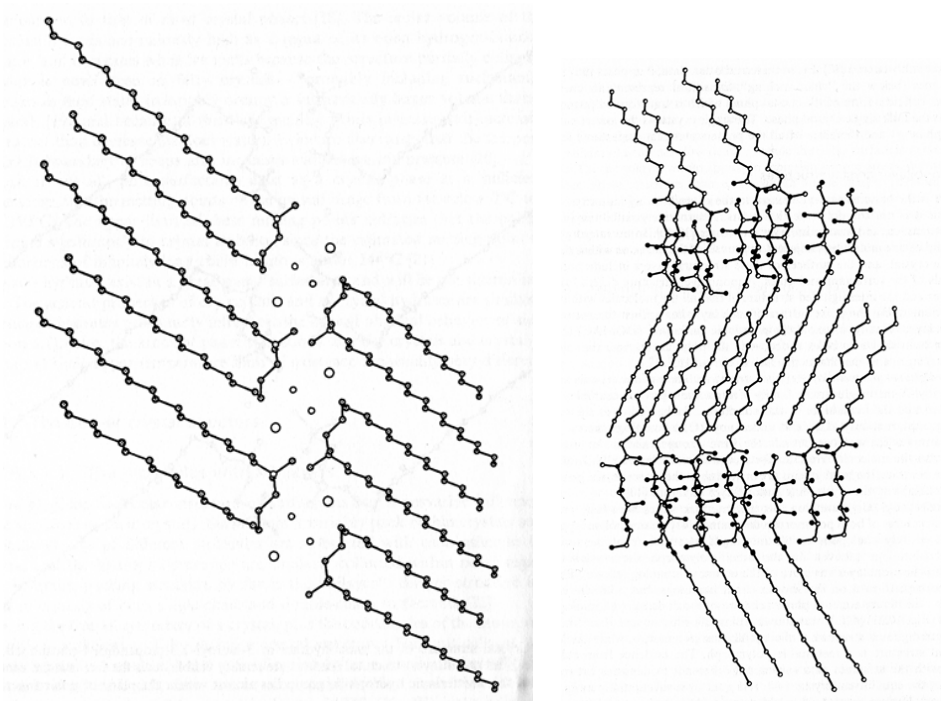

(a) (b)

(c) (d)

Figure 2.12: a) Bilayer crystal structure of dioctadecyldimethylammonium chloride monohydrate, b) interdigitated crystal structure of N-dodecanoyl-N-methylglucamine, c) monolayer crystal structure of the nonequilibrium polymorph of N-dodecanoyl-N-methylglucamine, d) midchain monolayer crystal structure of dioctadecylmethylammonium chloride. [Laughlin 94]

Surfactants in the crystalline state might be either dry or exist in the form of crystal hydrates. Crystal hydrates, which incorporate both components (the surfactant and the water) within one phase, whose composition is stoichiometrically defined, are regarded as phase components. This is a distinct form of miscibility and should not be described as solubility. If the molecules can densely pack within a structure that is space filling, dry crystals are preferred. Crystal hydrates are most probable in crystals of strongly polar surfactants, whose shape does not allow them to pack densely without water being present. Besides the improved packing through the addition of water, water molecules can also interact energetically with polar groups. One should note, that for certain aqueous soap systems also nonstoichometric crystal hydrates have been reported, which means that the amount of water within the crystal can vary within a certain composition range. Because of this, these crystals are often referred to as solid solutions. [Laughlin 94]

The determination of the correct crystal structure in surfactant systems has many challenges, especially the long equilibration times, which might exceed years, the hygroscopic character of many dry crystals and the occurrence of different equilibrium or non-equilibrium[11] polymorphs, which give rise to the occurrence of metastable or wrong crystal structures in the literature. Furthermore only for a single crystal at low temperatures might the crystal structure be near perfect. At higher temperatures non-perfect structured states exist, which might only be approximated by the single crystal studies. Such deviations become more likely near to a phase transition. [Laughlin 94]

For the examination of a crystalline phase under the effect of temperature, the thermal stability of the crystal has to be taken into account. Most ionic surfactant salts do not melt reversibly as the dry crystal, so their melting points cannot be determined. Physical data recorded above the thermal stability limit of a surfactant are meaningless [Laughlin 94]. The thermal stability of surfactants can be significantly enhanced by the addition of water. Moreover, since water often dramatically reduces the melting point of the compound, fluid phases may be accessible in concentrated water-containing mixtures that do not exist with the dry compound. Therefore the knowledge of the correct water content of the sample is crucial for interpreting thermodynamic results. [Laughlin 94]

A last remark has to be given to colloidal structures. As already mentioned, colloidal

[11] Non-equilibrium polymorphs occur often during fast freezing or e.g. if the crystallisation is accompanied by the freezing of water. They are kinetically stable forms and never coexist with the equilibrium crystal structure.

structure refer to micrometer to nanoscale domain structure in one-phase systems, which might differ, depending on preparation. In multiphase mixtures, the arrangement of the phases themselves within the phase, falls into this terminology. There might be different ways of imposing colloidal structure on multiphase systems, some being of equilibrium and some of non-equilibrium nature. The latter states should not occur in phase diagrams. Examples of such states are frozen open bilayer crystallites of up to a few layers or frozen unilamellar or multilamellar vesicles (see section 2.2.3.2). Frozen vesicles might, in some cases, resemble the structure of a bulk crystal, but the bilayer is often just in a more ordered form compared to the one in fluid vesicles. They are an energetic, non-equilibrium colloidal form of a crystal phase, which will, when given the opportunity, transform into the crystalline state. [Laughlin 94]

2.2.3.2 Lamellar phases

It has already been mentioned that aqueous surfactant systems have the ability to form liquid crystalline phases at temperatures above the Krafft eutectic. Liquid crystalline phases are those in which long-range order in 1,2 or 3 dimensions exists (as in crystals) but no short-range order can be found (as in liquids). This means that there is a defined phase structure but the molecules are free to move within this structure, even over long distances. Furthermore, in contrast to crystals, a large range of conformational states are allowed in liquid crystals and the molecules are free to change constantly and rapidly between those conformations. The composition of liquid crystals is not stoichiometrically defined, but might vary over a broad range. [Laughlin 94]

Liquid crystalline phases in aqueous surfactant systems are usually lyotropic in nature, which means that they only form upon addition of a minimum amount of solvent. Therefore, both solvation energy and thermal energy[12] are required for them to form, in contrast to thermotropic liquid crystals, which simply form under the influence of thermal energy. [Laughlin 94]

Several liquid crystalline phases can be distinguished[13], differing in their phase structure. These phases not only occupy defined regions within phase diagrams, but may also coexist with each other or with other phases. The lamellar phase (L_α) plays a central role in the evolution of the structure of liquid crystals. All other liquid crystalline phase structures may be viewed as perturbations of the structure of the lamellar phase due to bending or reshaping either towards the water side or the oil

[12] It has been shown, that all liquid crystals exist only at temperatures above 0K [Laughlin 94].

[13] Theoretically, one can distinguish between at least 18 different liquid crystalline phases [Laughlin 94].

side. [Laughlin 94]

The lamellar phase is structurally similar to the bilayer crystal structure mentioned in the previous section, with a certain amount of water present in between the bilayers[14]. Because of its layered structure, the lamellar phase is one of the smectic liquid crystalline phases. Such phases are birefringent. The birefringence depends on concentration and can become very weak for thin dilute phases. Furthermore, because of defects, which produce domain structure within the mixture, those phases are visibly turbid. Within domains, single-crystal-like order[15] can be found, whilst discontinuities occur at the boundaries. Those discontinuities are responsible for the scattering of light. Smaller domain structure and therefore more defects can usually be found in more concentrated samples, which therefore appear much more turbid. [Laughlin 94, Evans 94]

The mean separation between the bilayers is of high regularity[16], leading to a well defined long-range order in a direction perpendicular to the bilayer of altering water layers and bilayers. This periodicity might depend on concentration (expanding systems), which implies that the area per headgroup changes only slightly, if at all, with composition and therefore the water layer thickness increases with increasing water concentration. In some cases (non-expanding systems), the area per head group increases with increasing water concentration to such an extent that no observable change in periodicity is observed when water is added or removed from the lamellar phase. [Laughlin 94, Evans 94]

The bilayers have, in general, a lower thickness compared to the crystalline phase, caused by the introduction of gauche conformations in the hydrocarbon chains[17]. This thickness changes with the change of the area per headgroup and therefore also with temperature and composition. [Laughlin 94, Evans 94]

Within this bilayer, surfactant molecules can move freely. This is the reason why the bilayer is often described as a 2 dimensional fluid as the movement is mostly within the plane of one monolayer. However, a so-called flip-flop mechanism, where surfactant

[14] In very rare cases, where dry liquid crystals exist, no water might be present in the lamellar phase [Laughlin 94].

[15] Impurities usually concentrate at domain boundaries [Laughlin 94].

[16] Though there are small perturbations of the regularity caused by bending fluctuations of the bilayers.

[17] Only in the case of a large tilt in the crystalline structure, the bilayer might become thicker upon entering the liquid crystalline phase [Laughlin 94].

molecules switch between the monolayers, occurs too. However, this transversal diffusion has been reported for certain systems to be several orders of magnitude slower than the lateral diffusion [Zana 05]. In contrast to transversal diffusion, lateral diffusion depends on the length of the hydrocarbon chain, the head group hydration and temperature [Zana 05]. As already mentioned surfactant aggregates are always in equilibrium with monomers. These molecules can enter and exit the bilayers, leading to a transport of material between the individual sheets, though this process is slow for long hydrocarbon chains [Zana 05, Evans 94].

Bilayers may exhibit undulations. From the microscopic shape of these undulations the elastic free energy can be determined (Eq.2.13)[18]:

$$F(R_1, R_2) = \int_S (\frac{1}{2}\kappa(\frac{1}{R_1} + \frac{1}{R_2})^2 + \overline{\kappa}\frac{1}{R_1 R_2})\, dS, \tag{2.13}$$

where R_i are the principal radii of the curvature of the surface, κ is the mean bending constant and $\overline{\kappa}$ the Gaussian bending constant. Both bending constants depend on the chemical properties of the surfactant as well as temperature and the surfactant concentration. For the bilayer to remain nearly flat, κ must be positive and $\overline{\kappa}$ must be in the range $-2\kappa < \overline{\kappa} < 0$ [Roux 92].

Furthermore, in the case of $k_B T < \kappa$, the membrane will not be susceptible to thermal fluctuations. Otherwise, thermal fluctuations become important and push the bilayers further apart. These forces are called steric or undulation forces. The free energy of a multibilayer system, which interacts solely through repulsive steric interactions, depends on the fraction $\Phi = \delta/d$ of the bilayer repeating distance d and bilayer thickness δ [Helfrich 78]:

$$f(\Phi) \sim \frac{(k_B T)^2}{\kappa} \frac{1}{(1-\Phi)^2} (\frac{\Phi}{\delta})^3 \tag{2.14}$$

Therefore, a lamellar phase where bilayers interact mainly by steric repulsion, will reach its minimum free energy when the distance between the bilayers is infinite ($\Phi \rightarrow 0$). However, the effect of attractive forces, such as van der Waals forces, must also be taken into account. For small Φ, adding this term to Eq.2.14 leads to [Milner 92]:

$$f(\Phi) = \frac{3\Pi^2}{128} \frac{(k_B T)^2}{\kappa} \frac{1}{(1-\Phi)^2} (\frac{\Phi}{\delta})^3 - k_B T \chi \phi^2, \tag{2.15}$$

[18] The first term involves the mean curvature of the bilayer and the second term is the Gaussian curvature (the spontaneous curvature is neglected as it is assumed to be zero in our case).

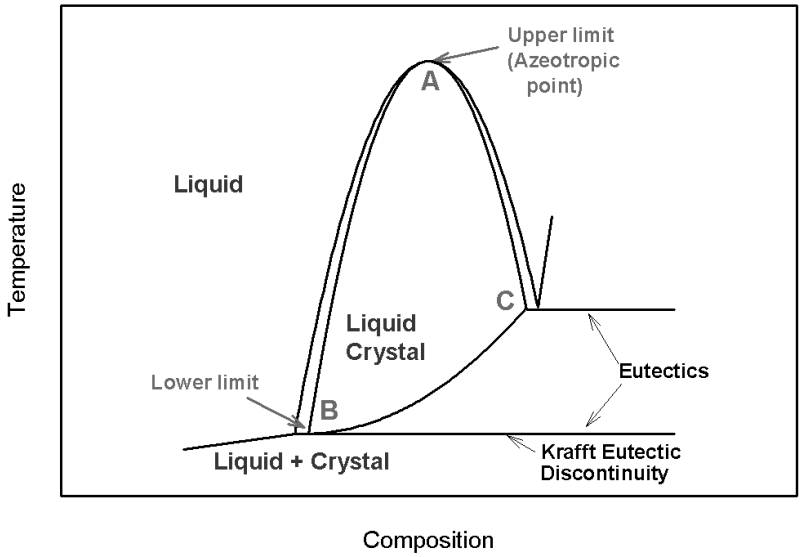

Figure 2.13: The general from of an idealised liquid crystal phase region [Laughlin 94].

where χ is a function of the interaction which, in the case of sufficiently weak enthalpic interactions between patches of layers of volume V, can be calculated by:

$$\chi = -\frac{1}{2V^2} \int 1 - exp(-U_V(r)/k_B T)\, d^3 r, \tag{2.16}$$

where $U(r)$ is the van der Waals interaction between areas of surface [Milner 92].

Even if the geometry allows dilute bilayers at lower concentration, van-der-Waals attractions between bilayers can be sufficiently large to overcome entropy and interbilayer repulsion. This causes phase separation where the water layers do not swell indefinitely (see Fig.2.20). Thus, instead of a dilute solution of large bilayers, a coexistence region between a 'fully swollen' lamellar phase and water[19] is observed.

An idealized form of a liquid crystalline phase in a phase diagram, which exhibits a Krafft-boundary,[20] is shown in Fig.2.13.

The symmetrical bullet shape at the upper part of the phase boundary is due to the typically higher entropy of the liquid compared to the liquid crystal. Apart from at the highest point (A), the liquid phase is separated from the liquid crystal by a coexistence region. At the left site of the liquid crystal, this coexistence region is the

[19] This might be as well a dilute liquid phase.
[20] For the more general case the reader is referred to [Laughlin 94].

solubility boundary, which is above the Krafft eutectic. The coexistence region is narrow for soluble surfactants and broad for poorly soluble surfactants. Only at the upper temperature limit (A), the liquid and the liquid crystal boundaries touch asymptotically at a unique composition. This point is called the azeotropic discontinuity (i.e. that the two coexisting phases have the same composition). An isothermal phase transition between the liquid and the liquid crystal phase can only be observed at such a point, while on either side of the azeotropic discontinuity, a coexistence region has to be passed. Occasionally such an azeotropic point can also be found at the lower temperature limit of the liquid crystalline phase. As a consequence, this liquid crystal region is isolated from other highly structured phases as an island which is completely surrounded by the liquid phase. [Laughlin 94]

However, in most cases, the lower temperature limit (B) is either the Krafft eutectic or another eutectic (in case more than one liquid crystalline phase exists in the phase diagram). Once the liquid crystal is cooled below its stability limit, it transforms into a more dilute liquid (or a liquid crystal of other structure) and a more concentrated crystal phase. There is also just one composition at which the liquid crystalline phase touches the Krafft boundary and again, only at this composition, an isothermal phase transition is observed. If a higher concentration liquid crystal is cooled below its thermal stability boundary, a biphasic region of the liquid crystal coexisting with a crystalline phase has to be passed, in which the liquid crystal becomes progressively more dilute with decreasing temperature. Only below the eutectic discontinuity the liquid crystalline phase is replaced by a dilute liquid phase. [Laughlin 94]

One should note that supercooling is invariably observed when the temperature of the liquid crystalline phase is reduced, and therefore liquid crystals are frequently observed as non-equilibrium states. These nonequilibrium states display a finite limit of swelling, just as do equilibrium phases. Their dilute boundary is an extension of the equilibrium boundary that lies above the eutectic. [Laughlin 94]

At the lower boundary of the liquid crystal its thermal energy and its water free energy is balanced by the crystal free energy. The amount of water required to form a liquid crystalline phase depends on temperature. At high temperatures, where the thermal energy is high, a comparably small amount of water is required to form a liquid crystal (C), while at the low eutectic temperature (B) the level of the chemical potential of the water is the highest that the liquid crystal can tolerate. Therefore, the liquid crystal concentration at this point is the most dilute that exists. Further addition of water leads to the formation of a more dilute liquid phase or a liquid crystalline phase of a

different structure. [Laughlin 94]

The higher composition limit of the liquid crystal (C) lies on another discontinuity, below which the coexisting phase is a crystal, while above, either a different crystal or liquid crystal or occasionally liquid phase is formed. The fact that there is an upper limit indicates that a minimum amount of water free energy is required for the liquid crystal to exist. Some dry crystals can also exist in a liquid crystalline form. Only in this case, the liquid crystal region terminates at the right-hand side boundary of the phase diagram. [Laughlin 94]

The gel phases In some surfactant systems, special forms of the lamellar phase have been reported [Levine 72, Zana 05, Israelachvili 98, Silver 86]: the L_β phase, the L'_β phase and the P'_β phase[21] (see Fig.2.14). The common property of all these phases (gel phases), is the highly decreased fluid character of the bilayer. All dynamic processes are several orders of magnitude slower within these phases than in the fluid L_α phase [Zana 05, Lentz 76, Blume 91, Silver 86]. The hydrocarbon chains are packed in a 2D hexagonal lattice [Blume 91, Silver 86]. Due to the closer packing of surfactant molecules, the volume of the bilayer in the gel-phase decreases [Heimburg 03]. This also leads to a significant decrease of the permeability of the bilayer[22] [Volodkin 08].

Even though the bilayers in a gel phase resemble a crystalline bilayer, due to their order in packing and in showing essentially no lateral diffusion, they are generally distinguished from crystalline phases. The liquid character of the phase could be caused by a significant, but minor, proportion of molecules which have some configurational freedom, although most hydrocarbons will be in an all-trans conformation [Jones 05].

It should be mentioned, that amongst other things the coexistence relationship of these phases with the crystalline phases in the phase diagrams is not clearly understood and it is still uncertain whether or not these phases should be regarded as liquid crystals [Laughlin 94].

The difficulty originates in the long equilibration times needed for phases below the Krafft eutectic to form. This leads, not only to the occurrence of metastable phases, but also to colloidal phase structures, which might resemble a lamellar phase, whilst just being a dispersion of crystals in a dilute fluid phase. For some systems, the reported gel

[21] This phase has been sometimes described as a phase in which a periodic arrangement between liquid and gel domains coexist [Heimburg 03, De Meyer 09, Qin 09, Riske 09].

[22] This property has been used to design new quasi-2D biocompatible films able to release a drug in controlled manner by a temperature increase into the L_α phase [Volodkin 08].

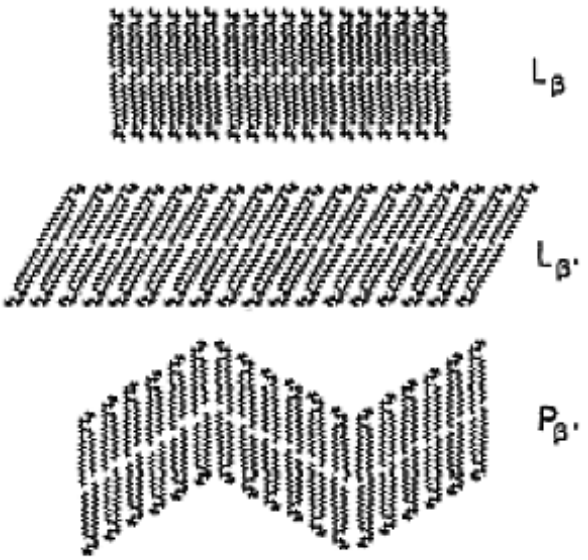

Figure 2.14: Typical structures of the gel phases L_β, $L_\beta^/$ and $P_\beta^/$.

phases could be shown to be very stable non-equilibrium phases, which are caused by overcooling of the fluid lamellar phase [Kawabata 09,Howe 08,Garidel 01,Wilkinson 84, Seddon 83, Tenchov 01]. On the other hand, for the DODMAC system, the reported gel phases could be shown to be caused by a colloidal structure superposed onto the crystal-liquid crystal coexistence region [Laughlin 94,Laughlin 92].

There is not a clear picture describing the 'melting' of such gel phases into the L_α phase. Close to these phase transitions a softening of the membrane and strong fluctuations in e.g. the volume and composition[23] [Lemmich 96, Nagle 98, Rheinstädter 06, Heimburg 03,Levine 72,Gedig 08,Kharakoz 00,Jones 05,Pabst 04] as well as a critical swelling of the water layers have been observed [Chen 97,Mason 00,Pabst 04,Richter 99]. This all leads to the discussion of whether the melting of the bilayers occurs via a 1^{st} order phase transition [Castelli 08,Kharakoz 07,Blume 91,Kharakoz 00,Leekumjorn 07], a 2^{nd} order one [Kharakoz 07, Chizhikov 06] or a 1^{st} order transition close to a critical point [Lemmich 96,Mason 00,Richter 99, Chen 97]. If vesicles are investigated instead of open bilayers, the phase transition appears over a broader temperature range [Lentz 76]. This could be explained by the distribution of vesicles of different sizes [Koynova 98] and its effect on lowering the cooperativity [Blume 91,Biltonen 90]. Also, the addition of other molecules leads to a broadening of the phase transition

[23]Those fluctuations also lead to an anomalous increase in water and ion permeability close to the phase transition temperature [Nagle 98].

[Lindström 06, De Gaetani 07, D'Angelo 08, Chowdhry 84].

The transition temperature between the gel phases and the fluid lamellar phases often falls in a temperature regime which might be of biological relevance [Heimburg 03]. This leads to a formation of domains in the multicomponent membrane, differing considerably in lipid content and physical properties. The L_α phase is considered as the most important bilayer phase as many biologically relevant processes occur in this phase. Those bilayers provide an efficient, planar permeability barrier, which still allows functional flexibility and lateral diffusion motions of associated membrane proteins [D'Angelo 08]. In contrast to this, the gel phase shows, amongst other things, a reduced binding affinity to proteins [Han 09, Wu 09].

Vesicles Vesicles are the form of bilayers which resemble the cell membrane most. They consist of one (unilamellar vesicles) or several (multilamellar vesicles or liposomes) bilayers, which are closed and form the surface of a sphere, which is filled with water (or a dilute liquid phase).

Unlike micelles, vesicles are non-equilibrium structures in binary aqueous surfactant systems [Laughlin 97, Bergmeier 97, Zana 05]. The non-equilibrium character results from the bending energy of a surfactant monolayer. A surfactant monolayer takes up a curvature equal or close to its spontaneous curvature, whose value depends on the surfactant chemical structure and the interaction between surfactants. Therefore, only flat bilayers (zero curvature) can be thermodynamically stable. This is different for systems consisting of more than one surfactant. In that case, the inner and outer monolayer can have different compositions.

Vesicles in binary surfactant systems are therefore colloidal structures, which exist either in a lamellar-liquid coexistence region or in a dilute lamellar phase [Laughlin 97]. The formation of this structure requires the input of a certain amount of thermal or mechanical energy [Bergmeier 97, Laughlin 97].

However once formed, vesicle systems are of great stability and therefore can be characterised almost like an equilibrium state. The bilayers in the vesicle systems can also undergo a phase transition into a gel phase. Furthermore in mixed vesicle systems, coexistence regions of ordered and disordered domains are found, which resemble the domain structure in the cell membrane [Wunderlich 78, Gordon 08].

In the case of surfactants with two long alkyl chains (i.e. poorly soluble surfactant

systems) the existence of a critical vesicle concentration (CVC) instead of a CMC is often mentioned. This implies that, already at low concentrations, a lamellar phase is formed, which coexists with a monomer solution. The existence of a CVC is highly contested in the literature. Its opponents claim that (disk-like) micelles might be present in such a narrow range of concentration as to go undetected by the presently available techniques. [Zana 05]

2.3 Phase transitions and metastable states

The equilibrium phase behaviour, as well as some aspects of the transitions between the equilibrium phases or the occurrence of metastable states in surfactants systems have been discussed within the previous sections. In this section, some general features of phase transitions will be summarized. Two models describing phase transitions, which will be of interest in this work, as well as a metastable state, which occurs during one of those processes, will be described.

In general one has to distinguish between isoplethal paths of phase transformations (i.e. keeping the composition constant) and isothermal paths (i.e. keeping the temperature constant). The case of changing both composition and temperature involves more complex transition behaviour and will not be discussed in this section. On a process path of phase transformation, one can pass three different regions: a one-phase region, a two-phase region and a three-phase region. Only at a one-phase region, the properties of the phase vary smoothly and continuously. For example, if the composition is changed, all mixtures of the composition are formed, the phase is simply dissolved. In contrast to this, if a two-phase or a three-phase region is entered, immediately the coexisting phases are formed, which involves a change in composition between the phases. This is, therefore, not a smooth process. The two-phase region at an azeotropic point is an exception to this.

In an ideal scenario, i.e. if the speed of changing the temperature or composition is slow enough to allow the system to reach equilibrium after each change, the phase reaction follows strictly the equilibrium phase behaviour and at each step the phases present can be predicted from the existing phase diagram.

However kinetic phenomena are often observed. These can be influenced by the required mass and heat transport in the system, which is strongly dependent on the system properties, such as the viscosity, particle size, surface area etc. or on the differences in entropy between the phases.

2.3.1 Nucleation and Growth

The thermal transition of an ordered phase (e.g. crystal) from a disordered system (e.g. liquid) is often described as a process of nucleation and growth. The formation of nucleation centres is required for the transition to proceed. Overcooling is therefore frequently observed in systems in which no nucleation sites are found.

The nucleation and growth mechanism can be described in two steps [Mullin 01, Nyvlt 71, Adkins 83]:

1. The formation of nuclei (e.g. small particles having the crystal structure)
2. The growth of the nuclei

The critical nuclei size (above which the nuclei start to grow) decreases with increasing degree of overcooling. However, if the temperature is too low, only limited formation of nucleation points can be found.

The nucleation rate can be further enhanced if nucleation sites exist in the system (non-spontaneous nucleation) [Nyvlt 71, Laughlin 94]. Those can be e.g. interfaces with other solid substances. In the case where there is control of the nucleation sites, the growth is highly reproducible.

Once a nucleus is created its growth is determined by the following steps [Nyvlt 71]:

1. Transfer of particle from the solution to the crystal surface
2. Movement of the particle
3. Embodiment of the particle into the crystal lattice

The growth rate of nuclei L depends, among other things, on the degree of supercooling, the relative velocity of the crystal with respect to the solution, the temperature and the character of the crystal surface [Nyvlt 71]. For small degrees of supercooling L increases linearly or exponentially with the degree of supercooling until a maximal value is reached. This value is maintained until the degree of supercooling is very large, which leads then to a decrease in L. This decrease might be caused by the increase in viscosity in the system [Nyvlt 71]. The rate depends highly on the way the crystal phase spreads into the solution (see Fig.2.15) [Hemminger 89]. The time dependence of the growth is affected by various properties of the system. A list of fitting equations can be found in [Hemminger 89].

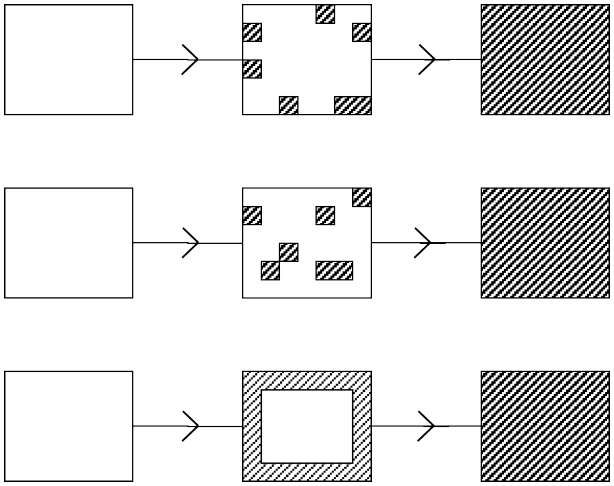

Figure 2.15: Types of nucleation growth: nuclation at the surface (top), nucleation in the whole volume (middle) and a surface activated transition (bottom) [Hemminger 89].

2.3.2 Dissolution (Leng model)

The process of dissolution in surfactant systems along an isothermal path, especially lamellar phases, is another non-equilibrium process, which finds wide attention in research due to its occurrence in our everyday lives. In [Leng 06], a model describing the dissolution process of lamellar phases is presented. This model has been developed for a special case: myelinic figures which grow at the sample interface into the surrounding water. In chapter 6 we will discuss the possibility to extend this theoretical description to the general case of the dissolution of lamellar phases.

The model describes a macroscopic sample of lamellar phase consisting of a large amount of bilayer stacks. The volume of a nicely ordered lamellar stack can vary over a large range - it can be very small up to a macroscopic size, if the sample is gently prepared. These bilayer stacks are randomly oriented as is also the orientation of the sample/air interface. Therefore defects, not only within the bilayers but also between the individual stacks, can be found in a sample.

If a droplet of lamellar phase is contacted with pure water, a dissolution process starts (see Fig.2.16). Water flows between the bilayers as well as along the defects pushing the bilayers further apart due to a force perpendicular to the flow velocity. As already mentioned, the water flow through a bilayer is negligible, therefore one can assume the bilayers to be impenetrable walls, which can only be shifted and bent. If all bilayers were oriented parallel to the droplet edge (assuming a perfect circle in 2-D), one could assume

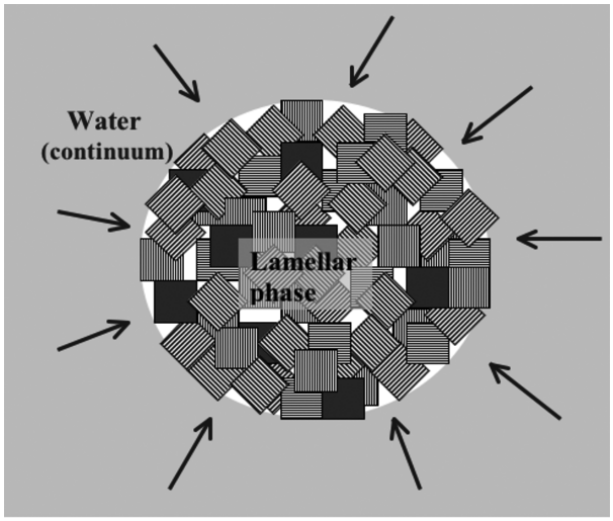

Figure 2.16: Dissolution of lamellar phase (not in scale) into a large water reservoir.

not to have any flow [Benton 86, Zou 06]. In this case, water would just exert a pressure on the droplet. But in the more common case, there are also bilayer stacks, which are oriented perpendicular to the droplet edge, through which the initial flow starts, forcing a swelling of these stacks. Furthermore there is an additional flow through the defects. Therefore the stacks which are not open to the water reservoir by orientation can also swell. Bilayers move apart up to the point at which they are at a distance where the repulsive forces are counterbalanced by the attractive forces. This leads to an increase in the whole droplet size due to volume conservation.
The initial flow through defects seems to be important for ensuring the start of the whole dissolution process.

2.3.2.1 Swelling kinetics due to mass conservation

As mentioned, the droplet of initial surfactant concentration ϕ_s^0 swells as water penetrates the surfactant phase and therefore, because of volume conservation, the lamellar patches must move apart. The model assumes the composition to be fixed by x=R, where R is the initial droplet radius. Furthermore, the surfactant phase which leaves the initial droplet contour is assumed to be fully swollen[24] having no flow between its lamellar sheets (in the case of the appearance of myelins, this is experimentally proven [Buchanan 99, Buchanan 00], see Fig.2.19). The swelling rate of the droplet can then be written as

$$\phi_{fs}\frac{\partial L_s}{\partial t} = j_{fs}(x = R), \tag{2.17}$$

[24]Only surfactant systems having a water-lamellar phase coexistence region are considered.

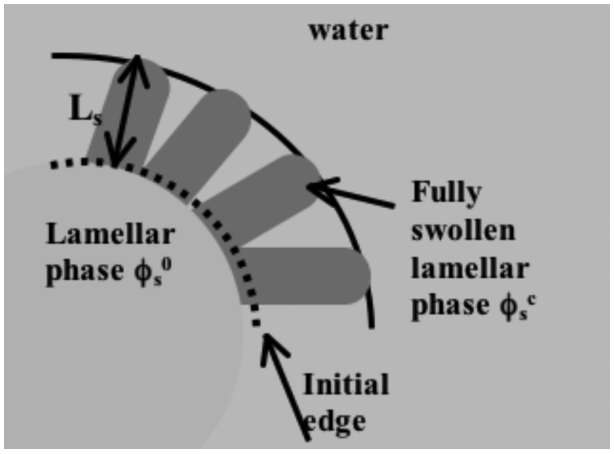

Figure 2.17: Definition of the swelling length L_s.

where $j_{fs}(x{=}R)$ is the volumetric flux of the fully swollen surfactant phase, i.e. surfactant molecules and intrabilayer water, and ϕ_{fs} is the volume fraction of the fully swollen lamellar phase (thus, in the case of myelins ϕ_{fs} equals the volume fraction of a close-packed assembly of cylinders) [Leng 06].

The length L_s is the distance between the initial droplet edge and the new edge. This distance is independent of our geometry, as shown in Fig.2.17 (keeping in mind, that the radius is large compared to the myelin diameter, i.e. the droplet surface is essentially flat as far as the myelins are concerned).

Mass conservation leads to

$$j_{fs}(x = R) = -j_w(x = R), \tag{2.18}$$

where j_w is the volumetric flux of water. Furthermore, for particle flux one knows that

$$\frac{\partial \phi_i}{\partial t} = -\nabla(j_i) \tag{2.19}$$

and

$$j_i = -D_i \nabla(\phi_i), \tag{2.20}$$

where $i{=}fs,w$ and D_i is a composition dependent interdiffusion coefficient. Its changes with time are neglected by considering only the initial swelling of the droplet.

Combining Eq.2.18-2.20 and neglecting the spatial dependence of the diffusion coef-

ficient gives a simple diffusion equation

$$\frac{\partial \phi_w}{\partial t} = D \frac{\partial^2 \phi_w}{\partial x^2} \tag{2.21}$$

describing the diffusion of the volume fraction of water close to the initial edge. The boundary condition is that at x=R, a lamellar phase is formed which is fully swollen:

$$\phi_w(x = R, t) = \phi_w^c, \tag{2.22}$$

where ϕ_w^c is the water concentration of the fully swollen lamellar phase. The initial conditions are

$$\phi_w(x < R, t = 0) = \phi_w^0 \tag{2.23}$$

and

$$\phi_w(x > R, t = 0) = 1 \tag{2.24}$$

This equation can be solved resulting in a water flux at the initial interface [Leng 06]

$$j_w(x = R, t) = (\phi_w^c - \phi_w^0)\sqrt{\frac{D}{\pi t}} = \Delta\phi_w \sqrt{\frac{D}{\pi t}} \tag{2.25}$$

Combining Eq.2.25 with Eq.2.17 and Eq.2.18 we obtain the kinetics of the swelling

$$L_s(t) = 2\frac{\Delta\phi_w}{\phi_{fs}}\sqrt{\frac{D}{\pi}t} = \sqrt{St}, \tag{2.26}$$

where S is the swelling coefficient of the sample.

2.3.2.2 Water flow between bilayers

In the model described above, the driving force for the whole process is the chemical potential difference $\Delta\Pi$ between the initial surfactant phase and the surrounding water. On the other hand, the flow of water into the lamellar phase is limited by its mobility λ_w [Leng 06].

One can write the following equation connecting the diffusion coefficient D (see Eq.2.26) with the osmotic pressure and the mobility of water in the lamellar phase [Leng 06]:

$$D = \phi_w^2 \xi_w \frac{\partial \Pi}{\partial \phi_w}, \tag{2.27}$$

where ξ_w is the slip coefficient of the water flow between the bilayers.

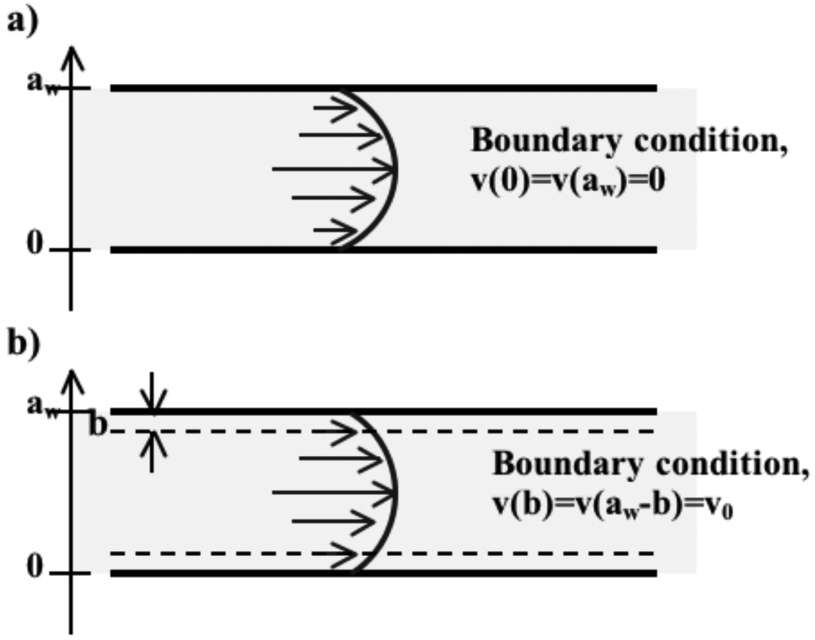

Figure 2.18: Poiseuille flow between 2 bilayers with no flow on the boundary (a) and between 2 bilayers having a hydration layer with a small flow on the boundary (b).

The simplest way to calculate the slip coefficient between lamellar sheets is to assume a Poiseuille flow between two fixed bilayers being separated by a water layer thickness a_w, as shown in Fig.2.18a. This gives the following equation [Brochard 75, Brochard-Wyart 74]:

$$\xi_w = \frac{1}{12}\frac{a_w\rho_w}{a_w\rho_w + \delta\rho_s}\frac{a_w(a_w+\delta)}{\eta} \overset{\delta<<a_w \; or(\rho\approx 1)}{\longrightarrow} \frac{a_w^2}{12\eta}, \tag{2.28}$$

where δ is the thickness of the bilayers, η is the viscosity of water and ρ_i is the density of the surfactant (s) or water (w).

Hydrodynamic calculations assume water to be a continuum. Looking at water layer thicknesses which go down to a width of a few nanometers, this assumption might seem not to be valid as suggested by [Poynor 06, Zhu 01]. In contrast to those opinions, measurements of the fluidity and viscosity of ultra-thin water films performed by Raviv et al. have shown that down to a thickness of 2-3nm the viscosity of water is the same as in the bulk [Raviv 01, Raviv 02, Raviv 04]. Therefore we assume a validity of hydrodynamic calculation and properties down to this thickness.

The flow described above is simplified to a high order. Leng *et al.* [Leng 06] propose a more accurate version (see Fig.2.18b). A probable hydration layer (which can be

determined experimentally) is a layer of water, which is bound to the bilayers and will therefore not move. This is taken into account when describing the Pouiseuille flow in the water filled gaps between the bilayers. An effective water-layer thickness $a'_w = a_w - 2b$, where b is the thickness of the hydration layer, is introduced. The hydration layer depends also on composition and is approximated by

$$b(\phi_w) = b_0(1 - \exp(-\phi_w/\phi_0)), \tag{2.29}$$

where b_0 and ϕ_0 are dependent on the surfactant system (e.g. for lecithin $b_0 = 0.2nm$ and $\phi_0 = 0.16$ [Leng 06]).

In addition, the flow of water at the hydration layer can differ from zero, being ν_0, with a slip coefficient $\xi^{/}_w$ of [Leng 06]

$$\xi'_w \approx \xi_w(1 + 6\frac{\epsilon}{a'_w}), \tag{2.30}$$

where ϵ=$h(\nu_0)$−$h(0)$ is the distance between the water-hydration layer interface and the place where the velocity is zero (see Fig.2.18).

Furthermore, the mobility might be influenced by the presence of defects which occur in the lamellar phase [Leng 06]. These defects could be modelled as cylindrical tubes of radius a perpendicular to the interface. The slip coefficient of the flow inside the defects is:

$$\xi_T = \frac{a^2}{8\eta} \tag{2.31}$$

2.3.3 Interface instabilities: Myelin formation

As already mentioned, during the dissolution process of lamellar phases[25], myelin instabilities can form (see Fig.1.2). Myelin figures have been reported since the 18th century, being one of the first liquid crystals observed. George-Luis LeClerc (Compte de Buffon, 1707-1788) compared the fascinating structures to writhing eels [Palffy-Muhoray 07, Oswald 05]. About a century later, myelins gained their name for the German physician Rudolf Virchow [Virchow 54]. His first contact with myelinic figures was while studying dead human tissue. After boiling the tissue down, he added it to water and observed it under a microscope. The idea was that, by doing this, one would break down the 'components' in the sample and, when added to water, these components would diffuse away. Therefore the components of the sample could be

[25]The lamellar phase does not have to consist of surfactant molecules. The myelin formation from aqueous block copolymer systems has also been reported in the literature [Battaglia 06, Battaglia 07].

observed and identified. While observing pieces of brain tissue dissolving, he saw nerve-like fibres extending from the samples and protruding into the solvent - he named these myelins.

The reason for obtaining the myelins was that there are many lipid membranes present in brain and lung tissue. After boiling, the lipids were essentially purified into a more concentrated state and upon the addition of water they reorganized into a lamellar phase. As the lamellar phase continued to swell, the myelin instability formed at the interface.

Soon it was understood that the observed myelinic figures were not nerve fibres but a liquid crystalline form of a lipid-water system [Neubauer 67, Rinne 33, Nageotte 36]. However, there is a remarkable similarity, not only in structure between the 'artificial' and biological myelin, but also in some of their physical properties, which will be discussed in the end of this chapter. Up until then, all further comments regarding the structure etc. will refer only to the 'artificial' myelin (the myelin).

It is well known that myelins are multibilayer tubules with alternating layers of water [Stoeckenius 59, Nageotte 36, Sakurai 77, Sakurai 90] of a width of a few tens of microns (see Fig.2.19). Myelins can sometimes fuse together, still keeping their original centres(see on the left in Fig.2.19). Individual myelins are connected on the contacting surface [Sakurai 77, Sakurai 90]. The centre of the myelin has been reported to consist of a water core of the order of a micron size for lecithin [Sakurai 90]. In contrast to this picture, [Kennedy 05] observes no sizable water core for the nonionic surfactant $C_{12}E_3$. The thickness of the myelin tubule has been reported to be the same as the thickness of its parent, stacked-bilayer [Zou 06]. Therefore the observed variations in myelin thickness around a sample could be attributed to the fact that the initial material contained many lamellar domains of various sizes. Upon cooling below T_m, myelins can adopt an angular configuration, lose water and the lamellar phase becomes rigid [Nageotte 36, Tiddy 82] (see bottom of Fig.2.22).

Myelins grow when water penetrates a sample of a concentrated surfactant solution, which has, on its isothermal path of dissolution for low concentrations in the phase diagram, a large coexistence region of lamellar phase with water [Buchanan 00, Buchanan 99]. It is generally accepted that the swelling in myelins (measured by the distance between bilayers) is the same as the maximum lamellar swelling in this coexisting region [Sakurai 90, Kennedy 05]. This might be explained by the following argument (see Fig.2.20). In a concentrated lamellar phase, there are strong repulsive

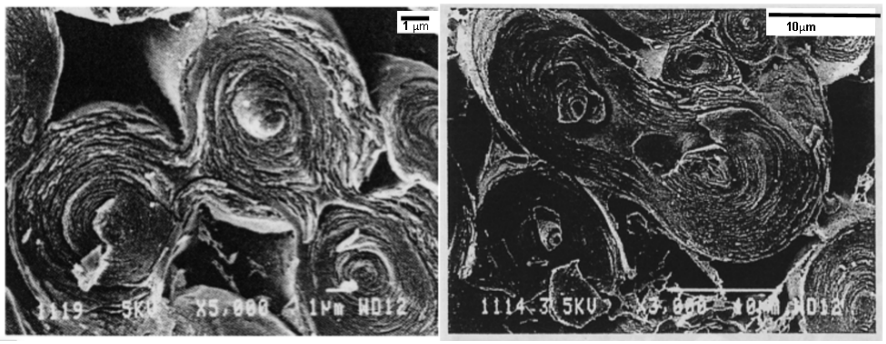

Figure 2.19: Cross-section of myelin tubules (by Cryo TEM) [Sakurai 90].

forces between the bilayers. Once water is added to the system, the distance between the bilayers will increase. At some point, attractive forces between the lamellar sheets might counterbalance the repulsive forces. In this case the lamellar phase is stable. Both the addition as well as the removal of water are not favourable - the lamellar phase is fully swollen. Only if this situation is stable over a broad range in the phase diagram, i.e. that the bilayers do not dissolve into smaller structures, e.g. micelles, can myelins form. Furthermore, the water phase does not need to be pure water, but might contain small fractions of micelles or monomers. It has been mentioned that myelins can also grow into a sponge phase [Buchanan 00, Mark 03]. Such myelins are highly unstable and reorganise immediately into the sponge phase after forming. This is consistent with a kinetic pathway theory where the time for bilayers to swell and to form myelins is faster than to form a sponge phase.

Furthermore, the lamellar sheets in a myelin tube are characterised by a marked fluidity and low permeability [Nageotte 36, Vogel-Weill 91, Gruger 94, Arunagirinathan 04, Haran 02, Neuzil 81, Degkwitz 38, Sandermann 77]. Therefore the addition of molecules which increase the permeability of water [Haran 02] or hinder molecular movement within the sheets [Neuzil 81, Degkwitz 38], or the freezing of the bilayers by lowering the temperature below T_m[26] [Nageotte 36, Chapman 66, Sandermann 77], suppresses myelin formation. The myelin structure is stabilised by hydrogen bonds as shown by Raman and IR spectroscopy [Vogel-Weill 91, Gruger 94].

From a thermodynamic point of view myelins are non-equilibrium structures. These structures can be stable over long periods of time. However, adding for example mechanical energy through shaking or shearing, or just increasing the temperature may immediately dissolve the myelinic structure or lead to reorganisation into multilamellar

[26] Therefore myelin formation can be used to determine T_m [Sandermann 77, Langlois 95].

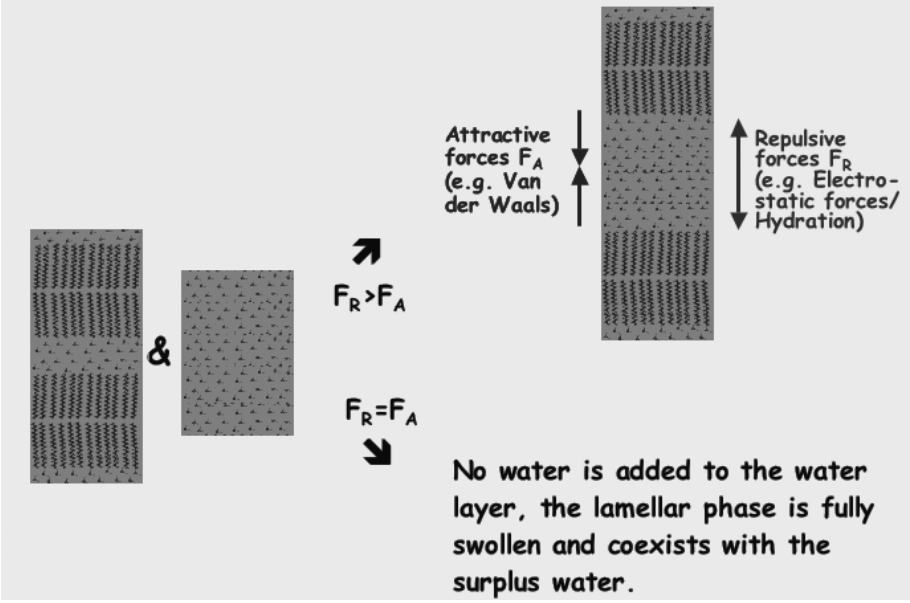

Figure 2.20: Concentrated lamellar phase can swell, when water is added, until the attractive forces balance the repulsive forces.

vesicles as, due to increased (Brownian) motion, some myelin tubules break and the exposed hydrocarbon edges reseal [Fonteijn 92]. The relative high stability of multilamellar vesicles, compared to myelins, also explains why no myelins are observed upon dissolution of a vesicle-rich lamellar phase (as reported in [Buchanan 00,Mark 03]). The long-lived nature of myelins in many systems allows studies of the stability and elasticity of the myelinic tubes. Myelins can be stretched, moved and bent in external fields (see Fig.2.21). Due to the magnetic susceptibility of the bilayers, myelins orient parallel to magnetic fields [Sakurai 83]. In an alternating electric field, they behave like large dipoles [Mishima 89]. These studies obtained bending moduli which display the soft character of the myelinic tubules [Sakurai 83].

This softness can explain the frequent morphological changes, which appear with time, such as coiling or branching (see Fig.2.22 top left and middle). Coiling leads to an increase of membrane-membrane contact and might be due to strong intermembrane attraction [Lin 82, Mishima 92]. As can be seen, there are two different types of coiling, the double helical and the case where one myelin is wound around another tube. Branching is usually caused by a myelin tip being stopped by a barrier (e.g. another myelin).

It has already been mentioned that, during myelin growth, water enters the lamellar phase via the myelin roots (the L_α/myelin interface) (see Fig.2.23). This causes a

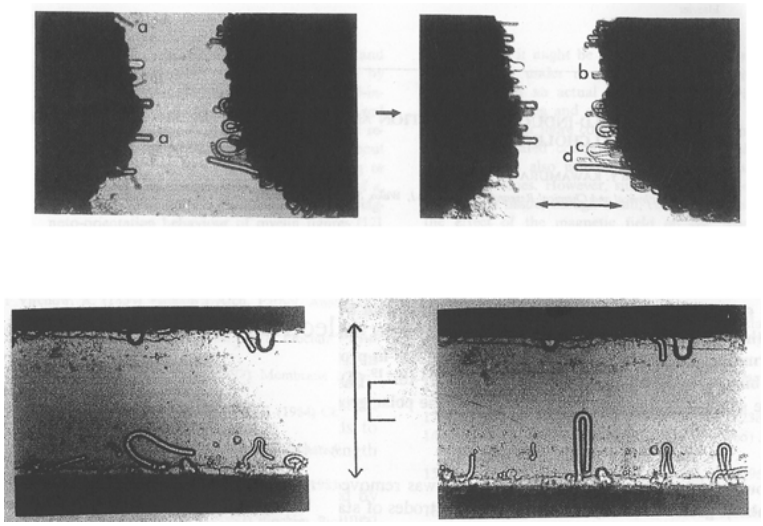

Figure 2.21: Magnetic [Sakurai 83] and electric [Mishima 89] fields influence the orientation of myelins. Myelins are reoriented parallel to the magnetic and electric field within a short time.

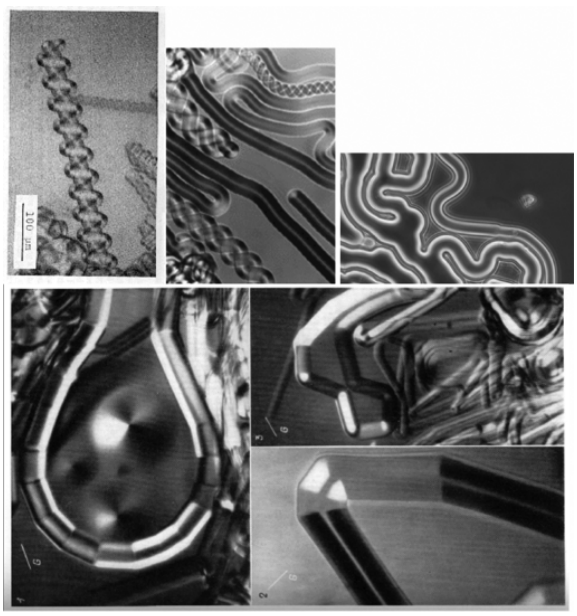

Figure 2.22: Morphological changes of myelin tubules as coiling or branching (top) and adopting an angular conformation (below).

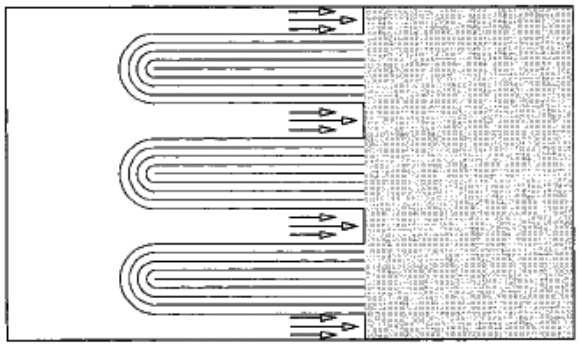

Figure 2.23: Water penetrates the lamellar phase via channels in between the myelinic tubes, not via the tips of the myelins [Buchanan 00].

swelling of the lamellar phase, which pushes the myelins further into the surrounding solution [Buchanan 99, Buchanan 00]. The growth has been characterised, in general, by successive regimes [Buchanan 99, Buchanan 00, Sakurai 84, Sakurai 85, Mishima 87, Dave 03, Taribagil 05]: pre-diffusional, diffusional and sub-diffusional. Various theoretical explanations and models have been proposed [Sakurai 84, Sakurai 85, Mishima 87, Dave 03, Taribagil 05], mostly based on the creation and subsequent diffusion of the myelins into the surrounding solution. Recent studies on the lecithin/water system [Leng 06] have quantitatively shown the influence of the surfactant concentration on the myelin growth kinetics. The obtained results suggest that myelin growth depends mainly on the kinetics of water diffusion, which is driven by the balance between the driving force (osmotic pressure [Lawrence 51, Angelova 86, Zou 06]) and water mobility, with growth constrained by the geometry of the myelinic tubules. Those considerations were the underlying basis for the theory developed in the previous section (see section 2.3.2).

Myelins in biology As already mentioned, the term myelin is wildly used in biology, referring mostly to the insulating sheath wrapped around the nerve axon [Morell 77]. The multilayer structure (see Fig.2.24) is due to the so-called Schwann cell, being wound spirally around the axon [Salzer 08]. However, in contrast to the artificial myelin, where water layers alter with bilayers, in the biological myelin the alternation pattern is the following: bilayer, cytoplasmic region, bilayer, extracellular region [De Felici 08]. The water content is about 40% [Vavasour 09, Finean 57].

There are several reasons why myelin sheaths cover axons in biological species: Firstly, the conductivity velocity of a signal is increased by the presence of the myelin sheaths [Sanders 46, Oswald 05]. Secondly, the signal transfer is much more 'energy efficient' [Waggett 08, Oswald 05]. This can be nicely illustrated when comparing the nerve in

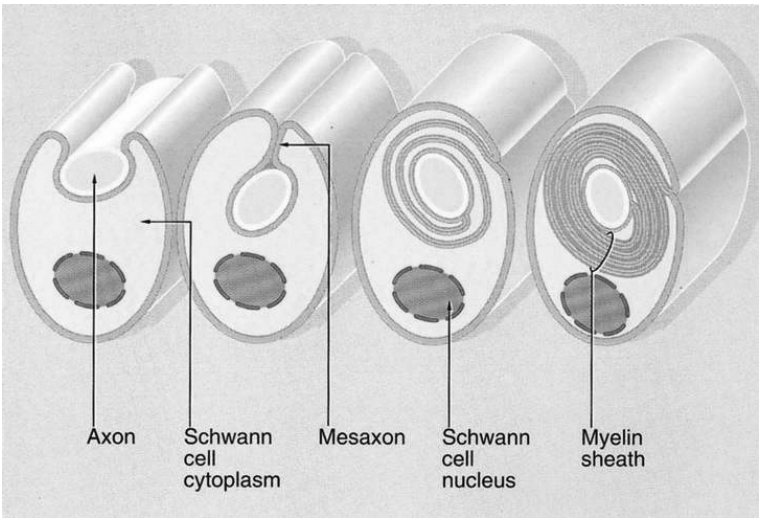

Figure 2.24: Process of myelination of an axon [Vanderbilt 09].

frogs and squids: a 12μm thick (myelinated) nerve fibre in a frog conducts a signal with a speed of 25m/s. The unmyelinated giant fibres of the squid transmit a signal just as fast; this fibre is though not only more than 40-fold thicker - it also requires 5000 times more energy than frog fibres. Myelin have therefore played a vital role in evolution. [Oswald 05]

Moreover, the myelinic structure shows a remarkable resistance to freezing and thawing. In the 5000-year-old Tyrolean iceman discovered in 1991 in the Alps, only myelins were found to be intact in molecular configuration and fine structure [Hess 98]. Myelin sheaths are also relatively stable when exposed to external pressure or stretching. In contrast to the axon, the myelin can adopt to the external stress by shifting lipid material due to the high fluidity in the membranes [Ochs 97].

However, the high speciality of myelinated nerve cells results in severe neurological disease upon the loss or disruption of the myelin sheaths, such as Multiple Sclerosis [Steinman 96, Frohmann 06, De Felici 08] or Alzheimer's disease [De Felici 08].

Chapter 3

Materials and methods

3.1 Introduction

For this thesis, two binary surfactant-water systems have been chosen: didodecyldimethylammonium bromide (DDAB) and triethylene glycol monododecyl ether ($C_{12}E_3$). Furthermore, for some experiments, DDAB has been mixed with its slightly longer analogue, dioctadecyldimethylammonium bromide (DODAB). These three synthetic surfactant systems are widely studied in literature. A summary of their most relevant properties is given in this chapter.

The study of the equilibrium and non-equilibrium behaviour of surfactant systems requires a combination of a wide range of experimental techniques, characterising the samples on different levels (see chapter 2.2.2.5):

- The molecular structure (3.3.1): The purity and thermal stability of the samples have been investigated by proton and 13-carbon nuclear magnetic resonance (^{1}H-NMR and ^{13}C-NMR), electrospray ionisation mass spectroscopy (ESI-MS) and thin layer chromatography (TLC). Attenuated total reflectance infrared spectroscopy (ATR IR) has been used to investigate the level of hydration of the crystalline phases.

- The conformational structure (3.3.2): A combination of powder X-ray diffraction and Raman spectroscopy, complemented with computational techniques, has been used to obtain information about the conformations of the surfactant molecules.

- The phase structure and phase stability (3.3.3): Small angle X-ray scattering (SAXS) has resolved structural information on the nanometer length scale. The density has been established using a vibrational tube densitymeter. Thermodynamic information on phase transitions has been obtained using differential scanning calorimetry (DSC).

- The colloidal structure (3.3.4): Microscopy, direct observation and confocal

microscopy has been used to resolve colloidal structures in 2 or 3 dimensions.

This chapter contains also the way the experiments are performed and how the setups are calibrated. Finally, a discussion of the possible errors and difficulties are given.

3.2 Materials

Detailed information about sample preparation can be found in chapter 4, 6 and 7 for DDAB, DDAB & DODAB mixtures and $C_{12}E_3$. All chemicals were used as received unless otherwise stated. DDAB (Sigma Aldrich, 99%) and DODAB (Sigma Aldrich, 98%) were stored in a desiccator at room temperature (T≈20°C). $C_{12}E_3$ (Nikkon, Chemicals, 99.9%) was stored in the fridge at T=6°C under a nitrogen environment.

3.2.1 Dialkyldimethylammonium halides

Dialkyldimethylammonium halides, abbreviated to

$$C_mC_nDA^+X^-$$

are some of the most common double-chained amphiphiles. C_m and C_n are two long hydrocarbon chains[1], D stands for the two methyl groups[2] and A for the quaternary ammonium. The halide X is most commonly bromide or chloride. Quaternary ammonium salts are neutral, i.e. the structure is independent of pH [Rubingh 91].

Phase behaviour A typical phase diagram for a dialkyldimethylammonium halide is presented in Fig.3.1 [Haas 98, Haas 99, Schulz 98, Dubois 98, Laughlin 90]. Above the Krafft temperature a lamellar phase is observed over a broad composition range in the phase diagram. The high thermal stability of the liquid crystalline phases for cationic surfactants is well known [Rubingh 91]. The dilute lamellar phase is described as a disordered phase, in which vesicles can often be found [Kunitake 84, Caboi 96, Haas 98,Haas 99,Patrick 96], while the concentrated phase is characterised by a mosaic texture [Caboi 96, Patrick 96]. The domain structure in the concentrated phase is known to increase with surfactant concentration [Youssry 08, Laughlin 94].

In some systems, the lamellar phase shows a miscibility over a certain composition range [Haas 99, Haas 98, Schulz 98, Dubois 92, Dubois 98], separating the lamellar

[1]For surfactants with two similar hydrocarbon chains the convention is to abbreviate the number of carbons in each chain instead, e.g. *DO* stands for Di-Octadecyl (2x18) or *D* for Di-Dodecyl (2x12) or Di-Decyl (2x10).

[2]Sometimes *DM* is used instead of *D*.

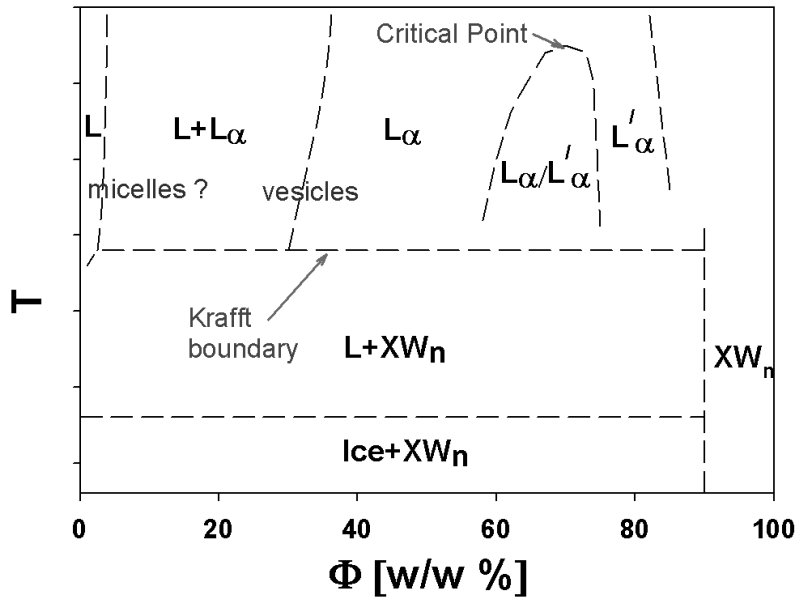

Figure 3.1: Sketch of a typical phase diagram of a dialkyldimethylammonium halide.

phase locally[3] into the 'swollen' lamellar phase L_α and the 'collapsed' lamellar phase L'_α, which is also known for other systems [Ockelford 93]. It has to be mentioned that only for dialkyldimethylammoium bromides has this coexistence region been reported [Dubois 98, Schulz 98, Haas 99, Haas 98], which could be explained by the different degrees of hydration when comparing bromide and chloride [Dubois 98]. This hydration is stronger for chloride than for bromide, which decreases the binding affinity of the counterion to the surface of the aggregates [Dubois 98, Marques 03, Horinek 09, Patrick 96]. In the collapsed phase, some counterions are expected to be bound to the bilayer.

The phase separation between the collapsed and swollen lamellar phase has been explained by the interplay of two repulsive forces of different decay lengths [Dubois 98, Ockelford 93, Montalvo 02], the hydration force[4] and the electrostatic repulsion force, which compete with a strong attraction. The hydration force is assumed to be the dominant repulsive force in the collapsed phase L'_α, due to the binding of counterions to the bilayer surface, leading to a 'neutral' bilayer.

Another explanation is based on changes in the electrostatic interactions when going to very small distances between the bilayers [Boroudjerdi 05]. For small distances

[3] The phase separation is only local not macroscopic [Montalvo 02, Marques 03].
[4] The protrusion and undulation forces can be neglected in these systems [Dubois 98].

(the strong coupling regime) the vertical position (perpendicular to the sheets) of the counterions is assumed to be only influenced by the surface charge of the bilayer, but not by the electrostatic field of the other counterions, while for long distances (the Poisson Boltzmann regime) the counterions vertical position is, to a large degree, influenced by the other counterions. For a system showing strong coupling, a separation between two phases with different distances between the 'charged plates' can be predicted [Boroudjerdi 05].

As can be seen in Fig.3.1, at lower surfactant concentration above the Krafft boundary, the swollen lamellar phase coexists with a dilute liquid phase. This lamellar phase is often described as a vesicle phase, showing unilamellar vesicles at low concentration. With increasing surfactant concentration, more multilamellar vesicles are observed [Caria 96, Marques 99, Youssry 08, Stenstam 03]. This behaviour is typical for bilayer forming amphiphilic systems [Youssry 08]. The formation of unilamellar and multilamellar vesicles of dialkyldimethylammonium halides has been studied extensively. Despite the easy formation of vesicles, they have to be considered as metastable structures and their appearance depends on sample preparation [Ninham 83, Viseu 00b, Lopes 08, Feitosa 08].

There is disagreement in the literature about the structure of the dilute liquid phase. Some people claim it to be a pure monomer solution, and therefore that the first aggregates form at the phase boundary to the coexistence region with the lamellar phase [Soltero 00, Matsumoto 89, Marques 00, Viseu 00a], while other claim small spherical and cylindrical micelles are formed at slightly lower concentration [Haas 98, Haas 99, Bai 01].

Below the Krafft temperature a dilute liquid phase (almost pure water) coexists with crystals or crystal hydrates [Laughlin 90, Schulz 98, Okuyama 88, Okuyama 84]. One should note that the upper limit of the Krafft boundary lies far below the melting point of the dry crystals in surfactant salts. The heat involved in the phase transformation at the Krafft Eutectic is of the order of 26-28mJ/mg$_{surf.}$ [Haas 98, Haas 99]. A large hysteresis is observed for the freezing of the lamellar phases due to the kinetic hindrance of the crystallisation of the surfactant [Haas 98, Haas 99, Laughlin 94]. This leads to the occurrence of metastable phases, which can be liquid crystal or crystal. In the case of vesicles, the occurrence of gel phases as the L_β phase at low temperatures has been frequently reported [Marques 02, Feitosa 06b, Feitosa 06a, Saveyn 09, Feitosa 00]. Also in these cases, long equilibration times are needed for the molecules to rearrange into the gel state [Blandamer 97, Feitosa 06a]. The melting temperature of this gel phase corresponds sometimes with the Krafft temperature of the system.

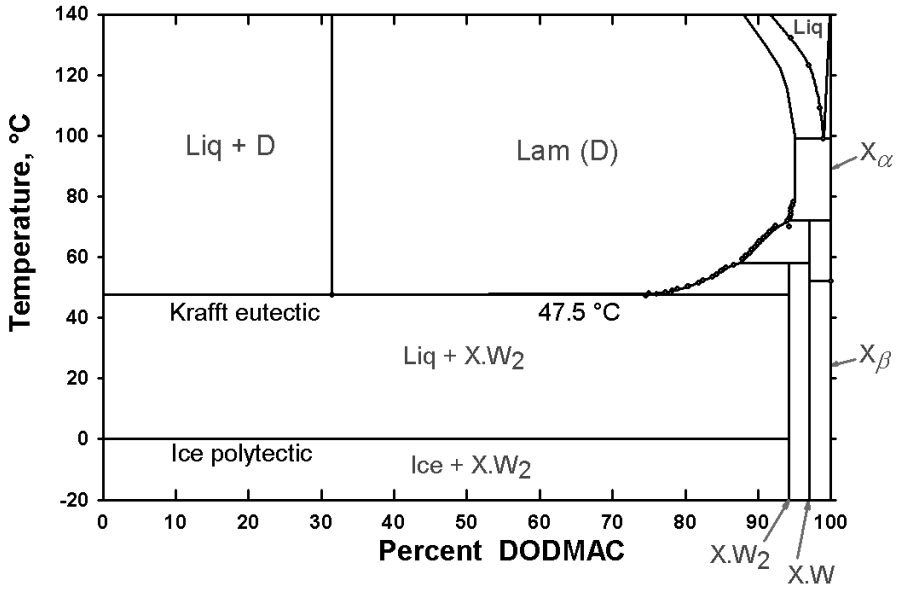

Figure 3.2: Phase diagram of dioctadecyldimethylammonium bromide [Laughlin 90].

It has to be mentioned that all phase studies on dialkyldimethylammonium halide systems are incomplete apart from one: the study on the dioctadecyldimethylammonium chloride (DODMAC) water system [Laughlin 90, Laughlin 91, Laughlin 92, Laughlin 94, Rubingh 91]. The obtained phase diagram presented in Fig.3.2 is complete and follows, in all parts, the rules of phase science (see chapter 2.2.2). All remaining phase diagrams have to be treated carefully and their incompleteness, which might include errors, should be kept in mind. One of the problems is often the thermal stability of the surfactant molecules. Quaternary ammonium salts decompose at higher temperatures, predominantly by nucleophilic attack, which is more severe for quaternary ammonium bromides and iodides than for chlorides [Rubingh 91]:

$$R_4N^+ + X^- \rightarrow R_3N + RX$$

Furthermore, a few percent of a near homolog or other impurities constitutes a significant level of another component, which leads to changes in the phase behaviour [Rubingh 91]. Such impurities are difficult to detect [Laughlin 90, Haas 98].

The last problem is the long equilibration time, especially for the crystalline phases[5], caused by the low monomer solubility, which implies that processes which go via monomer exchange occur rather slowly. Therefore, when the monomer exchange

[5] [Laughlin 90] reported equilibration times of up to 4 years.

between aggregates is so slow, the equilibration time and the historical treatment of the sample play an important role in the phase behaviour and microstructure of the system. [Marques 03]

Ternary systems The behaviour of ternary systems, with one or two dialkyldimethylammonium halides, has been of great interest. Most mixtures show the existence of lamellar phases over a large interval [Youssry 08] and the spontaneous formation of vesicles [Viseu 00b, Viseu 00a, Proverbio 02, Bergstroem 01, Marques 99, Marques 02, Caria 96]. The separation into a swollen and collapsed lamellar phase has been often reported [Li 02, Montalvo 02]. Vesicle formation can be enhanced by the addition of cationic single chain surfactants [Viseu 00a, Proverbio 02, Kodama 06, Aratono 07, Viseu 00b] or anionic surfactants [Bergstroem 01,Kacperska 00,Marques 99,Marques 00, Marques 02, Karukstis 03, Caria 96]. Their behaviour is attributed to two key factors: electrostatic interactions and non-ideal mixing (e.g. permitting the inner and outer monolayer in a vesicle to have different composition [Caria 96, Li 02, Marques 03]). Also, the formation of microemulsions in dialkyldimethylammonium halide systems has been reported [Silas 01, Warr 88, Monduzzi 01, Olla 04].

Applications Dialkyldimethylammmonium halides were the first totally synthetic amphiphiles which were found to form bilayer structures similar to those of phospholipids found in biological membranes [Kunitake 77]. Vesicles can already be formed at very low surfactant concentrations. These bilayers (formed by the pure surfactants or their mixtures) are suitable and stable models for membranes [Lindström 02, Viseu 04].

Biomembrane-like structures are of great use for exploring the electrochemistry of proteins, simulating their natural environment[6], showing excellent electrocatalytic activity and good stability [Chen 00b,Shao 05,Guto 06,Nassar 97,Rusling 93,Mimica 04, Chen 04, Hu 07, Chen 01, Fu 02, Guo 08, Zhao 09] and could therefore be incorporated in various sensors [Ignaszak 09, Shumyantseva 09, Peng 09].

Cationic lipids are especially interesting when adsorbed on particles, since cationic particles may electrostatically combine with a wide variety of oppositely charged biomolecules, cells or other biological structures [Lincopan 09]. Furthermore dialkyldimethylammonium halides find application in the improvement of fast ion exchange chromatography [Connolly 02, Hatsis 03, Connolly 04, Pelletier 06] and as efficient coatings in capillary electrophoresis [Melanson 00, Baryla 01, Diress 04,

[6]Only above the Krafft temperature these surfactants for suitable films to mimic biomembranes [Rusling 93, Chen 00b].

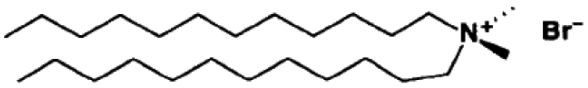

Figure 3.3: Molecular structure of the cationic surfactant DDAB.

Yassine 04, Mohabbati 08, Liu 08].

Because of their positive charge, the vesicles can interact with DNA, forming cationic lipid-DNA complexes [Silva 8, Feitosa 06a], which show great potential in gene delivery. Dialkyldimethylammonium halides are not directly toxic, but destroy the membrane due to electrostatic interactions of the cationic vesicle with negatively charged phospholipids in the cell membrane and therefore can be used as immunosuppressant agents [Montalvo 02, Fontana 03, Marques 03] or bactericides [Muthukumar 07, Pereira 8, Rosa 08, Fontana 03, Marques 03]. This cytotoxity can be reduced by using coated nanoparticles instead of pure vesicles [Li 08, Li 09, Lincopan 09] or by adding neutral helper lipids to the vesicles [Callow 09, Sobral 8].

In industry cationic surfactants are highly applicable as softeners or hairconditioners because of their low solubility and work by neutralizing the negatively charged surfaces [Montalvo 02, Groth 03]. Furthermore, their use as disinfections agents [Montalvo 02], herbicides [Undabeytia 04], wetting [Svitova 01, Fontana 03, Marques 03] and antistatic agents [Fontana 03, Marques 03] has been reported. Cationic surfactant stabilized microemulsions [Bumajdad 04], inverted micelles [Liang 03] could also be used to enhance the synthesis of particles or to serve as templates for microstructures [Harada 01, Moon 09].

3.2.1.1 DDAB (didodecyldimethylammonium bromide)

The synthetic cationic double-chain surfactant didodecyldimethylammonium bromide ($(C_{12}H_{25})_2N^+(CH_3)_2Br^-$, abbreviated to DDAB) is one of the most studied synthetic surfactants (see Fig.3.3) and has been known since 1977 [Kunitake 77].

Its properties are summarised in Tab.3.1. Its molecular mass is m=461g/mol. The molecular volume depends on the temperature and has been reported only for temperatures above 20°C, leading to a density of close to 1kg/dm^3 [Dubois 91]. The area per headgroup is about s=64-68Å^2.

The phase behaviour of DDAB has been extensively studied in the past [Dubois 91,

Molecular mass m	461g/mol
Molecular volume V_m	784Å^3 (20°C), 792Å^3 (40°C)
Density	0.98 kg/dm^3 ($\approx 20°C$) [Dubois 91]
Area per headgroup[a]	64-68 Å^2 (depends on Phi)
Chain length l_c	16.68Å(fully stretched) [Marques 03, Warr 88]
Chain volume V_c	703.7Å^3 [Marques 03, Warr 88]
Maximum swelling Δ^{*b}	≈80nm [Dubois 91]
Bilayer thickness $a_b{}^c$	24Å [Dubois 91]
Ion layer thickness a_{Br}	7Å [Dubois 91]
CVC	3.5 10^{-5}M [Undabeytia 04]
	6.5 10^{-4}% [Soltero 00, Matsumoto 89]
	0.053mM [Proverbio 02]
CAC	0.05mM or 0.14-0.18mM [Viseu 00a]
	2.3 10^{-3}% [Marques 99]
CMC	no [Soltero 00]
	0.3mM (25°C), 0.2mM (30°C), 0.11mM (35°C) [Bai 01]

[a]Temperature independent, decreases with increasing salt concentration [Dubois 91] varies with temperature [Dubois 98].

[b]Decreases with increasing salt concentration [Dubois 91, Dubois 00].

[c]Varies with temperature.

Table 3.1: Properties of the cationic surfactant DDAB.

Dubois 92, Dubois 98, Warr 88, Caboi 96, Patrick 96]. The newest phase diagram is shown in Fig.3.4 .

At temperatures above T_m, two lamellar phases have been reported: L_α[7] and L'_α[8]. For intermediate compositions there is a coexistence between both phases. The critical point where the two phases merge into a single point is at about 75°C (72°C [Caboi 96]) at 62.2% [Zemb 93, Marques 03]. The maximum swelling of the swollen lamellar phase corresponds to a water layer thickness of a^*_w ≈78nm [Dubois 91]. This distance has been shown to be set by an equilibrium of the osmotic pressure in the two coexsting phases and not by an equilibrium between the attractive and repulsive forces [Dubois 91]. The osmotic pressure within the lamellar phases has been obtained over the whole composition range (see Fig.3.5) [Dubois 92, Dubois 98].[9].

A flow birefringent sponge phase L_3 could be observed at temperatures above 22°C instead of a coexistence region of a lamellar phase with the dilute liquid, which has

[7]3-28% [Dubois 92, Dubois 98] or 3-30% [Montalvo 02, Zemb 93].

[8]83-91% [Montalvo 02] or >75% [Dubois 92, Dubois 98] or 75-85% [Zemb 93].

[9]In the presence of salt the same succession of phases has been obtained, but these are shifted to higher surfactant concentrations [Dubois 92, Dubois 98].

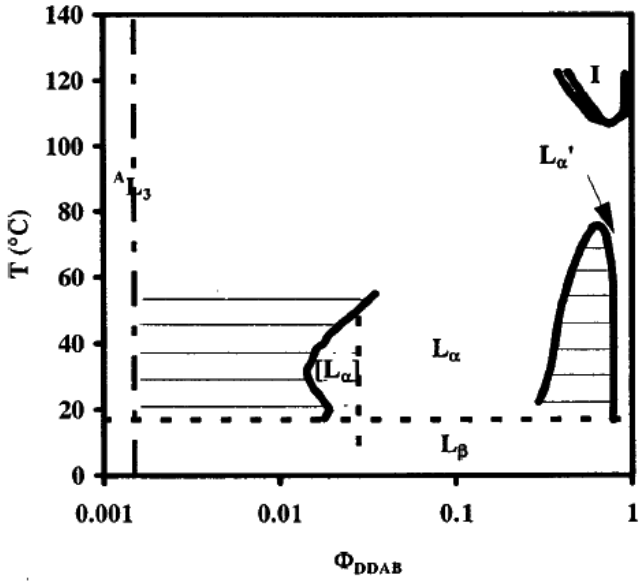

Figure 3.4: Concentration [w/w] versus temperature phase diagram of DDAB reported in [Dubois 98].

been shown to be a longlived metastable state[10] [Dubois 91].

The area per head group, as well as the bilayer thickness, depends on the surfactant concentration. Starting with 62.8Å^2 for swollen lamellar phase, a sudden increase of the area per headgroup to 67Å^2 is observed on going to the condensed lamellar phase, as the counterions are less bound in that phase. The area decreases again with increasing surfactant concentration. The bilayer thickness shows an opposite behaviour. The L_α to L'_α transition leads to a sudden decrease in thickness, which then increases again with increasing surfactant concentration. [Dubois 98]

The appearance of vesicles in the swollen lamellar phase is greatest at concentrations around 3-4% and 15-20% [Karukstis 03]. Up to a concentration of 5%, unilamellar vesicles can be found, while at higher concentration, only multilamellar vesicles are present in the DDAB system [Viseu 00a,Matsumoto 92]. In the coexistence region with the dilute liquid (<3%) multilamellar and unilamellar vesicles have been reported, with a decreasing ratio with decreasing surfactant concentration. As can be seen in Tab.3.1 there is no clear picture about the existence of a CMC in literature. Therefore, the bilayer aggregates, which are often in the form of vesicles might coexist with a monomer solution or spherical/cylindrical micelles.

[10] No L_3 has been observed in the presence of salt [Dubois 91].

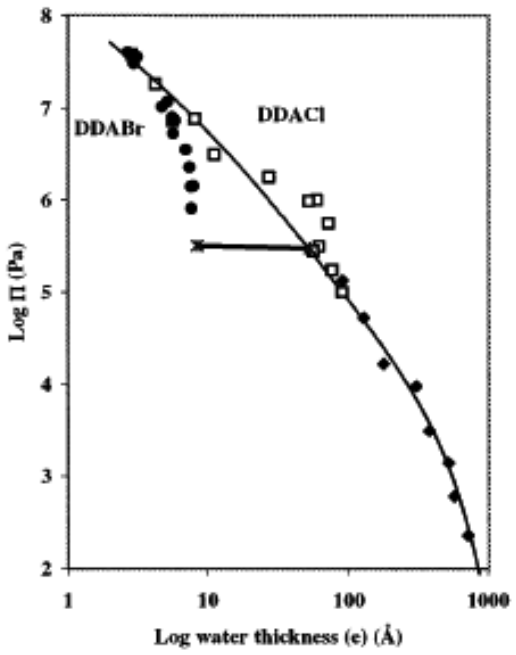

Figure 3.5: Osmotic pressure dependence of DDAB (circles) and DDACl (squares) at T=20°C on the water layer thickness between the bilayers. The solid line is a numerical theoretical approach. [Dubois 98].

Interestingly, in contrast to the other dialkyldimethylammonium bromide systems, an L_β phase has been reported not only for vesicular solutions [Dubois 91, Dubois 92, Dubois 98]. The phase transition temperature of 16°C[11] [Dubois 91] coincides with the transition temperature observed in vesicles [Feitosa 06b, Marques 02, Feitosa 06a, Blandamer 97, Marques 03]. The slightly higher phase transition temperature of the L'_α phase has been reported to be at 24°C [Zemb 93]. It should be noted, that the L_α phases and the L_β phase have been reported to be optically identical [Dubois 91].

The behaviour of the solid surfactant phase has been studied by DSC and X-ray diffraction [Godlewska 97,Dynarowicz 97,Godlewska 98]. The sample has been reported to degradate at 160°C and show 3 phase transition at lower temperatures. The phase transition at 30°C has been explained by the polytectic melting of the monohydrate to the pure crystal. At 58.6°C a transition into a liquid crystalline phase has been reported. The transition at 76.2°C is a polymorphic transition within the liquid crystal phase. Schulz *et al.* [Schulz 93] suggest that $2H_2O$ molecules are bound to each DDAB molecule.

[11] Determined by DSC.

Molecular mass m	631g/mol
Density in crystalline phase	1.04 kg/dm^3 [Okuyama 84]
Chain length l_c	25.5Å [Kajiyama 79, Kumano 84, Kodama 90]
Bilayer thickness a_b	42Å(L_α)
	36Å(crystal)
	[Kajiyama 79, Kumano 84, Kodama 90]
Tilt of chains in crystal phase	47° [Okuyama 84, Okuyama 88]
CVC	3.7 10^{-9}M [Feitosa 97]
upper Krafft temperature	51°C [Okuyama 88]
	55° [Schulz 98, Anderson 95]

Table 3.2: Properties of the cationic surfactant DODAB.

3.2.1.2 DODAB (dioctadecyldimethylammonium bromide)

Dioctadecyldimethylammonium bromide (DODAB) is an analogue of DDAB with 6 additional methylene groups in each hydrocarbon chain. Its properties are summarised in Tab.3.2.

The newest phase diagram is shown in Fig.3.6. Two lamellar phases have been reported: L_α (10-40%) and L'_α (60-97%) [Schulz 98]. Below the Krafft temperature a certain amount of water seems to be bound to the surfactant phase [Kajiyama 79, Kumano 84, Kodama 90, Schulz 93]. Furthermore the transition temperature increases with increasing surfactant concentration above 85% [Kajiyama 79, Kumano 84, Kodama 90]. The crystal structure of a monohydrate could be resolved [Okuyama 88] (see Fig.3.7, showing a tilt of the surfactant tails relative to the lamellar surface. The decrease in bilayer thickness, when compared to the L_α phase, is due to the tilt of the surfactants in the crystalline phase [Kajiyama 79, Kumano 84, Kodama 90].

At low concentration, the spontaneous formation of vesicles has been reported, which show 1-2 thermal phase transitions at 44°C [Cocquyt 5, Sobral 8, Feitosa 97] and 36°C [Saveyn 09, Cocquyt 5]. The transition temperatures depend on preparation [Anderson 95, Feitosa 00]. Furthermore bilayer fragments are often found instead of the vesicular solution [Anderson 95, Feitosa 97]. The transition at 44°C has been previously reported to correspond to the transition of a metastable gel (crystalline) phase [Kodama 90].

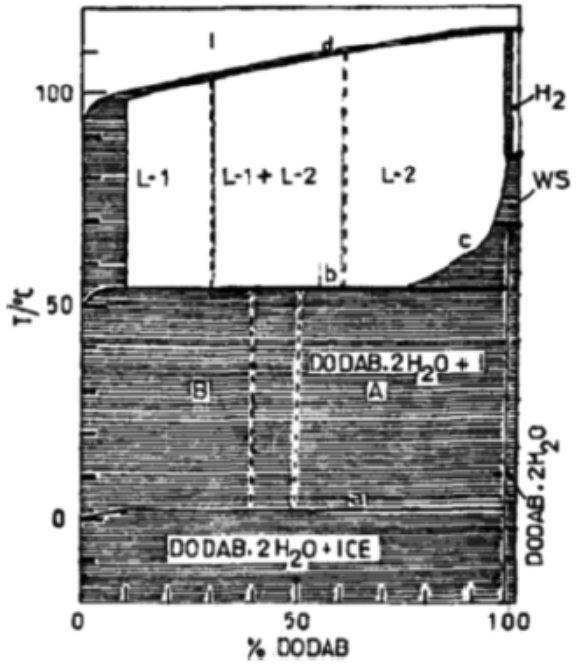

Figure 3.6: Reported phase diagram of the DODAB water system [Schulz 98].

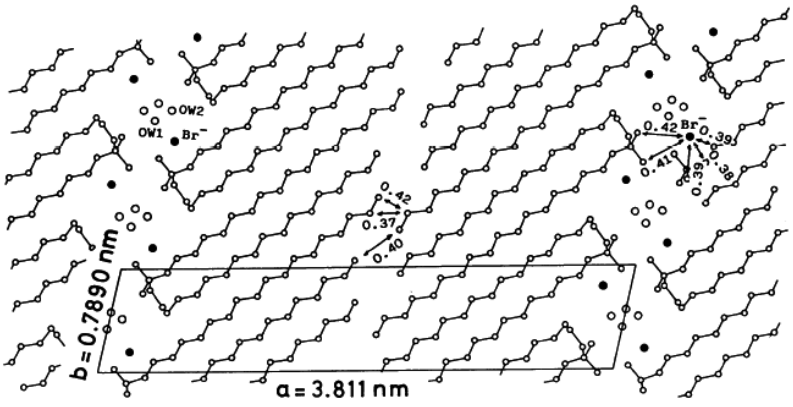

Figure 3.7: Crystal packing structure of the DODAB monohydrate [Okuyama 88].

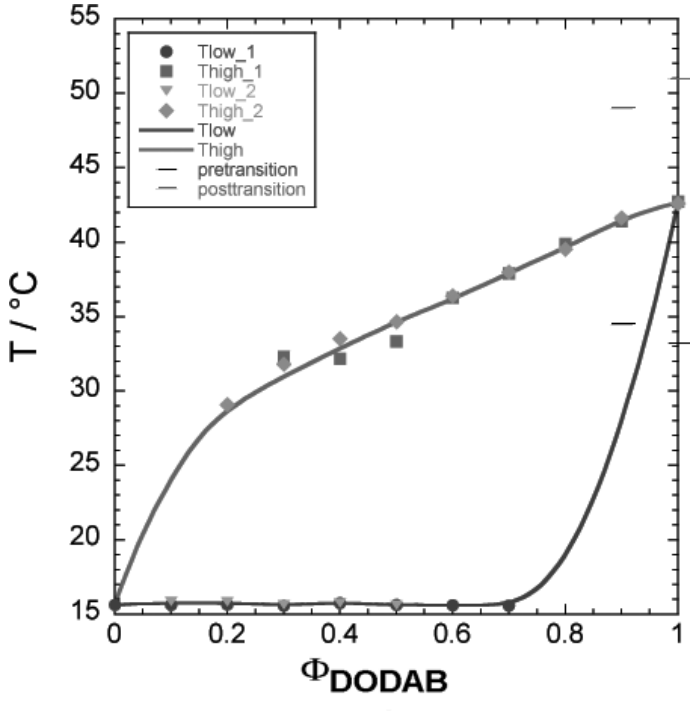

Figure 3.8: DSC data showing transition of mixed vesicles depending on DODAB concentration Φ_{DODAB} (data taken from [Feitosa 06a]).

3.2.1.3 DDAB and DODAB mixtures

Mixtures of DDAB and DODAB in vesicles have been studied in [Feitosa 06a] for total surfactant concentrations of 1mM (see Fig.3.8). The big difference in chain length causes a local demixing which enables one to distinguish between patches containing mostly DDAB molecules and those containing mostly DODAB molecules, which can be seen by the small effect the mixing has on the thermal phase transitions. One should note that for a high DODAB content the pretransition can also be seen. The additional peak at 51°C can be explained by the melting of DODAB crystals.

3.2.2 Polyoxyethylene surfactants

Polyoxyethylene surfactants are one of the most common groups of nonionic surfactants, and are widely used as emulsifying agents and detergents. They are usually abbreviated as:

$$C_nE_m,$$

where C_n stands for the saturated hydrocarbon chain of length n and E_m for the head group (EO group) consisting of m OCH_2CH_2 groups ending with an OH group. Their nonionic character result from the faculty of the EO groups to form hydrogen bonds

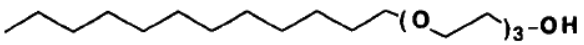

Figure 3.9: Molecular structure of the non-ionic surfactant $C_{12}E_3$.

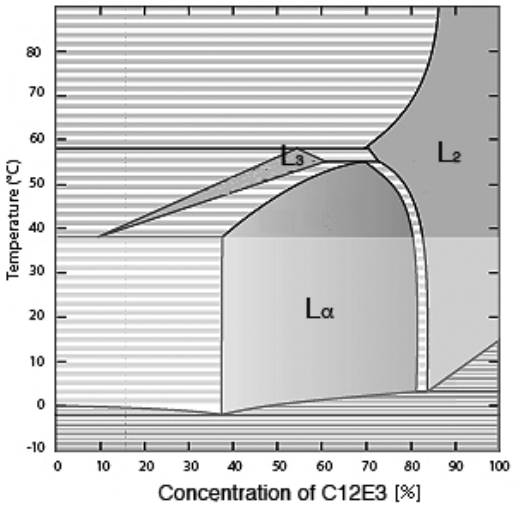

Figure 3.10: Reported phase diagram of $C_{12}E_3$ [Oswald 05].

with water. The phase behaviour of a range of the polyoxyethylene surfactants can be found in [Mitchell 83, Oswald 05].

3.2.2.1 C12E3 (triethylene glycol monododecyl ether)

In this work triethylene glycol monododecyl ether ($CH_3(CH_2)_{11}(OCH_2CH_2)_3OH$ or $C_{12}E_3$) was used (see Fig.3.9). The molecular weight of $C_{12}E_3$ is 318.49g/mol and its density at room temperature is 0.927g/ml. The relatively short head group of $C_{12}E_3$ favours the formation of lamellar L_α and reverse micellar phases L_2 over a broad composition range and down to comparably low temperatures, as can be seen in Fig.3.10 [Oswald 05, Laughlin 00, Laughlin 98]. At higher temperatures a sponge phase L_3 can be found. The low solubility of $C_{12}E_3$ causes a broad phase separation with a very dilute liquid over a composition range of up to over 80%.

All experiments have been carried out at room temperature (T$\approx 20°C$), around which the temperature dependence on the phase sequence is negligible. As shown in Fig.3.10, concentrated $C_{12}E_3$ forms inverted micelles L_2. With dilution one enters first a coexistence with the lamellar phase $L_\alpha + L_2$, then pure lamellar phase L_α, and then a coexistence region with the dilute liquid $L_\alpha + W$.

$C_{12}E_3$ is known to form myelins upon the dissolution of concentrated phases in water [Kennedy 05, Buchanan 00, Buchanan 99, Chen 00a, Laughlin 98]. Myelins form at the L_α/W interface and were described as relatively long-lived metastable states with an internal bilayer packing fraction of 45% [Kennedy 05]. The myelins are close packed tubes with an area packing fraction of about 90% [Buchanan 00].

The molecular structure of $C_{12}E_3$ allows the EO groups to form hydrogen bonds with water as well as between each other [Mitchell 83, Oswald 05, Ohno 05, Ohno 06]. The resulting hydrogen-bond network can be compared to those found in PEO[12] polymers; helical conformations are formed with increasing water concentration which trap an average of 2.9 water molecules per EO unit [Tasaki 96, Begum 97]; this structural motif can be found in all liquid phases as well as in the myelins [Kennedy 05, Ohno 05, Ohno 06]. In contrast, the hydrocarbon chains are (especially at lower concentration) predominantly in an all-trans configuration, except for close to the head group. This makes the interface of the bilayer flexible with respect to the conformation and orientation of the chains [Tonegawa 00, Masatoki 96b, Masatoki 96a, Matsuura 97]. Studies on monolayers have shown that the limiting area per molecule is about 36Å^2, and the layer is 23Åthick, consisting of the chain (12.5Å) and the headgroup (10.5Å) [Bell 96, Lu 93a, Lu 93b].

3.3 Methods

3.3.1 The Molecular Structure

The phase behaviour of a surfactant system is strongly influenced by its molecular structure. Therefore the purity and thermal stability of the samples has to be investigated. Furthermore, the water content of the solid phase and, with this, the possible existence of hydrated crystal structures has to be determined.

3.3.1.1 Nuclear Magnetic Resonance Spectroscopy (NMR)

Use of NMR ^{1}H-NMR and ^{13}C-NMR have been used to confirm the molecular structure of DDAB and its degradation products. An estimation of the water content in the solid samples has also been made with ^{1}H-NMR. One should note, that small amounts of impurities (<5%) especially of molecules similar to the surfactant (e.g. slightly shorter chains) cannot be seen with this technique.

[12] Polyethyleneoxide.

The principle of NMR Nuclei in an atom can have a spin $s>0$ (e.g. ^{1}H and ^{13}C have $s=1/2$ [13], while deuterium ^{2}D has $s=1$ and ^{12}C has $s=0$). If a magnetic field B is applied, those spins align with the field. However, two[14] different directions are possible corresponding to the alignment in direction of the field (lower energy state) or against the field (higher energy state). The energy difference increases with increasing magnetic field and depends on the gyromagnetic constant of the nucleus. In a simple experiment the electromagnetic radiation in the radiofrequency is kept constant (e.g. 250MHz, 600MHz) and the sample is investigated with changing the magnetic field measuring the resonance frequencies ν[15] of specific nuclei, e.g. protons in ^{1}H-NMR or carbons in ^{13}C-NMR. [Harwood 97]

However, the recorded resonance frequency of a specific nucleus is slightly different to the theoretical value according to its gyromagnetic constant and the applied magnetic field. This is caused by the disturbance of the magnetic field by the cloud of charge imposed by adjacent atoms and bonds: the applied magnetic field forces those electrons to circulate, generating an 'induced' magnetic field, which opposes the applied field at the nucleus. The nucleus is said to experience a diamagnetic shielding. Nuclei in electron rich environments will be more shielded. These small changes in the experienced fields mean that protons in different chemical environments will come into resonance at slightly different frequencies. [Harwood 97]

To remove the dependence of the signal on the equipment (ν depends on the applied B), the chemical shift is introduced:

$$\delta = 10^{6}\frac{\nu - \nu_{ref}}{\nu_{ref}}, [\delta] = ppm^{16}, \tag{3.1}$$

where ν_{ref} is the frequency of nucleus in a specific environment. In ^{1}H-NMR, a trace amount of tetramethylsilane (TMS) can be added to the sample as a reference. TMS shows a strong single peak, which is not affected by the sample, while the solvent peak might be slightly shifted. [Harwood 97]

The relative heights of the peaks, corresponding to one specific nucleus, are proportional to its relative occurrence in the molecule. This information can be easily obtained by integrating the NMR spectrum. Especially in the case of ^{13}C-NMR, a series of scans

[13] The natural abundance of this carbon isotope is however only 1% [Harwood 97].
[14] For spins of s=1/2 and only those are considered here.
[15] $\Delta E = h\nu$, where h is the Plank constant.
[16] Parts per million.

are required to increase the intensity of the peaks due to the low occurrence of spin active carbons, this has to be treated carefully, because of the slow relaxation time of the nuclei, i.e. the time for a nucleus to relax from its excited spin state into its ground state. A sufficiently long delay time between the scans, i.e. enough time to allow all nuclei to relax, is crucial for quantitative interpretation of the peak heights. Those relaxation times depend on the chemical environment. Therefore peaks might differ in height, even if the relative occurrence of the nuclei is the same.

Furthermore, in NMR, a splitting of the measured peaks can be observed. This is due to the interaction with other nuclei, which have a spin $s>0$, in its close environment. The number and ratio of peaks can give information about the number and type of nuclei which interact with the investigated proton or carbon, and about the strength of this coupling. E.g. a coupling to 1 neighbouring proton leads to a splitting of the peak into 2 peaks, while the coupling to 2 protons splits the signal into 3 peaks. This usually gives further information about the molecular structure. [Harwood 97]

To remove the influence of the neighbouring spins on the shape of the signal of a certain atom, the spectrum can be decoupled. That means, that the sample is first pulsed by a strong radiofrequency which corresponds to the chemical shift of a certain nucleus, which leads to its spin saturation and to the occurrence of a rapid interconversion of the spin states. In this situation, the adjacent nuclei see only a zero spin average from its neighbour, thus the spin is decoupled. The decoupling of the carbons from its neighbouring protons is frequently used to enhance and simplify the signal in ^{13}C-NMR. In ^{1}H-NMR it can be used to investigate high order spin systems. [Harwood 97]

Furthermore, the assignment of peaks which tend to overlap can be supported by pulsed 1D or 2D NMR methods. For example, ^{13}C DEPT (Distortionless Enhancement by Polarization Transfer) experiments use multiple proton and carbon pulses to produce a 1D ^{13}C spectrum, where the intensities of the signal are either positive or negative, depending on the number of protons bound to the carbon. In a DEPT135 experiment[17] the signal of the CH and CH_3 groups appear in opposite phase to the signal of the CH_2 groups. [Harwood 97]

An example of a 2D NMR technique, used in this study, is the heteronuclear single quantum correlation (HSQC) NMR experiment. This technique can be used to correlate the peaks of the ^{1}H-NMR spectrum with the peaks in the ^{13}C-NMR spectrum and

[17] 135 stands for the selection angle of 135°.

solvent peak in acetonitrile	1.94ppm (5)
solvent peak in methanol	3.31ppm (5), 4.87ppm (1)
solvent peak in chloroform	7.26ppm
water in acetonitrile	2.1ppm
water in methanol	4.8ppm
water in chloroform	1.56ppm
R-CH_3	0.8-1ppm
N-CH_3	2.5-3ppm
R_2-CH_2	1-2ppm
N-CH_2-R	2.5-4ppm
RCH_2CH_2R	5-6ppm

Table 3.3: For this work relevant chemical shifts used in ^{1}H-NMR. The numbers in the brackets corresponds to the expected number of peaks. [Gottlieb 97]

therefore correlate the carbon of a CH_n group with the directly attached protons. Each signal in the HSQC spectrum represents a proton that is bound to a carbon atom. In rare cases, strongly coupled nuclei can lead to additional signals in the spectrum. That is due to the fact that, once for example a proton is activated, it could transfer some of its energy to its strongly coupled neighbour. When then scanning for bound carbons a large peak occurs for the carbon bound to the proton, while the carbon which is bound to its coupled proton gives rise to a minor signal. [Harwood 97]

The setup used in this work The basic ^{1}H-NMR and ^{13}C-NMR measurements were performed on the ARX250MHz spectrometer (default parameters ^{1}H-NMR: 16 scan, acquisition time=4.358s, delay time=1.000s; ^{13}C-NMR: decoupled, 256 scans, acquisition time=1.114s, delay time=1.000s). The more advanced spectra (decoupled ^{1}H-NMR, DEPT135 and HSQC) were measured on the ARX600MHz spectrometer. Those experiments were manually performed by Dr. Marika DeCremoux. The samples were dissolved in deuteriated acetonitrile (CD_3CN), methanol (CD_3OD) or chloroform ($CDCl_3$).

The measured spectra were analysed with the software MestReNova. The regions in which the chemical shift of the groups lie are given in Tab.3.3 and Tab.3.4 for the ^{1}H-NMR and ^{13}C-NMR, respectively. The software also allows one to predict a ^{1}H-NMR and ^{13}C-NMR spectrum for the molecules, which can be used for comparison with the experimental results.

solvent peak in chloroform	77.22ppm (3)
R-CH_3	10-20ppm
R_3N-CH_3	50-60ppm
R_2-CH_2	15-40ppm (middle of chain ≈30ppm)
R_3N-CH_2-R	60-80ppm

Table 3.4: For this work relevant chemical shifts used in C-NMR. The numbers in brackets corresponds to the expected number of peaks. [Gottlieb 97]

3.3.1.2 Electrospray Ionisation Mass Spectroscopy (ESI-MS)

Use of ESI-MS ESI-MS has been used to detect impurities in DDAB, which are due to analogues of different chain lengths.

The principle of ESI-MS The motion of ions in an electric and magnetic field depends on the mass to charge ratio of the ion m/q. In an electric field with a potential difference of ΔU, ions are accelerated to velocity v following:

$$q\Delta U = \frac{1}{2}mv^2 \tag{3.2}$$

while in a magnetic field of strength B, ions, which fly perpendicular to that field, are deflected onto a circle of radius R:

$$qvB = \frac{mv^2}{R} \tag{3.3}$$

Mass spectrometry makes use of these two mechanisms, separating ions of different m/q ratios in the presence of electric and/or magnetic fields. It has to be noted, that the application of both equations in experiments require high vacuum conditions, so intermolecular exchange of energy is avoided. [Harwood 97]

A mass spectrometer consists of an ionization source and a mass analyzer. The ionization source adds charge to the neutral sample by various techniques, so that its motion can be influenced by an electromagnetic field. The gentlest ionisation source is electrospray ionisation. It enables molecules to be taken directly from a solution to the gas phase ionized state by passing the solution through the exit of a fine needle. This exit is held at an electrical potential of several kV. Therefore the charged droplets, containing the solvent and the sample drift to the counterelectrode. While doing so, the solvent evaporates, leading to a decrease in droplet size and therefore a higher charge density, until a limit (the so-called Rayleigh limit) is reached. At this point, a coulombic explosion occurs leading to multiply and singly charged ions, which then

isotope	natural abundance
^{79}Br	50.69%
^{81}Br	49.31%
^{12}C	98.9%
^{13}C	1.1%
^{14}N	99.634%
^{15}N	0.366%
^{1}H	99.985%
^{2}H	0.015%

Table 3.5: The relevant isotopes for this work and their natural abundance.

enter the mass analyser.

Fragmentation is generally not observed under such mild conditions [Harwood 97]. However, the charged droplets may contain a combination of molecules, which all have to be considered when analyzing the spectrum. Furthermore, there is a natural abundance of isotopes of extra mass h (see Tab.3.5) in the sample, which lead to a characteristic series of $(m + h)/q$ peaks, with $h = 0, 1, 2...$ with their relative heights depending on the isotope distribution.

The ions are recorded in a mass analyser. One of the common mass analyzers is the quadrupole ion trap, which is a 3-D analogue of a quadrupole. A quadrupole consists of 4 voltage carrying rods running along the length of the flight path. Along the rods a DC[18] signal is applied to ensure the movement of the particles parallel to the rods. In addition between each opposite rod an AC[19] signal is applied, which causes an oscillation of the particle. For a certain set of applied DC and AC voltages only ions of a particular mass to charge ratio m/q will reach the exit of the path on a stable trajectory. Therefore, mass scanning can be done by varying the two applied voltages while keeping their ratios constant. [Harwood 97]

One should note that MS can only indicate the purity of the sample. The integrated values below the peaks, correspond to the relative abundance of the species in the spectra. However this could only be directly correlated with the relative abundances in the sample if it can be assumed that all molecules show the same probability of ionisation and detection, which is not true. In order to obtain the correct values, the

[18] Direct current.
[19] Alternating current.

peak areas have to be calibrated using reference samples. Nonionic impurities are, in general, much less abundant (if at all) in the spectra, as they require the binding to another ion. Furthermore, some peaks are due to trace impurities in the solvent, vials or equipment. [Roach 09]

The combination of MS with pyrolysis Gas Chromatography has been suggested to be the best analytical tool for determining, quantitatively, the amounts of impurities in the sample of quaternary ammonium salts [Laughlin 90]. However, this technique was not available during this study and will therefore not be discussed in greater detail.

The setup used in this work ESI MS has been performed on the LCQ classic mass spectrometer (Parameters: Scan mode=+c ESI Full MS (150.00-2000.00), Source temperature=67.97°C, capillary temperature=180.20°, Ion injection time=141.38ms, elapsed scan time=1.98s) by Mr. Alan T. Taylor. The samples were dissolved in methanol. As the spectra are recorded in the 1+ mode, so that the ion mass for each peak can be directly displayed[20]. The spectrum was analysed using the Xcalibur-software.

3.3.1.3 Thin Layer Chromatography (TLC)

Use of TLC TLC could be used to assess impurities in DDAB samples, which were caused by thermal degradation, resulting in the formation of, amongst other things, the thermally stable amine.

The principle of TLC TLC is an analytic liquid chromatographic technique in which components are separated due to different adsorption characteristics on the stationary phase (silica gel SiO_2) and different solubility characteristics in the mobile phase (the developing solvent). The samples, which are dissolved in a solvent[21] are placed as fine evaporated droplets at the bottom of a TLC plate onto the silica gel. The very bottom of this plate is then put in contact with the developing solvent inside a closed container. A filter paper soaked in the solvent enables fully saturation of the atmosphere. The solvent will penetrate the silica gel due to capillary forces and slowly rise to the top of the plate, while solubilising the sample. The greater the adsorption of the species to the silica gel and the lower their solubility in the developing solvent, the shorter will be the distance which they will travel in the stream of the developing solvent.

[20] Peaks which would correspond to a 2+ ion appear in the spectrum as a series $(m + h)$, where $h = 0, 0.5, 1, 1.5...$ and can therefore easily identified.

[21] Not the developing solvent.

After elution, the spots containing molecules of certain adsorption and solubility characteristics have to be visualised. For this, either fluorescent particles could be incorperated into the silica gel, or a stain is sprayed onto the TLC plate after elution, which colours the spots upon chemical reaction with the molecules. Those stains can be used to either show all spots equally or spots in different colours/intensities depending on the chemical groups in the molecules.

The setup used in this work The developing solvent which was used in this work, has been reported to be ideally suited to distinguish between quaternary ammonium salts and the amine by Laughlin *et al.* [Laughlin 90]: this is chloroform:methanol:water:formic acid[22] (100:20:1:4). After elution the spots were visualised using the PMA stain: Polymolybdic acid:ethanol (10g:100ml).

3.3.1.4 Attenuated Total Reflectance Fourier Transformed Infrared Spectroscopy (ATR FTIR)

Use of ATR FTIR ATR FTIR spectroscopy was used to determine the hydration state of solid DDAB at room temperature.

The principle of ATR FTIR Infrared spectroscopy (as well as Raman spectroscopy see section 3.3.2.1) looks in general at transitions between rotational and vibrational energy levels in a molecule. In this work, only vibrations are considered as rotational spectroscopy can only be performed on samples in the gas phase [Griffiths 75]. The principle of molecular vibrations will be discussed in the section dedicated to Raman spectroscopy, because of their greater relevance for such experiments.

Transitions between vibrational levels become visible in IR spectroscopy due to absorption of the incident radiation in the sample, for frequencies ν, which correspond to the energy needed to raise the vibrations to a higher energy level

$$\Delta E = h\nu, \tag{3.4}$$

where h is Planck's constant. This frequency is also approximately the frequency of the investigated vibration (sum of vibrations or their overtones 2ν, 3ν etc.) (see section 3.3.2.1). However, radiation can only be absorbed by the nuclei in a molecule if a change in the dipole moment occurs during its vibration. Only those vibrations can be observed by IR spectroscopy and are so-called IR-active. [Griffiths 75]

[22] HCOOH

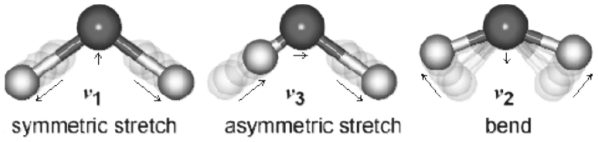

Figure 3.11: Vibrational modes of water [Chaplin 09b].

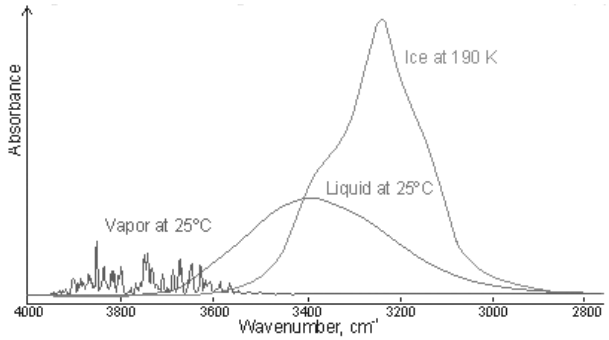

Figure 3.12: IR spectra of water in the gas, liquid and solid state [Chaplin 09b]

The unit which is most usually employed in vibrational spectroscopy is the wavenumber:

$$\overline{\nu} = \frac{1}{c}\nu, \tag{3.5}$$

where c is the velocity of light and [$\overline{\nu}$=cm^{-1}].

In this work, only the spectrum of water is considered. In the case of water, all three vibrational modes are IR active (see Fig.3.11), due to a change in the dipole moment in the direction of the movement of the oxygen atoms during the vibrations. The frequencies of those vibrations depend on the state of the water molecule and, therefore, so does the spectrum (see Fig.3.12). The approximate frequencies of those vibrations in different water states can be found in Tab.3.6. The shift to lower frequencies, as well as the increase in adsorption intensity of liquid water and ice, compared to the vapour, is due to the increased strength of hydrogen bonding [Chaplin 09b]. This apparent dependence on the state of the hydrogen bond network leads also to a temperature dependence of the spectra in liquid water. The molecular stretching vibrations shift to higher frequencies on raising the temperature, while for overcooled water, the vibrations are shifted to lower frequencies. The opposite happens for the less intense bending modes to a much smaller degree [Chaplin 09b].

Therefore analysis of the stretching peaks gives information about the hydrogen bond network and interactions with other molecules. However, the overlaying peaks are broad

gas	
$\overline{\nu}_2$	1594.75cm^{-1}
$\overline{\nu}_3$	3755.93cm^{-1}
$\overline{\nu}_1$	3657.05cm^{-1}
liquid (25°C)	
$\overline{\nu}_2$	1644cm^{-1}
$\overline{\nu}_3$	3490cm^{-1}
$\overline{\nu}_1$	3280cm^{-1}
ice (hexagonal)	
$\overline{\nu}_2$	1650cm^{-1}
$\overline{\nu}_3$	3220cm^{-1}
$\overline{\nu}_1$	3085cm^{-1}

Table 3.6: Vibrational frequencies of water [Chaplin 09b].

and vibrational overtones and combinational frequencies lead to a further complexation of the spectrum. Furthermore, same samples seem to show different types of water present due to ordering effects caused by other molecules [Schulz 98]. The spectrum is often analysed by supposing a number of Gaussian-shaped vibrational absorptions giving rise to the complex peaks. This leads to difficulties concerning the correct number of peaks and their molecular origins. Such an analysis is highly controversial [Chaplin 09a] and will therefore be treated with care in this work.

The spectrum of the water in the monohydrate and dihydrate of an DDAB analogue DODMAC has been reported in [Laughlin 90] and is shown in Fig.3.13. The most striking difference between the free water spectra and the water in the DODMAC hydrates is the occurrence of 2-3 sharp distinguishable peaks, while the free water spectrum is, as already mentioned, characterised by an overlap of broad peaks.

In practice, during an IR experiment, a 'white' source radiates energy over a wide range of frequencies onto the sample. In conventional setups, a grating is used to focus[23] a certain range of the spectrum onto the sample, which is then focused onto the detector and analysed. However, the unfortunately long acquisition times, caused by the separate recording of each point, led to the development of a Fourier Transformed (FT)

[23] By changing the angle and consequently the interference at the grid.

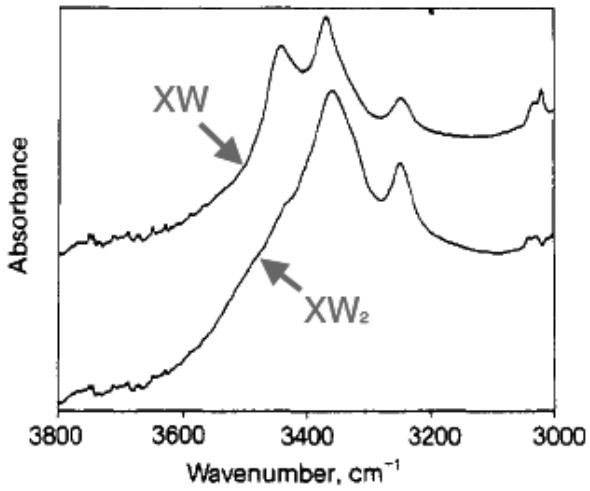

Figure 3.13: ATR-IR spectra of water in the monohydrate (XW) and dihydrate (XW_2) in DODMAC [Laughlin 90].

method. In FT IR the detector records a time-dependent signal. This signal consists of a superposition of the cosinus waves of each frequency. Fourier transformation is used to extract the frequencies and their intensities [Griffiths 75]. However because the peaks are not points but broad, the signal decays with time. The broader the peak is, the faster is the decay. Thus, a detector with a sufficiently fast response time is needed and the quality of the spectrum depends on the mathematical algorithm and the capacity of the computer used.

The conventional experimental setup requires solid samples to be prepared either as a KBr disk[24] or as a Nujol-film. Both preparation methods lead to the addition of external water (see Fig.4.6 in Chapter 4). The investigation of water therefore requires a different setup, which can be achieved when using an ATR attachment.

ATR uses the reflectance of the sample (see Fig.3.14) in contrast to traditional IR spectrometers, which analyse the samples by means of transmitting the infrared beam directly through the sample: the IR beam is focussed onto an optically dense crystal (i.e. diamond, zinc selenide or germanium) from the inner surface of which the beam is reflected. Although the reflection is called 'total', in fact the radiation beam penetrates slightly through the surface of the block a fraction of a wavelength into the sample (0.5-10 μm) during each reflection. Thus, if good sample contact is assured, e.g. by pressing the sample against the crystal, the outgoing radiation will 'carry' the absorption spectrum of the sample and is therefore attenuated. The quality of the

[24]The sample is mixed with a KBr powder and then pressed into a pellet.

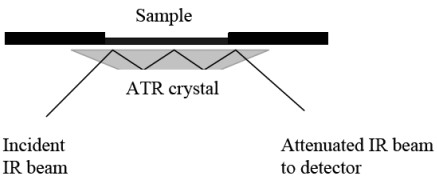

Figure 3.14: Schematic drawing of the IR beam propagating in a ATR setup.

spectra is affected by several factors [Griffiths 75]:

- the refractive indices of the ATR crystal and the sample ($n_{crystal}$>n_{sample} to ensure internal reflection),
- the angle of the incident IR beam, which should be smaller then the critical angle

$$\Theta_c = sin^{-1}(\frac{n_{sample}}{n_{crystal}})$$

- the depth of penetration, which is proportional to the wavelength of the incident beam. Thus photons with higher wavenumbers penetrate the sample less than photons with lower wavenumbers. Consequently, peaks on the right hand side of the spectra (high wavenumbers) often appear a little smaller than expected.
- the number of reflections. The total path that the beam travels through the sample is directly proportional to the numbers of reflection as are, therefore, the peak heights.
- the quality of the contact between the sample and the crystal, which ensures the maximum penetration of the beam into the sample.
- the number of averaged scans n. The dependence of the signal to noise ratio on the number of scan is:

$$\frac{S}{N} = \sqrt{n}$$

One should note that, because of the small amount of penetration into the sample, it is rather a study of the near surface regions then the bulk sample. Furthermore the recorded spectrum has to be background corrected. The background is, on one hand, caused by the variation of the emissivity of the source, as well as the sensitivity of the detector with frequency, and on the other hand, by gas molecules, which are in between the IR-source and the detector.

The setup used in this work The spectra were recorded on the Shimazdu 8400s FTIR with Pike Miracle ATR attachment at Glasgow University (5-8scans) and a

microscope with a ARO[25] objective (Smiths) at Edinburgh University (128scans) in the region of 600-4000cm^{-1}. The equipment in Glasgow had the possibility to ensure a good sample-crystal contact by applying a moderate pressure onto the sample. In contrast, the equipment in Edinburgh had the ability to record microscopy images of the sample and a spectrum could be recorded from specific points in the sample. The spectra have been corrected and analysed with the software WiRE 2.0 (Renishaw) and Origin 8.0.

3.3.2 The Conformational Structure

The conformational structure of a molecule changes widely within a phase diagram and influences phase transition and interactions between different phases. The conformational structure has been investigated for each phase and could then be used to identify those phases within biphasic regions. The changes in conformational structure during thermal phase transitions have also been studied.

3.3.2.1 Raman spectroscopy & microscopy

Use of Raman spectroscopy & microscopy Raman spectroscopy has been used to investigate the difference in the conformational properties of the DDAB molecule in aqueous solutions based on its vibrational states and dependence on temperature and water concentration.

Furthermore, the combination of Raman spectroscopy with confocal microscopy, offered, the possibility to view the sample structure due to contrast in molecular/conformational properties. Areas of different conformational properties could therefore be identified within one sample, giving better insight into the mixing behaviour of biphasic regions.

The principle of Raman spectroscopy As already mentioned, in Raman spectroscopy the vibrational (and rotational) states of a molecule are investigated, which can provide detailed information about the structure and symmetries of the molecules while being sensitive to conformational changes of large molecules and their intermolecular interactions. Vibrational transitions can either be directly measured using IR spectroscopy (see section 3.3.1.4) or indirectly, using Raman spectroscopy, which is concerned with the phenomenon of a change of frequency when light is scattered by molecules. In general, when considering a clear substance irradiated by monochromatic

[25] All reflective objective uses reflection absorption spectroscopy to analyse samples, which are mounted on an IR reflective glass slide.

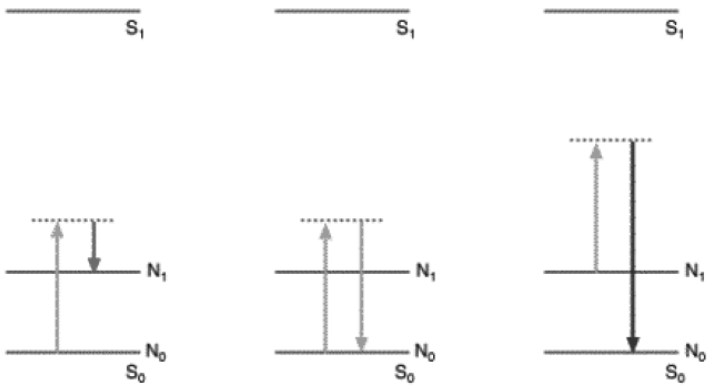

Figure 3.15: Schematic diagram of the energy levels of the Stokes-Raman (left), Rayleigh (middle) and anti-Stokes-Raman (right) Scattering.

light whose frequency is chosen so that it does not correspond to any absorption transition of the sample[26], almost the whole of the light will pass through the sample unaffected. However, a very small part (≈0.001%) of it will be scattered by molecules in directions different from that of the incident beam. This scattered light has, to a large degree, the same frequencies as the incident light (Rayleigh scattering). Only about 1% of this radiation shows a change in frequency, which was discovered in 1928 by Sir C.V. Raman. Those shifts in frequency are independent of the frequency of the incident light and characteristic of the molecules which give rise to the scattering. This frequency change can be related to transitions to higher (Stokes) or lower (Anti-Stokes) energy levels of vibrational states (see Fig.3.15).

However, not all vibrational transitions can be observed with Raman spectroscopy, which can be explained within a classical theory (classical polarisability theory [Gans 71, Banwell 94]). The scattered radiation arises from an oscillating electric dipole moment $\vec{P}$ induced[27] in a scattering molecule by the oscillating electric field $\vec{E}$ associated with the incident electromagnetic radiation:

$$\vec{P} = \alpha \vec{E}, \tag{3.6}$$

where α is the molecular polarisability, which is a measure of the ease of displacement of electrons in a molecule. It can be shown that α is, in most cases, a symmetric tensor, which reduces the number of distinct components to six. This kind of tensors can be

[26]The frequency has to be higher then IR-radiation, which corresponds to vibrational transitions, but lower then UV radiations, which can induce transitions between electronical levels.

[27]This electric moment has to be distinguished from the permanent moment, which the molecule may possess in its unperturbed condition.

associated with an ellipsoid (see Fig.3.16(a)).

The polarisability of the 'electron cloud' depends on the positions of the atomic nuclei[28]. From a classical point of view, if the nuclei are performing a periodic motion of frequency $\overline{\nu}_{osc}$ and if this motion involves a dependence of α on the position of the nuclei, the polarisability α changes also with this frequency (see Fig.3.16). This frequency corresponds to the frequency associated with the transition between energy levels (see page 84). When the molecule is now polarized by the incident light of frequency $\overline{\nu}_0$, the induced electric moment $\vec{P}$ will oscillate with the frequency $\overline{\nu}_0 \pm \overline{\nu}_{osc}$.

However, when plotting the change of the polarisability against the displacement of the nuclei (see Fig.3.16(b)), a striking difference between asymmetric and symmetric stretching modes of a centrosymmetric molecule can be observed. Only symmetric vibrations have a non-zero slope, even for very small vibrations (and only those are relevant). The 'parabolic-like' shape of the curve in the case of asymmetric vibrations leads to a diminishing of the first derivative around the equilibrium distance. This leads to the fact that, for centrosymmetric molecules (groups), all vibrations which are asymmetric are forbidden in Raman spectroscopy, in contrast to IR spectroscopy, in which case the permanent dipole moment has to change during the vibration, thus symmetric vibrations are forbidden. Therefore these coplementary techniques can be used together. Especially in aqueous solution, Raman is preferred over IR, because the broad and intense water peaks in the IR spectrum are much less visible.

This classical treatment can, however, only explain the occurrence of Raman bands, a quantum mechanical description is needed to explain the relative intensities of the scattered lines [Gans 71, Banwell 94]. The intensity I_{nm} of the scattered line involving the transition between the vibrational levels $n \rightarrow m$ is:

$$I_{nm} = \frac{64\pi^2}{3c^2}(\nu_0 + \nu_{nm})^4 P_{nm}^2, \tag{3.7}$$

where c is the velocity of light. P_{nm} is the induced transition moment matrix element associated with the transition between the initial vibrational state Ψ_n and the final state Ψ_m:

$$P_{nm} = \int \Psi_m P \Psi_n \, d\tau, \tag{3.8}$$

[28] If the incident frequency is large in comparison to the nuclear frequencies (IR-region), so that only the electrons can 'follow' and not the nuclei and if the frequency difference between an electronic absorption band and the incident light is also large compared with the nuclear frequency, one can show that the polarisability is a function only of the nuclear position.

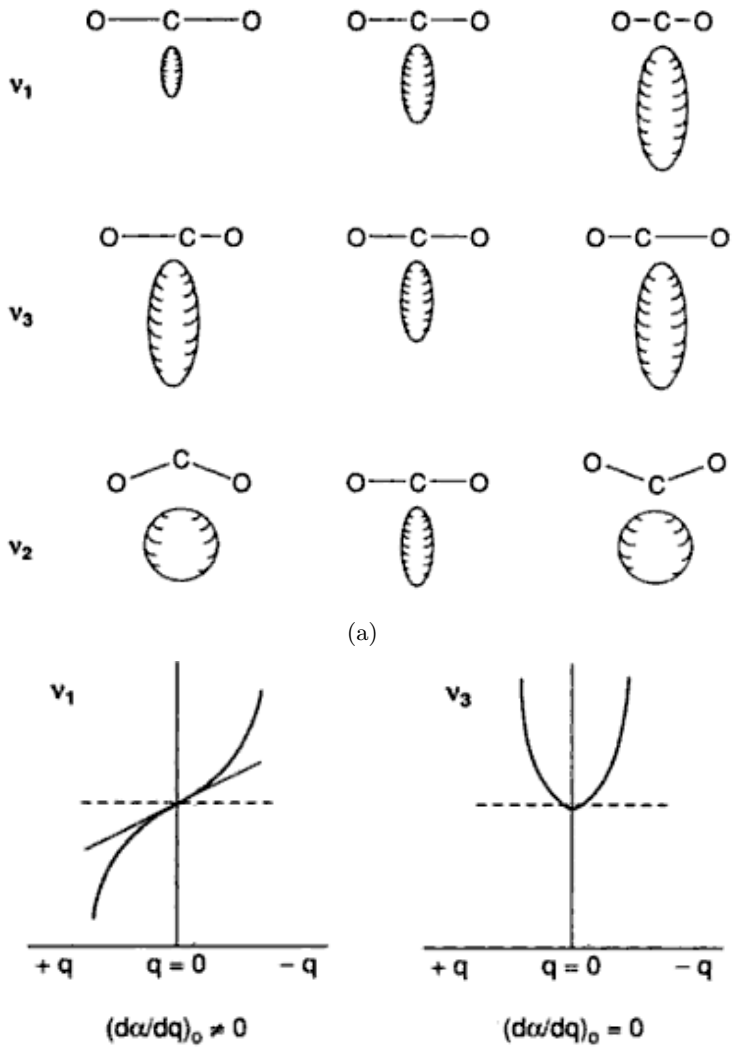

Figure 3.16: a) Changes in the polarisability ellipsoids during vibrations of the CO_2 molecule; b) Variation of the polarisability α with the displacement coordinate q during the symmetric vibration $\overline{\nu}_1$ and the asymmetric vibration $\overline{\nu}_3$ [Ferraro 03].

where P is the radiation induced dipole moment and the integral is extended over the whole range of coordinates r. The transition goes via all electronic states Ψ_r of the unperturbed molecule[29]:

$$P_{nm} = \frac{1}{h}\sum_r \left(\frac{M_{nr}M_{mr}}{\nu_{rn} - \nu_0} + \frac{M_{nr}M_{mr}}{\nu_{rm} - \nu_0}\right)\vec{E}, \tag{3.9}$$

where h is Planck's constant, ν_{rn} and ν_{rm} are the frequencies corresponding to the differences between the states denoted by the subscripts and M_{nr} and M_{mr} are the corresponding transition moments. The different terms can be positive or negative and therefore may indeed cancel out one another completely and so cause P_{nm} to vanish. The Raman line is then forbidden.

From Eq.3.9 and Eq.3.7 we see that I_{nm} is dependent on the intensity and frequency of the incoming light[30]. The dependence of the intensity of a Raman line upon frequency ν_0 of the exciting light is not only determined by the factor $(\nu_0 + \nu_{nm})^4$, but also by the denominator in the summation over the states r (Eq.3.9). This, however, has only to be considered if ν_0 lies near a particular absorption frequency ν_{rn} (Resonance Raman Effect).

Furthermore, the scattering intensity is proportional to the square of the induced dipole moment (Eq.3.8), which is proportional to the polarisability derivative over time. If a vibration does not greatly change the polarisability, then the intensity of the Raman band will be low. Typically strong scatterers are moieties with distributed electron clouds, such as $C = C$ double bonds. The pi-electron cloud is easily distorted in an external field. Bending or stretching the bond changes the distribution of the electron density substantially and causes a large change in induced dipole moment.

The total intensity for a system containing N_n molecules in the initial state n is the intensity of one molecule multiplied with N_n. According to the Boltzmann distribution, the population of higher energy levels is much lower than the population of the ground state. This can explain the lower intensities of the Anti-Stokes frequencies compared to the Stokes frequencies.

Further information about the symmetry of the investigated molecules, can be obtained

[29] This does not mean, however, that such transitions in fact occur in the scattering act. The summation arises purely as a consequence of the mathematical treatment of the perturbation problem, in which a wave function of the unperturbed molecule is expressed in terms of the full set of its unperturbed wave functions.

[30] Therefore a green or blue gives a more intense signal compared to a red laser.

by studying the effect of polarisation of the incident light on the spectrum [Kiefer 95]. However, such measurements are often only performed on single crystals or on powders of symmetrical molecules. In our case we work on highly disordered systems of low symmetry and therefore no polarisation studies have been performed.

The general Raman setup is designed in the following way: a monochromatic laser is focussed onto the sample and the scattered light is detected perpendicular to the laser. As already mentioned, the laser frequency influences the intensity and the background of the spectra. The intensity increases with laser frequency, but higher frequencies often lead to an increase of emission background in the sample (especially in biomaterials [Edwards 05]) as well as greater sample heating. The sample can be held in glassware and in aqueous solution due to the weak Raman scattering from the hydroxyl groups and silica [Edwards 05].

Because of the use of light in the visible region, beside the detector setups already described (the grating and the FT detector (see section 3.3.1.4)), a CCD camera can be used. A certain region of the spectrum (the width is limited by the numbers of pixels in the camera) is spread via a prism onto the CCD camera, enabling the simultaneous detection of that entire region. This leads to an increase in the recording speed. However, the noise in the spectra, caused by randomly generated electric signals, is often worse in the case of a CCD camera compared to a conventional grating setup. Atmospheric rays are often seen in the spectra and can only be eliminated by sufficient averaging and short acquisition times. For CCD cameras, the quality of each pixel might be different and this has to be taken into account during background correction.

Since 1975, Raman spectroscopy has been combined with microscopy, leading to the possibility of imaging samples due to the contrast in molecular structure. Furthermore, the combination with a confocal microscope (see section 3.3.4.3) gives a picture of high spatial resolution. As the laser is focused on a small part of the sample, the spectral information of the sample, depending on position, can be obtained.

The interpretation of the spectrum The vibrational Raman spectrum consists of a pattern of bands which is characteristic of the molecular species involved in the scattering. If the scattering material consists of several non-interacting molecular species then the Raman spectrum will consists of a superposition of the Raman spectra of the component species. Since the intensity of a characteristic Raman line is, to a fair approximation, proportional to the volume concentration of the species in question, Raman intensity measurements provide a basis for quantitative analysis

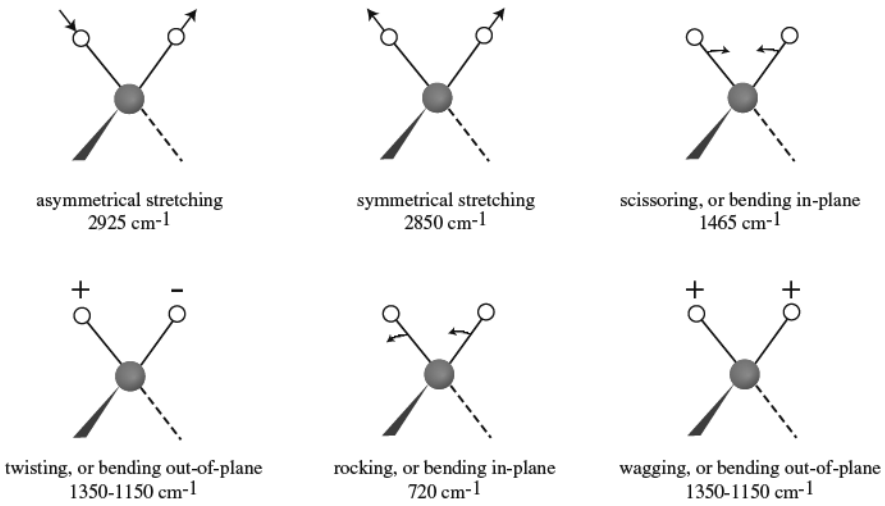

Figure 3.17: Stretching and bending vibrational modes for a CH_2 group.

[Gans 71, Edwards 05].

Raman bands can be associated with vibration of the entire molecule or characteristic groups within the molecule or groups of molecules. During a vibration, either the bond length (stretching) or the bond angle (bending) is altered. Fig.3.17 shows the possible stretching and bending vibrations for a CH_2 group as an example.

The spectrum can be divided into the region of

1. Characteristic group vibrations:
   - Involves only a small portion of the molecule, the remainder being more or less stationary
   - $>1500\text{cm}^{-1}$ (for organic molecules)
   - Almost independent of the structure of the molecule as a whole
2. Skeletal vibrations:
   - Involve many of the atoms within one molecule to much the same extent
   - Range 700-1400cm^{-1} (for organic molecules)
   - Difficult to assign particular bands, but the whole complex of the bands observed is highly typical of the molecular structure $\longrightarrow$ FINGERPRINT bands
3. Lattice vibrations [Hendra 75]:

- Commonly observed in crystalline samples
- $<600\text{cm}^{-1}$ (often referred to as LAM modes (longitudonal acoustic modes))
- In the case of crystalline n-alkanes (or melt-crystallised polymer), these bands arise from accordion oscillations along the all-trans chains and can be inversely related to the lamellar thickness l (e.g. for polyethylene

$$l \approx 3000/\overline{\nu}_{LAM})$$

- For surfactants, the LAM frequencies are very sensitive to the headgroup mass [Soutzidou 02]
- The modes depend on temperature. If the temperature causes e.g. a contraction of the unit cell and therefore a stiffening of the force field, this would lead to a shift to higher wavenumbers [Hendra 75]
- In liquids, strong, broad bands below 100cm^{-1}, associated with the vibration of a disordered 'crystal' lattice. [Griffiths 75]

Overtone and combinational frequencies have small intensities, but are often found in a complex spectrum and their intensities may sometimes be considerably enhanced by a resonance phenomenon between close bands. Those bands may interfere with each other, if the molecular symmetry and type of degenerated vibrations allow it, in such a way that the higher is raised in frequency, the lower depressed, having the same intensity, and the mean is where the mean of both should be. [Banwell 94]

To assign the observed bands to certain vibrational modes, a simple model can be used. This model is based on the fact that the position of the frequency corresponds, not only to the energy change of the transition between vibrational energy levels, but also to a fair approximation to the vibrational frequency of the molecule (or part of the molecule). A chemical bond is considered to be elastic, i.e. atoms in a molecule do not remain in a fixed relative position, but vibrate about some mean value r_{eq}. This mean position is such that the repulsive forces between the positively charged nuclei of both atoms and between their negatively charged electron 'clouds' are counterbalanced by the attraction between the nucleus of one atom and the electrons of the other. At this position, the energy is at a minimum, but once the atoms are pulled apart or squeezed together the energy rises. [Gans 71, Banwell 94]

Analysis of the apparently complex motion of a complex molecule shows that it consists of a definite number of so-called normal modes. Considering a molecule consisting of N atoms, three independent spatial coordinates lead to 3N degrees of freedoms. 3 of

these degrees correspond to a translational move of the molecule and 3 (in case of a linear molecule 2) to the rotation of the molecule. Therefore, the degrees of freedom n, which account for the relative positions of the nuclei, i.e. for internal motions are:

$$\begin{aligned} n &= 3N - 5 && \text{linear molecule} \\ n &= 3N - 6 && \text{non-linear molecule} \end{aligned} \tag{3.10}$$

For every small distortion, the vibrational motion of a molecule can be calculated for every conformation of a molecule by setting the linear or angular momentum of the motion to zero[31]. Such calculations can be carried out using computational methods (see section 3.3.2.2).

Certain general rules can already be concluded by considering a molecule consisting of two atoms, where those atoms are treated like metal balls and the bond between them like a spiral spring of restoring force:

$$F = -k(r - r_{eq}), \tag{3.11}$$

where k is the spring constant, giving rise to a parabolic energy curve

$$E = \frac{1}{2}k(r - r_{eq})^2. \tag{3.12}$$

The frequency of such a vibration, ν_{osc}, depends only on the reduced mass m_r

$$m_r = \frac{m_1 m_2}{m_1 + m_2}, \tag{3.13}$$

(where m_1 and m_2 is the mass of the two atoms involved) and the spring constant k:

$$\nu_{osc} = \frac{1}{2\pi}\sqrt{\frac{k}{m_r}}, \tag{3.14}$$

This frequency can be related to the frequency observed in a Raman/IR experiment using the model of a simple harmonic oscillator (see Fig.3.18). The quantization of the energy

$$E_l = (l + \frac{1}{2})h\nu_{osc}, \tag{3.15}$$

[31] By placing the Cartesian axes at the centre of mass of the molecule and rotating it with the molecules the motions can be restricted to vibrations.

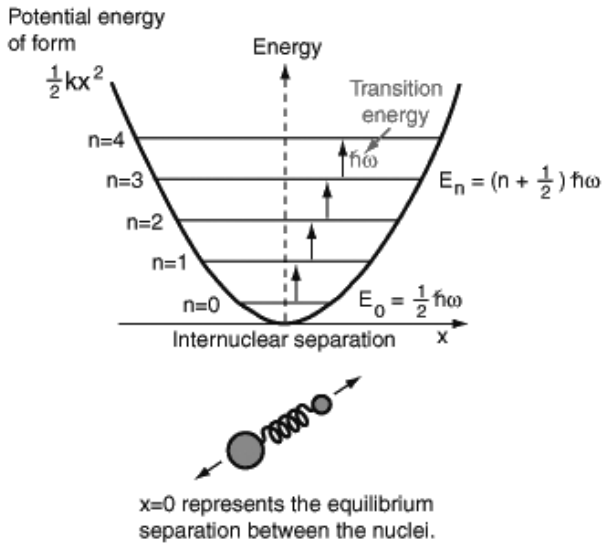

Figure 3.18: The vibrational energy levels of a diatomic molecule undergoing simple harmonic motion.

where l=0,1,2,... is the vibrational quantum number, leads to the occurrence of distinct energy levels and a minimal vibrational energy, which every molecule has. The degree of compression and extension changes upon changing the energy level, but the frequency of the oscillation remains the same (Eq.3.14). Furthermore from the Schrödinger equation it follows that only transitions between neighbouring energy states (i.e. Δl=$\pm$1) are allowed (the selection rules). In this approximation, the photon corresponding to the transition between vibrational states, has the same frequency as the vibration itself.

One should note that, in real molecules, bonds are not so homogeneous as to obey Hooke's law (Eq.3.11). For example, if the bond is stretched to a large degree, it might break and the molecule dissociate into fragments. The energy curve of a real molecule is more precisely modelled with an anharmonic oscillation curve. An anharmonic oscillator behaves like a harmonic oscillator, but with an oscillation frequency which decreases steadily with increasing l. However, for small compressions and extensions (<10%) the bond may be taken as perfectly elastic [Banwell 94] and for infinitely small vibrations the harmonic behaviour is reached and it is usually only these vibrations that are investigated in vibrational spectroscopy.

The anharmonic behaviour gives rise also to different selection rules: l=$\pm$1,$\pm$2,..., allowing additionally larger jumps. However, the rapidly diminishing probability of the larger jumps, as well as the low population of higher states at ambient temperatures, and for typical energy differences in the IR region (Boltzmann distribution), leads

to the fact that only the jumps 0→1, 0→2 and 0→3 are observed in practice, and those frequencies lie very close to the fundamental absorption and the 2nd and 3rd overtone [Banwell 94].

Therefore, to a first approximation, harmonic oscillation can be assumed, leading to the following rules, which can be used to assign the bands in a spectrum:

- higher mass result in lower $\overline{\nu}$
- increasing strength of the bond leads to higher $\overline{\nu}$
- the more polar a bond, the less intense in Raman spectra (easier to polarize nonpolar bonds) and the more intense it appears in IR spectra (greater chance to change the dipole)
- Shifts in frequency are usually caused by the interaction between different molecules, e.g. the degree of hydrogen bonding, which can weaken bonds and lead to lower frequencies, or the change of the physical state $\overline{\nu}_{gas} > \overline{\nu}_{liquid} \approx \overline{\nu}_{solution} > \overline{\nu}_{solid}$.
- Multiple bond and A-H bond stretching absorption frequencies are least affected by internal structural changes (except when intramolecular hydrogen bonding is involved) but are more susceptible to alternations in the external environment.
- Single-bond skeletal stretching vibrations between identical atoms, and the majority of bending vibrations are markedly influenced by internal structural changes.

[Banwell 94]

For complex molecules, it is useful to compare the data to other well-studied systems, or use computational methods to calculate approximate vibrational modes (see chapter 3.3.2.2) to support the assignment of bands.

There is some literature on the conformational properties of DDAB studied by Raman spectroscopy [Foucault 03, Suga 93, Arunagirinathan 04, Bell 96]. In Tab.3.8 (and the tables in [Foucault 03]) the band assignments of the DDAB molecule, or related molecules found in literature, are summarised. Its conformation is characterised by either hydrocarbon chains having sufficient fluidity with kinked conformation or as elongated chains with a rigid conformation. This could be identified from the shifts in the Raman bands corresponding to the C-C stretching, C-H bending and C-H stretching modes of the hydrocarbon chains [Arunagirinathan 04]. In liquid crystalline phases with

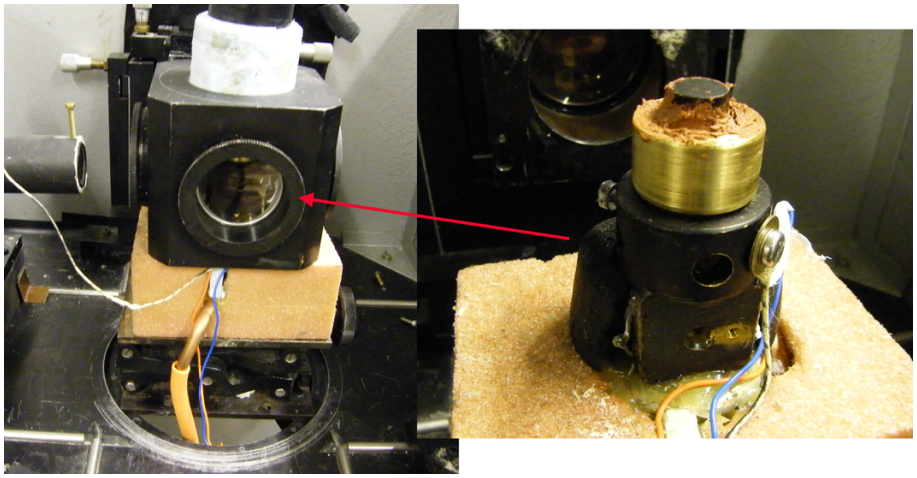

Figure 3.19: Homebuilt temperature control: the metallic cage is cooled with liquid nitrogen. A heating element is placed into a cylinder containing the liquid nitrogen, controlling the speed of evaporation through a tube, which leads to the temperature controlling stage. The sample vial is adhered to that stage with fine copper grain to ensure high thermal contact. The chamber is filled with cold dry air to prevent condensation.

melted hydrocarbon chains, the average environment of CH_2 and CH_3 groups hardly vary from one phase to another. The observed changes in the Raman spectra can therefore be associated with conformational changes [Arunagirinathan 04]. It has been stated that gauche conformations of the chains lead in general to lower frequencies then the corresponding trans conformations [Bell 96].

The Raman spectrometer used in this work Vibrational spectra of bulk samples in solution were obtained using a Coderg T-800 triple grating spectrometer. The samples were held in vials of a diameter of 10mm, which were temperature controlled within 0.1°C precision in a home-build chamber (see Fig.3.19). The green line (514.5nm) of an Argon laser was used as the excitation source. The laser power at the sample was estimated to be 500mW[32]. To obtain a better signal to noise ratio the laser power was, in special cases, increased to 750mW. This was expected to lead to a slight increase in sample temperature. The slit size was set to 400μm which gave a resolution of approximately 1.5cm.

In the case of a solid sample, the powder was placed into a notch in an aluminium plate. Because of the strong heating effect on white powders, a low power red line (676.4nm) of a Krypton laser was used as the excitation source.

[32]The optics decrease the initial laser power of 1000mW by about 50%.

Molecular group	frequency [cm^{-1}]	remarks
-CH_3 and -CH_2-	2850-3000	strong, 2-3 bands
		CH stretching modes
	2975, 2985, 2930/40	CH_3, CH, CH_2 (asym)
	2881, 2887, 2854	CH_3, CH, CH_2 (sym)
CH_2	2938,2927,2853	CH sym. stretching in DDAB [Suga 93]
	2850	CH sym stretching in DDAB [Bell 96]
CH_3	2876	CH sym. stretching in DDAB [Suga 93]
	2942, 2877	CH sym. stretching in DDAB [Bell 96]
	2960	CH asym. stretching in DDAB [Bell 96]
-CH_3 and -CH_2-	1400-1470	medium
		CH bending modes
CH_2	1459,1445	CH bending in DDAB [Suga 93]
	1416	in PE[a] melt [Kiefer 95]
	1440	in all-trans conf. of PE [Kiefer 95]
-CH_2-	1390-1370 (-1297)	medium
		CH sym. bending modes
-CH_2-	1300	twisting
		indep. of conf. in PE [Kiefer 95]
-CH_2-	800-950	weak
		CH rocking modes
		only in PE melt [Kiefer 95]
C-C	750-1350	weak
	1000, 932, 903	CC stretching modes
	1060	asym. in PE (all-trans) [Tarazona 97]
	1130	sym. in PE (all-trans) [Tarazona 97]
	1080	PE (disordered) [Tarazona 97]
C-C-C	300	bending
		indep. of conf. [Tarazona 97]
>NCH_3 (some -N-CH_2)	2780-2820	medium
		CH stretching modes
-$N(CH_3)_2$	2890	CH stretching mode
CH_3N^+	2973	CH sym. stretching in DDAB [Suga 93]
-C-N-	1000-1250	medium
		CN stretching modes
	772	CN stretching in DDAB [Suga 93]

[a] polyethylene

Table 3.7: Raman frequencies relevant for this work. [Bell 96, Suga 93, Hendra 75, Arunagirinathan 04]

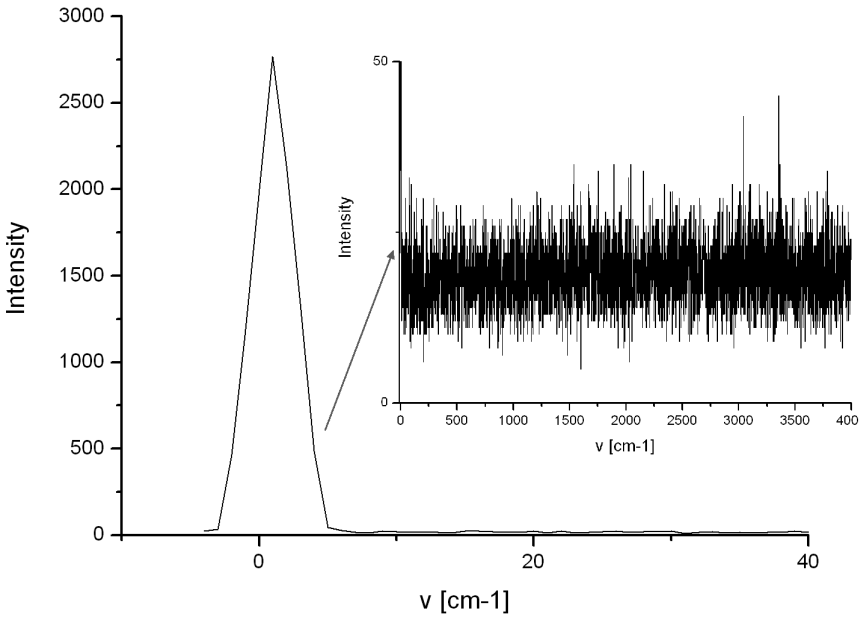

Figure 3.20: Emission lines in the Raman spectrum of the green laser.

The absence of other emission lines of the laser (other than the line that was used as an excitation source), which might appear in the spectra has been tested. For this, the laser intensity was radically reduced, so that no Raman effect occurs and only the emission lines can be seen (see Fig.3.20). No line, apart from the expected line at $0cm^{-1}$ (i.e. a fundamental frequency of $19350cm^{-1}$), could be detected.

The spectra has been recorded between $\overline{\nu}$=-$4cm^{-1}$ and $\overline{\nu}$=$4000cm^{-1}$ ($\Delta\overline{\nu}$=$1cm^{-1}$, accumulation time/step=1s $\rightarrow$ overall scanning time t≈80min[33]). The reason for starting at a negative wavenumber was to obtain a peak corresponding to laser emission at the beginning of the spectrum at $\overline{\nu}$=$0cm^{-1}$ (see Fig.3.21). This peak is used to control calibrate the wavenumber shift, which might be shifted slightly due to an error in the electronics. To prevent destruction of the analyzer by the high power of the laser beam, during the scan of the first wavenumbers shutters which decrease the intensity 10^7 times are closed. After the laser peak, these shutters have to be opened. Therefore the real Raman signal of the sample was recorded after the wavenumber, at which the last shutter had been opened typically, $\overline{\nu}$ ≈$25cm^{-1}$. Furthermore, before each scan the optics were adjusted to maximise the output signal.

A fluorescence background signal was observed, especially in more concentrated samples, or samples with an increased opaqueness, (see Fig.3.22). This signal was

[33]Including the time used by the analyzer for going to the next wavelength.

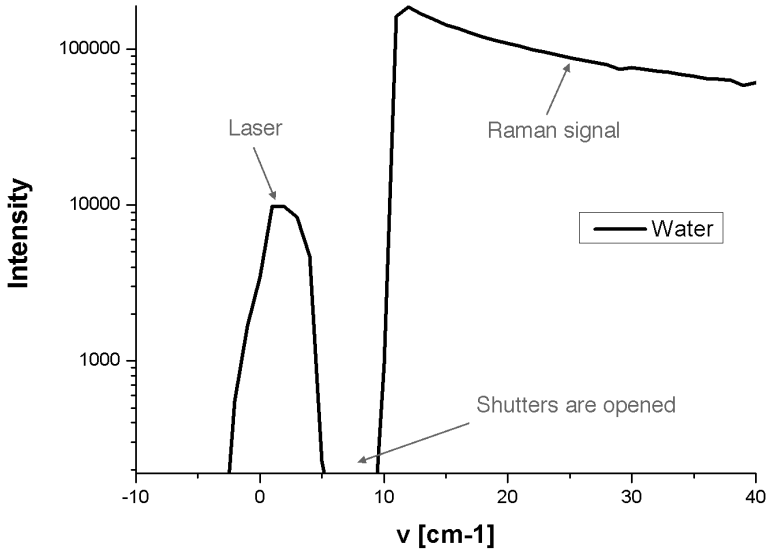

Figure 3.21: The beginning of the recorded Raman spectrum of water. The peak around $\overline{\nu}$=0cm^{-1} corresponds to scattered laser light. The real Raman signal from the sample starts at $\overline{\nu}$ ≈25cm^{-1}.

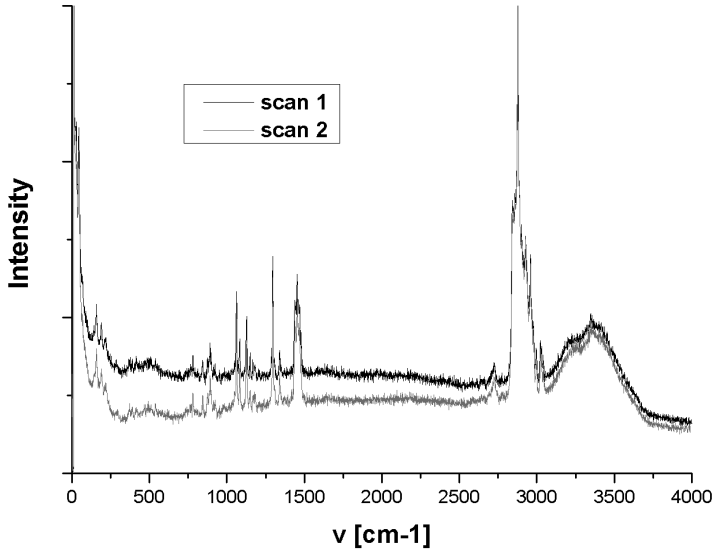

Figure 3.22: The decrease of background fluorescence after treating the sample with a high intensity laser.

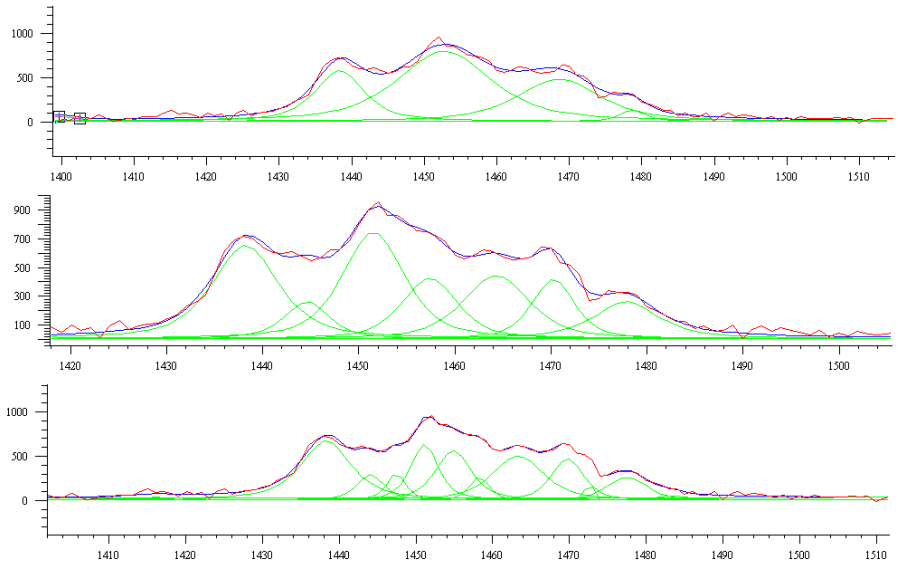

Figure 3.23: The dependence of the fit (blue) of the Raman signal (red) using Wire2.0 on the number and starting position of the used Gaussians (Lorentians) (green).

observed to decrease with time and could partly be burned out of the sample upon treating it with a pulse of intense laser power. The observed background was approximated by a polynomial fit and removed from the spectrum using Wire2.0. One should note, that this correction was difficult for the region of $\overline{\nu}$<300cm^{-1} due to the broad and intense band. Its height and slope was consequently affected.

After background correction, the spectra were normalised using the peak between $\overline{\nu}$=1400-1550cm^{-1} using Origin8.0:

$$\int_{1400}^{1550} I(\overline{\nu})\, d\overline{\nu} = 1 \tag{3.16}$$

Selected peaks were fitted with a combination of Gaussians (Lorenzians) using the Wire2.0 software, until a fit was obtained, which was of sufficient quality. One should note that for peaks resulting from a combination of overlapping bands, the fitting results depend strongly on the choice of starting position and shape of the peaks and on the number of peaks (see Fig.3.23). The risk is, that 'peaks' resulting from the noise oscillation are mistaken as shoulders etc. For comparative results, peaks have been always obtained in the same manner. Therefore, for similar curves, similar results have been obtained. The analysed peaks are in no way supposed to be treated as final definitive band numbers, they are only used to compare different sets of data.

All the experiments involving Raman spectroscopy were done in collaboration with Mr. Hugh Vass.

The Raman microscope used in this work To record the Raman spectrum at different locations in a sample, measurements on a confocal Raman spectrometer (Raman 300 with BX40 microscope, 10x objective) were performed. The sample of thickness of 100μm was temperature controlled in a homebuilt sample cell (ΔT<0.5°C, see section 3.3.4.2). The 632.8nm line of the HeNe laser was used as the excitation source. The initial laser power was 200mW.

A CCD camera was used to collect the Raman signal in regions of interest (i.e. 600-1000cm^{-1}, 1200-1600cm^{-1} and 2800-3000cm^{-1}). A maximum region of 800 wavenumbers could be detected at once. Before each measurement, the detection setup was calibrated, using the laser peak and the peak of silicon (520.07cm^{-1}). One should note that, at certain wavenumbers, sharp peaks occur due to the failure of some pixels in the CCD camera. By recording 2 regions of the spectrum slightly shifted with respect to each other and comparing the peaks, those artefacts could be identified and removed using LabSpec4.18.

The maximal signal/noise ratio has been obtained for a hole size of 300μm (500μm for opaque samples), a slit size of 150μm (300μm for opaque samples) and a laser intensity of 100%. The resulting spot size of the laser at the sample was 21μm (36μm for opaque samples). After choosing a region of interest with the attached microscope, the focus was adjusted so that the maximum signal/noise ratio was obtained.

The spectra were obtained after averaging 5-10 scans, each of which was recorded over 30s, leading to a total recording time of up to 5min. The spectra were stable over a long period of time (up to 90min) with changes only in the intensity of the fluorescent background (see Fig.3.24), and therefore not affected by the used laser intensity. The fluorescent background is strong compared to the background using the Raman spectrometer, especially the shape of the water peak above 3000cm^{-1} depends strongly on the choice of baseline.

The spectrum quality was, in general, of poor quality compared to the Raman spectrometer, especially in opaque samples (see Fig.3.25). However the peaks in the region 1200-1600cm^{-1} and 2800-3100cm^{-1} could be compared and used for further studies (see Fig.3.26). The bands are slightly shifted to lower wavenumbers, which might be caused by poor calibration in some measurements. In the peak between

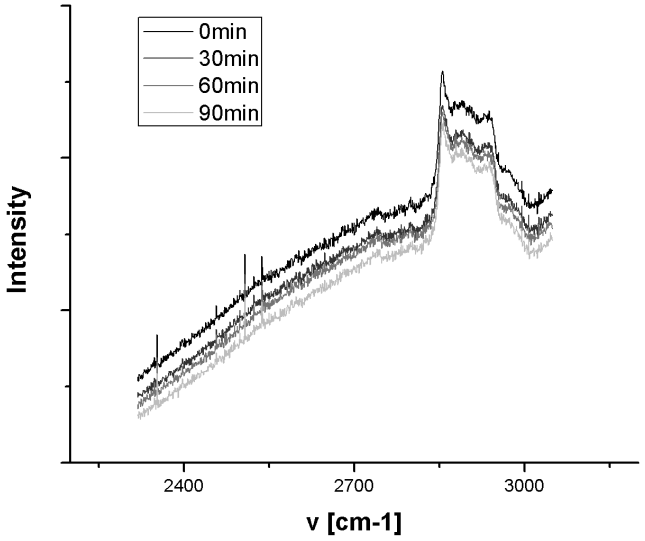

Figure 3.24: The dependence of the non-corrected Raman spectrum (using the Raman microscope) with time.

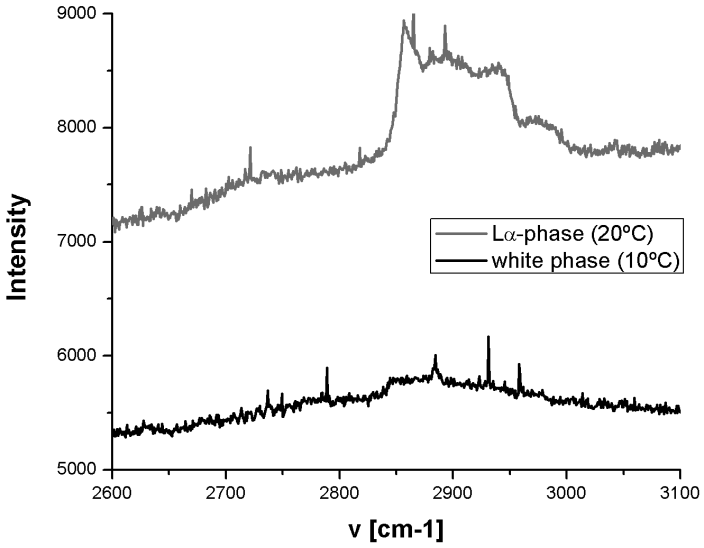

Figure 3.25: The decrease in signal intensity and quality of the not corrected Raman spectrum (using the Raman microscope) going from a clear (L_α) to an opaque (white phase) sample.

2800-3100cm^{-1}, a small change in the shape can be observed. This was caused by the different detection geometry used in the setups. While the Raman signal is recorded at an angle of 90° in the spectrometer, in the Raman microscope the recording angle is 180°. A test measurement at the spectrometer under the same detection geometry as used in the microscope confirmed this explanation (see Fig.3.26(e)). Those differences had to be taken into account, when analysing the spectra.

One should note that in case of white samples (liquid and solid), showing a strong laser reflection, some artefacts in the spectra have been observed (see Fig.3.27). These might be caused by the backreflection of the laser on the metal cover of the homebuilt sample-cell. Covering the sample-cell with a matt black plate with a hole of a diameter of about 1cm, removed these artefacts from the spectra.

The recorded spectra were background corrected (polynomial fit) using LabSpec4.18 and Wire2.0, with respect to the spectrum of pure water in the sample cell. The peaks were normalised, by choosing a peak in the spectra which is least influenced by the measurement series, using LabSpec4.18 or Origin8.0.

3.3.2.2 Single molecule calculation

Use of single molecule calculations Single molecule calculations have been used to support the assignment of the experimentally observed Raman frequencies and confirm influences of different conformational states on the observed spectra.

The principle of Single Molecule Calculation [Atkins 05] Computational methods can be used to derive the properties of a molecule from first principles, i.e. quantum mechanical calculations. Those calculations are called *Ab Initio* methods and all have the aim to solve the time-independent molecular Schrödinger equation:

$$\mathcal{H}\Psi = E\Psi, \tag{3.17}$$

where Ψ is the wavefunction and E the energy. The Hamiltonian operator $\mathcal{H}$ for a system of nuclei (index n) and electrons (index e) has the general form:

$$\mathcal{H} = T_e + T_n + V_{en} + V_{ee} + V_{nn}, \tag{3.18}$$

where T_i and V_{ij} are the corresponding kinetic and potential energies.

This equation cannot be solved analytically even for simple molecules, and therefore

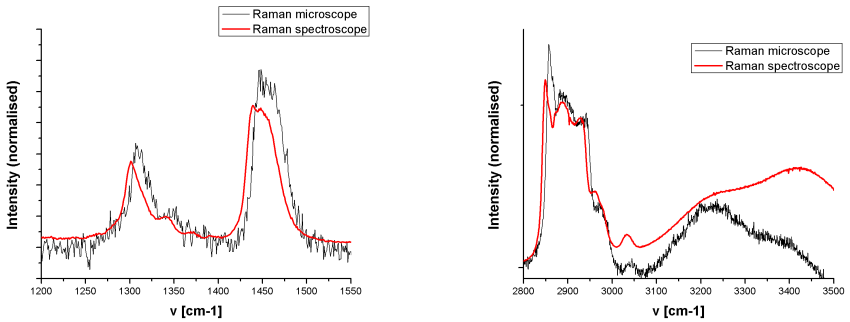

(a)

(b)

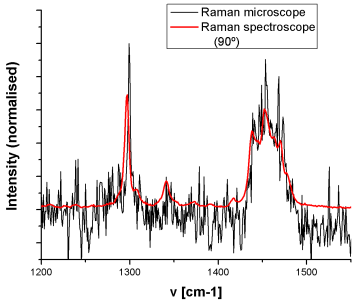

(c)

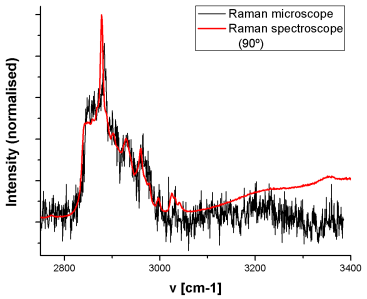

(d)

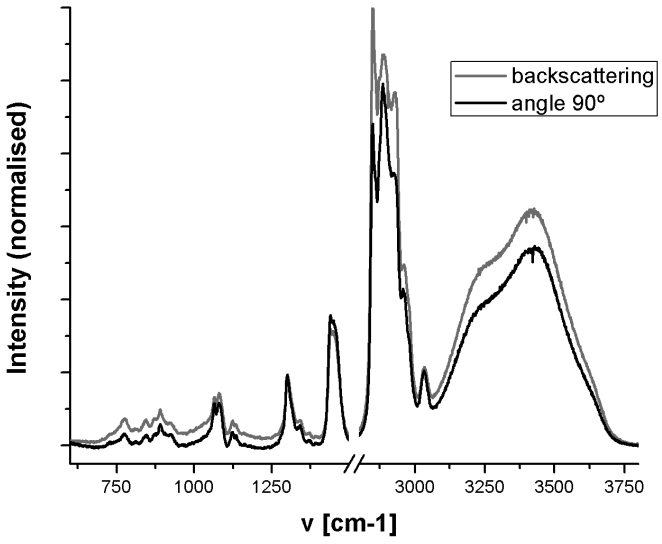

(e)

Figure 3.26: Comparison of the spectrum obtained by Raman microscopy and Raman spectroscopy for the lamellar phase (a,b), and the 'white' phase (c,d). Comparison of the effect on detection geometry on the spectrum obtained by Raman spectroscopy (e).

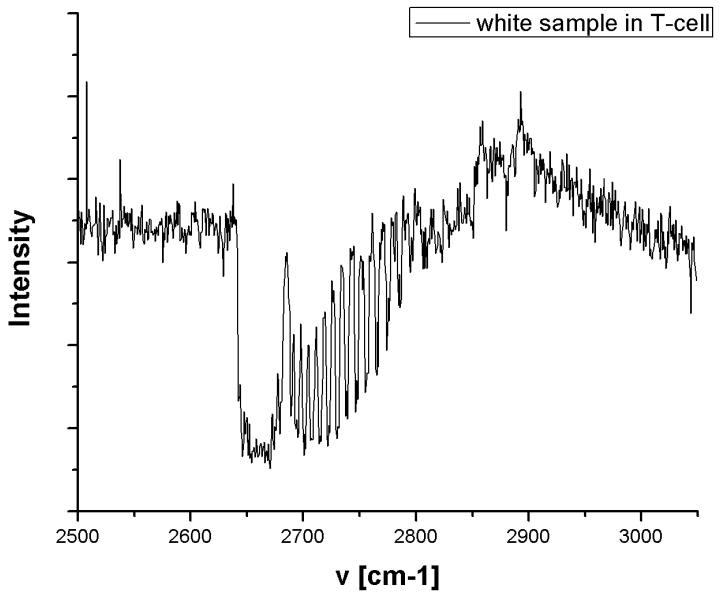

Figure 3.27: Artefacts in the Raman signal, caused by a strong reflection of the laser on the white sample and the metallic sample cell.

a range of approximations have to be made. The first approximation (Born-Oppenheimer approximation) separates the problem into an electronic and nuclear problem. Because the electrons are light compared to the nuclei, it can be assumed that they instantaneously adapt to any change in position of the nuclei and thus depend only on the position of the nuclei, but not on their momentum. Therefore those movements can be separated, the nuclei regarded as fixed in position and for each position the Schrödinger equation is solved for the electrons in the static electric potential arising from the nuclei (T_n=0, V_{nn}=const). One should note, that this approximation is good for molecules in their electronic ground state but poor for excited states, large amplitude vibrations or the motions of light nuclei [Atkins 05, Richardson 01].

The use of the Born-Oppenheimer approximation reduces the molecular Hamiltonian to an electronic Hamiltonian describing the motion of n electrons in the field of N point charges, simplifying Eq.3.17 and Eq.3.18 to

$$\mathcal{H}_{elec}\Psi_{elec} = E_{elec}\Psi_{elec}, \tag{3.19}$$

where Ψ_{elec} is the electronic wavefunction and E_{elec} the electronic energy (the total potential energy is $E_{tot}^{pot} = E_{elec} + V_{nn}$), and

$$\mathcal{H}_{elec} = T_e + V_{en} + V_{ee}, \tag{3.20}$$

respectively. One should note, that for every molecular configuration a different electronic wavefunction will be obtained.

However, even with this approximation, only the H_2^+ molecule can be solved analytically. The problem is the third term in Eq.3.20, which treats the coupling between electrons. The position of the electrons are influenced by the positions of the other electrons. If this term did not exist, the electronic wavefunction would simply be the product of the one-electron wavefunctions. The coupling (the exchange and correlation) is caused by two factors. One is the Pauli-principle, i.e. the rule, that electrons of the same spin cannot occupy the same region of space. The other is the electrostatic correlation, due to the coulombic repulsion between each electron, which is itself modified due to the Pauli-principle, which changes the repulsion between electrons of the same spin. To prevent the violation of the Pauli principle, a special form of the overall wavefunction (e.g. a Slater determinant) is used and spinorbitals are introduced, i.e. the orbital Ψ is written as a product of the spatial wavefunction Ψ_r and the spin Ψ_s. Still, the difficulty lies in the problem of how to include the effect of the Pauli principle on the electron-electron interaction and the correlation between the electrons.

There are two different groups of computational methods, which differ in the theoretical approach to deal with the electron-electron interactions V_{ee}, the first being the Hartree-Fock approach and the second being the DFT approach.

Hartree-Fock The Hartree-Fock approach treats the electron-electron interactions V_{ee} in an average way. Each molecule is considered to be moving in the electric field of the nuclei and the average field of the other $n-1$ electrons.

In this approximation, the Hamiltonian is replaced by the Fock operator, which consist of a one-electron Hamiltonian h_1 and the correction term due to the electron-electron

interaction:

$$\begin{aligned} F_i &= h_i + \sum_{j \neq i} [2J_{ij} - K_{ij}] \\ J_{ij} &= \int \Psi_i(1)\Psi_j(2)\frac{1}{r_{12}}\Psi_i(1)\Psi_j(2)\, d\tau_{12} \\ K_{ij} &= \int \Psi_i(1)\Psi_j(2)\frac{1}{r_{12}}\Psi_i(2)\Psi_j(1)\, d\tau_{12} \end{aligned} \tag{3.21}$$

J_{ij} is the Coulomb operator, which takes into account the classical coulombic repulsion between electrons in different orbitals and K_{ij} is the modification of the coulomb repulsion due to the Pauli principle.

One should note that this approximation only includes the electron-electron interaction to a very small degree. In Post HF methods, the electron coupling is approximated more precisely (see [Atkins 05]), however such calculations are difficult to perform.

Density functional theory (DFT) An alternative approach is given in DFT methods, which simplifies the calculation to a large degree, whilst taking the electron correlation into account to a certain degree. DFT methods are based on the fact that the ground-state energy and all other ground-state electronic properties are uniquely determined by the electron density

$$\rho(r) = \sum_{i=1}^{n} |\Psi_i(r)|^2, \tag{3.22}$$

where Ψ_i are the one-electron spatial orbitals. However, the form of the dependence of the electronic energy E on $\rho(r)$ is not explicitly known[34]. The problem is again the exchange and correlation energy E_{XC}, which takes into account all non-classical electron-electron interactions in:

$$E[\rho] = T_e + V_{en} + V_{clas,ee} + E_{xc}, \tag{3.23}$$

where T_e is the kinetic energy of the electrons, V_{en} the electron-nucleus attraction and $V_{clas,ee}$ are the classical coulomb interaction between the total charge distribution at r_1 and r_2.

Different forms of Eq.3.23 have been suggested, which have been compared to HF results. They differ mainly in the degree to which the correlation is taken into

[34] E is a functional, i.e. a function of a function.

account. In this work, two standard DFT-methods have been used: BLYP and the more advanced B3LYP, both of which are commonly used for organic compounds. The quality of the calculation is mainly influenced by the choice of the functional.

Self consistent field The problem with both methods is that 'the answer' has already to be known to perform the calculation (in HF, the wavefunction (Eq.3.21) and in DFT the charge density distribution). This problem is solved by the self consistent field method:

1. A set of trial wavefunctions (charge density) is guessed

2. These wavefunctions are used as input parameters in the HF theory (DFT theory) to obtain a new set of wavefunctions (charge density)

3. The second step is repeated until convergence is satisfied

One can see that both methods are computationally expensive, especially when going to large systems. This restricts the calculations to system sizes of about 100 atoms. The biggest problem is that, in each step, the calculation of wavefunctions is required. This can be simplified by approximating the spatial wavefunction by a linear combination of known basis function.

$$\Psi_r = \sum_i c_i \Phi_i \tag{3.24}$$

This approach reduces the problem of solving wavefunctions to one of solving linear equations in order to find the best coefficients c_i. However, the quality of the calculations depend strongly on the size and quality of the basis set (especially for HF methods) [Atkins 05, CCCBDB 06].

Gaussian type orbitals (GTOs) There are a broad variety of functions which can be used as basis functions, varying in the quality of modelling of the shape of orbitals (usually tested on atomic orbitals, the shape of which is well known) and in the easiness of performing computational calculation with them. GTOs are one of the most common basis functions, due to their simple behaviour in calculations[35]. The general form of a cartesian gaussian is:

$$\Phi_{ijk}(r - r_c) = (x - x_c)^i (y - y_c)^j (z - z_c)^k e^{-\alpha |r - r_c|^2}, \tag{3.25}$$

[35] E.g. the first derivative of a GTO or the product of two GTOs is another GTO.

where r=(x, y, z) is the position of the electron and r_c=(x_c, y_c, z_c) the centre of the gaussian. The factors i, j and k are natural numbers depending on the type of orbital:

$$\begin{aligned} i = j = k = 0 &\longrightarrow \text{s-type orbital} \\ i + j + k = 1 &\longrightarrow \text{p-type orbital} \\ i + j + k = 2 &\longrightarrow \text{d-type orbital} \end{aligned} \tag{3.26}$$

However, a simple GTO very poorly approximates the real shape of an orbital, therefore, usually, a linear combination of GTOs (a so-called contracted GTO) is used to model one orbital:

$$CGTO = \sum_i d_i GTO_i \tag{3.27}$$

The coefficients d_i are obtained by modelling the corresponding atomic orbital and are kept constant during the calculation. One can see that this is fine for orbitals which are close to the core of the atom as the shapes of those orbitals are least influenced by the bonds between the atoms. This is, however, not the case for valence orbitals. For those, the coefficients should be changed during the calculation. This is achieved by using two (or more) basis functions (which can be simple or contracted GTOs) in Eq.3.24 for each of the valence orbitals, and therefore allowing changes of shape of the orbital during the calculation and not just its relative intensity with respect to all orbitals. Those basis sets which allow two or more basis functions for the valence orbitals, but only one for the core orbitals, are known as a split valence basis set. They are most commonly used in computational methods which rely on GTOs.

In addition, polarisation functions can be added to the basis set to try to model the polarization effect caused by the distortion of the shape of the electron cloud of one atom by the electron cloud of the neighbouring atom. Polarization functions are commonly functions of a higher quantum number l than are present for the atom, i.e. e.g. p-orbitals for H and d-orbitals for C or N. Furthermore, in the case of modelling anions or excited states in which electrons may be further removed from the nucleus than in the ground state, diffusive basis functions could be added, which have a larger spatial extent than the normal ones.

In this work the most frequently used basis set is the

$$6 - 31G(d, p)$$

split valence basis set, where G stands for gaussian type orbitals. The core orbitals are modelled with one basis function which is a contraction of 6 GTOs, while the valence orbitals are modelled with 2 basis functions (one consisting of 3 GTOs and the other of 1 GTO). The letters *d* and *p* indicate that the polarisation functions of p-type for e.g. H and d-type for e.g. C are added.

In general, one can conclude that *Ab Initio* calculations are the most reliable computational methods available and provide descriptions of the electronic structure that are purely based in quantum mechanics. They provide predictions for properties that are completely independent of any empirical input. The quality of the calculations can be systematically improved (by improving the basis set) for HF methods (and those differences can be rationally explained by explaining the differences between theory and experiment), while the advantages of DFT are that they include some components of the electron correlation for much the same computational cost. This means that it is a highly efficient way of performing a more advanced calculation. However, the difficulty is, that DFT methods are not systematically improvable like wavefunction based methods and so it is impossible to estimate the error associated with the calculation without reference to experimental data or other types of calculation.

Once the electronic energy is obtained, a number of molecular properties can be determined. This section will focus on the relevant properties for this work: the equilibrium geometries and the vibrational frequencies of those geometries.

Geometry optimisation The molecular potential energy for a stationary molecule depends on the configuration of the molecule. This dependence is illustrated in the potential energy surface (see Fig.3.28). On this potential energy surface certain points can be identified, depending on the first derivative (the slope) and the second derivative (the curvature) of the potential energy with respect to nuclear coordinates:

- **Maximum** The slope is zero, the curvature is negative in all directions.
- **Minimum** The slope is zero, the curvature is positive in all directions.
- **Saddle Point** The slope is zero, the curvature is negative in at least in one direction and positive in at least one other.

All these points are called stationary points. The first derivative vanishes, which means, that each of the forces exerted on a nucleus by the electrons and the other nuclei must vanish:

$$f_i = \frac{-\delta E}{\delta q_i}, \tag{3.28}$$

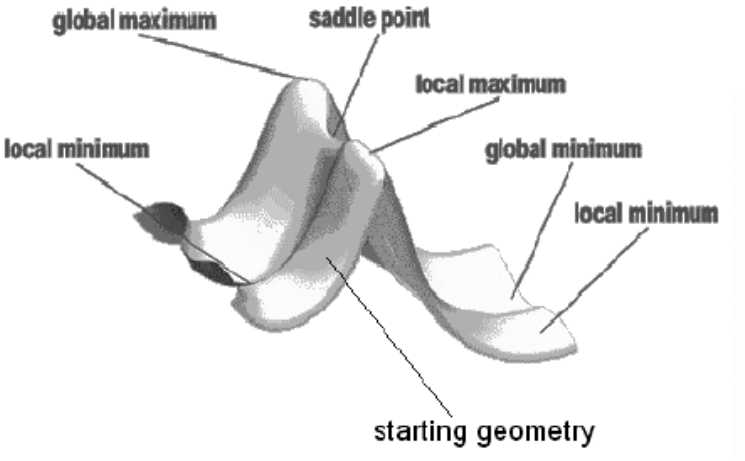

Figure 3.28: General form of a 2D potential energy surface.

where q_i are the internal coordinates. The equilibrium structure is either in the global or a local minimum.

Because it is impossible (requiring an immense computational cost) to compute the whole PES, with its first and second derivatives, in order to find all equilibrium structures and find the one coming from a global or local minimum, a search algorithm has to be used, leading from a starting geometry to an equilibrium structure. Most algorithms (as does the one used in this work) lead to a geometry, in which the magnitude of the forces are sufficiently close to zero (the tolerance limit), and therefore a stationary point is found. The searching path leads, in general, to the stationary point which is closest to the starting geometry.

The calculation of the derivatives of the potential energy is crucial for the efficient determination of equilibrium structure. The determination of the first derivative is comparably easy, but the second derivative requires the derivation of the coefficients c_i in Eq.3.24. Therefore the second derivative, commonly called the Hessian matrix, is often approximated numerically, based on the position of other known points on the PES.

The algorithm, which is used by Gaussian 03, includes the following steps (the Berny optimization algorithm) [Gaussian03 09]:

1. A starting structure is provided, and its potential energy and first derivative (if possible) calculated. The Hessian (second derivatives) is estimated.

2. A quadratic function is fitted to this point in the PES in order to find the position

of a minimum in space. The step to the found minimum is suggested.

3. The step is accepted, if it lays within the trust radius[36]. If the step exceeds the trust radius, the step is reduced in length to the trust radius by searching for a minimum of the quadratic function on the sphere having the trust radius.

4. The potential energy and the forces of the new point are calculated . The Hessian is updated (only approximated, not analytically calculated)[37]

5. A linear search is performed between the latest point and the best previous point. Depending on the knowledge of the derivatives of those points, a polynomial function (power 3-5) is fitted (the higher the power, the more has to be known about the points). Only if the second derivatives are available, the function is allowed to have more than one minimum.

6. If the latest point is the best point so far, the step is always accepted. If all polynomial fits fail, a quadratic function is fitted and the situation is the same as for the first point.

7. If the latest point is not the best point, the step is only accepted if it lays in between the two points. If all polynomial fits fail in providing an acceptable point, the step is taken to be the midpoint of the line connecting the most recent and the best previous point.

8. This procedure is repeated until a stationary point is found. The convergence is tested against criteria for the maximum force component, root-mean square (RMS) force, maximum step component and RMS step.

As already mentioned, this algorithm leads to the stationary point closest to the starting geometry. Therefore, a range of equilibrium conformations can be found, by providing different starting geometries. The global minimum, being the most stable equilibrium conformation, can only be found, if all minima are found and their energy values compared. For every equilibrium conformation, the vibrational Raman spectra can be estimated.

Frequency Calculation The vibrational frequencies can be extracted from the Hessian matrix, which has already been computed during the geometry optimization. This is because the potential energy can be expressed as the first few terms of a Taylor

[36]Which basically determines the maximum step size.
[37]The approximation is better, the more points are known in the surrounding.

series for small displacements $x = r - r_0$ around the equilibrium position r_0:

$$V(x) = V(0) + \sum_i \frac{\delta V}{\delta x_i} x_i + \frac{1}{2} \sum_{i,j} \frac{\delta^2 V}{\delta x_i \delta x_j} x_i x_j + ... \tag{3.29}$$

The first term can be neglected, as the absolute value is not searched, the second term vanishes, because the expansion is around a equilibrium position[38] and the terms higher then second order may be neglected in a first approximation. Therefore the potential energy can be approximated with the Hessian matrix. As already stated in section 3.3.2.1, a harmonic approximation for the potential energy can be used to describe the vibrational frequencies (Eq.3.12), leading to the force constants of the normal modes (after diagonalizing the Hessian matrix):

$$k = \frac{\delta^2 V}{\delta x_i^2} \tag{3.30}$$

It is worth noting that, only for a global/local minimum, all calculated frequencies will be positive (real), while for any stationary point other then a minimum some of the frequencies will be negative (imaginary frequencies). This fact can be used to confirm that a minimum is found after a geometry optimisation.

However, the PES is not harmonic, but rather approximated by a Morse function (see Fig.3.29). This anharmonicity causes the vibrational energy levels to be more closely spaced, and therefore the calculated frequencies are always slightly above the real values. Anharmonic corrections can be taken into account by including higher order terms in Eq.3.29. However, those calculation are computationally very demanding. In practice, vibrational frequencies produced by *Ab Initio* methods are often multiplied by a so-called scaling factor, which are for different methods reported in the CCCBDB (computational chemistry comparison and benchmark database [CCCBDB 06])). These scaling factors are based on the comparison of observed vibrational frequencies and theoretical frequencies (for each basis set) (see Tab.3.8). They are obtained from the sum over all the vibrational frequencies. The scaling factors are small for basis sets including polarization functions compared to the ones without, which suggests, that polarisation functions are important for a good prediction of vibrational frequencies.

As already discussed in section 3.3.2.1, the calculation of the Raman intensities requires an integration over all electronic states (see Eq.3.7 and Eq.3.9). However, this is

[38] That is one of the reasons, that it is important to run an unrestricted geometry optimisation before the frequency calculation.

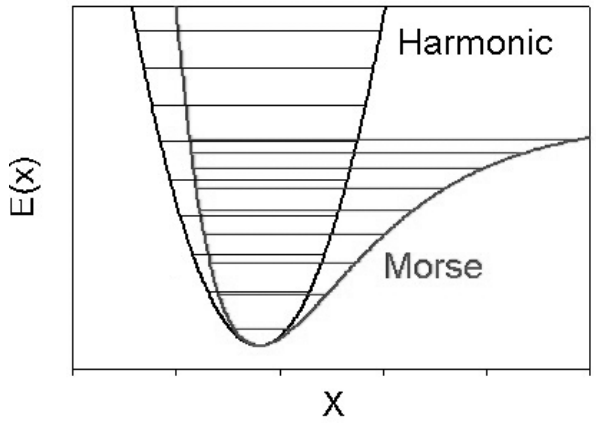

Figure 3.29: Comparison of the shape of the harmonic function and the Morse function.

method	**scaling factor**	error	nb. molecules	nb. vibrations
HF/6-31G(d,p)	**0.903**	0.026	272	2719
BLYP/6-31G(d,p)	**0.992**	0.027	270	2715
B3LYP/6-31G(d,p)	**0.961**	0.045	271	2716

Table 3.8: Scaling factors relevant for this work [CCCBDB 06].

not computationally achievable. Therefore, another approximation has to be used to compute the Raman intensities. The approach is based on a Taylor expansion of the potential energy over an external electric field $\mathcal{E}$. This leads to an expression of the expectation value of the electric dipole moment $< \mu_i >$ [Atkins 05], which is, in the presence of the electric field, the sum of the permanent dipole moment μ_{0z} and the contribution induced by the field [Atkins 05]:

$$\begin{aligned} < \mu_i > &= -\frac{dE}{d\mathcal{E}}_0 - \frac{d^2E}{d\mathcal{E}^2}\mathcal{E} - ... \\ &= \mu_{0i} + \alpha_{ii}\mathcal{E} + ... \end{aligned} \tag{3.31}$$

where α_{ii} the polarizability. Gaussian 03 obtains the approximate values for α by numerically differentiating the analytic dipole derivatives with respect to an electric field [Gaussian03 09]. However, one should keep in mind that the obtained values are approximated to a high degree and should therefore be treated with care.

Methodology in this work All calculations were carried out using the software package Gaussian 03 running on a SUSe 9.x Linux HPC cluster consisting of 68 AMD Opteron processing cores contained within EaStChem's Research Computing Facility's Hare cluster. Default convergence criteria were used for all calculations

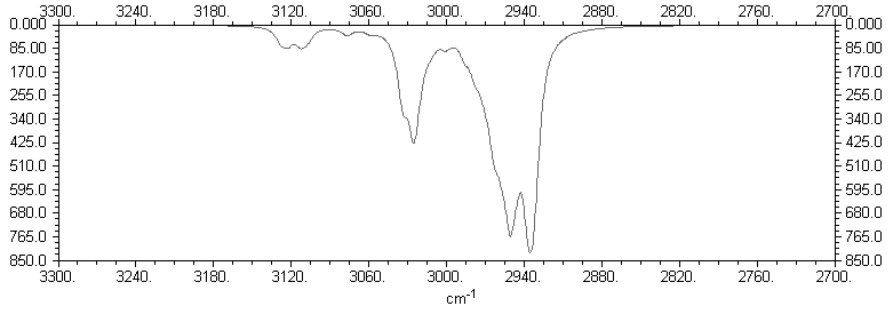

(a) halfwidth=5

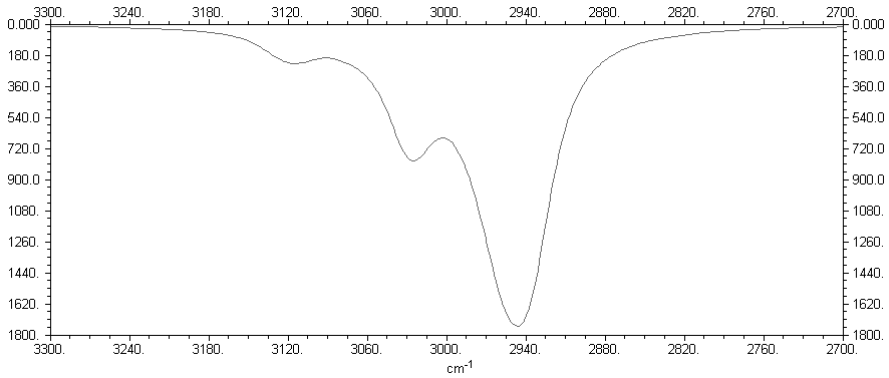

(b) halfwidth=20

Figure 3.30: The effect of the chosen halfwidth of the Lorentzians fitting the CH stretching peak of DDAB obtained computationally (BLYP/6-31G(d,p))

(maximum force=0.00045, RMS force=0.0003, maximum displacement=0.0018 and RMS displacement=0.0012). The molecules were build in Chemsketch. The Gaussian input file was created by Arguslab, and manually modified if necessary (e.g. if more processors[39] were required). The obtained geometries were viewed in Arguslab or GabEdit. The vibrational modes were investigated in GabEdit, which offered the possibility of visualising the corresponding motion in the molecule. Furthermore GabEdit offered the possibility to display a Raman spectrum by fitting gaussians or lorentzians of a certain constant halfwidth to the obtained frequencies and intensities. The shapes of the peaks in regions where they overlap depend strongly on the used halfwidth (see Fig.3.30). The C-H stretching peak resembled the experimental data most for a halfwidth=2.

The geometry optimisation was carried out for various starting geometries, varying in the number of gauche conformations in the alkyl chains. The required level of

[39]For frequency calculations 8 processors were needed and the memory was set to 15GB.

approximation was tested on the starting geometry, which was expected to lead to the most stable conformation. The geometry was optimised for different methods:

1. HF 3-21G
2. HF 6-31G(d,p) (Raman)
3. BLYP 6-31G(d,p) (Raman)
4. B3LYP 6-31G(d,p) (Raman)

In every step a better basis set is used. To minimize the computational cost, the input geometry was always the geometry of the previous step. The Raman frequencies were computed for the two DFT methods and a HF method for comparison. The obtained frequencies and relative intensities were very similar. As expected, the frequencies were shifted towards slightly lower frequencies according to the scaling factors (Tab.3.8). The obtained potential energies decreased with the quality of the basis set. All changes were comparably small and could be explained by the theory. For all further starting geometries, the Raman spectra were obtained from the BLYP 6-31G(d,p) method.

3.3.2.3 Powder X-ray diffraction

Use of powder X-ray diffraction Preliminary powder X-ray diffraction data have been used to confirm the differences in crystal structure at low and high temperatures in the DDAB sample.

The principle of powder X-ray diffraction Powder X-ray diffraction investigates the structural properties of a sample in the Armstrong to nanometer region. The principle is similar to that of small angle X-ray scattering described in section 3.3.3.1. The only difference is that the sample is investigated at wide angles, therefore bands correspond to structures at a smaller lengthscale.

In crystalline samples, the position of the diffraction peaks depends on the size and shape of the unit cell of the sample. Therefore different unit-cells will lead to different diffraction patterns. [Urban 07]

The setup used in this work Preliminary powder X-ray diffraction experiments were done on the Bruker AXS D8 powder diffractometer in CSEC. A scan has been carried out at room temperature for the powder and at $T \approx 10°C$ for the 'white' phase. The temperature control was of low precision. Furthermore, the sample dried out with time. The data were background corrected, however no detailed analysis was carried out.

3.3.3 The phase structure and phase stability

The phase structure, being characteristic for the phase itself, and density have been investigated depending on concentration and temperature using small angle X-ray scattering and densitometry for samples in the lamellar phase and the low temperature crystalline phase. Furthermore, differential scanning calorimetry has given information about the thermal limits of the phases as well as about the type of phase transitions between the phases.

3.3.3.1 Small angle x-ray scattering (SAXS)

Use of SAXS SAXS has been used to obtain information about the repeating distance in lamellar phases depending on surfactant concentration and temperature. Furthermore, the strong scattering at low angles (Porod regime) of the 'white' samples could support the crystalline character of this phase.

The principle of SAXS Small angle X-ray scattering in lamellar phases can be interpreted by direct analogy with the optical diffraction grating: each plane of bilayers in the array corresponds to a single slit in the grating. The Bragg reflections are due to constructive interference between the X-ray radiation scattered by the planes and correspond to the principal grating diffraction maxima.

The planes of the array act as a set of parallel mirrors and reflect the X-ray radiation, thereby introducing phase differences because of their spatial separation. The scattered radiation will give rise to a Bragg reflection, if the phase difference introduced by pairs of parallel planes is an integral multiple of a wavelength. This condition (Bragg's law) can be written as

$$2D^* \cdot \sin\Theta = n\lambda, \tag{3.32}$$

where n is an integer, Θ the angle made by the planes of the array and the incident beam, and D^* the perpendicular spacing between the planes. It can be seen that for given repeating distance D^* in a lamellar phase (membrane thickness δ + water layer thickness a_w) a discrete spectrum of Bragg orders will be observed. As can be seen in Eq.3.32, the repeating distance D^* increases with decreasing Θ, thus, the larger the angle, the smaller the investigated spacing. Therefore, SAXS data are commonly displayed depending on

$$q = \frac{2sin\Theta}{\lambda}, \tag{3.33}$$

which removes the dependence of the peaks from the wavelength λ of the radiation. [Levine 72]

In general, the shape (thickness, relative intensity of the different orders of the Bragg peak, etc.) can be used to reveal further information about the structure of the lamellar phase (e.g. Caillé model). However, high quality data, displaying at least 4 orders of Bragg peaks, are commonly required for such calculations. This kind of analysis could not be done on the data obtained in this study, therefore the reader is referred to e.g. [Petrache 98].

Furthermore, particles in a nanometer to micrometer size give rise to Rayleigh scattering of the radiation at low angles. Most structural information can be obtained from the so-called Guiner regime (a plateau in the scattering peak at very small angles), however this regime was not obtainable in our samples. The decay of the peak (Porod regime) with its characteristic decay proportional to q^{-4} could give an estimate of the size of the crystals in the samples. A detailed discussion of those regimes can be found in e.g. [Oberdisse 07].

The setup used in this work The SAXS measurements have been performed on the Bruker Nanostar (K_α radiation of a copper anode, $I_{beam}=10^6$/cm/s, beam size=0.5mm, detector size=1024x1024pixel) at the research center in Jülich (Germany). The instrument was calibrated to obtain total intensity values using the RAW counting rate of standard polymer FEP1400 giving 57.39. The data were measured on randomly orientated samples in glass capillaries (thickness 1.5mm). A scan of an empty glass capillary was used for background correction. The samples were temperature controlled in a homebuilt cell ($\Delta T=0.5°C$[40]).

The detected 'rings' were radially integrated using Bruker software and the data background corrected using a Fortran program (for code see section A.2). The data were further analysed using Excel.

All experiments have been carried out in collaboration with Wim Pyckhout-Hinzen.

3.3.3.2 Oscillating U-tube (density measurements)

Use of density measurements The density of dilute DDAB samples has been measured depending on temperature and phase using an oscillating U-tube densitometer.

[40] A temperature gradient along the capillary caused the large uncertainty in temperature control. For future measurements, homebuilt metal cuvettes were built to ensure even temperature control along the entire glass capillary.

The principle of the measurements A U-tube densitometer measures the frequency of the oscillation of a tube (U-shaped), which is completely filled with a liquid sample. The frequency of oscillation can be related to the density of the phase. However, this relationship does not take into account the effect caused by viscosity on the oscillation[41]. Therefore, the values obtained in this work can only give an indication of the dependence on temperature and phase, but are not quantitative values.

Furthermore, the density ρ of a solution containing two components, can be related to the densities ρ_1 and ρ_2 of each of the components:

$$\frac{m_1 + m_2}{\rho} = \frac{m_1}{\rho_1} + \frac{m_2}{\rho_2}, \tag{3.34}$$

where m_i is the mass of each of the components in the sample, which can be related to the weight concentration ϕ

$$m_1 = \frac{\phi}{1-\phi} m_2 \tag{3.35}$$

leading to an expression for the density of one of the components dependent on the measured sample density and the density of the other component

$$\rho_1 = \frac{\rho\rho_2}{\rho_2 - (1-\phi)\rho}\phi \tag{3.36}$$

The setup used in this work The Oscillating U-tube densitometer DA-510 at Glasgow University has been used. The instrument was calibrated with deionised water at 4°C, 10°C and 20°C. The setup required a sample volume of about 1ml, which had to be introduced into the tube without droplets of air. This was difficult for viscous samples. Therefore, measurements were performed on dilute solutions of 5%, 10% and (only for control) 25% over a temperature range of 2-30°C. The observed quantitative dependence on temperature was independent of surfactant concentration of the sample. The data were compared to the measured density dependence of pure water in the same range. The data were then analysed using Origin8.0.

3.3.3.3 Differential Scanning Calorimetry (DSC)

Use of DSC DSC has been used to identify the thermal boundaries of the phases in the phase diagram and give information about the properties of the investigated thermal phase transitions.

[41] Newer setups give the possibility to include viscosity corrections.

The principle of DSC [Hemminger 89] Differential scanning calorimetry is one of the standard methods for investigating phase transitions or measuring heat capacities of a sample. There are two different types of DSC equipment; one is the heat-flux-DSC, which measures the difference in the heat flux to the sample against a reference sample, while the sample and the reference probe undergo a determined temperature-program. The second is the Power-Compensation-DSC, which measures the difference in the heating power needed for having both sample and reference sample at the same temperature throughout the whole program. In this work a heat-flux-DSC has been used (henceforth referring to as DSC).

In principle, the sample and reference sample are placed into an oven, with the temperature set by a temperature program. In general, this program consists of dynamic steps, i.e. heating/cooling with a constant rate β, and/or isothermal steps, i.e. holding the temperature constant over a certain period of time. From the oven, certain heatfluxes $\Phi_{S/R}$ flow to the sample/reference sample. The heatflux to the reference sample is adjusted to keep its temperature equal to the temperature of the oven. The temperature difference between the sample and the reference sample Δ_{SR} is measured, which is proportional to the difference of the heat flux $\Phi_{S/R}$ from the oven to both samples.

In the case of an exothermic reaction, the released reaction heat flux Φ_r reduces ΔT_{OS} (the temperature difference between the oven and the sample) increasing the temperature of the sample and thus leading to an increase in the measured signal. The relation between the reaction heat flux and the measured temperature difference can be expressed as:

$$\Phi_r = -K\Delta T_{SR}, \tag{3.37}$$

where K is a calibration factor, which depends ideally only on T.

As already mentioned, DSC measures this heat flux (by measuring the temperature difference) depending on the temperature of the reference cell (which is defined by the choice of the temperature program). It has to be noted that the temperature of the sample differs from the set temperature, even when no reaction occurs. This is due to the differences in heat capacity between the sample and the reference cell. In the case of an exothermic/endothermic reaction a peak is seen in the DSC plot. By integration over the peak, the total reaction heat q_r (or the enthalpy change during the reaction) can be obtained:

$$q_r = -K \int_{t_1}^{t_2} (\Delta T_{SR} - \Delta T_{baseline}) dt \tag{3.38}$$

Furthermore, the onset temperature of the peak (the most independent temperature in the curve) is generally defined as the transition temperature. A deviation from the real onset temperature can be caused by an inhomogeneous sample temperature and the influence of high heating/cooling rates, which had been taken into account during the measurements.

The setup used in this work The DSC measurements on solution were carried out on the Mettler DSC30 (Düsseldorf University, Germany) in disposable crucibles made of Aluminium under a nitrogen flow of 20ml/min. Before the measurements, the equipment has been calibrated using Indium, Gallium, Lead and Bismuth with scanning rates of $2°C$, $5°C$ and $10°C/min$. In case of weights above 10mg, an aluminium oxide filled reference crucible was used. The 'white' phase sample was loaded into the crucible in a cold room ($5°C$) and immediately put into the precooled device.

The dependence of the onset temperature and peak width on scanning rate has been measured for rates of 10°C, 5°C, 2°C, 1°C and 0.1°C. The onset temperature was within the experimental error for scanning rates of 1°C, as was the peak width. However, one should note that the temperature calibration was of low precision, i.e. that the error of the relative temperature, being only 0.3°C, is much smaller than the error of the total temperature 2°C.

Furthermore, the dependence of the peak width has been investigated depending on sample mass and sample height. No dependence could be found, therefore it can be assumed, that the observed effects are not caused by a temperature gradient in the sample. In addition, control measurements on pure water were performed to ensure the observed effects were not caused by the equipment.

All measurements have been performed in collaboration with Peter Roloff.

3.3.4 The colloidal Structure

In biphasic regions in the phase diagram, micron scale colloidal structures form of one phase dissolved in the other. Using optical techniques, the dependence of the colloidal structure on temperature, relative concentration of the coexisting phases and the pathway to obtaining those phases has been investigated. Furthermore, the kinetics of the dissolution of the lamellar phase in water to give myelinic figures were investigated.

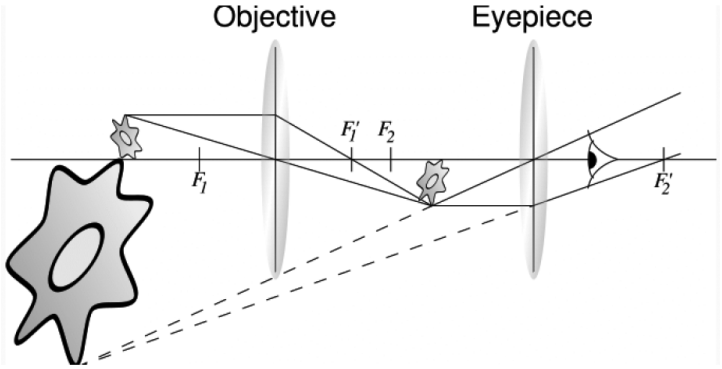

Figure 3.31: Ray diagram for a simple compound microscope.

3.3.4.1 Optical Microscopy

Use of microscopy As a microscope provides magnification of an image, enabling the resolution of structures on the micrometer length scale, this technique could be used to study the size and shape of myelins and identify the occurrence of multilamellar vesicles or crystalline structures in samples depending on surfactant concentration and temperature.

Principle of microscopy [Beales 05] Optical microscopy provides high angular magnification below the resolution of the human eye. It is a technique which uses visible light and a system of lenses to magnify images of small objects.

A schematic ray diagram of a simple compound microscope is shown in Fig.3.31. The objective lens forms a real, magnified and inverted image of the specimen in the plane of the field stop of the eyepiece. This image then acts as an object for the eyepiece lens, which produces, like a magnifying glass, an inverted virtual image of the original specimen. The total angular magnification of the lens is given by $M = M_o \times M_e$, where the indices o/e refer to the objective and the eyepiece, respectively.

Modern laboratory microscopes have more complicated optics. Objectives and eyepieces are a sophisticated combination of lenses which reduce chromatic and spherical aberrations, resulting in high quality images. Therefore the whole optical path has to be very accurately set up and controlled. Based on the numerical aperture *(N.A.)* - a parameter describing the brightness of the images depending on the amount of light collected by the objective lens[42] - the optical resolution and the wavelength

[42]In fact the image intensity is proportional to $(N.A.)^4$ and M^{-2}, so a small increase in the numerical aperture at a given magnification has a significant effect on the brightness of the image.

of light used λ sets a definite limit d to the optical resolution. Assuming that optical aberrations are negligible, the resolution d is given by (the Sparrow criterion):

$$d = \frac{0.51\lambda}{N.A.} \tag{3.39}$$

The role of the recording camera [Nat 05] These days, images from a microscope are generally recorded by a camera and stored on a PC. This enables image correction and analysis using numerical programs. The quality of the camera and the choice of data format have a large effect of the quality of the image and the ease of analysis.

A digital image is a 2D array of values representing light intensity, where each point represents one pixel. Each pixel belongs to an imaging sensor, which detects a grey level or colour that specifies the brightness or colour of that pixel. A digitized image has three basic properties: resolution, definition and number of planes.

- The spatial resolution of an image is determined by the product of the numbers of rows and columns of pixels.
- The definition of an image indicates the number of shades that one can see in the image. This number is limited by the bit depth of an image, which is the number of bits used to encode the value of a pixel. For a given bit depth n, a pixel can have 2^n different values. Higher definitions of images lead to a larger storage size, but enable a more precise measure of light intensities.
- The number of planes in an image corresponds to the number of arrays of pixels that compose the image. A greyscale image is composed of one plane, while a colour image is composed of three planes - one for the red, the blue and the green component.

Common images have a bit depth of 8-bit, 16-bit or colour encoding of 8-bit or 16-bit, giving an image definition of 256, 65536, 4*256 or 4*65526[43], respectively.

An image file is not only composed of a list of pixel values, but also of a header, which contains (depending on the file format) image information about the horizontal and vertical resolution, pixel definition and the original palette. Some formats (e.g. portable network graphics *PNG*) also allow the storage of information about calibration, pattern matching templates and overlays.

The choice of the file format and its definition must take into account the purpose of the

[43] In colour models, an additional 8-bit or 16-bit value goes unused.

measurements and the type of planned image analysis. Most image analysis programs require 8-bit greyscale pictures. The resolution of an image depends on the number of pixels which are in the camera sensor. The number of planes is also determined by the nature of the camera sensor, as colour images require the possibility to record light intensities of the red, blue and green components, while greyscale pictures only require a sensor recording the overall light intensity.

For time dependent measurements, the shutter speed of the camera and the storage time of an image also have to be taken into account.

The setup used in this work The microscopic structure of a range of samples were obtained using an Olympus BX50 or Nikkon Eclipse 80i microscope. A long working distance lens was required to focus on the sample and to maximize the field of view with high resolution, thus a x10 (Δxy=$(0.8\mu\text{m})^2$) phase contrast objective was chosen. The images were stored in a PC using a RMA 4376 (Media Cybernetics) camera or an EOS D30 (Canon) camera, respectively. If needed, the sample was held in a temperature controlled stage (Linkam LTS350/TMS93/LNP, ΔT=0.1°C) or a homebuilt sample cell (see section 3.3.4.2, ΔT<0.5°C, allows addition of water to sample).

Different types of structures could be resolved: crystals, myelins and vesicles. The experimental information about the more advanced types of measurements done are summarised below.

The crystals of the white phase were resolved by temperature controlled (polarized) microscopy (Nikkon Eclipse 80i, 10x objective). The sample was temperature-controlled in the homebuilt temperature cell at temperatures between 10-20°C in 1°C steps. No time effects on the images could be observed, once the temperature was stabilized within the whole sample. (chapter 4 and 5)

To investigate the freezing and melting of DDAB crystals, the sample was loaded into a capillary (0.2x4mm) using capillary forces. The viscosity did not allow the capillary to be filled over 50%. The ends were glued using Araldite. The temperature was controlled (Linkam) between (-25)-30°C (dT/dt=$\pm$0.1-2°C/min). The crystalline phase appeared black in the images (see Fig.3.32). The image size was 1.4x1.0mm^2. The images were analysed with a LabView code (see section A.1.3.3), measuring the increase in black area of the images with time. (chapter 5)

For statistical studies on the width distribution of myelins depending on the thickness of

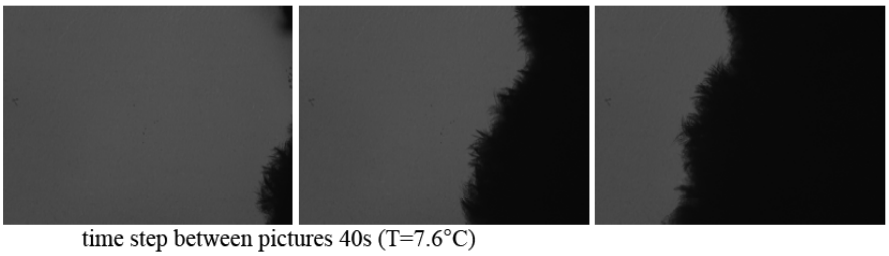

Figure 3.32: The freezing transition of a lamellar phase at T=7.6°C. The time step between each picture is 40s.

the sample (b=25, 50, 100, 200, 300, 400 and 600 μm, see page 118), several images were recorded (Olympus BX50, x10 objective) after a dense 'forest' of myelins surrounded the sample. These images were manually analysed by taking measurements of the width of as many myelins as possible (≈100), enabling a size distribution to be built up (see Fig.7.3). With the exception of the tip, the width of each myelin was found to be constant over its entire length and with time.

3.3.4.2 Direct Observation

Use of a direct observation setup The direct observation setup was used to observe the dissolution of a whole droplet (diameter≈5-10mm) of (aqueous) surfactant phase as a function of surfactant concentration and temperature. The setup is designed to image the sample without significant magnification, whilst still being able to resolve structural changes, e.g. myelin formation at the sample/water interface.

Principle of the setup [Starrs 99, Leng 06] The direct observation setup was first designed by Starrs *et al.* [Starrs 99] at Edinburgh University and further developed in [Leng 06]. A sketch of the optical principle of the setup is shown in Fig.3.33. In general, the setup consists of a main illumination component, which transforms light from a halogen bulb through an aspheric condenser and an achromat into a parallel beam. To reduce degradation of the samples, the beam is UV-filtered. A set of mirrors is used to direct the beam onto the horizontal sample cell. The light, emerging from the sample cell, is deflected by a first-front mirror and, using two identical achromatic doublets, focused on a camera, which is connected to a PC. The resolution of the image is of the order of a few microns.

It has to be noted that a direct observation setup only gives a 2-D projection of the sample. This means that any variations in height of the sample cannot be detected and other methods have to be used to take them into account in further analysis (see

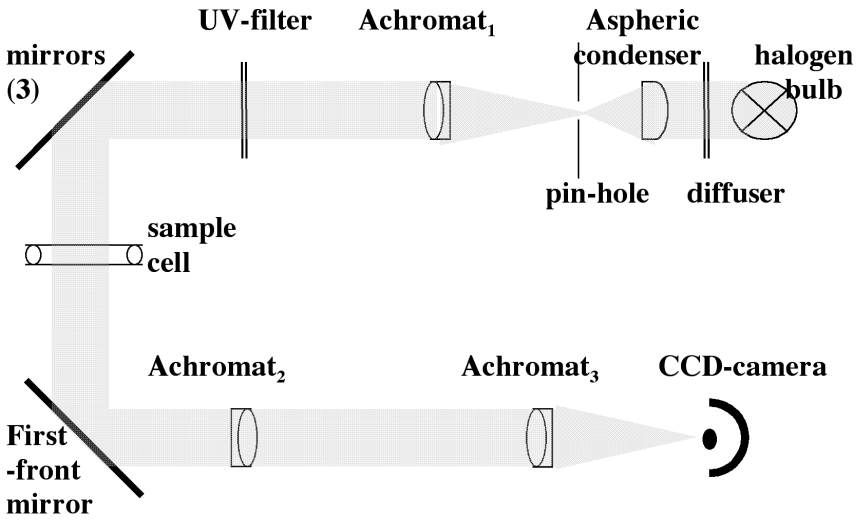

Figure 3.33: Sketch of a direct observation setup.

section 3.3.4.3).

The setup used in this work The use of good optics, which lead to a strong increase in image quality (sharpness and contrast) was found to be crucial for this work. The following specific components were chosen for a direct observation setup, which was designed at the Heinrich-Heine University (Düsseldorf, Germany) for the experiments described in chapter 6[44].

- **Even illumination** The light emitted from a halogen bulb was diffused using a 220-grit sandblast surface on glass (see Fig.3.34(a)). The glass of the diffuser is treated with two orthogonal passes during the sandblast and so these filters offer an even diffusion across the surface. This causes the illumination to be even and not in the shape of the halogen bulb.

- **Point-like source** The light was focused onto a pinhole using an aspheric condenser (see Fig.3.34(b)). Aspheric condenser lenses efficiently correct for spherical and comatic aberrations. One aspherical condenser can replace a multiple spherical element design, reducing the number of back reflections and ultimately leading to higher transmission yield.

- **Parallel beam** An achromat doublet (see Fig.3.34(c)) was used to transform the light into a parallel beam. Achromatic lenses consist of two optical components

[44]The experiments described in chapter 7 have been performed on the original setup designed in Edinburgh.

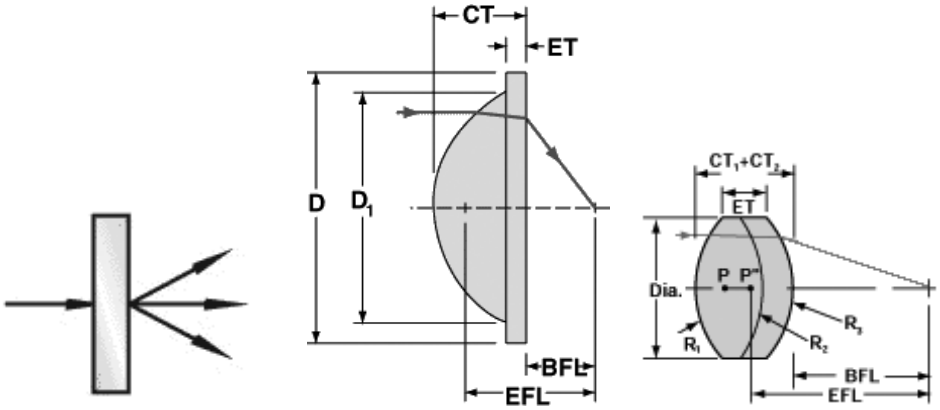

Figure 3.34: Sketch of the optical paths through a diffuser (a), aspheric condenser (b) and achromatic doublet (c).

cemented together to form an achromatic doublet, which is computer optimized to correct for on-axis spherical and chromatic aberrations.

- **UV-filter** The beam was UV-filtered to minimise degradation of the sample.
- **Illumination the sample cell** The sample cell was horizontal, therefore the beam needed to be directed onto it using a set of three mirrors.
- **Focussing the light onto a CCD camera** The light emerging from the sample cell was deflected by a first-front mirror. This mirror is highly polished on the front side and covered with a thin layer of metallic coating for reflecting light in different regions of the spectrum. Using two identical achromatic doublets, the light is than focused onto a camera. Depending on the exact position of the achromatic doublets, the image falling onto the CCD array has a magnification in the range of 0.5-2.5. The CCD camera was controlled using the program LabView 8.0 (see section A.1.1).

The technical specifications of the optical components can be found in section A.3.

The temperature controlled sample cell The sample was temperature controlled using a homebuilt sample cell (see Fig.3.35) made of an aluminium alloy, which ensures good thermal conductivity, whilst being easy to manipulate in shape. The temperature control was ensured by the incorporation of an extended channel for a cooling liquid (here water) into the cell. The cell was designed to surround a sample, placed on two microscopy slides, separated by a spacer of thickness b=100μm. Because water had to be added during the measurement, two holes were drilled into the sample cell. One hole

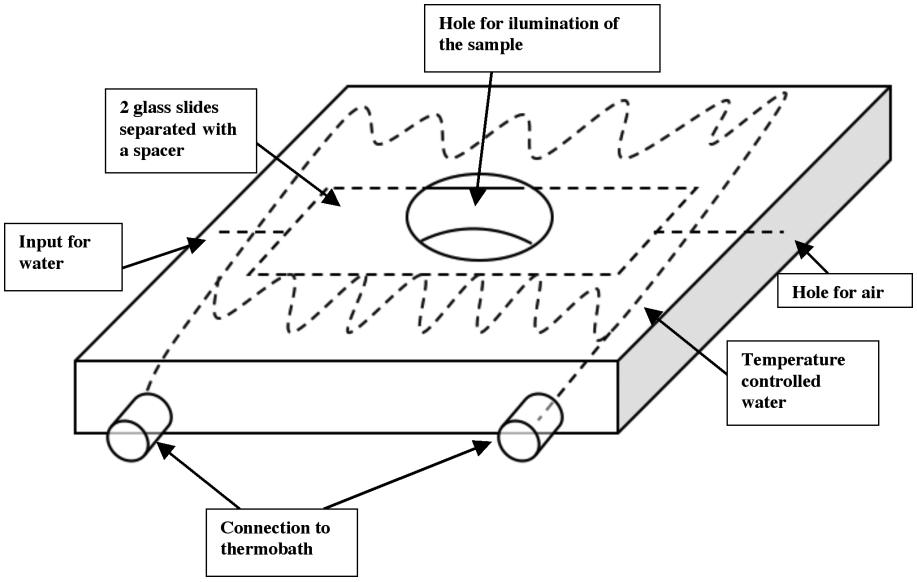

Figure 3.35: Sketch of the temperature controlled sample cell

was connected to a syringe containing the water. This water was held in the water-bath to equilibrate. However, there was the slight difference in temperature between the water bath and the sample cell. This was minimised by introducing the water slowly to the system and therefore giving a comparably long time for flow through the hole in the sample cell, before the sample was reached. The other hole served as an exit for the air, when water is introduced.

The sample cell was build by the workshop of the school of Physics & Astronomy at Edinburgh University.

The homebuilt sample cell was connected to a thermo-regulated bath with a cooling function. The precision of the sample cell was checked using a thermocouple situated between the glass slides and compared to a thermometer measuring the temperature of the water inside the thermo-statted water-bath. The temperature varied by less than 1°C in the region of interest and remained stable over a long period of time, which was taken into account during the measurements. No gradient within the sample cell could be measured. The precision of the temperature was therefore estimated to be greater than 0.5°C.

The dissolution experiments The experiments were designed by Leng et al. and described in [Leng 06]. For this, a droplet of the sample of desired concentration was carefully placed onto a glass slide. A second glass slide was placed on top, thereby

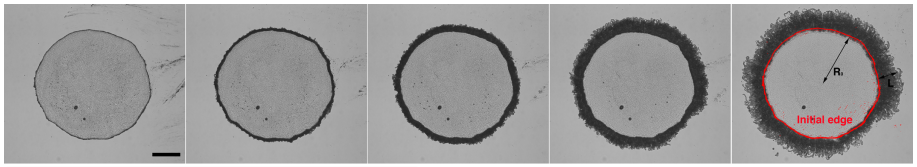

Figure 3.36: A typical time series for a dissolution experiment observed with the direct observation setup ((a) t=1.2s, (b) 2.4min, (c) 23min, (d) 2.1h, (e) 9.7h going to the right, scale bar=2mm). On (e) the definition of the lengths R_0 and L are shown.

squashing the droplet into a flat cylinder, measuring between 4-10mm in diameter. A spacer of thickness b was placed between the two glass slides to maintain a fixed, controlled separation (DDAB: thickness b=100μm, $C_{12}E_3$: b=25[45],50,100, 200, 300, 400 or 600 μm).

The optics were adjusted to ensure appropriate magnification before water was carefully introduced at the edge of the glass slides from where capillary forces drew the water in between the slides and the dissolution process commenced. To prevent the capillary force from changing the separation between the glass slides, a weight was put on top of the second glass slide, so that the glass slides were pressed together as far as possible. However, for measurements in the sample cell, this was not possible, which lead to a decrease in the separation between the glass-slides, and therefore a further squashing of the sample of several tens of microns just before water touched its surface. This was commonly observed during the experiments. Furthermore, upon evaporation of water, the amount of water between the glass slides decreased, which slowly released the pressure between the glass slides. This lead to a slow increase in separation between the glass slides for longer times and therefore limited the measurement time to about 15min. It was noted, that water could not be introduced to the sample a second time, without disturbing the dissolution process because of the introduced flow of water.

The images were recorded at appropriate intervals and stored on the attached PC (see section A.1.1.4). An experimental time of 12min (DDAB) and 1h ($C_{12}E_3$) was chosen as growth within this time was generally stable and diffusive. The time series of resulting images (see Fig.3.36) were then analysed using LabView (see section A.1.3), locating the outer edge of the droplet and measuring the increase of the droplet size $A(t)$. From this information, the swelling length *l(t)* (which is approximately the mean

[45]For a thickness of 25μm a spacer of 50μm was placed on one side and no spacer on the other side. Therefore the upper glass slide was tilted. The droplet was placed in the middle of the sample and the separation between the glass slides therefore assumed to be 25μm.

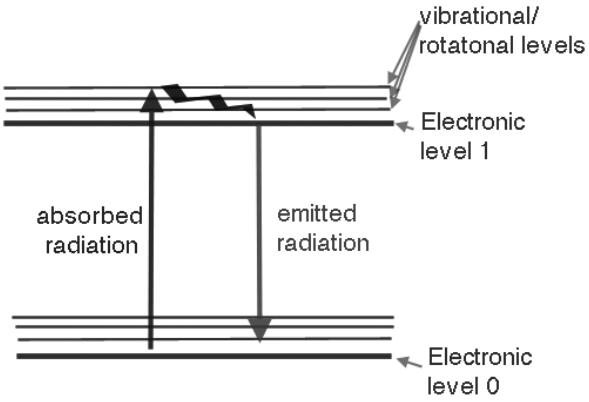

Figure 3.37: The phenomena of fluorescence

length of the myelins, when myelins grow) was obtained:

$$\begin{aligned} l(t) &= R(t) - R_0 \\ &= \sqrt{A(t)/\pi} - R_0 \end{aligned} \tag{3.40}$$

assuming a spherical droplet, where R_0 is the radius of the initial droplet (see Fig.3.36).

All further analytical analysis was done using Microsoft Excel.

3.3.4.3 Confocal Laser Scanning Microscopy

Use of a Confocal Microscope Confocal microscopy was used for obtaining a 3-D profile of the myelinic forest at the interface of a droplet.

Principle of fluorescence To fully understand the concept of a confocal microscope, a short summary of some important properties of fluorescence is given. Every molecule has a certain energy level structure, which describes electronic as well as vibrational and rotational state (see Fig.3.37). If the molecule is illuminated with radiation of an the energy which corresponds to the gap between two electronic levels, photons can be absorbed. The molecules have a limited lifetime in the excited states, after which a photon will be emitted (in case of luminescent decay). The energy level structure in the excited state and the ground state is the same as the excitation transition (about 10^{-15}s) is too quick for nuclear rearrangements (Frank-Condon principle). However, after absorption, rapid rearrangement without emission of a photon (where the electron relaxes to the lowest vibrational/rotational state) takes place. This leads to the fact that the emitted radiation is of lower energy than that absorbed one (Stokes-shift). This

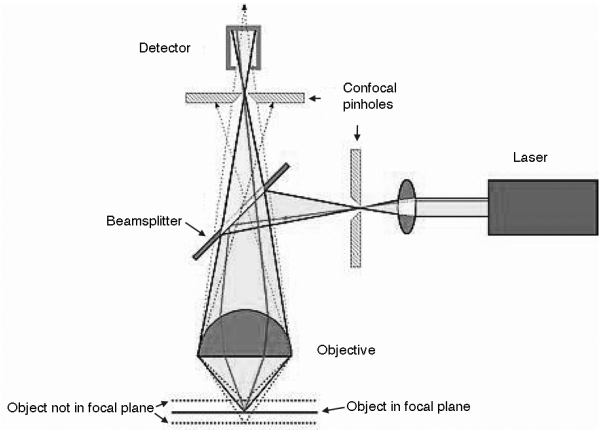

Figure 3.38: The principle of a confocal microscope

makes it possible to select between the excitation source and the radiation emitted by the molecules.

Some molecules give a good fluorescent response, however, some, such as the surfactant molecules used in this work, do not have their own intrinsic fluorescence and therefore dyes (or fluorophores) need to be added to the samples. Dyes are characterised by their quantum yield

$$Q = \frac{\text{rate of emission}}{\text{rate of emission} + \text{rate of nonlumi. decay}} \tag{3.41}$$

and the life time

$$\tau = \frac{1}{\text{rate of emission} + \text{rate of nonlumi. decay}} \tag{3.42}$$

Furthermore fluorescent measurements are time limited, as the fluorescence can be lost by the phenomena of photobleaching. Furthermore, other chemical reactions may occur in the excited molecule. Therefore a given fluorophore can only be excited a certain average number of times. [Beales 05]

Principle of confocal microscopy [Kelly 06] The principle of a confocal laser scanning microscope (CLSM) is sketched in Fig.3.38. The crucial elements are the two confocal pinholes and the beamsplitter. The two pinholes make sure that only light coming from the object in the 'confocal plane' is detected, thus enabling z-axis scanning and emerging xy scanned pictures to be merged into a 3-D image. The beamsplitter directs the incoming light, which is used to excite the fluorescence particles as a mirror, and lets the emission light pass unaffected to the detector. A mirror galvanometer changes the exact position of the focal point, scanning the sample along the x- or y-axis.

	Rhodamine B	**DiIC$_{18}$**
Melting point	210-211°C	68°C
Molecular weight	479.01u	933.87u
λ_{max}	543nm	549nm
Extinction coefficient	$106000 cm^{-1}M^{-1}$	$148000 cm^{-1}M^{-1}$
Quantum yield	0.7	moderate
Excited state lifetime		1ns
Supplier	Fluka	Aldrich
Purity	standard Fluka grade	97%

Table 3.9: Properties of the used dyes Rhodamine B and DiIC$_{18}$.

The pinhole size is most responsible for the resolution of the images (determining also the width of the focal plane *dz*) with its optimum width of 0.5μm. On the other hand, the light intensity decreases with decreasing pinhole size. Thus, a bigger pinhole gives a stronger signal, but with lower resolution in the z-direction. Averaging of scanned frames or reducing the scanning rate using a small pinhole is therefore a more optimal choice than increasing the signal by opening the pinhole when time dependent resolution is not required.

The depth which can be investigated is usually not more than 40μm due to scattering and aberration of light passing the sample[46].

Dyes The dyes used in this work are commonly used to label bilayers. They have large hydrophobic parts and, therefore, tend to preferentially partition into the membrane's hydrophobic core. The properties of dyes are summarized in Tab.3.9.

Rhodamine B ($C_{28}H_{31}N_2O_3Cl$) is a dye with high solubility in alcohol. The structure is presented in Fig.3.39(a). The emission and excitation spectra are shown in Fig.3.39(b) and Fig.3.39(c), respectively. In ethanol, its excitation and emission maxima are 543nm and 590nm, respectively.

DiIC$_{18}$ ($C_{59}H_{97}ClN_2O_4$) is highly fluorescent and quite photostable in bilayers; transfer of this probe between intact bilayers is negligible. It is a long-chain dialkylcarbocyanine with a high extinction coefficient, moderate quantum yield and short excited state lifetime in bilayer systems [Beales 05]. The structure as well as its excitation and emission spectra are presented in Fig.3.40. In methanol, its excitation and emission

[46]This can be increased using the 2-photon (or multiphoton) technique.

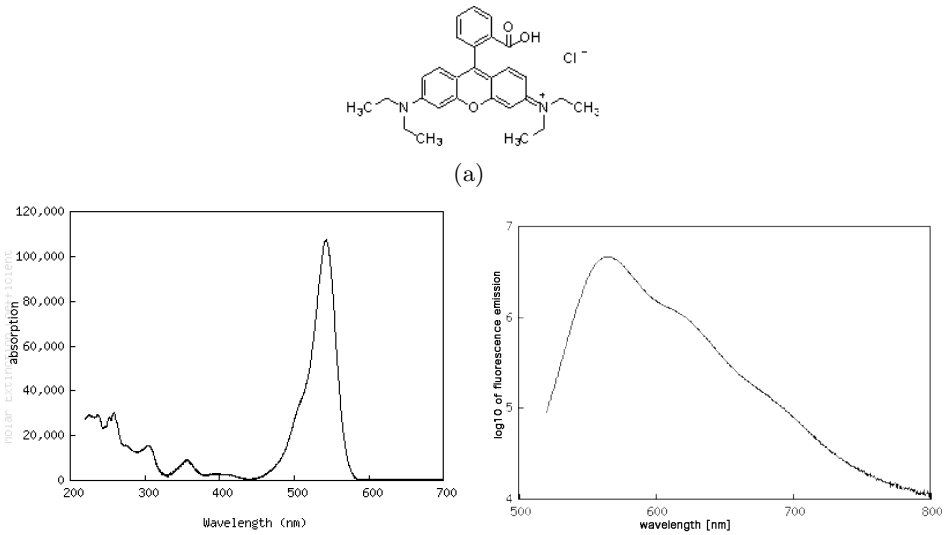

(a) (b) (c)

Figure 3.39: Molecular structure (a) and absorption (b) and emission (c) spectra of Rhodamine B [Du 98].

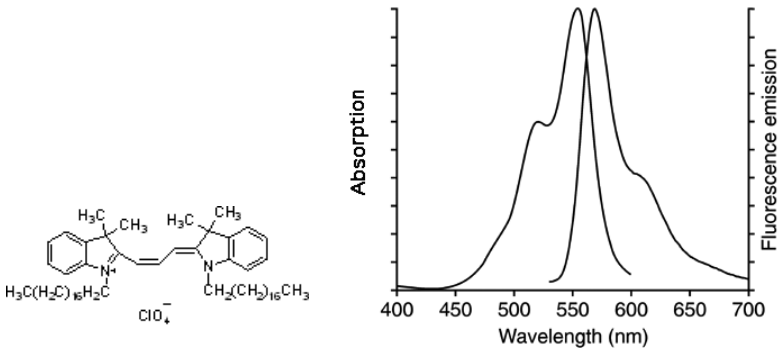

(a) (b)

Figure 3.40: Molecular structure of $DiIC_{18}$ (a); excitation and emission spectra of $DiIC_{18}$ (b) [Beales 05].

spectra contain peaks at 549nm and 565nm, respectively.

The setup used in this work A bioRad Radiance 2100 Confocal Scanning Microscope System with an inverted Nikkon Eclipse TE300 micrsoscope (10x objective, resolution $\Delta xy = (1.6\mu m)^2$) was used. The inverted microscope, which looks at the sample from the bottom, was used, as the myelins were assumed to assemble in the upper region of the sample. The optimum excitation wavelength was 514nm and 543nm for those samples containing the contrast dyes Rhodamine B and $DiIC_{18}$, respectively.

For the measurement, a droplet of a sample was sandwiched between a microscope slide and a coverslip, separated by a spacer of thickness of 100, 200, 300, 400μm after approximately 3, 15 and 30min. The size of the initial droplet was chosen to be sufficiently large (at least of height of 3mm) to ensure the droplet was squeezed between the plates. This ensured a significant contact interface between the lamellar phase and the glass slides at the top and the bottom as well as a vertical interface between droplet and air (later water). Millipore water was placed at the edge between the plates and was brought into contact with the droplet through capillary forces. All experiments were performed at room temperature (T≈20°C).

A typical scan (Δz=5μm, scan time 3s/image) starting from the bottom of the sample is shown in Fig.3.41). As can be seen, there is a strong loss in signal intensity, when the light has to go deep into the lamellar phase. For the analysis, it was assumed that if lamellar phase was detected at a certain depth, it is present also above this depth. In contrast, there was no intensity loss of the signal while passing through pure water, therefore the position of the tip of the myelins could be detected for comparably deep samples, if there was a sufficient slope in the depth profile. The scans can therefore give a sufficient image of the position of the myelin tips depending on depth. Furthermore, it can be seen that the intensity loss in the myelin region was greater than that of the lamellar phase, due to the higher scattering of the myelin tubules.

The tilt of the profile could be nicely displayed in 3-D projection (obtained using Confocal Assistant4.02). The pictures were analysed using the Vision Assistant (see section A.1.3.4), measuring the area A_{surf} occupied by surfactant phase. The position of the myelin interface x was calculated with:

$$x = A_{surf} - A_0 - y_{prof}, \tag{3.43}$$

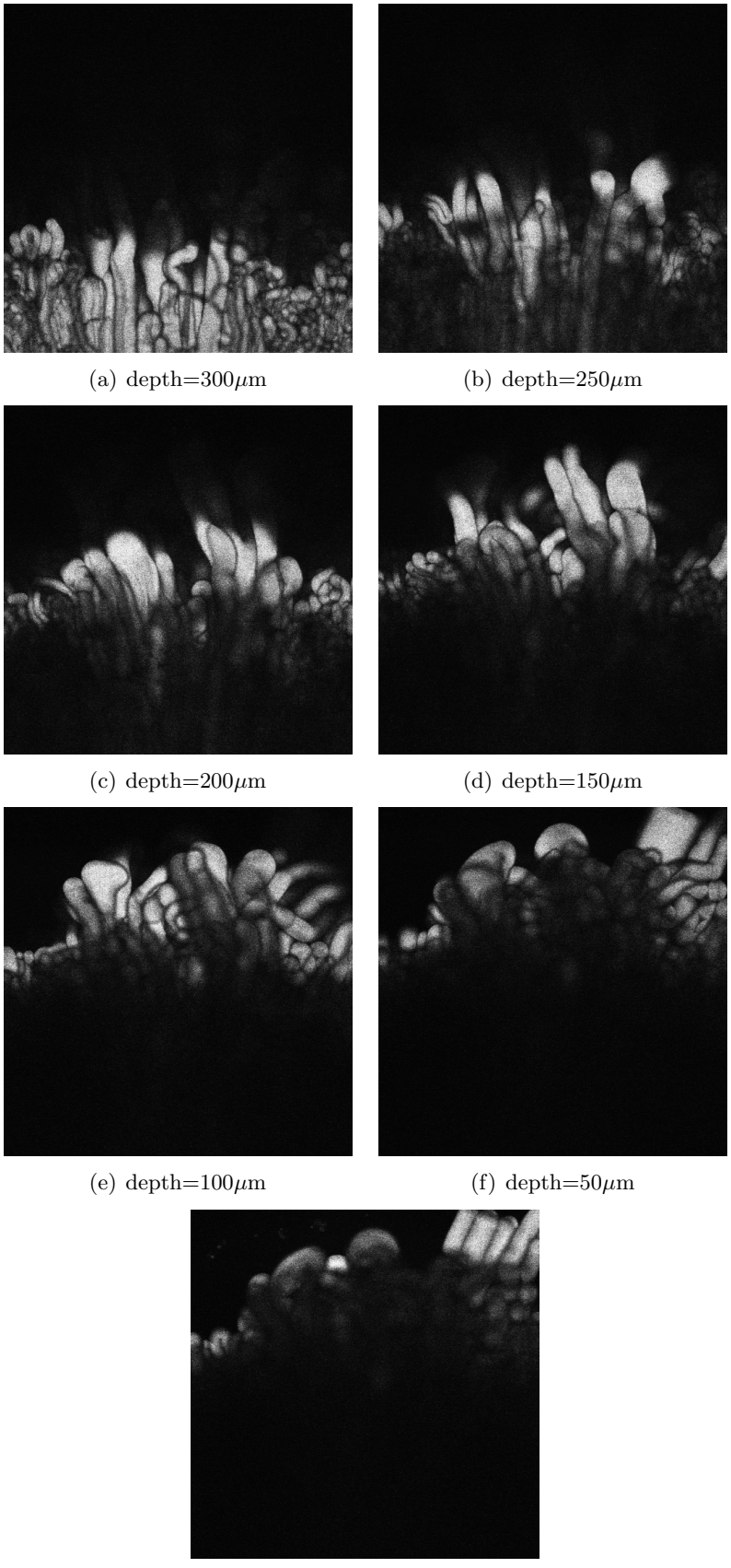

(a) depth=300μm (b) depth=250μm

(c) depth=200μm (d) depth=150μm

(e) depth=100μm (f) depth=50μm

(g) depth=0μm

Figure 3.41: A confocal microscopy scan from the bottom of the sample to the top (spacer thickness=300μm, time=27min, picture size=$(821\mu\text{m})^2$).

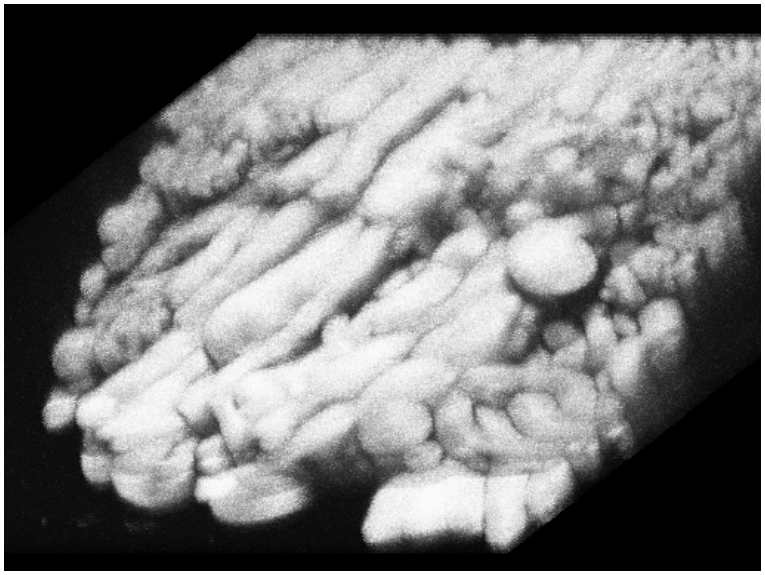

Figure 3.42: 3-D image (upside down) of Fig.3.41.

where y_{prof} is the width of the profile (approx with a straight line), which is displayed in the image, $A - 0$ takes into account the tilt of the profile:

$$A_0 = \frac{1}{2} l_{image} \sin(\arccos(\frac{l_{image}}{y_{prof}})), \tag{3.44}$$

where l_{image}=821μm is the width/length of the picture. Because the relative position of the myelins between the scans was not known (the objective was moved between the scans), the data are displayed relative to a value x_0:

$$x_0 - x(depth = 0\mu m) \tag{3.45}$$

The numerical data were analysed using Origin8.0. The movements of the myelins during the scan was taking into account, by scanning the profile in both directions and averaging the values (see Fig.3.43). The time corresponding to the average profile was estimated by

$$t_{ave} = t_{end,scan_{i+1}} - t_{start,scan_i}. \tag{3.46}$$

However, this time has a comparably large error (especially for deep samples). The effect of the movements of the myelins is stronger at the beginning of the growth, which can be explained by the $t^{\frac{1}{2}}$-dependence of the myelin growing rate.

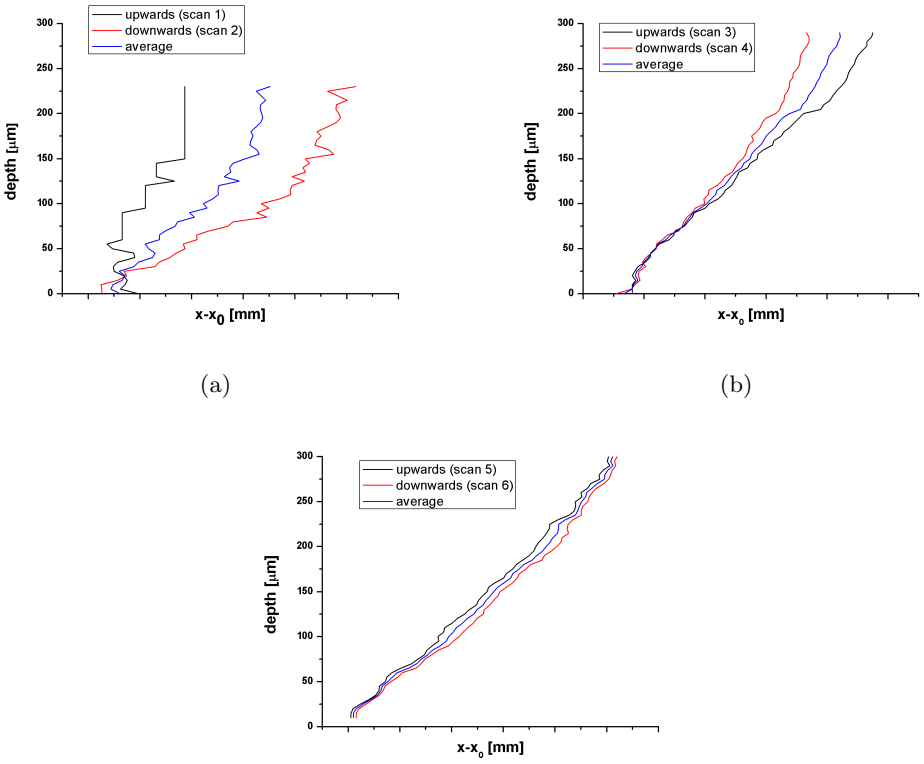

Figure 3.43: Depth profiles scanned upwards (black) and downwards (red) as well as the calculated averages (blue) after 5min (a), 16min (b) and 27min (c) (scan 5 see Fig.3.41).

Chapter 4

The equilibrium phase diagram of DDAB

4.1 Introduction

The equilibrium phase behaviour of the binary DDAB-water system has been extensively studied in the past [Dubois 98]. The published phase diagrams cover a temperature range from about 10 to over 100°C, and the entire range of surfactant concentrations. A detailed overview of the literature has been given already in chapter 3.2.1.1. Two phases have to be highlighted as being crucial for this further work: the lamellar phase (L_α or $L_\alpha^{/}$), which occurs above 16°C and the gel phase (L_β) below 16°C, both in a surfactant weight concentration range between about 3% and 90%. Those phases were intended to be compared during their dissolution in water (see chapter 6). One should note that both phases have been described as being optically un-identifiable. Their transition temperature T_M has been obtained by doing DSC measurements [Dubois 91].

However, while equilibrating DDAB samples just below this transition temperature, after 2 months, a sudden increase in turbidity was observed. The change of optical properties was observed to be faster at lower temperatures (within minutes at temperatures below 5°C). When heating above the T_M, the sample became clear again. The transition into this white phase was reversible.

This observation led to an intense study of the equilibrium phase behaviour of DDAB at low temperatures, resulting in a hypothesis of a new phase diagram, which will be presented in this chapter. After this, the thermal transition between the low temperature phase and the high temperature phase was investigated, to confirm the given hypothesis (see chapter 5). Furthermore, the dissolution behaviour of the lamellar phase itself and lamellar phase being influenced by the low temperature phase has been studied (see chapter 6).

4.2 The dry DDAB: sample purity and thermal stability

The cationic double-chain surfactant DDAB was purchased from Aldrich (purity 99%) and Fluka (purity 99%) for comparison and stored in a desicator at room temperature ($T \approx 20°C$).

About 5g of DDAB was recrystallised from ethyl acetate as suggested by [Aratono 07, Ono 05, Bumajdad 04, Dubois 98], to obtain information about the influence of impurities on the observed phase behaviour. For this, DDAB was dissolved in the minimum volume of ethyl acetate and diethyl ether was added dropwise, to slowly reduce the polarity of the solvent system, until the solution began to become cloudy. The vessel was covered to avoid extensive evaporation and the solution cooled in the freezer. After 4h, the flask was removed and the precipitate filtered. The nature of the precipitate was such that a large amount of product remained in the vessel. This was recrystallised from the same solvent system with extensive precipitation induced by an excess of diethyl ether rather than cooling. The precipitate was filtered to dryness in air and this process repeated twice. The pure product was dried with phosphorous pentoxide under a nitrogen atmosphere. Because of the high capacity of the DDAB powder to absorb water, from time to time, the sample was dried under vacuum for 48h and maintained under a nitrogen atmosphere.

The recrystallisation was performed by Simon Dalgleish.

The structure of the DDAB surfactant was confirmed using ^{1}H-NMR and ^{13}C-NMR (see Fig.4.1 and Fig.4.3, respectively). In the ^{1}H-NMR spectra, the peaks could be easily assigned to the expected chemical groups. Their chemical shifts and integrated values agree essentially with the theoretical values. However, integration over broad peaks depends strongly on the choice of the baseline, therefore no strong conclusion about the chain length could be drawn. The multiplicity of the peaks could be explained in terms of spin-spin coupling. The peak around 3.2ppm, which is assigned to the ethylene group closest to the nitrogen, shows higher order coupling. A decoupled ^{1}H-NMR on the 600MHz equipment has been performed to confirm this (see Fig.4.2). The spectrum was decoupled from the peak at 1.7ppm, belonging to its neighbouring ethylene group (at the β position). In this case the peak around 3.2ppm changes into a singlet. Decoupling from the peak around 1.34ppm, which was first assumed to be related to the ethylene at the γ position, did not show any influence on the peak[1]. It can be concluded that the two ethylene groups neighbouring the nitrogen (the ones at

[1]In contrast, the peak assigned to the ethylene groups at the end of the chains changed into a singlet, which suggests decoupling from the ethylene group next to this ethylene group.

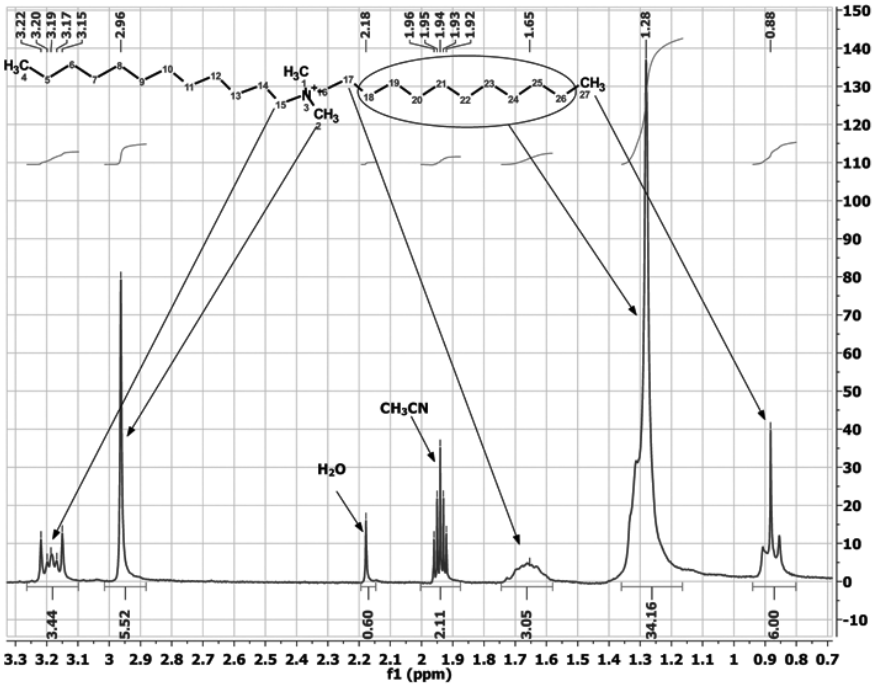

Figure 4.1: ^{1}H-NMR spectra of the recrystallised sample of DDAB in acetonitrile.

the α and β positions) in the DDAB molecule form a high order spin system.

^{13}C-NMR could be used to confirm the length of the hydrocarbon chain (see Fig.4.3). 12 peaks (one of double height) could be resolved, corresponding to 13 different carbon atoms. The atoms in the middle of the chain have very similar chemical environments and therefore appear very close to each other in the spectra. The relaxation time for CH_2 groups is comparably small $T_1 \approx 0.3$s [Barnhart 82]. For a time of $5T_1 < 2.114$s, 95% of the nuclei will be in the ground state and the peak heights should give information about the number of carbons under each peak[2]. The peak integrals were all very similar, while 1 peak was about double the size (see Fig.4.3 below) and can be assumed to belong to 2C having a very similar chemical shift. The spectrum is in good agreement with the calculated spectra of DDAB and with values in the literature. This suggests the main component in the sample is DDAB.

The assignment in both spectra was confirmed by a 1D ^{13}C 135DEPT (see Fig.4.4) and a 2D NMR HSQC experiment (see Fig.4.5). The high spin coupling between the two ethylene groups next to the nitrogen gave rise to two additional peaks (at

[2]Even despite the fact that an uncoupled spectra has been recorded, which usually affects the integrals slightly.

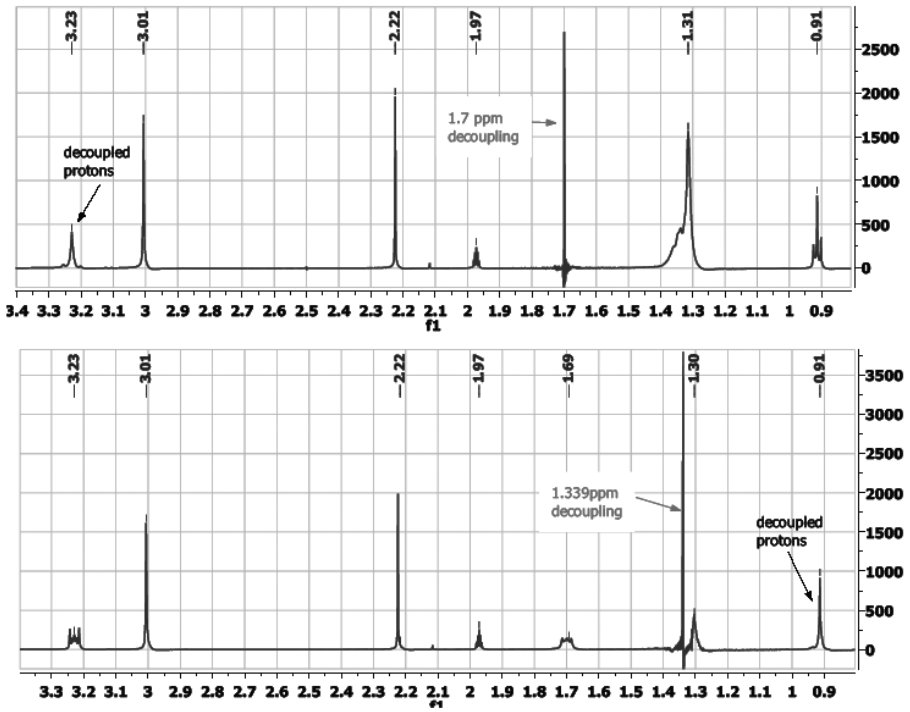

Figure 4.2: Decoupled ^{1}H-NMR (600MHz) spectra of DDAB in acetonitrile, showing the formation of a high order spin system between the ethylene groups in the hydrocarbon chains on α and β position.

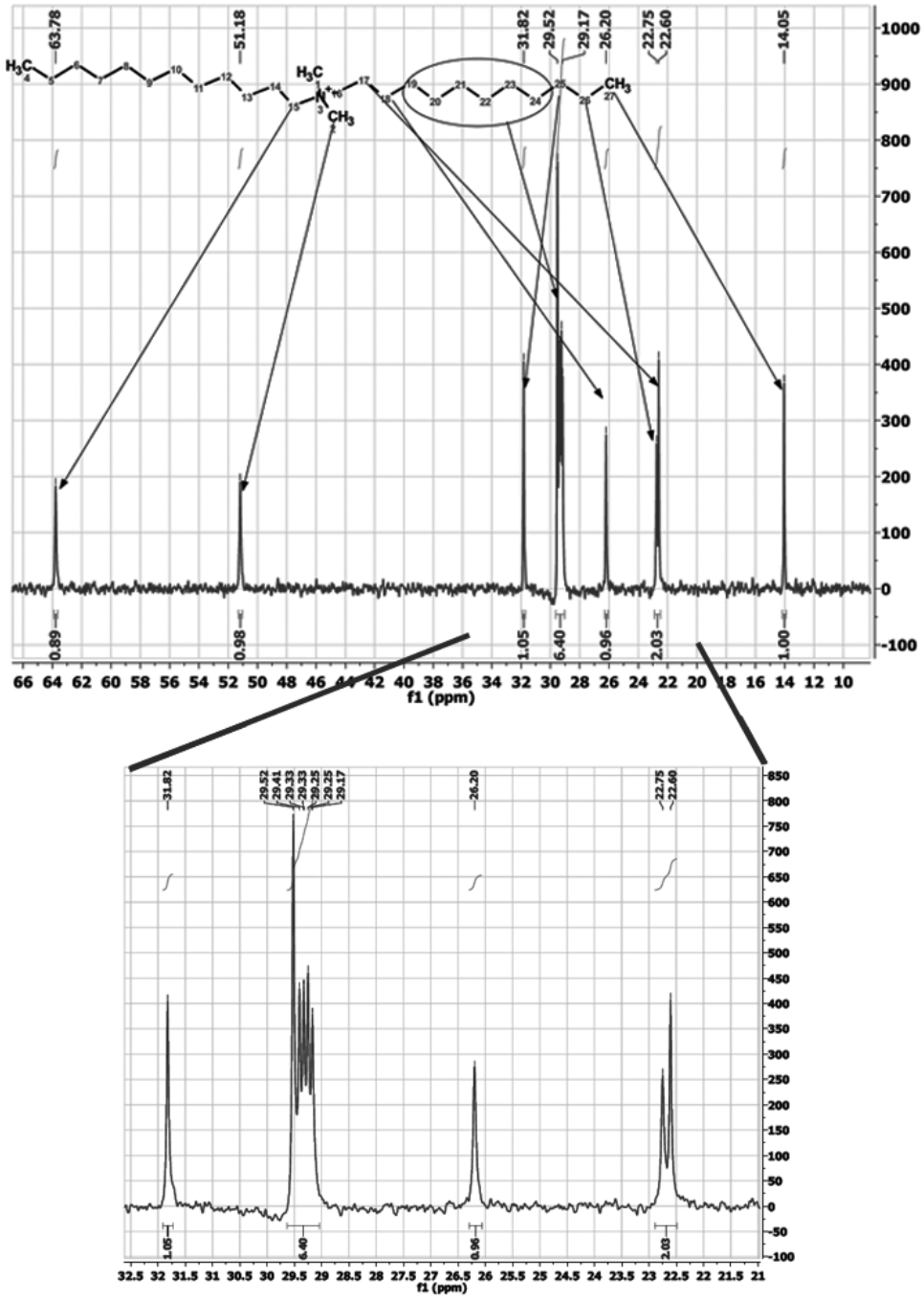

Figure 4.3: ^{13}C-NMR spectra of the recrystallised sample of DDAB in chloroform confirming the length of the hydrocarbon chain.

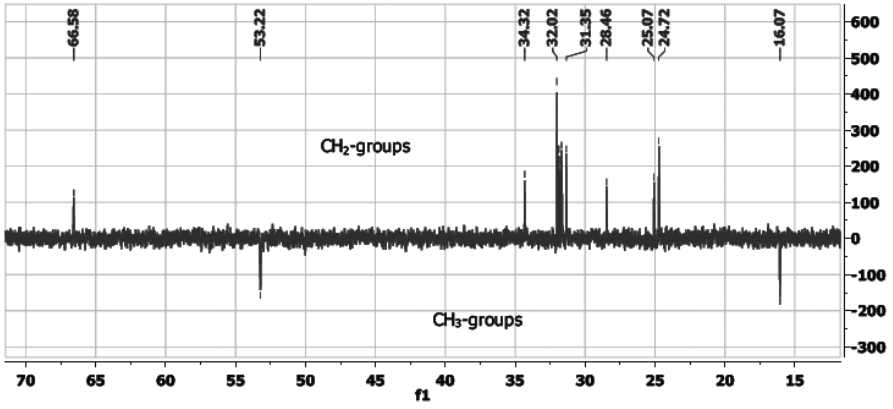

Figure 4.4: ^{13}C 135DEPT experiment of DDAB differentiating between the peaks related to the CH_2 and CH_3 groups in the sample.

δ=(3.21,24.59)) and (δ=(1.69,66.27)) in the HSQC spectra.

Three types of impurities were expected in the sample. The first is water, caused by the high water affinity of the sample, the second is from DDAB analogues of slightly different chain lengths, which could not be removed by recrystallisation, and the third is degradation products caused by thermal degradation at higher temperatures.

4.2.1 Water content in the sample

To obtain a first estimation of the water content in the sample, the ^{1}H-NMR spectra could be used (see Fig.4.1). Samples were prepared using a snap top vial of dry acetonitrile in a glove box (nitrogen environment) to minimize the effect of water uptake from the atmosphere during sample preparation. The water content in the sample, estimated from integrating the water peak at δ=2.18ppm, was less than H_2O/4DDAB are likely to be present in MeCN, or ingress into the NMR tube during measurement. Therefore this is only an upper value.

When using ATR IR, the recrystallised sample shows no water peak in the ATR IR spectrum (see blue and green line in Fig.4.6). The difference in quality between the blue and green line, especially on the CH stretching peaks (2800-3000cm^{-1}), is due to the exposure of pressure on the sample to ensure good sample contact, which was only possible in the Glasgow equipment.

This leads to the assumption that, in contrast to DODAB [Okuyama 88] and DODMAC [Laughlin 90] the mono- or di-hydrate are not the stable dry forms at room temperature

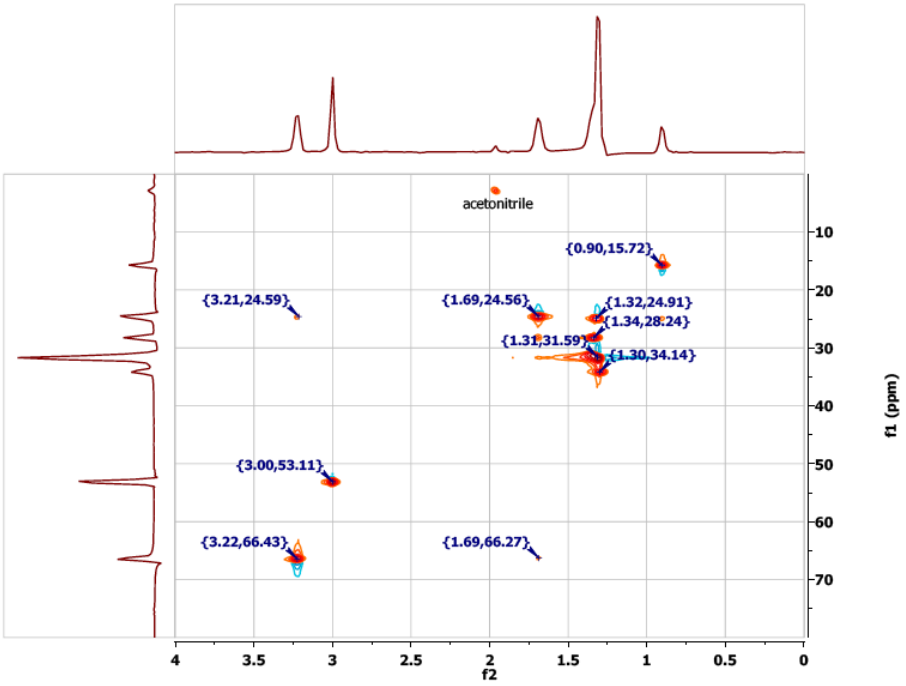

Figure 4.5: HSQC-NMR of DDAB confirming the high spin coupling between the two ethylene groups in the hydrocarbon chains next to the nitrogen.

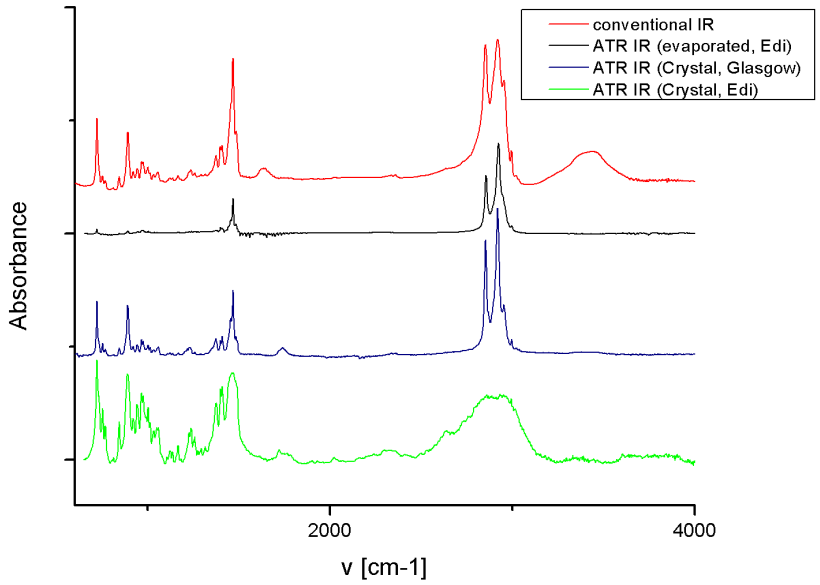

Figure 4.6: IR spectra of dry DDAB sample recorded in Glasgow and Edinburgh at room temperature (T≈20°C). The lack of the water peak in the samples obtained by ATR suggest that the stable crystalline form of DDAB is a zero-hydrate.

and that DDAB can be prepared without associated water.

The Edinburgh equipment offered the possibility of imaging the sample and selecting different regions for comparison. The spectra were found to be, in general, affected by the sample thickness. While thick samples lead to a loss in overall signal intensity, thin samples had very low signal to noise ratios.

To investigate the water structure in highly concentrated samples, an 85% solution (L'_α phase) was observed during evaporation at room temperature. The morphology of a flattened sample on an ATR microscopy slide is highly diverse as can be seen in Fig.4.7(a). Very thin layers show no water signal in the IR, while thicker patches give rise to a water peak, which corresponds to free water between the bilayers (see red and black lines in Fig.4.8, respectively). The water peak can be fitted with two main broad Gaussians around 3370cm^{-1} and 3475cm^{-1}, which can be assigned to the symmetrical and asymmetrical stretching modes, respectively.

With time, the sample morphology changes in the water rich regions, as can be seen in Fig.4.7(b) and Fig.4.7(c). Initially round patches appear on the initially smooth surface. After time, a 'dark phase' covers the sample. The water intensity of the region decreases with time as can be seen in Fig.4.8, suggesting the evaporation of water. From the two different morphological changes, one can assume that in a first step, the sample water concentration decreases, while maintaining the phase structure, while the more concentrated sample is quickly covered by a quasi crystalline phase.

Upon evaporation, the water peak changes in intensity, while the shape seems not to be affected by the evaporation process (see Fig.4.9). Thus the hydrogen-bond network of the confined water seems not to change significantly. The water peak remains broad and shows no appearance of sharper peaks, as has been reported for the DODMAC system (see Fig.3.13). Therefore, one can conclude that at room temperature no crystal hydrates are stable, but even at very low water concentration the water is in its free liquid state. Because one could expect a change in water structure upon a radical decrease of waterlayer thickness, the data suggest that (at later times) a coexistence between a concentrated lamellar phase and dry DDAB forms instead of a more concentrated lamellar phase.

In conclusion, the data suggest that a zero-hydrate is the stable form of dry DDAB at room temperature. The water affinity does not lead to the formation of a mono- or di-hydrate, but presumably only to a slight dissolution of crystals at their interface

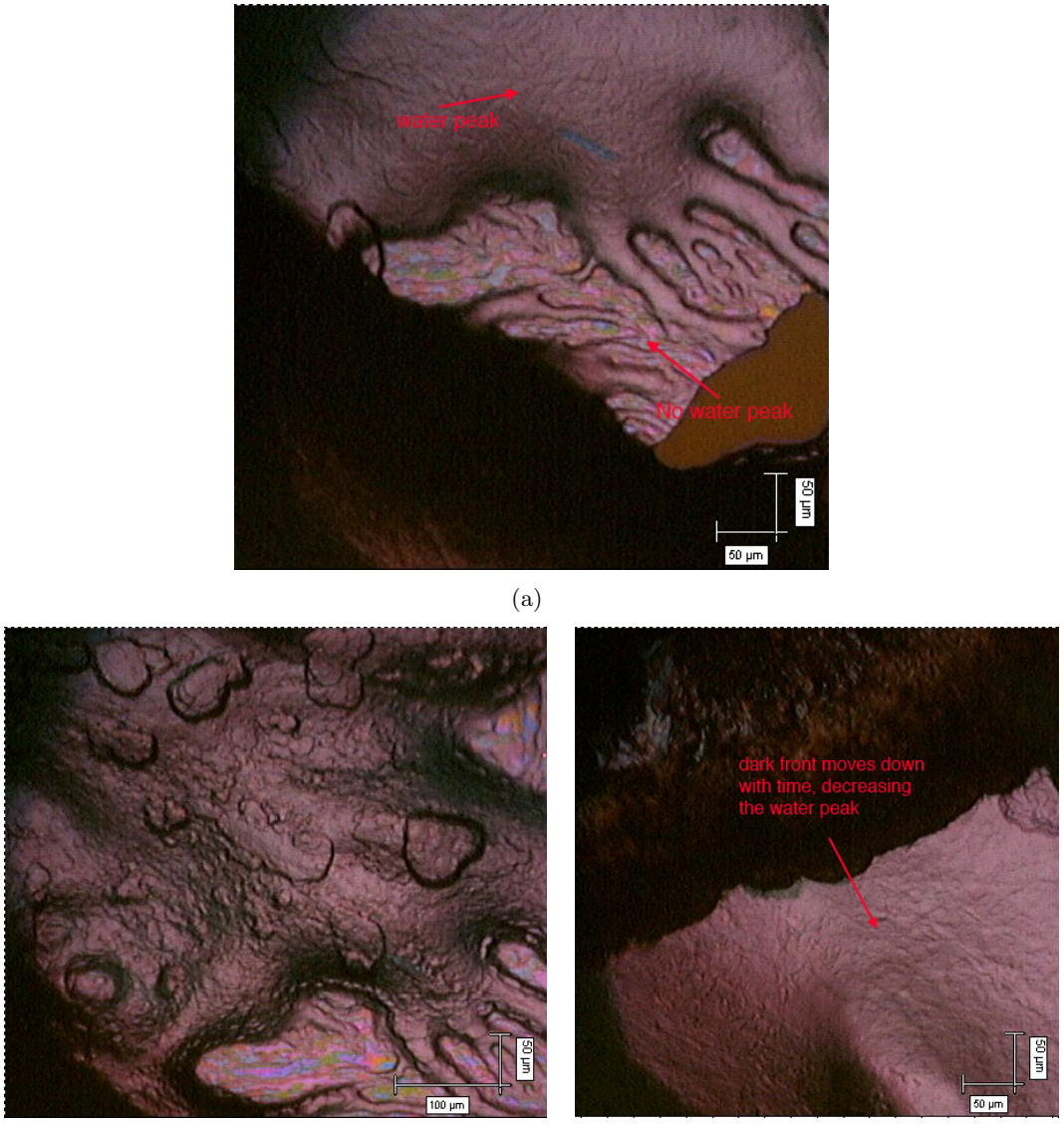

Figure 4.7: Structural diversity and changes in the 85% solution upon evaporation.

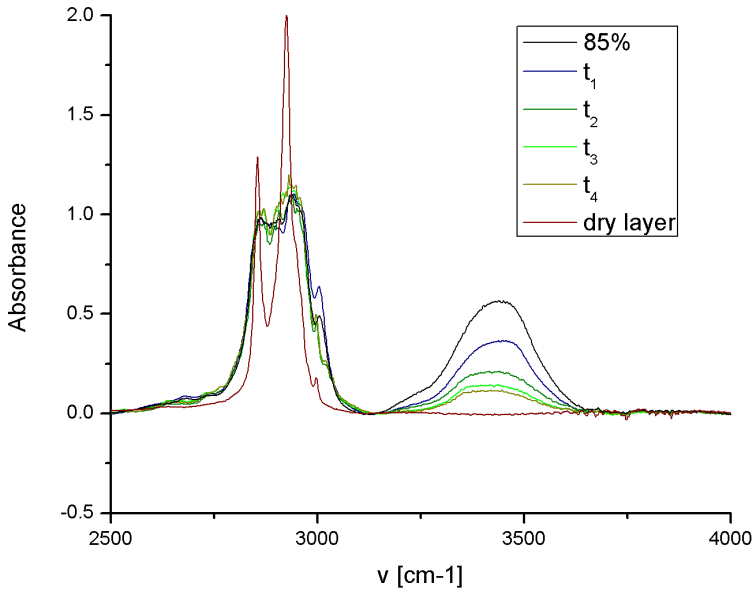

Figure 4.8: Change of the IR spectra of a 85% solution of DDAB upon evaporation. A decrease in the water peak can be observed with time, while the peaks corresponding to the DDAB molecule become sharper.

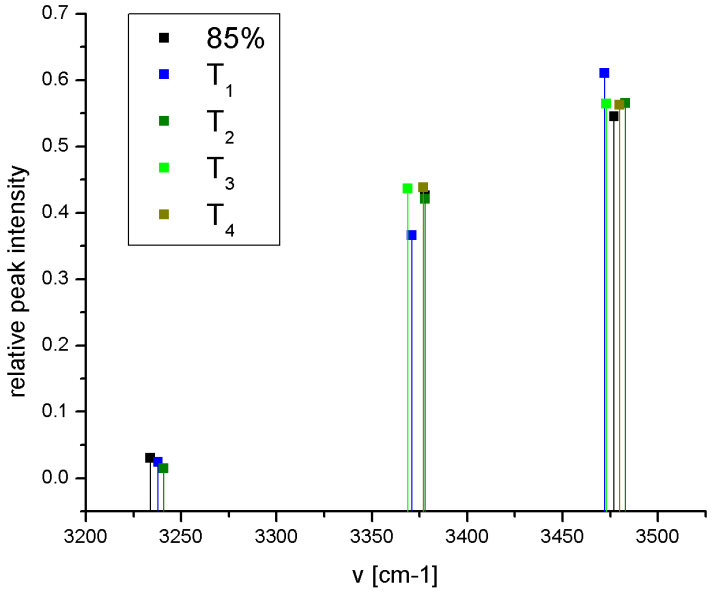

Figure 4.9: Relative heights and position of the fitted Gaussians below the water peaks in Fig.4.8, showing that the relative proportions and hence hydrogen-bond network of the confined water does not change significantly.

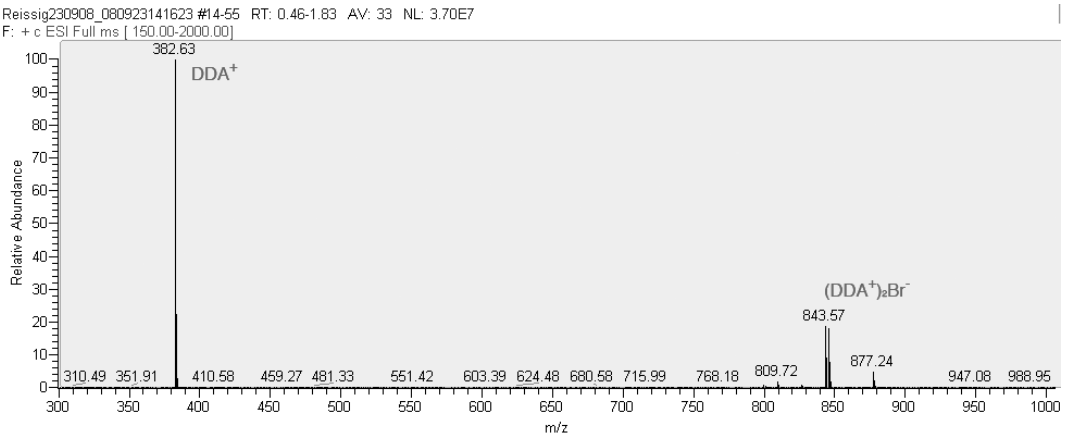

Figure 4.10: Positive mass spectrum of the recrystallised DDAB, confirming the high purity of the sample.

with water.

4.2.2 Dialkyldimethylammonium bromides of different chain lengths

As already mentioned, ^{13}C-NMR has confirmed DDAB to be the most abundant molecule in our sample. However NMR cannot give clear information about impurities of less than about 5%. To obtain a more detailed picture of the occurrence of DDAB-analogues in the sample, ESI MS has been used. Sample spectra were measured before and after recrystallisation. The most intense peaks could be related to the DDAB molecule (see Fig.4.10):

1. $(DDA)^+$ (expected masses in Daltons: 382.44 (100%), 383.44 (28.5%), 384.45 (4.0%))

2. $(DDA^+)_2Br^-$ (expected masses in Daltons: 843.80 (100%), 844.80 (57.0%), 844.81 (1.3%), 845.8 (97.7%), 845.81(16.2%), 846.80 (55.5%) 846.81 (4.3%), 847.81 (16.2%), 848.81 (2.9%))

The spectrum around the main peak is very clean. Only traces (well below 1%) of the DDAB analogue $C_{12}C_{13}$DAB and $C_{13}C_{13}$DAB could be found after recrystallisation (see Fig.4.11).

The sample can therefore be considered as highly pure.

4.2.3 Thermal degradation of DDAB

At temperatures above $T \approx 100°C$ a colour change from a white sample to a yellowish-brown can be observed, when exposing the sample to air. This colour change is more

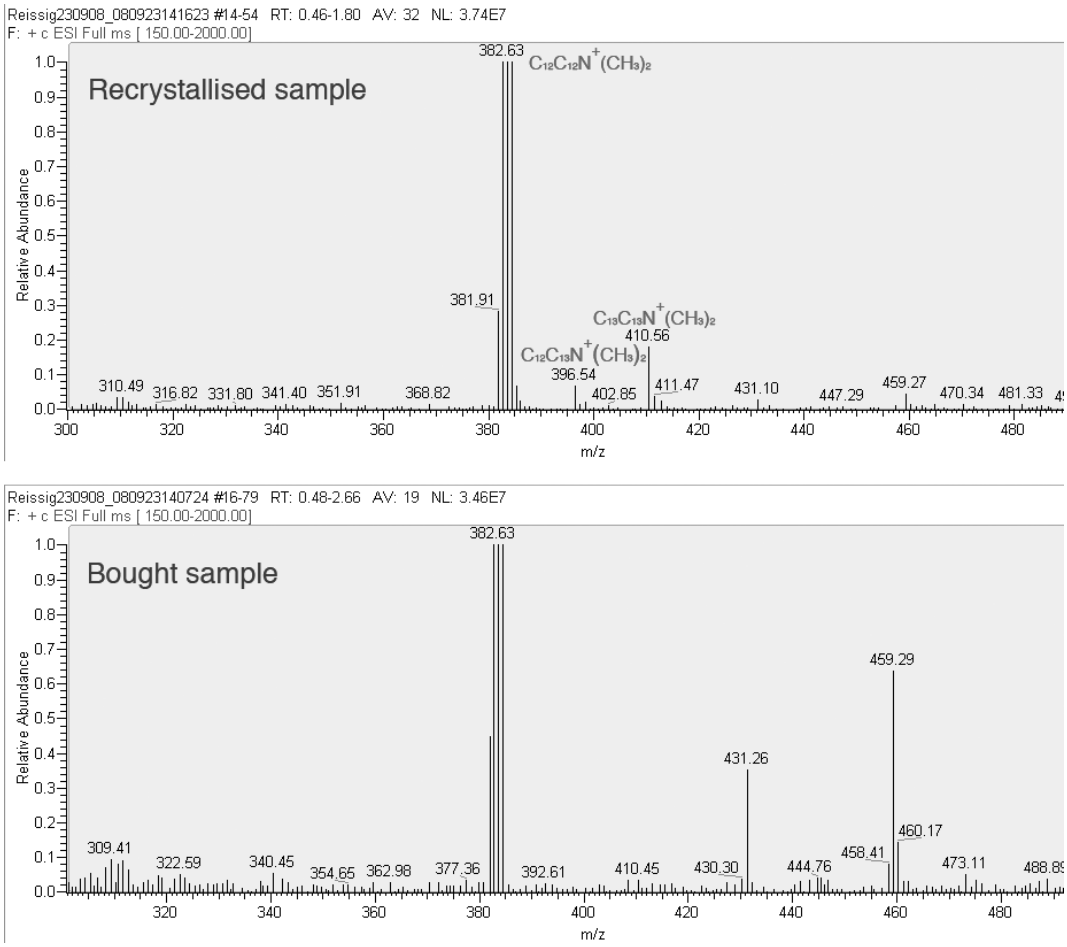

Figure 4.11: Relevant sections of the mass spectra of the recrystallised and bought sample, showing a decrease/vanishing of peaks caused by impurities upon recrystallisation.

apparent at higher temperatures and often accompanied by a melting of the DDAB powder. The colour change can be related to the degradation of the quaternary ammonium ion into the thermally stable amine [Laughlin 94, Rubingh 91] and is caused by the N-oxidation of the amine. No oxidation is expected for the quaternary ammonium salt. In addition, the oxidation of bromide ions is possible, but expected to activate a further decomposition of the product.

To confirm the degradation of the sample, the coloured samples have been investigated by TLC, depending on temperature and exposure time. Pure samples show only one spot on the TLC-plate after eluation, while degradated samples exhibit additional spots (see Fig.4.13). The degradation of the sample is expected to be caused by nucleophilic attack by the bromide ion [Laughlin 94] (see Fig.4.12). Under ambient conditions the bromide is expected to attack the nitrogen and displace one of the methyl groups bound to the nitrogen giving the amine, which is expected to be the strongest spot on the TLC plate. As already mentioned, this amine might be oxidised, which would further shift the spot on the TLC plate.

The oxidation is expected to cause further degradation of the amine, e.g. forming alkanenitriles, which could be also identified in other systems [Laughlin 09]. At higher temperatures, nucleophilic attack of the bromide ion on N^+ to detach an alkyl chain also becomes more probable, even though this exhibits a higher energy barrier. Furthermore, trace amounts of water are expected to lead to the formation of alkanols, also due to a nucleophilic attack. One should note that the decomposition via Hofmann elimination, which is often mentioned in context with quaternary ammonium salts leading to the formation of an alkene, is not expected to occur. This pathway requires a strong base, while bromide is commonly considered as a weak base [Laughlin 09]. ^{1}H-NMR of the degraded sample gave a very complex picture, showing a combination of a number of peaks, of which some could be related to these suggested degradation products.

Samples which are only slightly coloured, cannot be distinguished from the pure sample using TLC. Therefore, the amount of degradation is negligibly small. Such small impurities are not expected to influence the phase behaviour of the surfactant. The minimal temperature at which degradation could be identified for samples heated for a period of 1 week is 90°C, which is assumed to be close to the degradation temperature of DDAB.

At a temperature of $T \approx 150$°C a rapid melting of the coloured sample could be observed by visual inspection. This is close to the temperature which has been previously

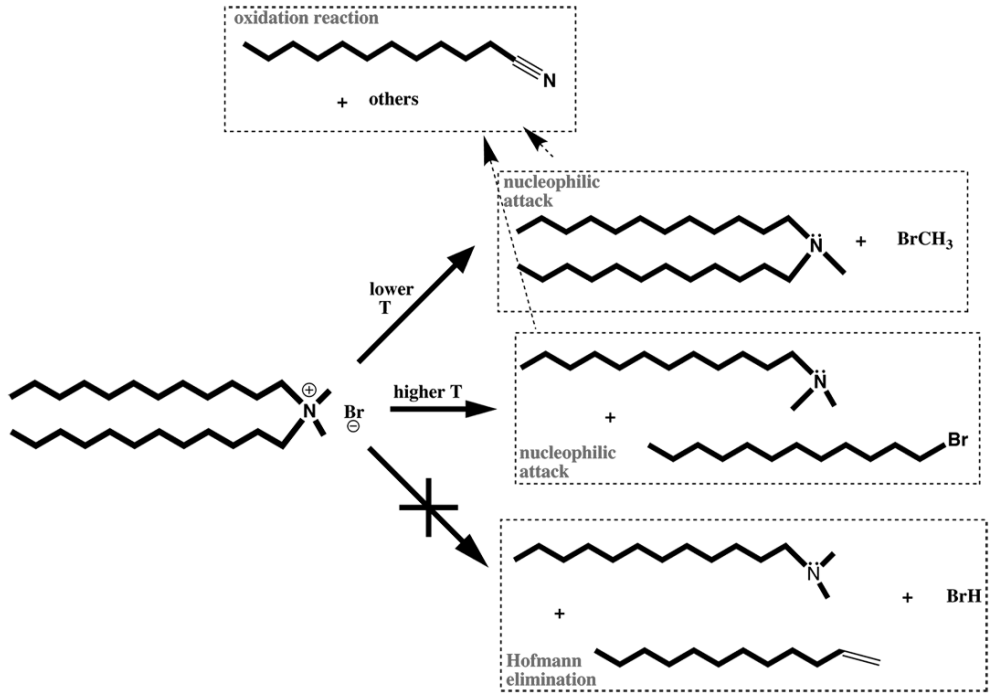

Figure 4.12: Suggested degradation pathways of DDAB.

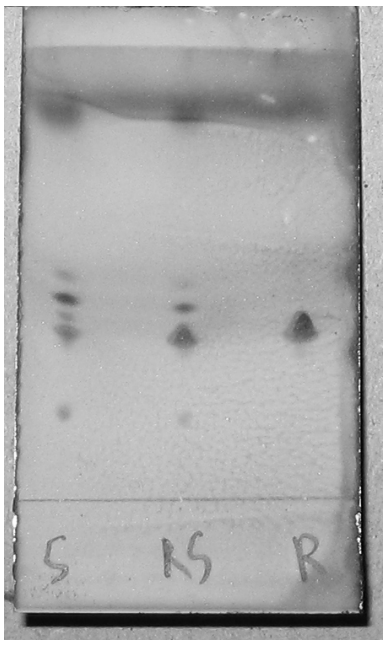

Figure 4.13: TLC of the sample (S) after heating to 150°C against a reference sample (R), which was kept at room temperature, showing the thermal degradation in the sample.

reported as the melting temperature of the sample [Aldrich 09]. This temperature is, however, well above the decomposition temperature of the sample and does not correspond to the melting of the DDAB molecule, but to a rapid decomposition into the amine, which is at this temperature in a liquid state. Therefore, the use of a melting point analysis for determining the purity of the sample is meaningless as has already been suggested for related systems [Haas 98, Haas 99].

Sample purity

In summary, the purity of the sample could be shown to be very high and to be a DDAB zero-hydrate at room temperature. The phase behaviour should not be influenced by the trace amount of impurities, but should be characteristic of the DDAB molecule. Furthermore, the thermal stability limit of the sample is well above the maximum temperature in the experiments performed in this study.

4.2.4 Conformational properties of the solid sample

The Raman spectrum of the solid has been obtained (see grey line in Fig.4.14). This spectrum is independent of time. Most peaks could be assigned and are in agreement with the literature (see Tab.4.1), indicating the existence of an all-trans extended chain structure [Foucault 03].

Peaks in both regions 1050-1150cm^{-1} (skeletal vibrations of the C-C stretching modes) and 2800-3000cm^{-1} (C-H vibrations) have been reported to be sensitive to the conformation of the hydrocarbon chain [Foucault 03]. The dominance of the asymmetric C-H stretching vibration near 2880cm^{-1} over the symmetric C-H stretching vibration near 2850cm^{-1} indicates a high order in the hydrocarbon chains [Foucault 03]. Furthermore, the 1070cm^{-1} and 1121cm^{-1} bands are characteristic of C-C stretching vibrations for the trans conformation of the chain [Foucault 03].

At the low frequency range of the spectrum, LAM vibrations could be identified, characteristic for well ordered systems such as crystals. It has to be noted that these vibrations clearly differ from the LAM vibrations obtained for a crystalline phase present at low temperatures (in the so-called 'white' phase, see section 4.3.4). This suggest a different crystalline structure in the powder and in the low temperature phase, which could be explained by the possible existence of a stable hydrate at low temperatures. Furthermore, an additional band at around 1082cm^{-1} appears in the low temperature crystalline phase, which is characteristic for the presence of gauche conformations [Foucault 03].

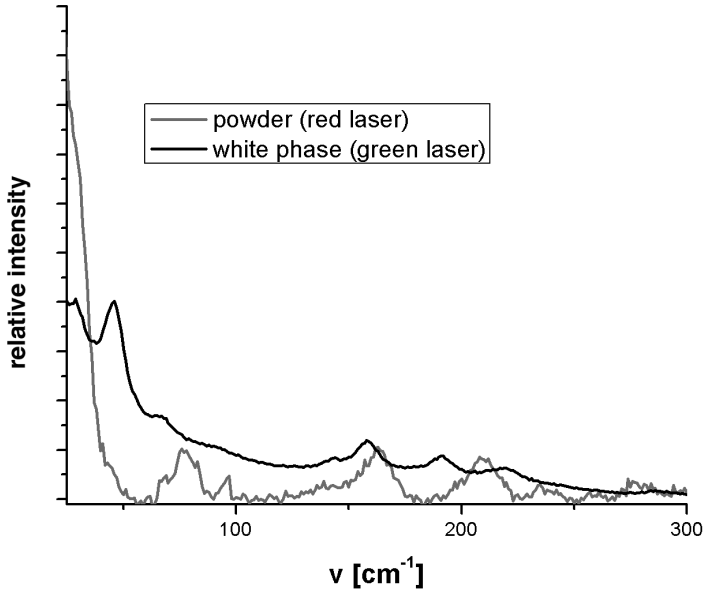

(a)

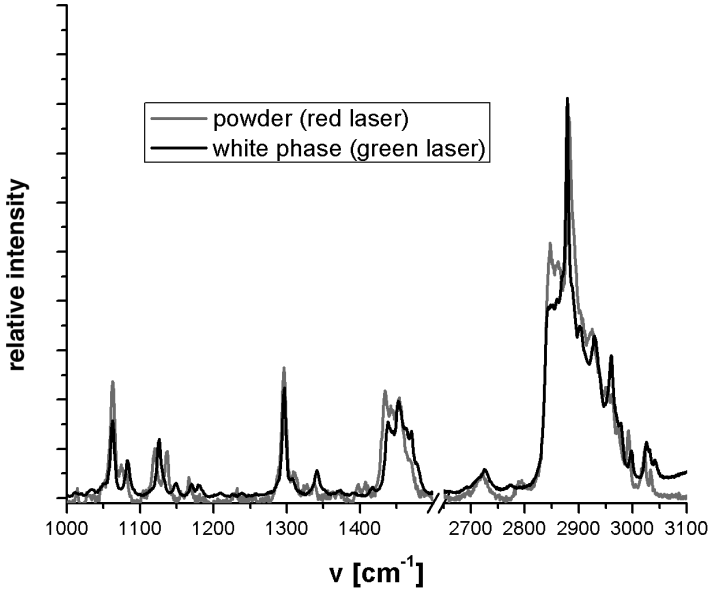

(b)

Figure 4.14: Raman spectrum of the DDAB powder at room temperature and the crystalline 'white' phase at temperature T<14°C. The differences in the spectra, especially in the region of the LAM frequencies, suggest the existence of two different crystalline forms.

Peak centre .[cm^{-1}]	Peak width [cm^{-1}]	Peak height	Proportion of Gaussian fit %	**Area %**	Assignment
77	11	1990	0	**2**	LAM mode
142	18	575	50	**1**	LAM mode
163	18	1507	32	**2**	LAM mode [Foucault 03]
209	12	1491	0	**2**	LAM mode
237	15	393	40	**0**	LAM mode [Foucault 03]
278	12	658	6	**1**	LAM mode [Foucault 03]
417	19	897	45	**1**	LAM mode [Foucault 03]
440	7	529	50	**0**	unassigned [Foucault 03]
465	4	893	69	**0**	unassigned [Foucault 03]
479	9	354	59	**0**	
521	11	236	22	**0**	unassigned [Foucault 03]
564	3	236	90	**0**	unassigned [Foucault 03]
725	10	763	52	**1**	CH_3 rock from $N^+(CH_3)_2$ group [Foucault 03]
761	14	1813	42	**2**	CH_3 rock from $N^+(CH_3)_2$ group [Foucault 03]
879	10	1124	51	**1**	
891	9	1243	51	**1**	CH_3 rock, CN^+ stretch [Foucault 03]
918	3	263	56	**0**	CN^+ stretch [Foucault 03]
943	10	242	57	**0**	unassigned [Foucault 03]
979	14	254	53	**0**	unassigned [Foucault 03]
1062	8	4605	42	**3**	C-C sym stretch + CH_2 wag. [Foucault 03]
1120	8	1700	42	**1**	unassigned [Foucault 03]
1136	6	1717	18	**1**	C-C asym stretch + CH_2 (gauche) wag. [Foucault 03]
1167	5	675	15	**0**	CH_2 rock [Foucault 03]
1232	1	403	50	**0**	CH_2 wag, crystalline and CH_2 twist [Foucault 03]
1296	8	4932	48	**3**	CH_2 twist [Foucault 03]
1311	7	814	34	**0**	
1332	17	340	51	**0**	CH_2 wag [Foucault 03]
1403	14	321	54	**0**	
1434	10	3715	50	**3**	CH_2 bend [Foucault 03]
1443	7	1769	50	**1**	CH sym bend from $N(CH_3)_2$ [Foucault 03]
1454	15	3557	50	**4**	CH_2 bend [Foucault 03] CH asym bend from $N(CH_3)_2$ [Foucault 03]
1469	10	995	53	**1**	
2719	24	794	100	**1**	unassigned [Foucault 03]
2791	23	652	50	**1**	unassigned [Foucault 03]
2845	17	8105	100	**8**	CH asym stretch of CH_2 [Foucault 03]
2862	19	7001	50	**10**	CH asym stretch of CH_2 [Foucault 03]
2882	16	12243	29	**16**	CH sym stretch of CH_3 [Foucault 03]
2900	23	5110	0	**11**	
2924	27	4994	62	**10**	CH sym stretch of $N^+(CH_3)_2$ [Foucault 03]
2950	18	3241	50	**4**	
2962	9	2839	50	**2**	CH asym stretch of $N^+(CH_3)_2$ [Foucault 03]
2974	9	2361	72	**1**	
2992	6	1763	96	**1**	unassigned [Foucault 03]
3021	12	1619	0	**2**	

Table 4.1: Raman bands of the powder DDAB at room temperature.

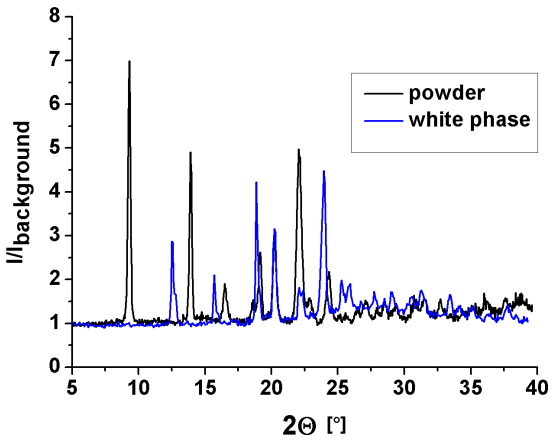

Figure 4.15: Preliminary X-ray diffraction data of the DDAB powder at room temperature and the crystalline 'white' phase, suggesting the existence of two stable crystalline phases in the investigated temperature range.

Preliminary powder X-ray diffraction measurements have been performed to confirm the existence of two stable crystalline forms in the DDAB samples in the investigated temperature range (see Fig.4.15). The diffraction pattern also clearly differs for both phases. A further study of the temperature dependence of the diffraction pattern at temperatures T<20°C is planned to investigate the thermal stability and equilibrium temperature range of each of these phases.

4.3 Properties of DDAB aqueous solutions (3%-85%)

4.3.1 Solution preparation

Samples with a volume of several cm^3 were prepared spanning the region of different pure lamellar phase across a range of surfactant mass concentrations from 3% to 85% by diluting with distilled water (3%, 5%, 7%, 10-85% in 5% steps). Samples were shaken and put on a roller until they had a homogeneous appearance. More concentrated samples were additionally stored for several days at $40°C$ for equilibration. To get rid of air bubbles, all samples were centrifuged. Samples in the coexistence region were turbid. Samples above 75% and below 25% were optically clear. The whole range of samples were stored at room temperature.

The samples were equilibrated for one week up to several months at the required starting temperature of the performed measurement. No dependence on the extent

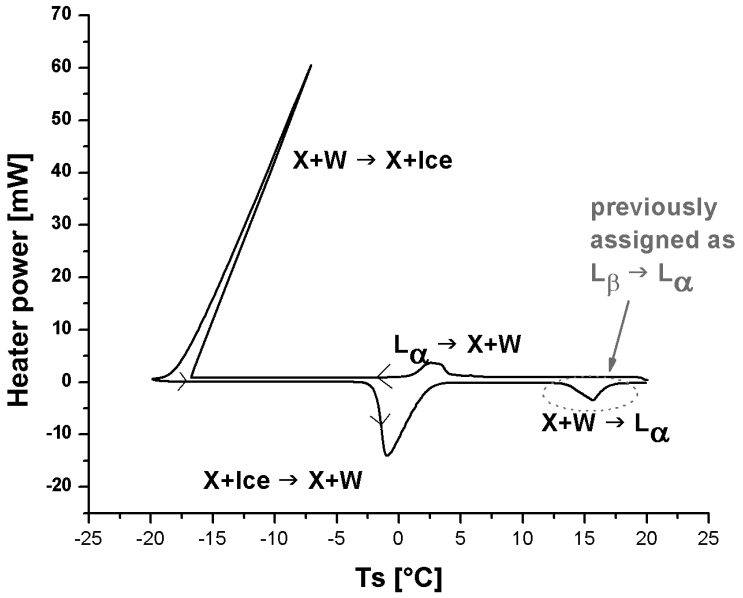

Figure 4.16: DSC plot of a aqueous DDAB solution (ϕ_{DDAB}=25%) in the temperature range T=-20°C to +20°C (scan rate: ±1°C/min). The peaks are assigned in the plot based on the phase diagram presented in Fig.4.34.

of equilibration time was observed.

4.3.2 Thermodynamic properties of the solution

The thermal properties of the solution have been investigated by DSC (as described in section 3.3.3.3) in the temperature range T=-20°C to +20°C. Fig.4.16 shows a DSC plot characteristic of samples which are at room temperature in the L_α phase. Two freezing and two melting transitions can be identified. The large hysteresis between the positions of cooling and the heating peaks indicates slow kinetics for the phase transition process and the existence of comparably stable overcooled phases over a broad temperature range.

The reversible transition centered near 0°C can be assigned to the freezing and melting of water based on the similar temperature and enthalpy values[3]. The second phase transition has been previously assigned to the $L_\beta \rightarrow L_\alpha$ phase transition [Dubois 91], with the transition temperature corresponding to the chain melting temperature T_M. The L_β phase had been described as a clear phase. However, whilst equilibrating

[3] Also based on the dependence of the enthalpy on sample concentration.

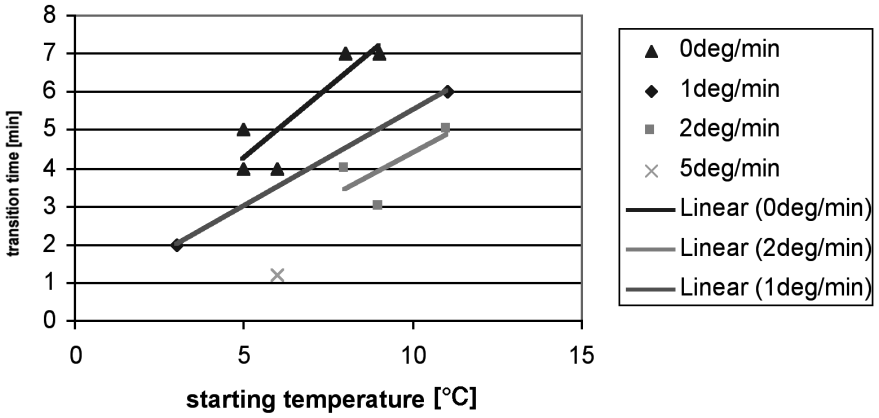

Figure 4.17: The duration of the first freezing transition in the DSC plots (the $L_\alpha \rightarrow$X+W phase transition) depending on starting temperature of the transition (which depends on the sample history) and on cooling rate. The lines show a least squares fit to the data.

DDAB samples for a long time (up to several months) within this temperature region, an unexpected increase in turbidity was observed in the samples (see Fig.4.25). The change of optical properties was observed to be faster at lower temperatures (within minutes at temperatures below T=5°C). When heating the sample above the T_M, the sample becomes clear. A detailed study of the properties of this 'white' phase is presented in section 4.3.4.

Interestingly, the degree of overcooling possible for the L_α phase, as well as the transition kinetics, depend on the sample history (see Fig.4.17). This behaviour is typical for a nucleation and growth process, where the amount of maintained nucleation centres often determines the kinetics. A detailed study of the transition kinetics can be found in the following chapter in section 5.2.

The shape of the X+W$\rightarrow L_\alpha$ transition depends on surfactant concentration (see Fig.4.18). The transition gets broader and the transition maximum is shifted towards higher temperatures with increasing concentation.

In the following sections the lamellar phase as well as the 'white' phase are characterised in more detail.

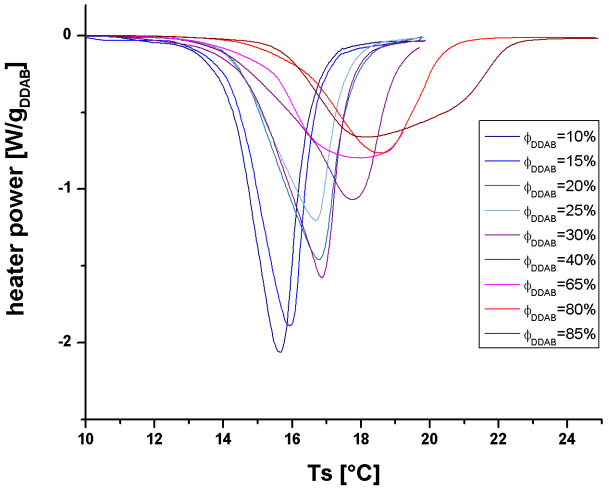

(a)

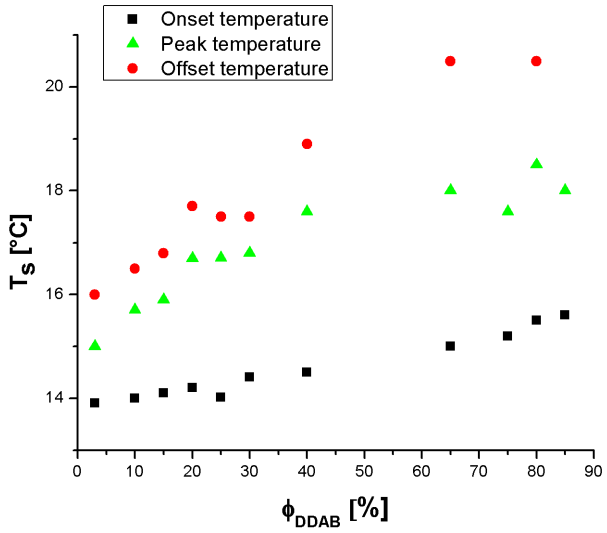

(b)

Figure 4.18: DSC plots (a) and onset, peak maximum and offset temperature (b) of the X+W→L_α transition for samples of different surfactant concentration. Note, the transition becomes broader with increasing surfactant concentration. For samples in the L'_α phase at room temperature, the transition behaviour is very complex.

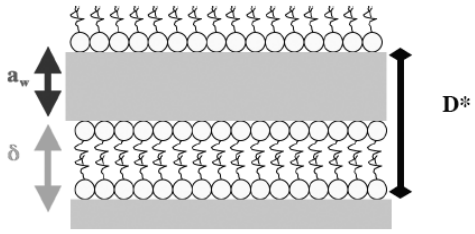

Figure 4.19: The definition of the repeating distance D^* in the lamellar phase.

4.3.3 The L_α and L'_α-phase

The lamellar phase has been already studied extensively in the literature [Dubois 91, Dubois 92, Karukstis 03]. However, in this section some of the reported measurements are repeated for control and some measurements added in order to compare the lamellar phase properties (on different length scales) with those of the 'white' phase (see section 4.3.4).

4.3.3.1 The Phase structure

The lamellar phase could generally be observed through crossed polarisers, confirming the presence of a birefringent lamellar phase except at very low concentration, when the birefringence was comparably weak, giving the sample the appearance of a isotropic solution. The concentration range of lamellar phase existence could therefore not be investigated using crossed polarisers.

The phase structure of a lamellar phase in the range of 5-25% DDAB concentration was therefore investigated with SAXS in more detail (see section 3.3.3.1). The concentration range was limited to the one-phase region of swollen lamellar phase and by the detector limit (Bragg peaks for concentrations below 5% were covered by the beam stop). As can be seen in Fig.4.20, the Bragg peaks, and therefore the repeat distance in the lamellar phase D^*, depends on surfactant concentration ϕ_{DDAB}. The measured q values correspond to the length

$$D^* = a_w + \delta,$$

where a_w is the water layer thickness and δ the bilayer thickness (see Fig.4.19). The dependence between the water layer thickness and the sample concentration can be approximated using a simple geometrical dependence:

$$a_w = \frac{\rho_{H2O}}{\rho_{DDAB}} \frac{1 - \phi_{DDAB}}{\phi_{DDAB}} \delta \tag{4.1}$$

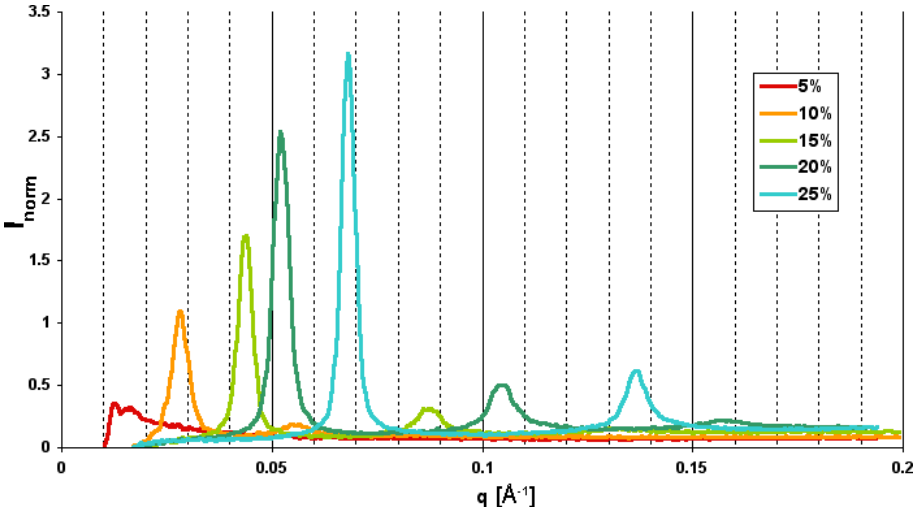

(a)

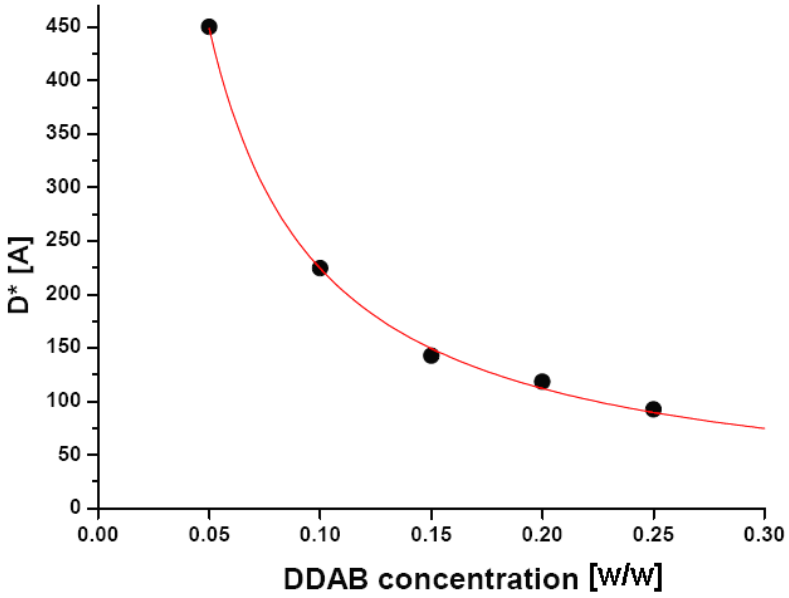

(b)

Figure 4.20: Bragg peaks obtained by SAXS for lamellar phases of DDAB for different surfactant concentration (a) showing an decrease in repeating distance with increasing ϕ_{DDAB} (b). The line shows the least squares fit to Eq.4.2 with δ=22.4±0.4 and R^2=0.9905 in the region ϕ_{DDAB}=0.1 to 0.25.

This equation can be used to describe the dependence of D^* on surfactant concentration ϕ_{DDAB} (see Fig.4.20(b)). Fitting the experimental data, the corresponding bilayer thickness δ (at ϕ_{DDAB}=100%) can be estimated (taking into account that the density $\rho_{DDAB} \approx \rho_{H2O}$):

$$D^* = a_w + \delta \approx (\frac{1 - \phi_{DDAB}}{\phi_{DDAB}} + 1)\delta \tag{4.2}$$

Because of the poor quality of the data at 5%, the equation was only fitted to the D^* values of 10-25% surfactant concentration. The obtained bilayer thickness of (22.4±0.4)Å is close to the reported literature value of 24Å [Dubois 91]. Therefore, this simple geometrical packing model shows good agreement with the experimental data within the experimental error and can be used to determine the bilayer thickness.

The value of the maximal concentration of the swollen lamellar phase has been tested by phase separating a sample in the L_α+L'_α coexistence region by centrifugation and measuring the repeating distance D^* of the dilute phase. The obtained q value of 0.81 corresponds to a surfactant concentration of approximately 29% which is therefore in good agreement with the literature value of 28% [Dubois 92, Dubois 98].

Finally, it should be mentioned that no significant effect of overcooling on the SAXS data of the lamellar phase within experimental error could be observed.

4.3.3.2 Conformational properties of the lamellar phase

The conformational properties of the lamellar phases have been investigated using Raman spectroscopy. A typical spectrum of the lamellar phase is shown in Fig.4.21 and the fitted bands in Tab.4.2. The spectra does not change with time, or number of scans, or with the historical treatment (e.g. freezing). The Raman spectrum shows no dependence on DDAB concentration and is the same in the L_α and L'_α phase (see Fig.4.22). The relative intensity of the DDAB peak and water peaks is not linearly dependent on concentration, however an increase in the water signal is seen relative to the DDAB signal on increasing water content.

Furthermore, the homogeneity of the spectra throughout the sample has been confirmed using Raman microscopy. The Raman peaks in the C-H stretching region, C-H bending and C-C twisting regions were of sufficient quality (see Fig.3.26) to confirm the homogeneity within one sample, even over a long period of time (up to 90min).

The increased gauche content in the hydrocarbon chains and so the increased fluidity of the lamellar phase compared to the solid phases (see Fig.4.14), can be observed

Peak centre .[cm^{-1}]	Peak width [cm^{-1}]	Peak height	Proportion of Gaussian fit %	**Area %**	Assignment
771.873	34	1435	24	**1.91**	
840.327	19	857	31	**2.48**	CH_2 rock in CH_2-NCH_3 [Foucault 03]
848.055	12	645	43	**3.45**	
871.859	16	1254	48	**3.82**	
890.442	15	2329	49	**3.94**	CH_3 rock, CN^+ stretch [Foucault 03]
909.704	27	1228	51	**4.09**	CN^+ stretching [Foucault 03]
927.503	16	972	55	**4.42**	
1066.31	32	4917	32	**2.56**	C-C sym stretch & CH_2 wag. [Foucault 03]
1083.9	14	3466	100	**8.04**	C-C stretch (Gauche conformation) [Foucault 03]
1127.23	19	1417	100	**8.04**	C-C asym stretch & CH_2 (gauche) wag. [Foucault 03]
1301.41	18	7497	67	**5.43**	C-C twisting
1320.57	52	2739	100	**8.04**	
1437.48	14	10406	70	**5.64**	CH_2 bend [Foucault 03]
1454.54	32	15893	62	**4.95**	CH_2 bend [Foucault 03] CH asym bend from $N(CH_3)_2$ [Foucault 03]
2848.86	17	32476	73	**5.90**	CH asym stretch of CH_2 [Foucault 03]
2880.23	45	36197	71	**5.74**	CH sym stretch of CH_3 [Foucault 03]
2910.07	52	23753	84	**6.74**	
2931.2	22	15084	90	**7.21**	
2963.93	45	16964	43	**3.46**	CH asym stretch of $N^+(CH_3)_2$ [Foucault 03]
3032.78	29	6945	51	**4.14**	
3218.61	210	15428	87	**6.98**	water
3434.24	243	26168	100	**8.04**	water
3619.56	101	3148	100	**8.04**	water

Table 4.2: Fitted bands of DDAB in the L_α phase.

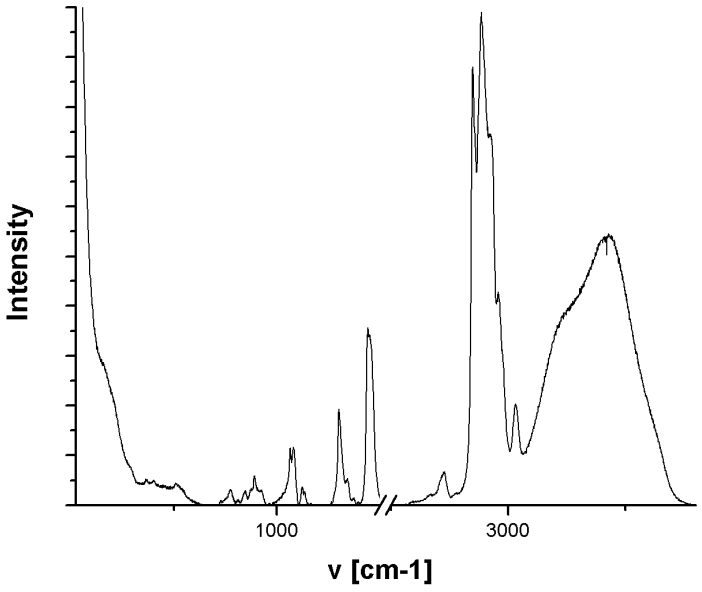

Figure 4.21: Typical Raman spectrum of the L_α phase of DDAB obtained at ϕ_{DDAB}=10% at T=20°C.

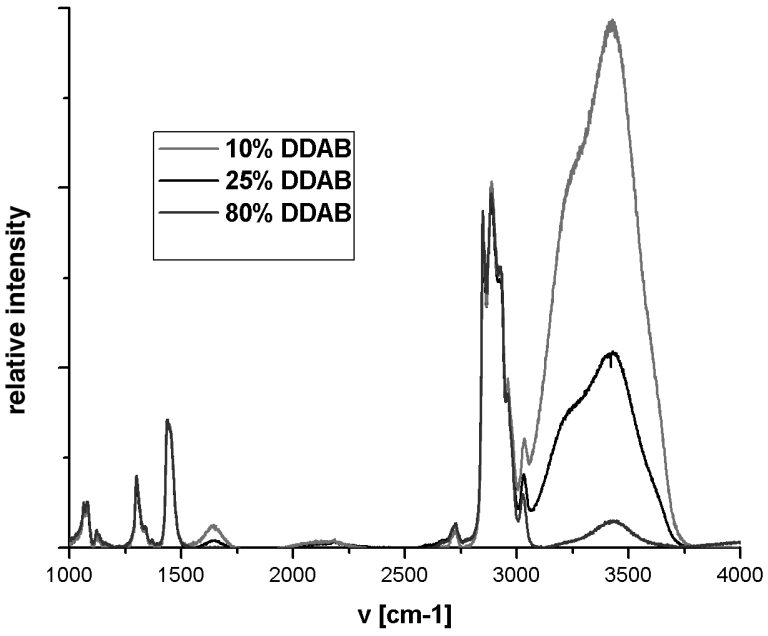

Figure 4.22: Raman spectrum of three DDAB solutions at different concentrations, showing a decrease of the water peak with increasing surfactant concentration.

Φ_{DDAB}[%]	wavenumber [cm^{-1}] $\pm$10cm^{-1}	relative intensity [%] $\pm$2%
10	3220	38
(L_α)	3440	58
(20°C)	3620	4
10	3240	42
(L_α overcooled)	3420	55
(1°C)	3620	3
25	3220	37
(L_α)	3440	60
	3620	3
85	3240	15
(L'_α)	3430	85
0	3210	48
(16°C)	3420	50
	3620	3
0	3210	47
(6°C)	3420	51
	3620	3

Table 4.3: Observed peak Raman frequencies in the OH stretching region of water.

in the appearance of a strong band at 1088cm^{-1} in the C-C bending region of the spectrum [Foucault 03]. Furthermore, an increase in the ratio of the symmetric C-H stretching vibration, compared to the asymmetric C-H stretching vibration I_{2850}/I_{2880} confirms the fluid-like character of the bilayers, which is also supported by the observed broadening of the bands, and the disappearance of the LAM frequencies in the spectrum.

Properties of the water in the samples The water peak has been compared to those in pure water (see Tab.4.3). The frequencies are similar, with only the relative intensities changing. Within water, there is a decrease in the relative intensity of I_{sym}/I_{asym} when lowering the temperature, i.e. increasing the order in the system. This increase is also observed upon the addition of DDAB to the sample. This might suggest a higher degree of order for water, which is confined between bilayers of DDAB.

4.3.3.3 Temperature range & overcooling

The Raman spectrum for temperatures above 18°C for a solution of ϕ_{DDAB}=25% shows the signal for a pure lamellar phase . As already mentioned, the L_α phase can be overcooled. This overcooling has no effect on the Raman bands corresponding to the DDAB molecule, however, the overcooling has an effect on the water peak in the spectrum (see Fig.4.23 and Fig.4.24). These changes are in contrast to the expected

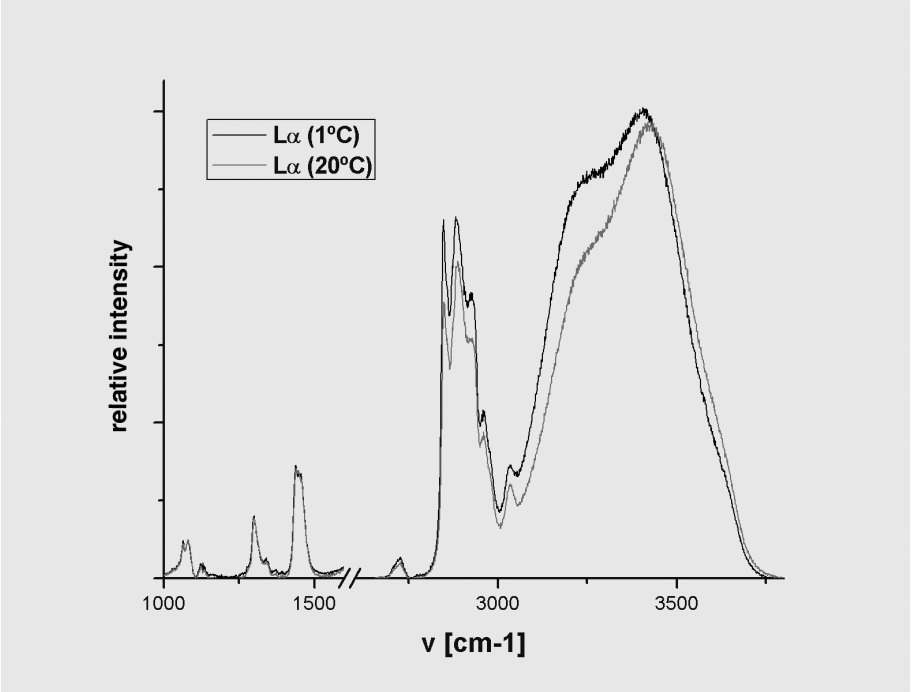

Figure 4.23: The changes in the water bands upon overcooling the L_α phase to 1°C, observed by Raman spectroscopy.

changes for bulk water: there is a increase in the ratio I_{sym}/I_{asym} instead of a decrease once the phase is overcooled.

4.3.4 White phase

As already mentioned, if the sample is sufficiently cooled, a strong increase in turbidity is observed in the sample, until it appears entirely white (see Fig.4.25). This suggests a phase coexistence in the samples, with the white colour being due to scattering at the phase boundary. Crystals could be observed for thin samples (below 100μm) under a microscope (see Fig.4.26).

The liquid phase could be partly extracted by centrifugation or sedimentation (see Fig.4.25(a)) due to the density mismatch in the sample (see page 159) at surfactant concentrations below 10%. For higher surfactant concentrations, no phase separation could be observed. This might be due to the electrostatic repulsion between the crystals, or by constraint in packing.

No surfactant molecules could be identified in the liquid phase, therefore it can assumed that only a very low monomer concentration is present. This is also in agreement

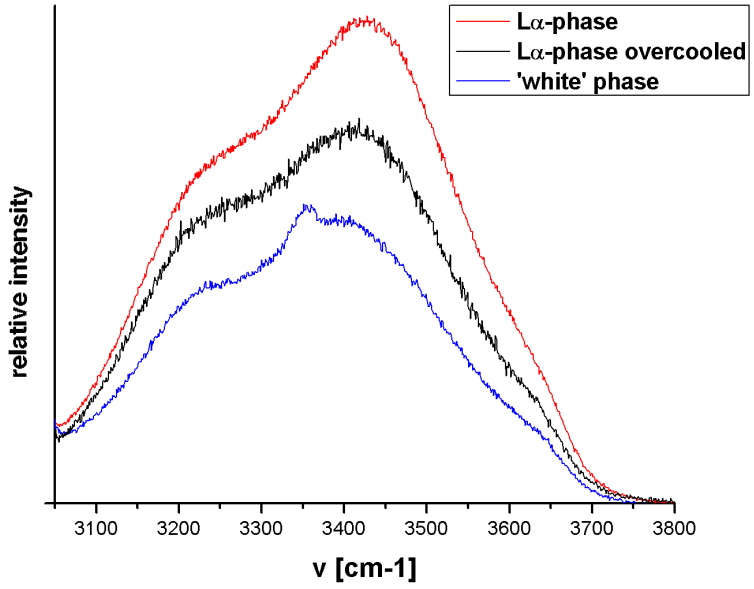

Figure 4.24: Characteristic shape of the Raman water peak for different samples. The 'white' phase spectra is discussed in section 4.3.4

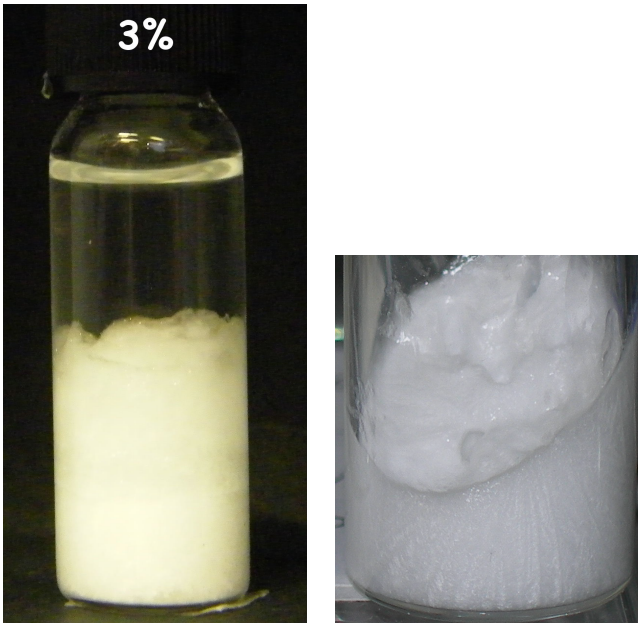

(a) Φ=3% (b) Φ=25%

Figure 4.25: Photographs of samples in vials in the white phase. The 3% sample did phase separate with time.

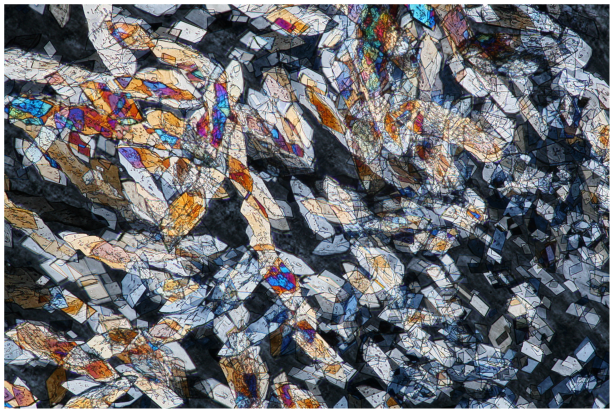

Figure 4.26: The white phase observed using polarised microscopy (image size 1.5x2.2mm).

with the SAXS measurements on the separated white phase (by centrifugation or sedimentation) at room temperature. Such samples show the repeating distance D^* corresponding to a lamellar phase of surfactant concentration ϕ_{DDAB} of 10%.

4.3.4.1 Phase structure of the crystalline phase

The phase structure of the 'white' phase has been investigated in more detail using SAXS. In this phase, no series of Bragg peaks can be resolved, as would be expected for a lamellar phase. This is in disagreement with the existence of a previously reported L_β phase [Dubois 91]. In contrast, high scattering intensities at small q values (below 0.05) have been observed (see Fig.4.27). The decay of this scattering peak follows a q^{-4} law.

A possible explanation of the observed strong scattering behaviour at low q values is the Rayleigh scattering of single crystals in the sample (see Fig.4.26). As the crystals tend to be large, the Guiner regime cannot be detected with the experimental setup, which would give information about the crystal shape and size. The q^{-4} dependence can be described with the following equation:

$$I = (\Delta\rho_e)^2 \Phi \frac{S}{V} q^{-4}, \tag{4.3}$$

where $\Delta\rho_e$ is the difference in the electron density between the crystals and the water, Φ the volume fraction of the crystals and $\frac{S}{V}$ the surface area to volume ratio of the crystals.

The electron density for the DDAB molecule is estimated to be $\rho_{e,DDAB}$=9.46·10^{10}cm^{-2} and for water $\rho_{e,H2O}$=9.34·10^{10}cm^{-2}, which would lead to $\Delta\rho_e$=1.14·10^{9}cm^{-2}. For a

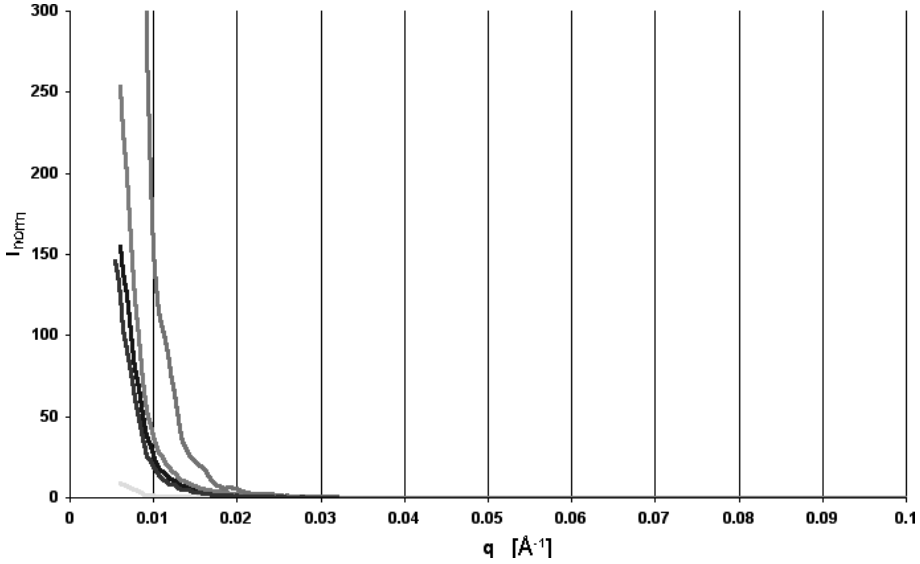

Figure 4.27: The q^{-4} behaviour for the scattering intensity, I, at small q values for several samples of the 'white' phase are shown. These can be explained by Rayleigh scattering of the single crystals in the phase.

prefactor of the q^{-4} decay of the peak of about $1.3{\cdot}10^{24}\text{cm}^{-5}$ and Φ=20%, the surface area to volume ratio of the crystals would be $\frac{S}{V}$=$5{\cdot}10^{6}\text{cm}^{-1}$. For a rectangular crystal of size $L \cdot W \cdot D$ of $L{\approx}W{\approx}10\mu$m (see Fig.4.26), that would correspond to a depth of $D{\approx}0.5\mu$m using

$$\frac{S}{V} = \frac{2LW + 2LD + 2WD}{LDW}. \tag{4.4}$$

For larger values of $\frac{S}{V}$ or higher concentration of the crystalline phase, an increase in peak intensity is expected. This can explain the variations of the peak heights seen in the samples.

In general, one can say that the absence of Bragg peaks in the small angle region in the scattering spectrum of the 'white' phase, and the strong scattering at low q values, suggests the low temperature phase to be a phase of crystals dispersed in water, in contrast to the previously reported assignement of an L_β phase. Furthermore, the preliminary X-ray diffraction data confirm this picture (see Fig.4.15).

The density has been measured for samples in the 'white' phase of ϕ_{DDAB}=5% using an oscillating U-tube densitymeter. The density corresponding to the DDAB molecules ρ_{DDAB} can be extracted from the measured density values ρ of the sample, based on

the water density ρ_{H2O} for the corresponding temperature using Eq.4.5:

$$\rho_{DDAB} = \frac{\rho \cdot \rho_{H2O}}{\rho_{H2O} - (1-\phi)\rho}\phi \tag{4.5}$$

The density of the DDAB molecules in the 'white' phase is about 15% higher compared to the lamellar phase[4], giving ρ_{DDAB}=(1.1±0.2)kg/dm^3. Therefore the comparably high density in the crystals, compared to the surrounding liquid phase in the 'white' phase, can explain the sedimentation behaviour discussed earlier.

4.3.4.2 Conformational properties of the crystalline phase

A typical Raman spectrum of the 'white' phase has been already shown in Fig.4.14. This spectrum is identical for concentration ϕ_{DDAB}=10% and 25%. Only the signal to noise ratio is better for the higher surfactant concentration. The signal has a strong fluorescent background, which has been deducted from the spectrum. The signal to noise decreases significantly upon decrease in temperature, but the peaks and peak shapes do not change with temperature. The upper temperature limit of a pure Raman signal of a 'white' phase was found to be 14.1°C.

Furthermore, the homogeneity of the spectra throughout the sample has been confirmed using Raman microscopy. The Raman signal of the C-H stretching region, C-H bending and C-C twisting region were of sufficient quality (see Fig.3.26) to confirm the homogeneity within one sample, even over a long period of time (up to 90min).

A number of sharp peaks could be identified for the 'white' phase (see Tab.4.4). The peaks were in general found to be much sharper, compared to the lamellar phases. Furthermore, a range of peaks could be identified for the region below 600cm^{-1}, which indicates an increase of observed lattice vibrations in the sample, which is, in general, typical for crystalline phases. The Gaussian fit was of high quality due to the sharpness of the peaks.

The water peak in the 'white' phase is different from the water peak in the L_α phase (see Fig.4.24). An additional peak around 3350cm^{-1} could be identified. This peak is more intense at lower temperatures. The intensity ratios of the symmetric and asymmetric stretching increases strongly with increasing temperature, as does the overall intensity of the combined water peak. In contrast to the lamellar phase, upon increase of surfactant concentration, an increase of the intensity ratio is seen. One could

[4]The measured value of the density of the DDAB molecules in the lamellar phase of ρ_{DDAB}=(0.97±0.01)kg/dm^3 is in good agreement with the reported literature values [Dubois 91].

Peak centre .[cm^{-1}]	Peak width [cm^{-1}]	Peak height	Proportion of Gaussian fit %	**Area %**	Assignment
45.9208	8	17765	100	**3.71**	LAM mode
68.271	7	4536	50	**1.86**	LAM mode
111.27	7	2039	50	**1.86**	LAM mode
141.434	5	2423	67	**2.49**	LAM mode
157.854	16	7330	48	**1.77**	LAM mode [Foucault 03]
190.827	11	5342	45	**1.68**	LAM mode
241.494	14	1280	50	**1.86**	LAM mode
287.886	18	576	66	**2.46**	LAM mode
371.98	13	2057	61	**2.26**	LAM mode
390.547	10	1397	36	**1.33**	LAM mode
415	15	1589	45	**1.69**	LAM mode [Foucault 03]
446.462	19	680	38	**1.43**	unassigned [Foucault 03]
468.723	12	1451	46	**1.7**	unassigned [Foucault 03]
509.33	11	2293	47	**1.73**	
523.172	4	572	46	**1.72**	unassigned [Foucault 03]
769.896	7	2251	50	**1.86**	CH_3 rock from $N^+(CH_3)_2$ group [Foucault 03]
844.724	8	3639	2	**0.06**	CH_2 rock in CH_2-NCH_3 [Foucault 03]
884.843	6	3269	50	**1.86**	
891.027	8	5907	24	**0.88**	CH_3 rock, CH^+ stretch [Foucault 03]
1033.57	8	1490	58	**2.15**	
1062.23	6	20066	14	**0.53**	C-C sym stretch, CH_2 wag. [Foucault 03]
1082.82	7	9461	6	**0.23**	C-C stretch (Gauche conformation) [Foucault 03]
1126.15	8	14552	33	**1.21**	C-C asym stretch, CH_2 (gauche) wag. [Foucault 03]
1148.79	7	3530	37	**1.37**	
1170.13	7	3101	34	**1.26**	
1180.88	9	3052	38	**1.42**	
1296.52	6	28494	46	**1.71**	CH_2 twist [Foucault 03]
1307.88	8	3786	33	**1.24**	
1341.1	8	6034	35	**1.31**	
1437.73	8	13739	46	**1.71**	CH_2 bend [Foucault 03]
1445.39	13	11716	47	**1.73**	CH sym bend from $N(CH_3)_2$ [Foucault 03]
1453.27	8	17757	51	**1.88**	CH_2 bend [Foucault 03] CH asym bend from $N(CH_3)_2$ [Foucault 03]
1461.05	9	13404	48	**1.8**	
1469.61	9	13131	45	**1.66**	
2841.68	13	37154	56	**2.09**	CH asym stretch of CH_2 [Foucault 03]
2852.52	15	31277	43	**1.58**	CH asym stretch of CH_2 [Foucault 03]
2863.01	14	32018	48	**1.79**	CH asym stretch of CH_2 [Foucault 03]
2870.57	8	26946	50	**1.87**	
2877.96	6	67482	74	**2.74**	CH sym stretch of CH_3 [Foucault 03]
2886.1	18	43611	49	**1.83**	CH sym stretch of CH_3 [Foucault 03]
2902.95	17	27856	44	**1.65**	
2916.5	19	17014	49	**1.82**	
2930.1	17	23919	50	**1.87**	
2942.97	31	14342	47	**1.76**	
2959.89	5	8059	49	**1.82**	
2960.5	16	18706	47	**1.73**	CH asym stretch of $N^+(CH_3)_2$ [Foucault 03]
2976.4	15	12197	39	**1.46**	
2996.97	9	7084	67	**2.48**	unassigned [Foucault 03]
3026.36	12	9871	50	**1.87**	
3040.6	14	4275	51	**1.89**	
3249.7	260	16119	54	**1.99**	water
3355.64	71	4297	42	**1.56**	
3445.12	188	16055	91	**3.37**	water
3596.22	122	4149	100	**3.71**	water

Table 4.4: Fitted bands of DDAB in the 'white' phase.

suggest that the disorder in the system therefore increases upon increasing surfactant concentration and increasing temperature.

The Raman spectrum of the 'white' phase differs markedly from the spectrum of the lamellar phase (see Fig.4.28). The most striking differences are the appearance of bands below $\overline{\nu}$<700cm^{-1} as well as the increased sharpness of the peaks throughout the spectrum. Compared to the lamellar phase, the C-C stretching peak at 1080cm^{-1} decreases in intensity, suggesting a lower gauche content in the 'white' phase. The same can be deduced from the reduced ratio of I_{2850}/I_{2880}. In general, one can say that the Raman spectrum supports the crystalline character of the 'white' phase.

In this chapter, the Raman spectra of the powder, the L_α phase and the 'white' phase of DDAB have been presented. It has been shown that the position of bands are in agreement with those data found in the literature and therefore that many of the bands could be assigned. It could be shown that there are significant differences in the C-H stretching region, as well as in the C-C stretching region in the spectra. In order to correlate these changes to conformational changes in the molecule, single molecule calculations (see section 3.3.2.2) have been carried out.

Raman frequencies have been calculated for several DDA$^+$ conformations, which differ in the gauche content of the chains. The most stable configuration which has been found is shown in Fig.4.29(a). However, the corresponding Raman spectrum differs remarkably, especially in the region of the C-H stretching modes from the experimentally obtained spectrum of the powder or 'white' phase (see Fig.4.30). Calculation have been made on isolated molecules in the gas phase, and neglect the effects of packing in solid and lamellar structures.

However, general trends can be seen in these calculations. The introduction of gauche kinks in the chain influences the ratio of the peaks I_{CHsym}/I_{CHasym} (see Fig.4.30-4.33). Gauche kinks at positions closer to the head group lead to a peak shape similar to the peaks in the powder or 'white' phase, whilst kinks towards the end seem to be characteristic of the L_α phase. Furthermore, the three band structure between 1000cm^{-1} and 1150cm^{-1} seems also to confirm this assignement. The peak in the middle, which probably corresponds to the experimental peak at 1080cm^{-1}, does not vanish for the all-trans conformation of the alkyl chain, but decreases with increasing amount of gauche kinks close to the head groups.

The conformation of DDAB molecules with a kink close to the head group is also

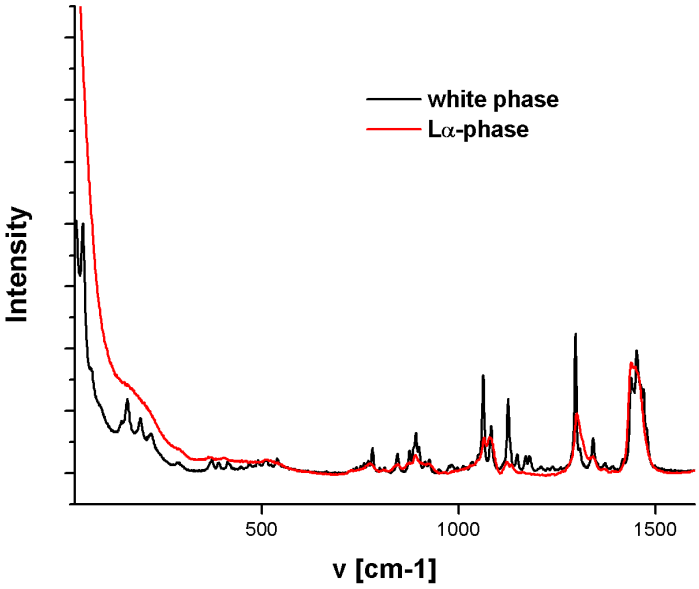

(a)

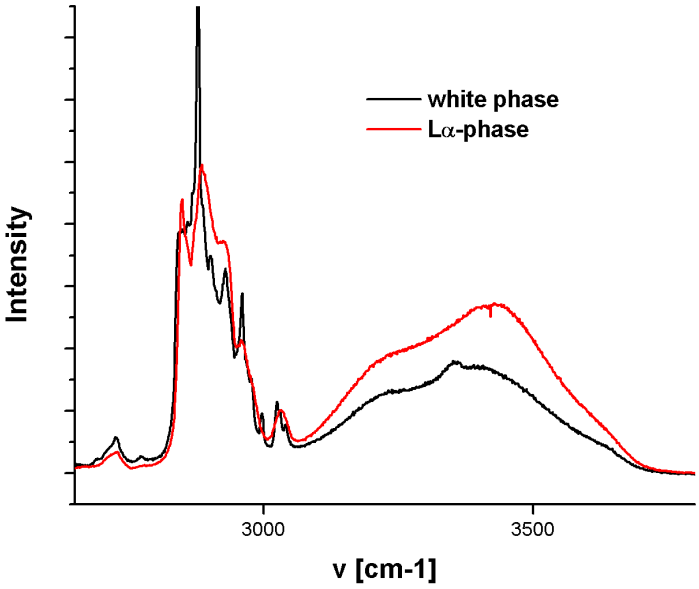

(b)

Figure 4.28: Comparison of the Raman spectrum of the lamellar phase (ϕ_{DDAB}=10%, T=20°C) and the 'white' phase (ϕ_{DDAB}=25%, T=13.8°C).

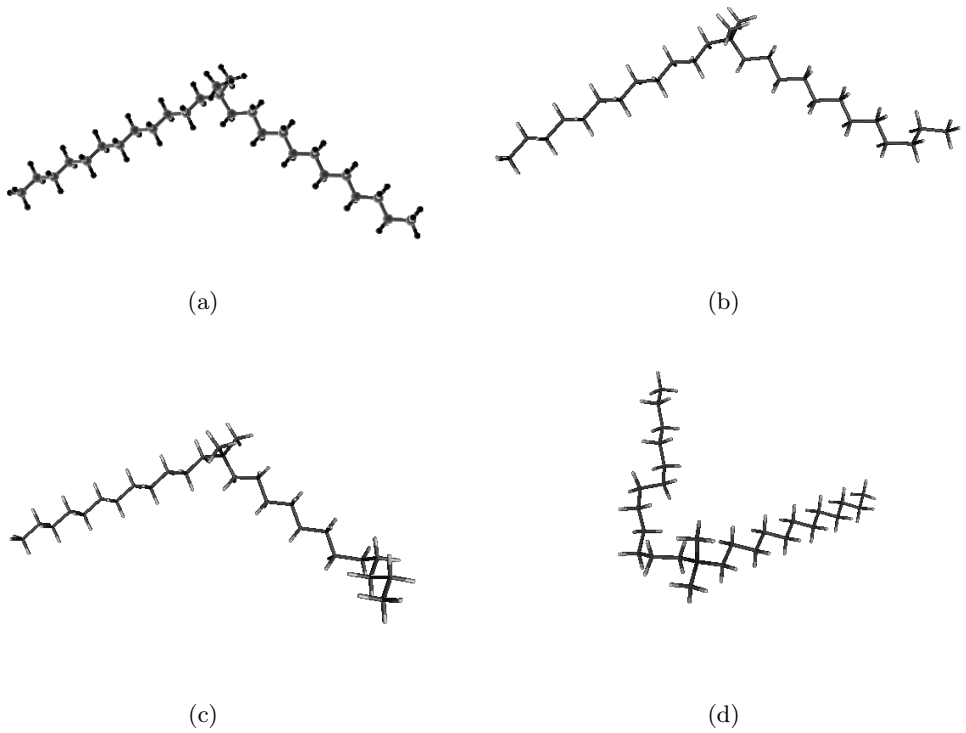

(a) (b)

(c) (d)

Figure 4.29: Optimised geometry of the most stable DDA^+ conformation (a) and three conformations having a gauche kink in the chain (b-d) obtained from single molecule calculations in the gas phase.

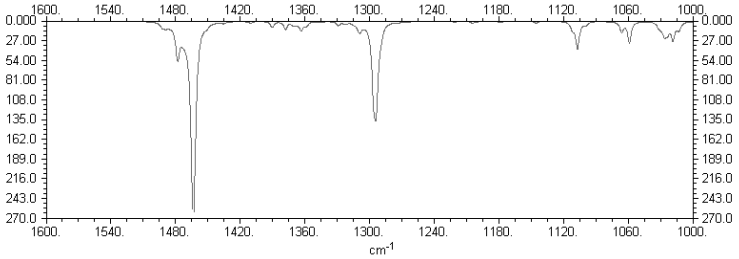

(a)

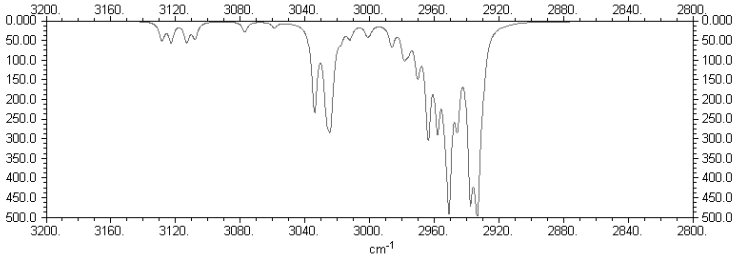

(b)

Figure 4.30: Calculated Raman spectrum of the DDA^+ ion in its most stable conformation (see Fig.4.29(a)).

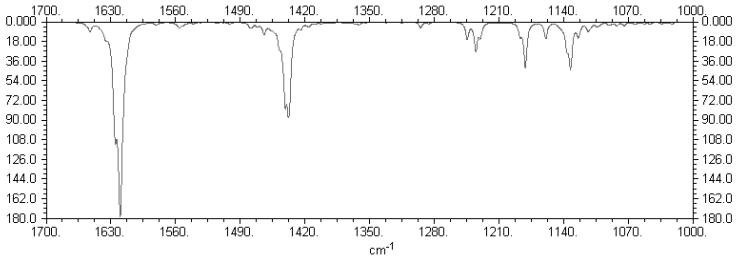

(a)

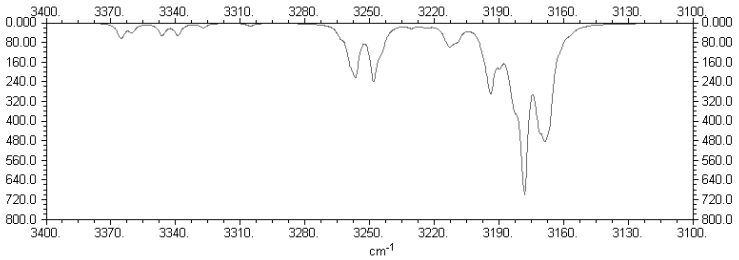

(b)

Figure 4.31: Calculated Raman spectrum of the DDA^+ ion with a gauche kink at the end of the chain (see Fig.4.29(b)).

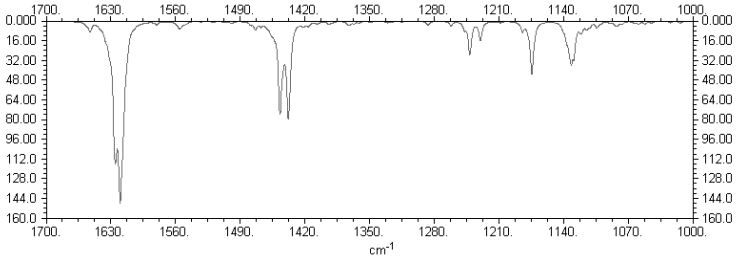

(a)

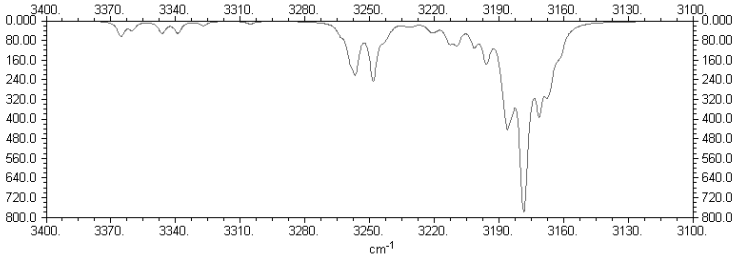

(b)

Figure 4.32: Calculated Raman spectrum of the DDA^+ ion with a gauche kink in the middle of the chain (see Fig.4.29(c)).

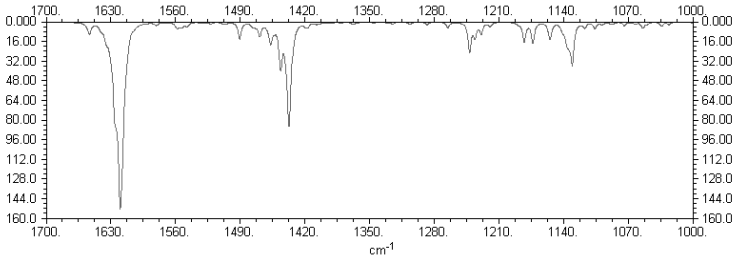

(a)

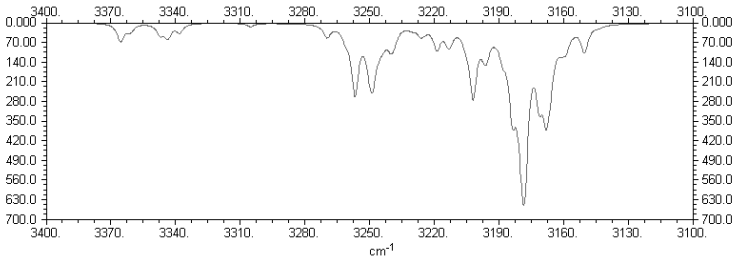

(b)

Figure 4.33: Calculated Raman spectrum of the DDA^+ ion with a gauche kink close to the head group (see Fig.4.29(d)).

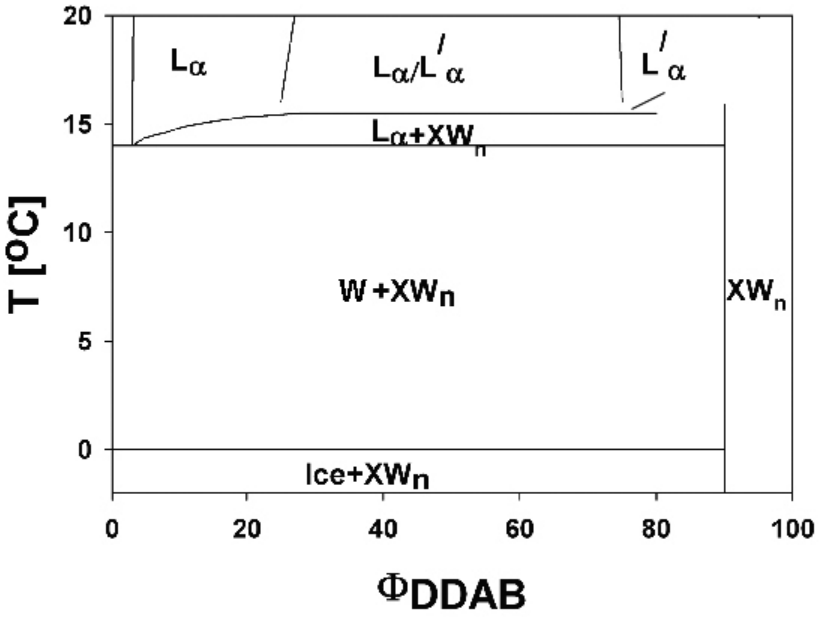

Figure 4.34: Sketch of the proposed new phase diagram of the DDAB/water system.

closest to the crystal structure obtained for its slightly longer analogues DODAB (see Fig.3.7) and DODMAC (see Fig.2.12(a)).

All the performed measurements describing the structure of the 'white' phase lead to the conclusion that this phase consists of a crystalline phase and a dilute liquid phase. The upper temperature limit of the 'white' phase can be assumed to be the Krafft temperature of the aqueous DDAB system, and the liquid phase a very dilute monomer solution.

4.4 The proposed new phase diagram

The results desribed in the last sections cannot be explained within the frame of the phase diagram of DDAB reported in the literature [Dubois 98]. Therefore, a modified form of the phase diagram for low temperatures is proposed (see Fig.4.34).

The previously reported L_β phase is replaced by a coexistence region of a crystalline phase XW_n and a very dilute (near pure water) monomer solutions W. This means that W can be drawn with a composition at ϕ_{DDBA}=0. This is consistent with the phase transition for W to ice seen at 0°C and the invariance of XW_n composition below this transition temperature. The hydration state of the crystalline phase at low

temperatures is not known which would fix the position of the vertical line separating the $W + XW_n$ and XW_n regions at high ϕ_{DDAB}. However, the crystalline form differs in structure from the zero-hydrate found in the DDAB powder at room temperature, which might be either because it is hydrated or it is another polymorph of the zero-hydrate. The accurate transition temperature between the two crystalline phases is not known, and therefore that part of the phase diagram is represented by broken lines.

At higher temperatures, the phase diagram is consistent with the phase diagram reported in the literature. Two lamellar phases can be found, the swollen L_α phase and the collapsed L'_α phase, which coexist over a broad temperature and concentration range.

Both the L_α and the L'_α phase have to have at their lower limits an eutectic discontinuity (see section 2.2.3.2). The eutectic discontinuity of the L'_α phase can, in general, lay above or below the eutectic of the L_α phase. Both versions have been reported for other systems [Rhinne 56,Laughlin 09]. The observed results however suggest, that there is a region in the phase diagram in which the L_α phase coexists with the crystalline phase (which is further confirmed in experiments presented in chapter 5). Therefore, it can be assumed that the eutectic limiting the L_α phase corresponds to the Krafft eutectic, whilst the lower limit of the L'_α phase can be found at higher temperatures. The exaxt position of the discontinuity limiting the collapsed L'_α phase cannot be determined from the performed experiments.

The form of the presented phase diagram is consistent with the theoretical rules of phase science (see section 2.2.2), however the exact positions of the boundaries drawn in broken lines is not known. The thermal stability limit of DDAB is at about 90°C, which is therefore the upper limit of the phase diagram.

4.5 Conclusions and future work

In this chapter, a detailed study of the equilibrium phase behaviour of the DDAB/water system has been presented. The samples, which were used in this study, were shown to be of high purity, the reported results did not change with additional purification.

The obtained results could not be explained within the frame of the previously reported phase diagram [Dubois 98]. The results are based on a range of experimental techniques, which characterise the samples at different length scales. The low temperature phase, which was previously reported to be a L_β phase, could be shown to be a coexistence

region of a crystalline phase XW_n and a dilute monomer solution W. This phase differs not only in optical properties (being white in contrast to the clear L_β phase), but its crystalline character could be confirmed by Raman spectroscopy, small and wide angle X-ray scattering and microscopy. Therefore the previously reported L_β phase is concluded to be a non-equilibrium overcooled L_α phase.

The hypothesis of a new phase diagram has been derived from the reported experimental results, which follows all the phase rules presented in section 2.2.2. The exact position of the phase boundaries, especially at high concentrations, could however not be derived from the experimental data. In the following chapter, a detailed study of the thermal phase transition involving the crystal/water coexistence region and the L_α phase is presented, testing the correctness of the obtained phase diagram.

In future, a detailed study of the high temperature region is needed in order to obtain the exact position of the lower limit of the collapsed L'_α phase as well as the hydration state and thermal stability limit of the crystalline phase found at low temperatures.

Chapter 5

Thermal phase transition in the DDAB/water system

5.1 Introduction

In the last chapter, a hypothesis of a new phase diagram of the DDAB/water system at low temperatures was presented (see Fig.4.34) and the new crystalline phase characterised. However, among other things, the region of L_α+XW_n coexistence, resulting from the non-isothermal melting of the XW_n+W phase, was only concluded from theoretical rules of phase science.

In a further step, the features of the non-isothermal phase transition of the $L_\alpha \leftrightarrow XW_n + W$ transition were investigated in more detail. While the freezing transition, being simple in principle, has been followed using only microscopy (see section 5.2), a range of experimental techniques were needed to give insight into the melting process. The non-isothermal character of the melting process could be confirmed with DSC and densitometry (see section 5.3.2).

The coexisting phases during the phase transition were characterised using Raman spectroscopy and microscopy (see section 5.3.4), as well as temperature-controlled small angle X-ray scattering (see section 5.3.3). Furthermore, SAXS could be used to obtain a better estimation of the phase boundaries drawn in Fig.4.34, connecting the L_α phase with the L_α+XW_n coexistence region.

5.2 The $L_\alpha \rightarrow XW_n + W$ freezing transition

5.2.1 The pathway of the transition

The freezing of the lamellar phase formed by DDAB into crystals, was observed using temperature controlled microscopy along the isoplethal path at ϕ_{DDAB}=25% (see Fig.5.1). The pathway could be identified as:

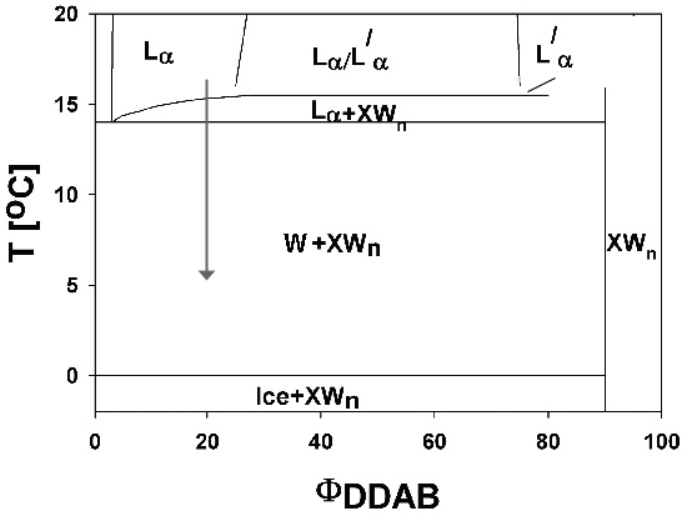

Figure 5.1: Isoplethal path (red) for the study of the $L_\alpha \rightarrow XW_n + W$ freezing transition.

$$L_\alpha \rightarrow \text{ overcooled } L_\alpha \rightarrow XW_n + W$$

As already mentioned in section 4.3.3.3, the properties of the overcooled L_α phase are comparable to the properties of the equilibrium L_α phase. Therefore, no attention was paid to this process. Furthermore, the temperature at which the overcooled L_α phase finally freezes has been already shown to depend on the history of the sample (see section 4.3.2). This section therefore focuses on the investigation of the freezing transition.

5.2.2 The nucleation and growth mechanism of the freezing transition

The mechanism of the freezing transition has been investigated using temperature controlled microscopy. According to the optical properties, two different types of freezing mechanism could identified (see Fig.5.2). A high degree of overcooling below 5°C resulted in changes in the appearance of the whole sample, shown in Fig.5.2(a). Additionally, a fast growth of opaque areas, which correspond to areas consisting of a large amount of crystals, can be observed. In the end, the sample appears completely black in the image, corresponding to a high density of crystals.

This observation can be explained by a combination of two different mechanisms; the creation of nucleation points, which are associated with an increase in turbidity of the sample, as well as the fast growth of existing nucleation points. The formation of new nucleation points requires a high degree of overcooling of the samples and can

be enhanced by introducing nucleation sites. For example, contact with the rough glue/sample interface enhances freezing, compared to the glass/sample or sample/air interface.

It has to be noted that the recorded images give only a local image of the sample. The whole sample is sketched in Fig.5.3. The crystalline phase starts to grow from the L_α/glue interface, which suggests that the glue provides a good surface for the nucleation of DDAB crystals. The crystalline phase develops in a quasi 2-D growth along the capillary until the air/sample interface is reached. One should note that this interface also moves during the thermal phase transition (see Fig.5.4).

The changes in position of the air/sample interface can be explained by the competition between the air and the sample caused by density changes. Upon cooling the L_α phase, a decrease of air volume of about 5% (taking the geometrical curvature of the interface into account) is observed, which is close to the predicted volume change of air due to the density change with temperature, according to the ideal gas law. The density of the L_α phase changes only slightly (see Fig.5.10(a)). Once parts of the samples are transformed into the crystalline phase, the density of which is about 15% lower compared to the L_α phase (see section 4.3.4), the air/sample interface shifts towards its initial position until the whole sample is frozen. The position of the interface of the frozen sample does not change upon heating until the transition temperature of 14°C is reached. At this temperature the sample expands, which is caused by the melting of crystals into the lamellar phase. Once the fluidity of the sample is high enough that the pressure change in the air can change the position of the interface, the interface shifts back to its initial position.

As already reported in the previous chapter, at temperatures just below the phase transition temperature, no freezing is observed unless pre-existing nucleation points are present and start to grow. The number of these nucleation points depends on the sample history. The number of pre-existing nucleation points was found to increase, for example, by cooling the sample just after the melting of the sample, without allowing long equilibration time.

One should also note that the size of the crystals change with the transition temperature. During the growth of crystals at temperatures close to the phase boundary, the size of the crystals is large, as is shown in Fig.5.5. This is combined with a change in growing speed. For each temperature, the increase in the area occupied by the crystals in the pictures with time shows a linear dependence on time (see Fig.5.6).

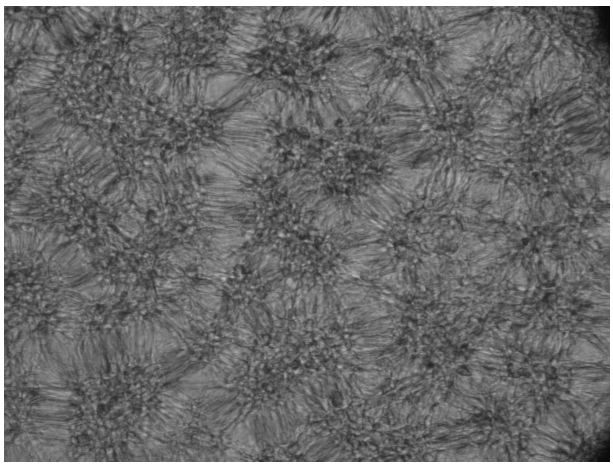

(a) nucleation

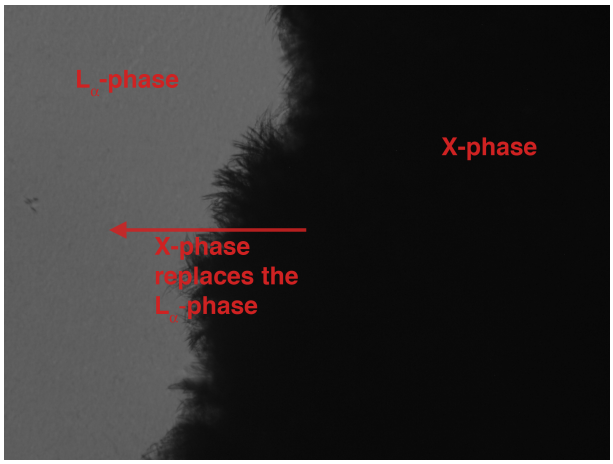

(b) growth

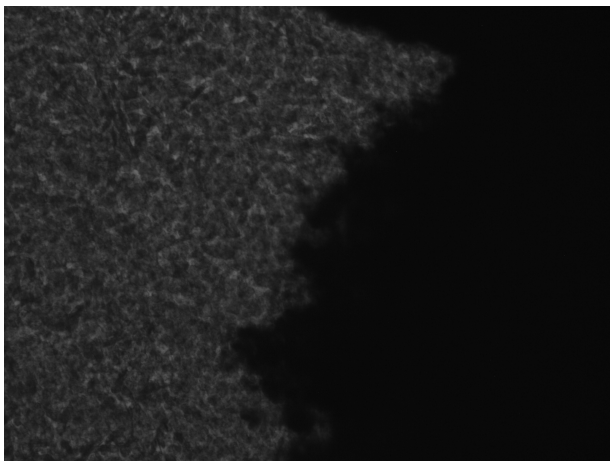

(c) nucleation & growth

Figure 5.2: Optical changes occurring during the $L_\alpha \rightarrow XW_n + W$ freezing transition (image size=1.4x1.0mm^2).

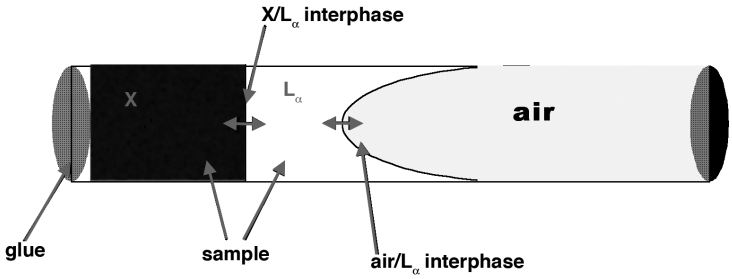

Figure 5.3: Sketch of the thermo-statted sample (capillary 0.2x4x50mm^3).

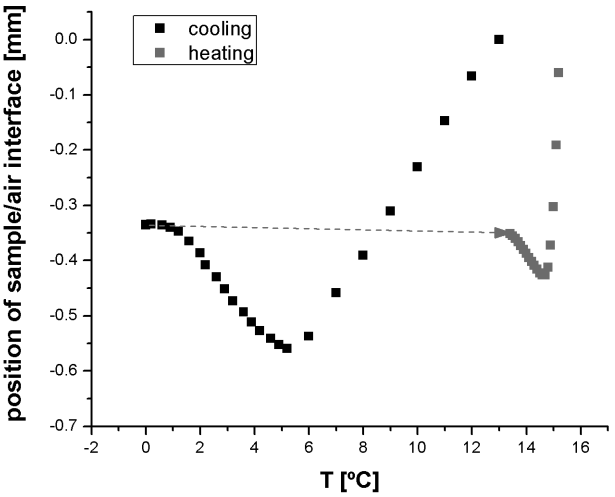

Figure 5.4: Changes of the position of the sample/air interface depending on temperature during freezing of the lamellar phase.

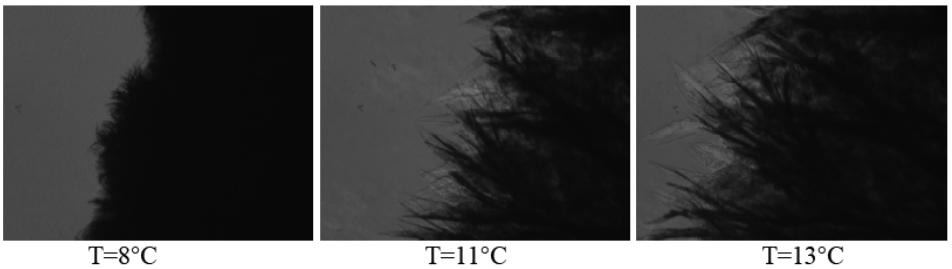

Figure 5.5: The dependence of the size of crystals on transition temperature (image size=1.4x1.0mm^2).

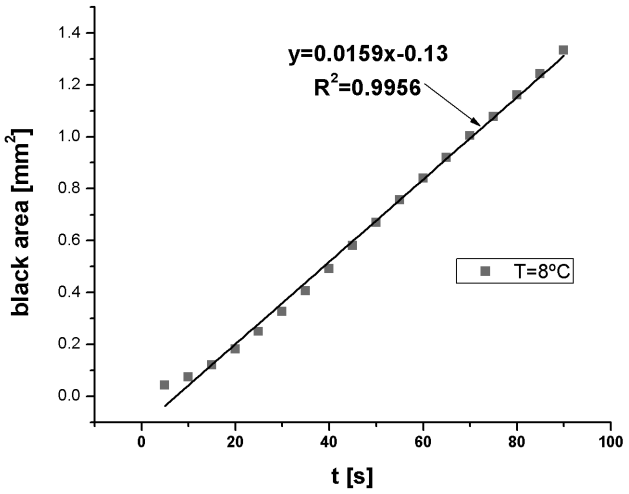

Figure 5.6: Increase in the area occupied by crystals in the pictures during the phase transition at T=8°C.

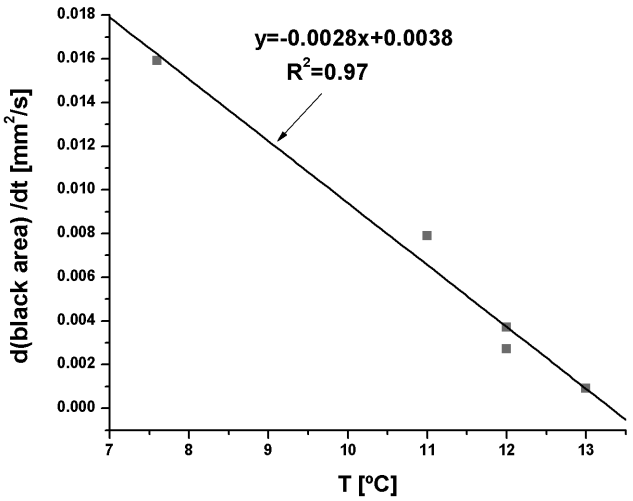

Figure 5.7: The growth speed of the crystalline phase depends on sample temperature.

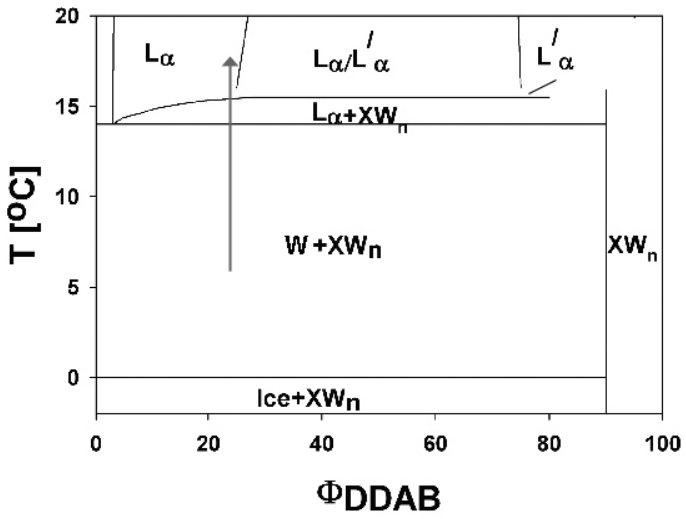

Figure 5.8: Isoplethal path (red) for the study of the W+$XW_n \rightarrow L_\alpha + XW_n \rightarrow L_\alpha$ phase transition.

Therefore, for each temperature, a least-squared fit line can be fitted to the data points to obtain the rate of crystal growth.

Fig.5.7 shows the dependence of this growing speed of the crystalline area on sample temperature. The growing speed is very small for temperatures close to the phase boundary. Furthermore, it should be mentioned that the samples had to be cooled to a lower temperature to start the process for well equilibrated samples in the L_α-phase. Only samples with a 'fresh memory' show phase transitions close to the phase boundary.

In summary, the observed results can, as expected, all be explained within the framework of a nucleation and growth process (see section 2.3.1).

5.3 The non-isothermal phase transition $W+XW_n \rightarrow L_\alpha + XW_n \rightarrow L_\alpha$

5.3.1 The pathway of the transition

In a next step, the melting of the crystals in the XW_n+W coexistence region into the L_α lamellar phase has been investigated using a range of experimental techniques. As can be seen in Fig.5.8, this is predicted to be a non-isothermal phase transition, apart from at the most dilute point of the lamellar phase (≈3%). The transition was investigated along the isoplethal path at ϕ_{DDAB}=25%. The first aim was to confirm

the non-isothermal character of the phase transition (see section 5.3.2):

$$\mathrm{W}+\mathrm{X}W_n \rightarrow L_\alpha+\mathrm{X}W_n \rightarrow L_\alpha$$

Then, the composition and structure of the coexisting phases in the L_α+XW_n coexistence region were identified (see sections 5.3.3 and 5.3.4).

5.3.2 The non-isothermal character

It has been already mentioned in section 4.3.2 that the width of the melting peak observed by DSC increases with increasing surfactant concentration. Furthermore, it can be shown, that the melting of the DDAB crystals to form the lamellar phase can be interrupted at any point during the melting process (see Fig.5.9). Upon stabilising the sample temperature within this region (defined by the peak width (see Fig.4.18)) if the melting process is interrupted, a certain amount of crystals remain. The partly molten sample can then be (partly) refrozen. This clearly indicates that the peak width is not simply due to phase transition kinetics and, that there is not a strict defined melting temperature for all crystals, but that the amount of crystals in the sample decreases slowly with increasing temperature. This confirms the non-isothermal character of the W+XW_n→L_α phase transition as going via a coexistence region of the crystals XW_n dispersed in the L_α-phase.

One has to note that these observed effects are real and have not been caused by the instrument. The melting of ice → water has been investigated in the same way. Once the temperature is stabilised at a temperature within the observed melting peak, the melting continues, as expected, until the whole ice is molten, characteristic of a kinetic limitation to melting.

The same effect can be observed for the samples, when measuring the change in density of DDAB caused by small temperature variations, within this transition region (see Fig.5.10). When investigating the samples with microscopy, a decrease in the number of crystals with increasing temperature can be observed within the range of the investigated phase transition (see Fig.5.11). Once the temperature is stabilised in the sample, the images do not change with time and the number of crystals remain constant, as expected for a non-isothermal phase transition. One should note that, not only the number of crystals changes, but also the appearance of the crystals. The crystal images become less sharp, which might indicate the melting of the crystal at the surface.

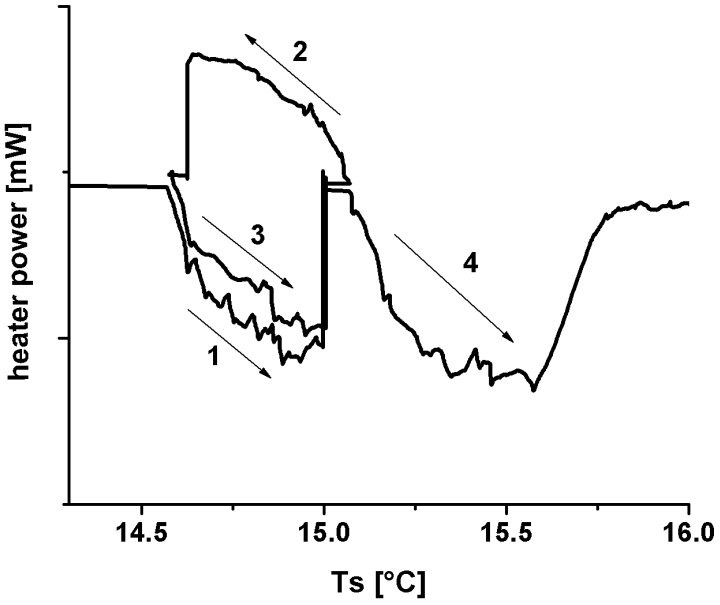

(a)

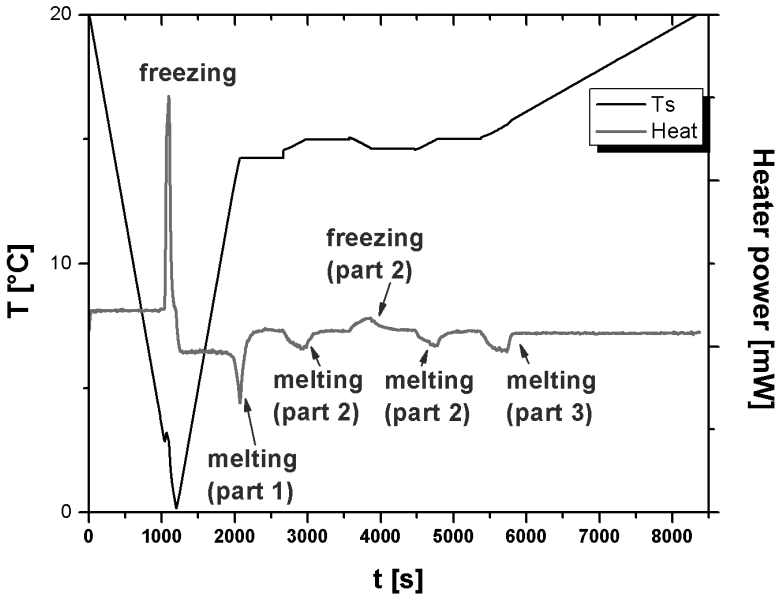

(b)

Figure 5.9: The non-isothermal character of the XW_n+W$\rightarrow L_\alpha$ phase transition shown by DSC. The melting can be interrupted at any temperature on the melting peak and the partly melted sample refrozen. The dependence of the measured heat on sample temperature (a) and time (b) is shown.

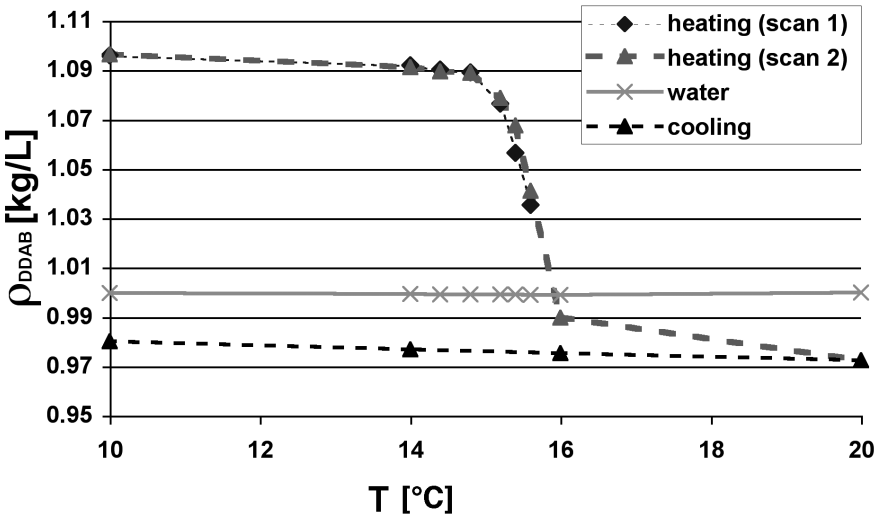

(a)

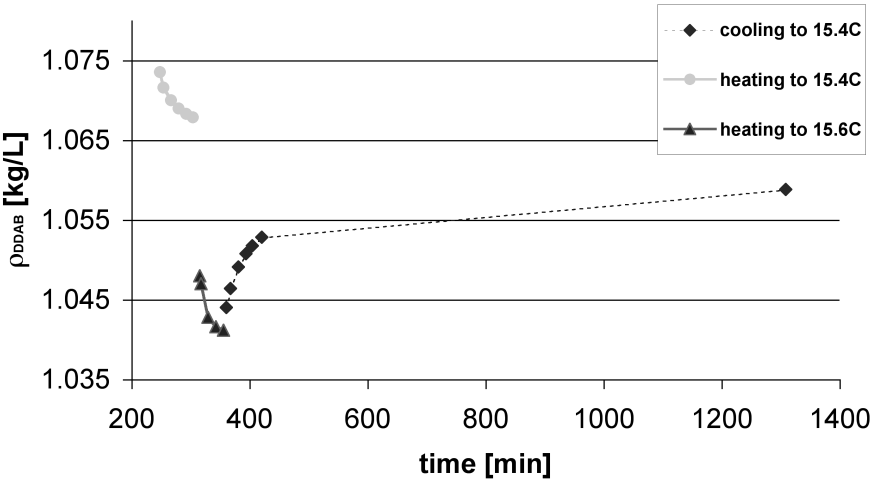

(b)

Figure 5.10: The dependence of the measured density of DDAB on temperature (a). The density can be stabilised at every temperature within the melting transition (b) by halting the temperature change.

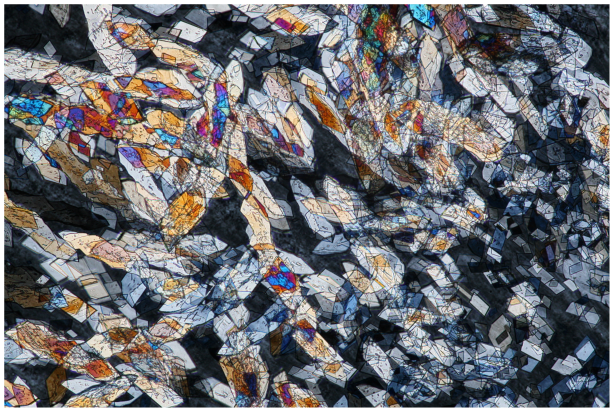

(a) T=14°C

(b) T=15°C

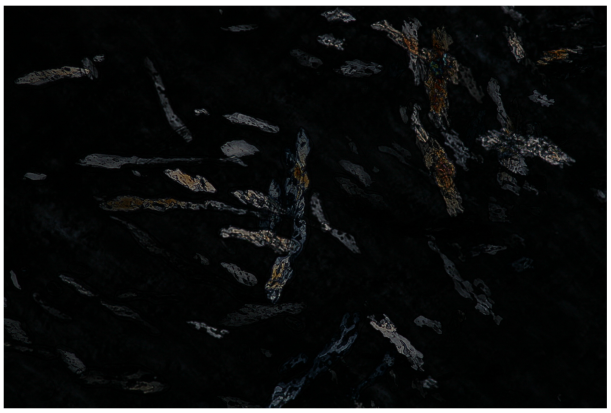

(c) T=16°C

Figure 5.11: Decrease of the relative amount of crystals in the sample upon increasing the temperature observed by polarised microscopy (ϕ_{DDAB}=25%).

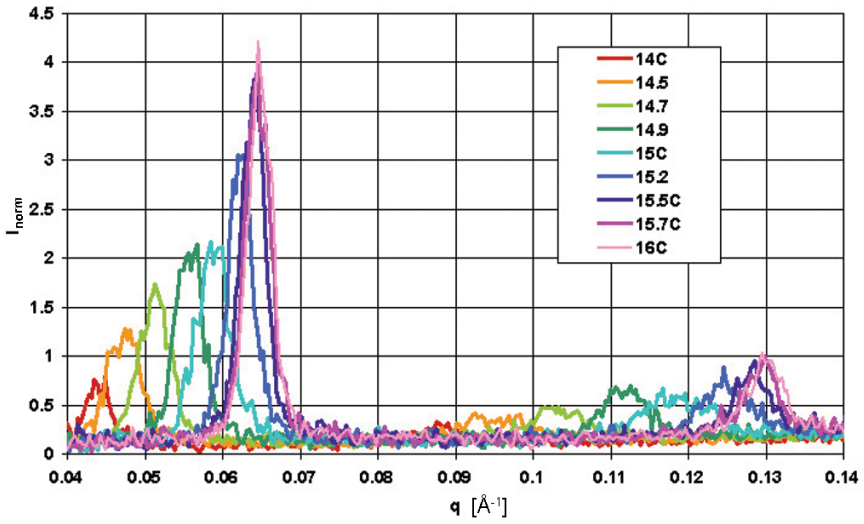

Figure 5.12: SAXS data for different samples in the coexistence region during the melting of the DDAB crystals, showing that the coexisting phase is a lamellar phase.

However, the dependence of composition of the liquid phase on temperature could not be investigated by microscopy because surfactant phases of low concentration appear as isotropic phases under the microscope. SAXS has been used to investigate the phase structure in this narrow coexistence region.

5.3.3 The phase structure in the biphasic region

The phase structure of the sample during the melting process of the DDAB crystals could be obtained from the temperature controlled SAXS measurements. One should note that precise temperature control within the sample was difficult (see section 3.3.3.1), and therefore only a trend with increasing temperature should be deduced from the data. The temperatures in the figure are only given for orientation of the approximated temperature increase.

Once the melting process of the sample starts, a set of Bragg peaks occurs in the SAXS data, similar to the ones obtained during measurements of the swollen L_α phase (see section 4.3.3.1). The repeating distance of the lamellar phase decreases with increasing temperature, as shown by the increase of the q values of the Bragg peaks. This is consistent with the picture of a lamellar phase of increasing surfactant concentration with increasing temperature, caused by the gradual melting of the crystals.

The SAXS data show the same non-isothermal characteristics, which have been reported

in the previous section, i.e. that each of these q values can be maintained by stabilising the temperature during the transition. Therefore, it can be concluded that once the melting process starts, the dilute liquid phase W is replaced by a dilute L_α phase. Upon increasing the temperature slightly, a further degree of crystal melting occurs and the released DDAB molecules increase the concentration of the lamellar phase. These results are in agreement with the predicted new phase diagram in chapter 4 (see Fig.4.34).

The obtained D^* values and their dependence on temperature for the coexisting lamellar phase could be used to derive the position of the L_α/L_α+XW_n phase boundary in the phase diagram. However, the temperature control during the measurements was imprecise which would lead to large errors. New metal cuvettes, which can hold the capillaries used in the SAXS measurements, have been designed of aluminium alloy and are planned to be used in future for this purpose.

5.3.4 The conformational changes within the coexistence region

Furthermore, Raman spectroscopy could be used to follow conformational changes in the sample during the phase transition (see Fig.5.13 and Fig.5.14). It can be seen that the changes corresponding to the C-C stretching modes take place at slightly lower temperatures than the changes in the C-H stretching region. The transition depends on temperature and the surfactant concentration of the sample (see Fig.5.15). For less concentrated samples, the Raman spectrum changes at lower temperature into the spectrum of the L_α phase, and change happens at higher temperature with increasing surfactant concentration (see Fig.5.15). For example, the spectrum of a sample of ϕ_{DDAB}=10% recorded at 15.5°C is similar to the spectra recorded at 16.5°C of the 25% sample.

The transition in the region 2800-3000cm^{-1} can also be seen in the spectra recorded with a Raman microscope (see Fig.5.16). However, the temperatures are slightly shifted, which is caused by the lower accuracy of temperature control. The data are good enough to investigate the homogeneity of the Raman signal within one sample.

As can be seen in Fig.5.17, Fig.5.18, Fig.5.19 and Fig.5.20, within the coexistence region, the sample is not homogeneous. Raman microscopy enables us to focus on several regions in the sample which are characterised by different sample morphology. Some of the regions show the Raman signature of the crystalline phase, whilst at other regions, a coexistence of the signal, corresponding to the L_α and to the crystalline

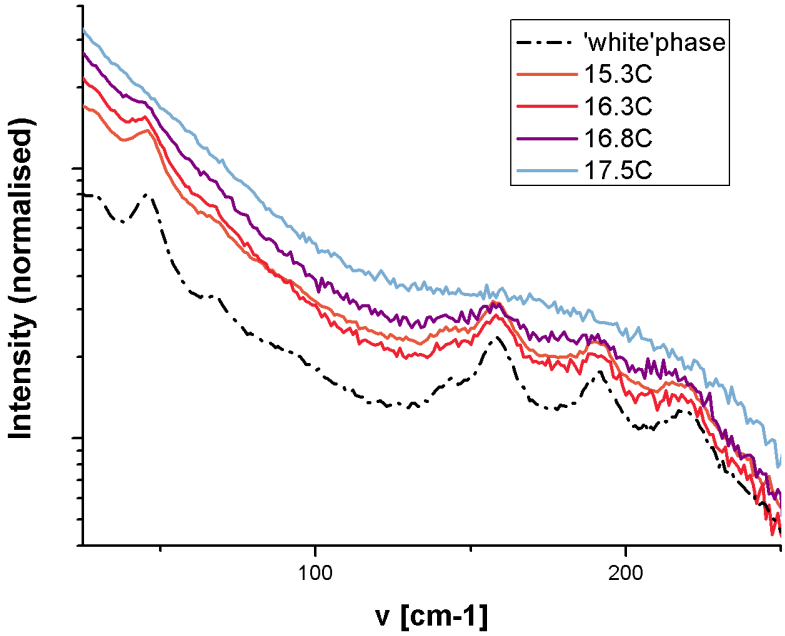

(a)

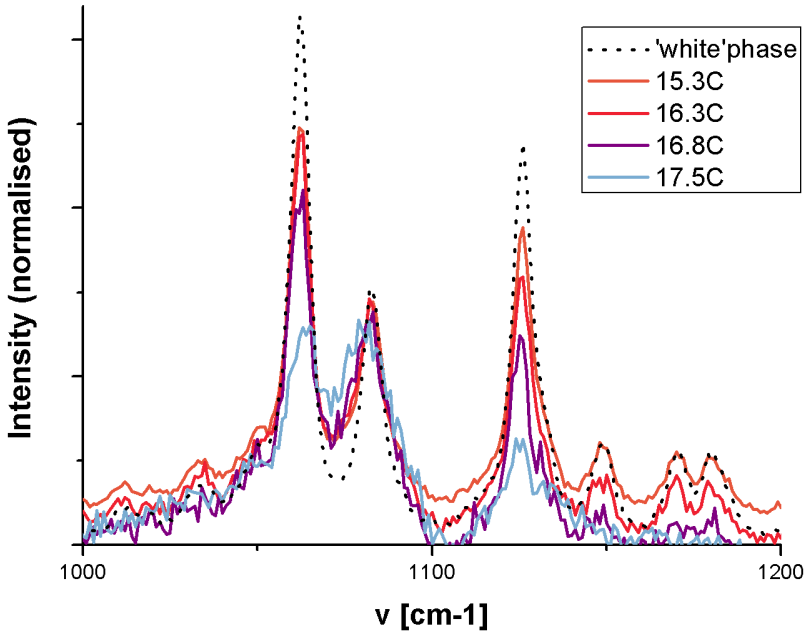

(b)

Figure 5.13: Changes in the Raman spectrum during the non-isothermal phase transition W+$XW_n \rightarrow L_\alpha$+$XW_n \rightarrow L_\alpha$ in the range of LAM frequencies (a) and bands corresponding to the C-C stretching modes (b).

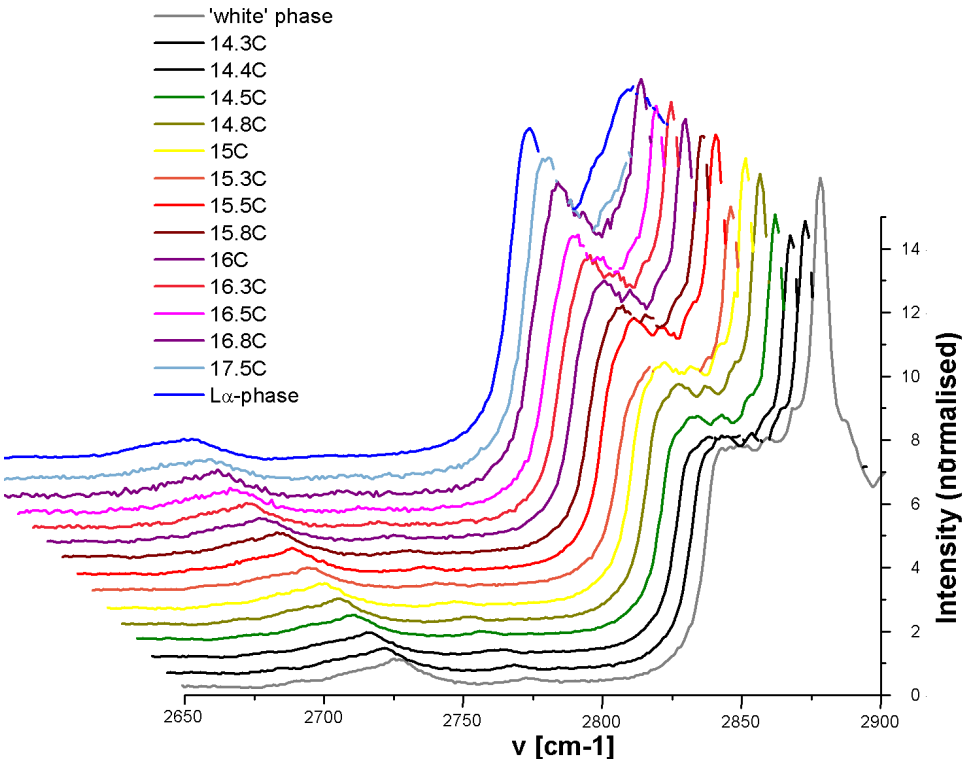

(a)

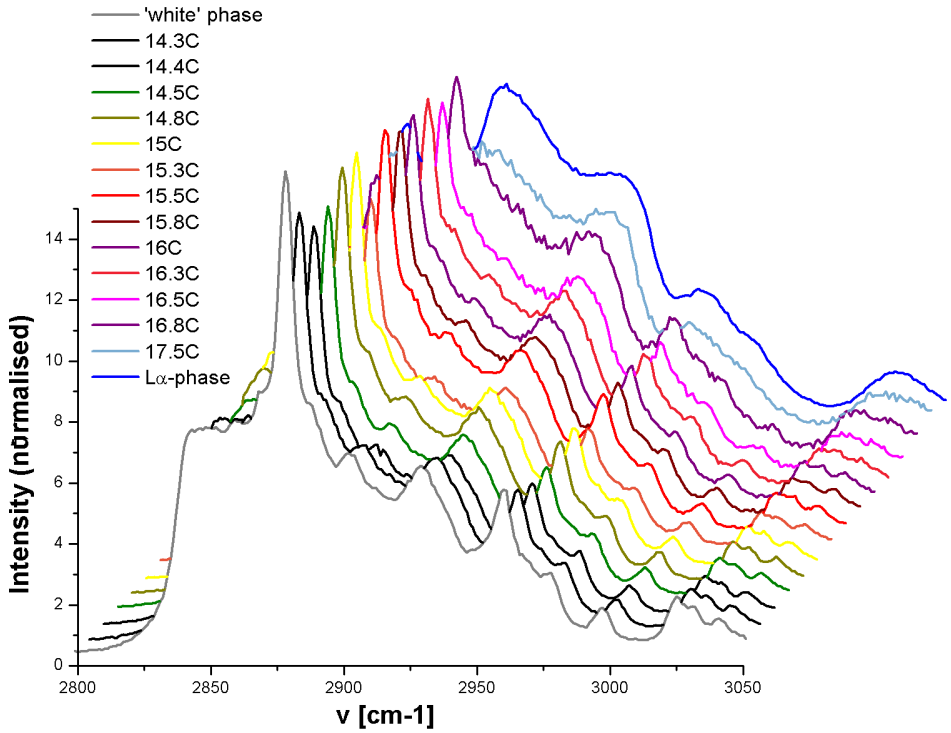

(b)

Figure 5.14: Changes in the Raman spectrum during the non-isothermal phase transition W+$XW_n \rightarrow L_\alpha + XW_n \rightarrow L_\alpha$ in the region characteristic for C-H stretching modes.

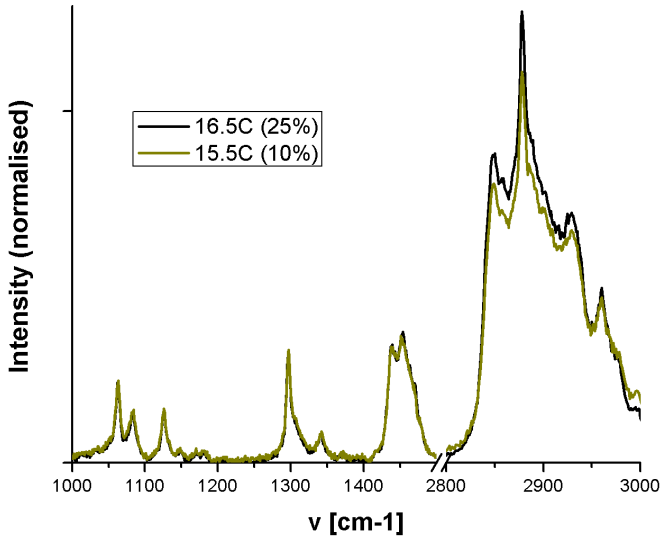

Figure 5.15: Comparison of the spectra of ϕ_{DDAB}=10% at 15.5°C and ϕ_{DDAB}=25% at 16.5°C.

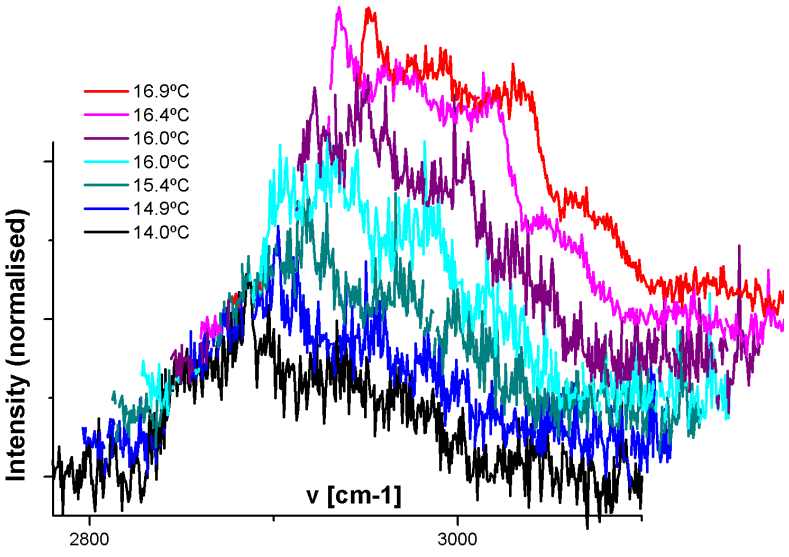

Figure 5.16: Changes in the Raman spectrum of the C-H stretching region during the non-isothermal phase transition W+XW_n→L_α+XW_n→L_α observed with the Raman microscope.

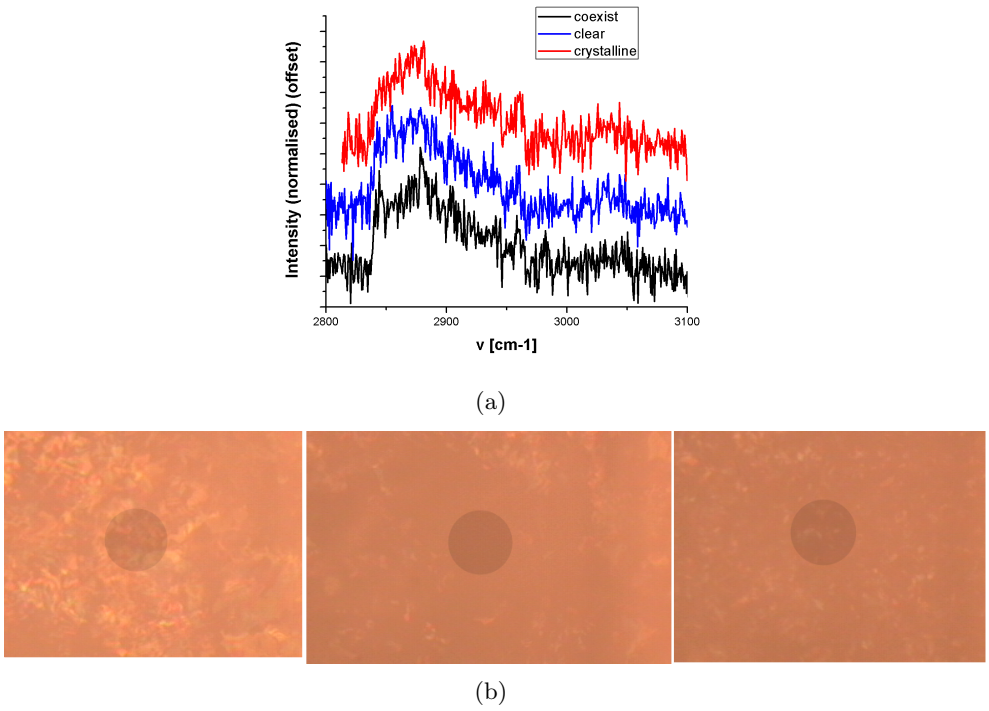

(a)

(b)

Figure 5.17: Raman signal at different regions of the sample at 13.9°C.

phase, has been seen. It should be noted that even regions in which no crystals can be resolved under the microscope did not show the pure signal of the L_α phase until the transition of the whole sample was almost completed (see Fig.5.20). This suggests that even small amounts of crystals, or tiny crystalline patches, are present and have an influence on the measured conformational structure of the apparently lamellar phase areas in the coexistence region.

In the next chapter, it will be shown that these tiny crystalline patches seen by conformational properties influence the dissolution behaviour of the samples (see section 6.2.3).

5.4 Conclusion and future work

In this chapter, the thermal phase transition along the isoplethal path, for a surfactant concentration of ϕ_{DDAB}=25%, has been studied. The results can be explained in terms of the new phase diagram proposed in the previous chapter. The coexistence region of the crystalline phase XW_n with the swollen lamellar phase L_α has been confirmed.

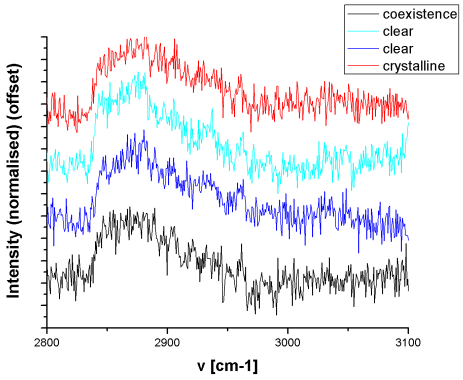

(a)

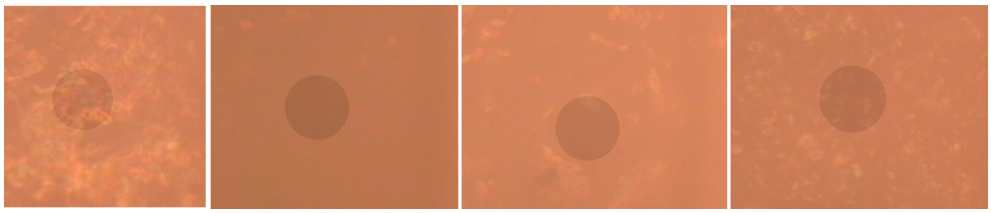

(b)

Figure 5.18: Raman signal at different regions of the sample at 14.9°C.

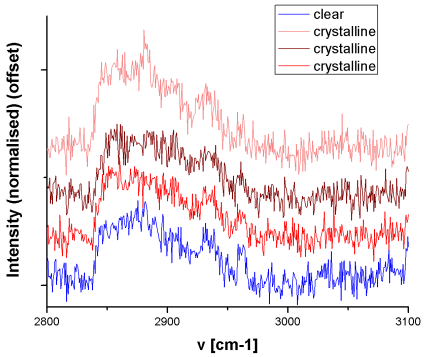

(a)

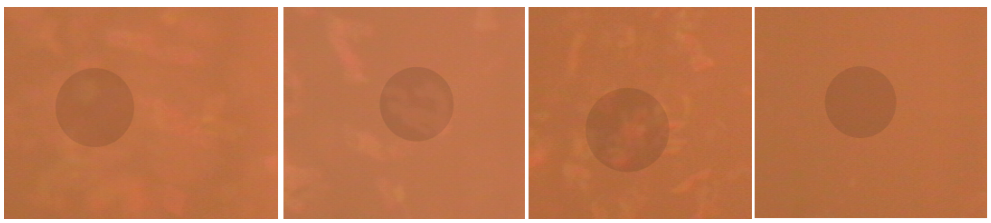

(b)

Figure 5.19: Raman signal at different regions of the sample at 15.5°C.

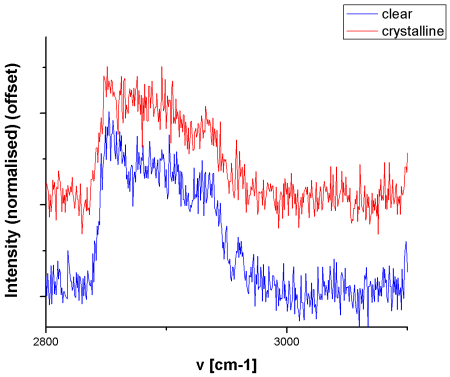

(a)

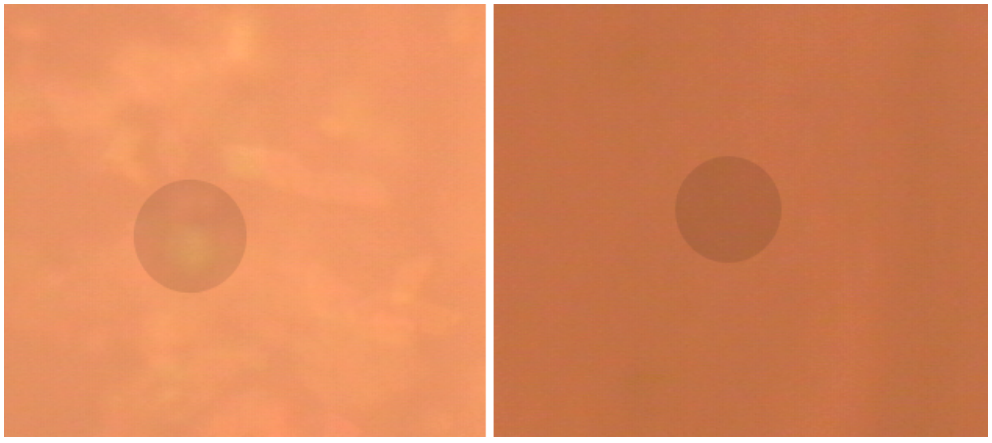

(b)

Figure 5.20: Raman signal at different regions of the sample at 15.9°C.

The structure of the L_α phase in this coexistence region was obtained by SAXS. In future with more accurate measurements, this method can be used to obtain the precise position of the $L_\alpha/L_\alpha+XW_n$ phase boundary in the phase diagram.

Chapter 6

Dissolution of the lamellar phases formed by DDAB

6.1 Introduction

In the last two chapters, a detailed study of the equilibrium phase behaviour of the binary DDAB-water system, as well as of the phase transformations along particular isoplethal paths have been presented. Next the kinetics and mechanism of dissolution caused by a change in concentration were investigated. This study focuses on the dissolution of the lamellar phase, which has been of great interest over the past two decades [Buchanan 00, Mark 03, Leng 06, Miller 93].

After contact with water, lamellar phases (L_α) can show spectacular instabilities: multibilayer tubules (so-called myelins) grow from the L_α/water interface into the water. These cylindrical interface instabilities have already been described in section 2.3.3. They grow when water penetrates a sample of a concentrated surfactant solution, which has in its phase diagram a sufficient coexistence region of lamellar phase with water at low concentration [Buchanan 00, Buchanan 99]. Therefore, myelin formation can be observed for lamellar phases formed from DDAB (see Fig.6.1).

As already discussed in section 2.3.2, the dissolution of the flexible lamellar phase to form myelins is described by the Leng-model, which considers the process to be governed by the interplay of the osmotic pressure difference between the lamellar phase and the surrounding water and the mobility of water between the bilayers. The complex phase behaviour of DDAB, especially the formation of two lamellar phases with different characteristics (the L_α and L'_α phases) over a wide range of the phase diagram (from about 3% to almost 90% surfactant mass concentration), allows a detailed study of the dependence of myelin formation on the properties of this initial lamellar phase (see section 6.2).

Figure 6.1: Typical image of myelin figures observed during the dissolution of lamellar phases formed by DDAB (image size 1.5x2.2mm).

The bilayers in the lamellar phase, as well as in the myelinic figures, are characterized by a marked fluidity, but also a low permeability [Vogel-Weill 91, Gruger 94, Arunagirinathan 04, Haran 02, Neuzil 81, Degkwitz 38, Sandermann 77]. The addition of molecules which increase the permeability of water [Haran 02] or hinder molecular movement within the sheets [Neuzil 81, Degkwitz 38], suppresses myelin formation, as does the freezing of the bilayers by lowering the temperature (e.g. into the L_β phase). In this context, it is worth mentioning that, not only is the mobility of bilayers neglected in the Leng-model describing the myelinic growth kinetics, but also the myelinic tubules are added only as a geometric factor.

This opens the possibility of the following experiment: a comparison of the dissolution kinetics of lamellar phases forming myelins and those lamellar phases which do not form myelins. Ideally this would be done for the same surfactant system, and for lamellar phases of comparable properties with regards to e.g. the osmotic pressure behaviour and the water layer thicknesses. If both dissolution processes can be described with the Leng-model using only geometrical factors at the interface, the occurrence of myelins could be assumed to not influence their dissolution kinetics.

The previously reported phase diagram of the binary DDAB/water system as shown in section 3.2.1.1 describes a system ideally suited for the comparison of the dissolution of the L_α phase (myelins are formed) and the L_β phase (myelin formation is suppressed).

However, in the last two chapters a detailed study of the equilibrium phase behaviour of DDAB at low temperatures and the influence of temperature changes has been presented, resulting in the hypothesis of a new phase diagram. In this diagram, the

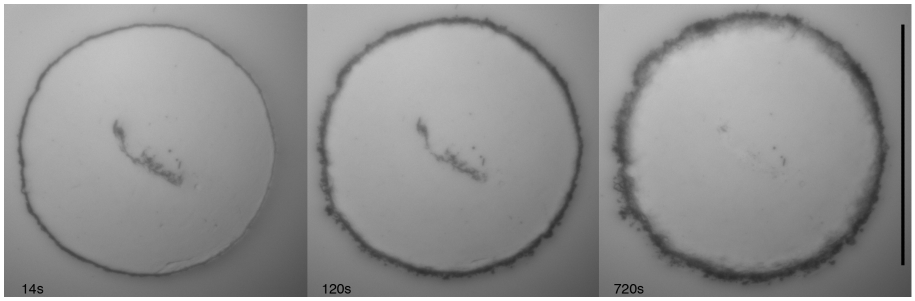

Figure 6.2: A typical time series for a dissolution experiment of a droplet of lamellar phase of DDAB (ϕ_{DDAB}=20%, T=20°C) observed with the direct observation setup (scale bar=1cm, S=0.000081mm^2/s).

previously stated L_β phase has been replaced by a coexistence region of crystals with water and a dilute lamellar phase, at temperatures below 14°C and between 14°C and 16°C, respectively. Therefore, this planned series of experiments could not been carried out.

But, to our surprise, we also observed no myelin formation in this system during the dissolution of lamellar phase in coexistence with a sufficient amount of DDAB crystals, though this is still in the L_α-phase (see section 6.2.3). To investigate this behaviour in more detail, better control of the composition of the lamellar phase within the coexistence region was required, which is in the case of the binary DDAB/water system mostly limited by the narrow temperature range of the coexistence region (about 2°C). Therefore, we considered the use of a ternary surfactant system: DDAB/DODAB/water. The phase behaviour of DODAB, differing from DDAB only by its longer hydrocarbon chains, has been discussed in section 3.2.1.2. In summary, both phase diagrams follow the same order of phases, only the phases are shifted to higher temperatures and higher concentration in the case of the DODAB/water system. In the ternary system at room temperature, a coexistence of lamellar phase (mostly DDAB) in coexistence with crystals (mostly DODAB) is formed over a large concentration range (see section 3.2.1.2 and 6.3.2).

6.2 Myelin kinetics during the dissolution process of the L_α-phase of DDAB

Myelin kinetics were investigated using dissolution experiments described in section 3.3.4.2. Once a droplet of concentrated lamellar phase was brought into contact with water, the droplet swells (see Fig.6.2) and myelin formation can be observed. The swelling is, in general, homogeneous in all directions, and therefore the edge of a round

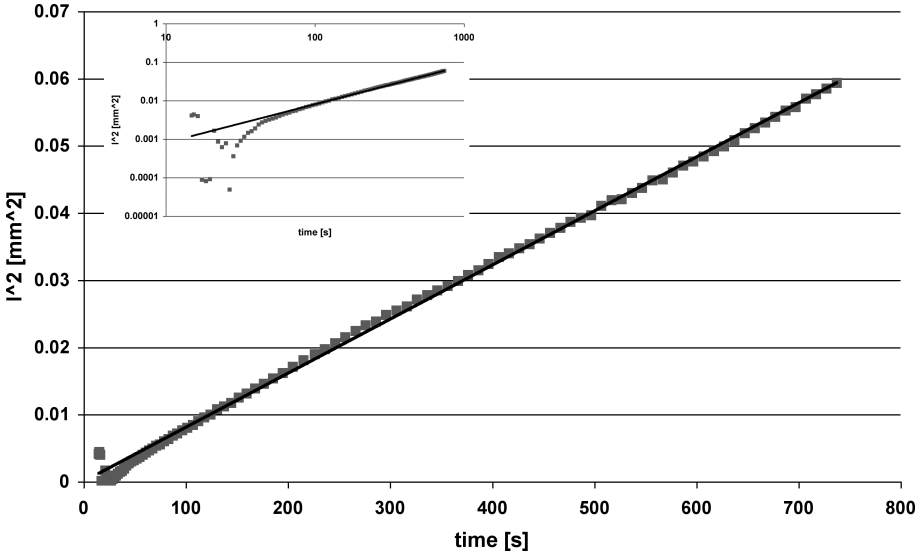

Figure 6.3: Typical dependence of the swelling length l on time t (see Fig.6.2, $\phi_{DDAB} = 20\%; T = 20°C$). The solid line shows the least-squares fit to Eq.6.1.

droplet can be fitted with a circle as suggested in section 3.3.4.2 and A.1.3.2 and the myelin length can be calculated using Eq.3.40 to give the swelling length of the droplet.

For samples of low concentration, the interface between the water and the surfactant phase was almost invisible due to a low refractive index difference and poor contrast. Most of these pictures had to be analysed manually giving a relatively large error. Furthermore, the determination of the initial droplet size, the parameter R_0, was difficult, because the introduction of water between the glass slides lead to a reduction in the separation between the glass slides for these samples.

The increase in the droplet size, characterised by the swelling length *l(t)* (see Eq.3.40), as a function of time, is shown in Fig.6.3. In particular, the inset log-log plot clearly indicates a $l(t) \sim t^{1/2}$ behaviour; the solid lines represent such a fit. A $t^{1/2}$ dependence is characteristic of a diffusive process. This dependence has been observed independent of temperature and initial surfactant concentration of the sample.

This suggests that the length dependence can be analysed using the following equation:

$$l + l_0 = \sqrt{S(t + t_0)}, \tag{6.1}$$

where S is the swelling coefficient and t_0, l_0 take into account the effects of limited temporal and spatial resolution. Typically, values of l_0<20μm were found. However,

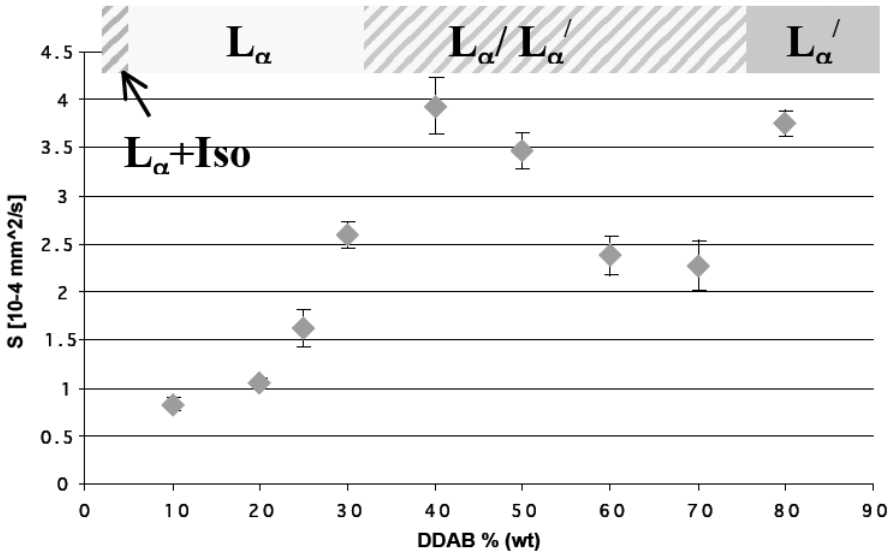

Figure 6.4: Swelling rate S versus initial surfactant concentration ϕ_{DDAB} at $20°C$.

Fig.6.3 shows that the data points at the beginning of the scan are highly scattered. The poor data quality at the start of the swelling process does not allow one to tell if this scattering is caused by the initial swelling behaviour (a prediffusive regime). After a few seconds, a stable diffusive regime has been observed, which will be analysed in the following sections.

6.2.1 Dependence of the swelling rate on surfactant concentration

The swelling behaviour of the lamellar phase formed by DDAB has been investigated for temperatures between $12°C$ and $26°C$ over the range of ϕ_{DDAB}=10-80% of surfactant concentration. The dependence on surfactant concentration for T=$20°C$ is shown in Fig.6.4. The observed dependence was found to be similar for all temperatures; only the swelling coefficients were shifted towards higher or lower values (at increasing or decreasing temperatures, respectively). The $20°C$ values were chosen to represent the concentration dependence, because the literature osmotic pressure data was obtained at this temperature and these can be used for comparison with the theoretical model introduced in section 2.3.2. At the top of Fig.6.4, a sketch of the phase diagram shows that the lamellar phase at room temperature consists of pure swollen lamellae up to $\phi_{DDAB}\approx$28% and pure collapsed lamellae above $\phi_{DDAB}\approx$75%. For the coexistence region, additional considerations in the theoretical calculation are needed. Therefore the next section will focus on the swollen lamellar phase (see section 6.2.1.1), after which a detailed discussion for higher surfactant concentrations will be given (see section 6.2.1.3).

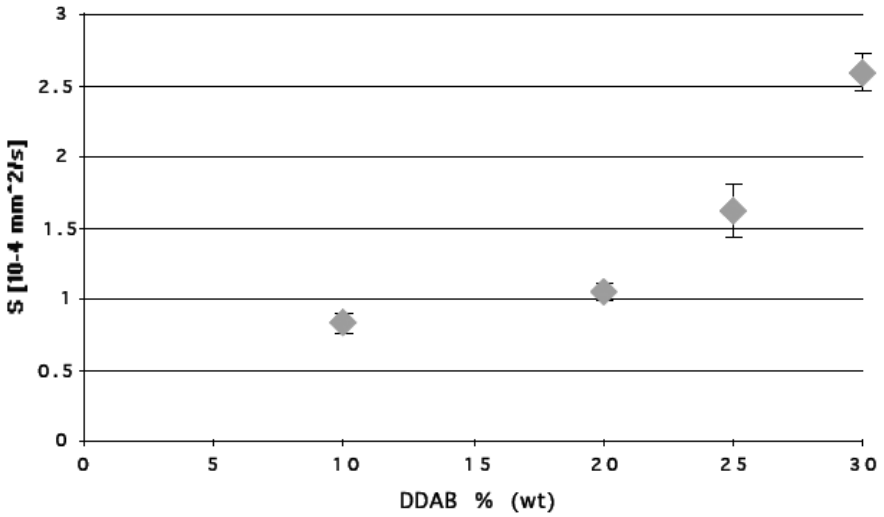

Figure 6.5: Swelling rate S of DDAB forming a swollen lamellar phase at 20°C.

6.2.1.1 Dissolution of swollen L_α-phase ($\phi_{DDAB} < 28\%$)

As shown in Fig.6.5, a slow increase of the swelling coefficient with increasing surfactant concentration can be observed. It has to be mentioned that samples with $\phi_{DDAB} \leq 10\%$ were difficult to analyse. This is partly due to the increased probability of finding vesicles in the sample, which drift away, after the sample is contacted with water, with a similar speed (or slightly higher) as the sample swelling rate. Furthermore the sample edge was easily destroyed while contacting the droplet with water, which causes patches of lamellar phase to flow away, making the interface difficult to detect.

The swelling behaviour of the swollen lamellar phase could be described using the model discussed in section 2.3.2. It assumes that the driving force is the osmotic pressure difference, whereas the decreasing water layer thickness (going to higher concentrations) limits the water mobility and thus the swelling speed. The osmotic pressure data derived from the plot available in the literature [Dubois 98] was fitted for surfactant concentrations below 30% and T=20°C using the following equation (see Fig.6.6):

$$\log \Pi = -2.85(\log a_w)^4 - 24.1(\log a_w)^3 - 76.3(\log a_w)^2 + 105(\log a_w)^4 - 47.0 \quad (6.2)$$

It was reported that no analytical equation fitted the data properly, and numerical calculations were needed, however the quality of the fit was sufficient for the calculations performed in this section, as only the shape and order of magnitude of the calculated values were used for comparison. It should be mentioned that the osmotic pressure for composition of e.g. ϕ_{DDAB}=2.8% would be expected to be close to zero, as a coexistence

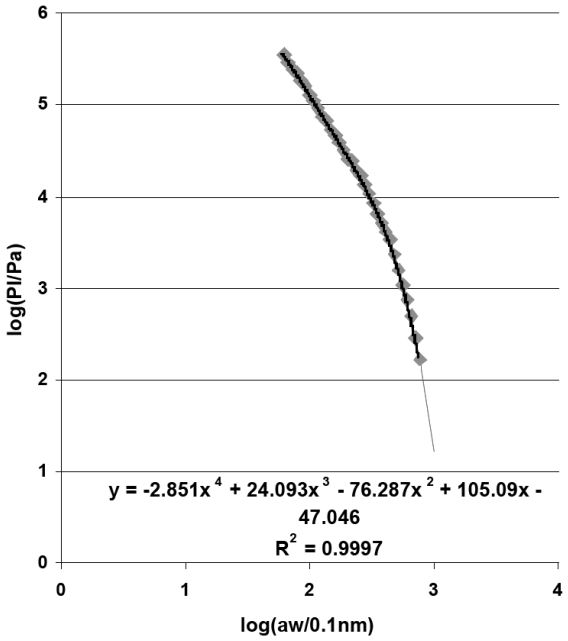

Figure 6.6: Fit of the osmotic pressure data presented in [Dubois 98].

of a solution close to pure water and lamellar phase is observed upon further dilution. However, the above equation, as well as the data in the literature, do not show this behaviour. Nevertheless, using this osmotic pressure data and based on our model using Eq.2.27 and Eq.2.28 with small modifications, a prediction for the interdiffusion coefficient D can be obtained:

$$a_w = \frac{\phi_w}{\phi_{DDAB}}\delta = \frac{1-\phi_{DDAB}}{\phi_{DDAB}}\delta \tag{6.3}$$

$$\xi_w = \frac{(a_w)^2}{12\eta} \tag{6.4}$$

$$D = \phi_w^2 \xi_w \frac{\partial \Pi}{\partial \phi_w} = \phi_w^2 \xi_w \frac{\partial \Pi}{\partial a_w}\frac{\partial a_w}{\partial \phi_w} = \frac{1-\phi_{DDAB}}{\phi_{DDAB}}\frac{(a_w)^2}{12\eta}\delta\frac{\partial \Pi}{\partial a_w}, \tag{6.5}$$

where ϕ_{DDAB} is the surfactant concentration given as a weight or volume fraction (their values differ less than 1% for temperatures above $16°C$ as $\rho_{DDAB} = 0.98kg/l$) and δ=24Å [Dubois 91].

The calculated dependence of the interdiffusion coefficient D on surfactant concentration is presented in Fig.6.7. The coefficient describes the diffusion of water between the lamellar sheet according to the osmotic pressure and the water mobility assuming a poiseuille flow between the bilayers. The influence of a constant hydration layer or

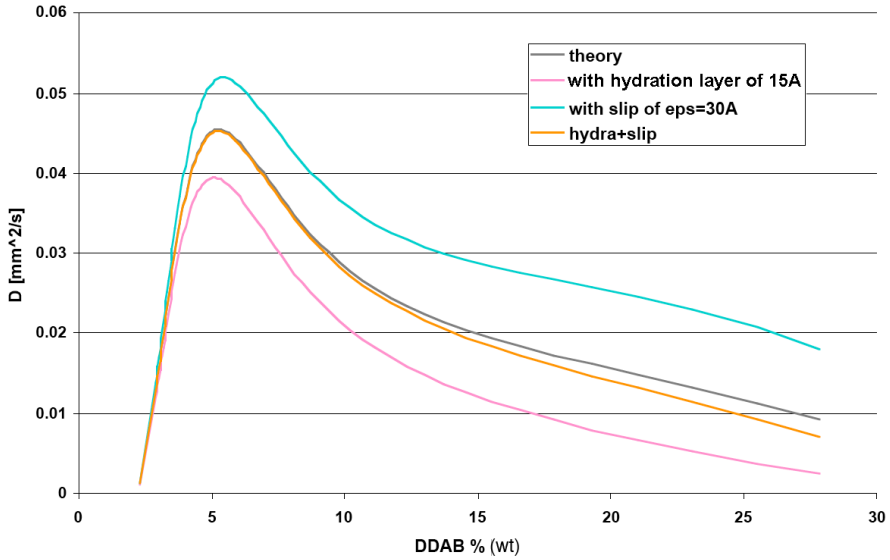

Figure 6.7: Interdiffusion coefficient of DDAB calculated using Eq.6.3, 6.4 and 6.5 with no hydration layer, with hydration layer of thickness of 15Å, with ϵ=30Å and with both.

slip is also shown in Fig.6.7. As the water layers are relatively thick, the hydration layer thickness does not have a big influence. Also the flow at the boundary has to be assumed to be very large to show an influence on the interdiffusion coefficient.

The swelling rate S has been calculated for the three different flow-types:

$$S = \left(\frac{2\Delta\phi_w}{\phi_{fs}}\right)^2 \frac{D}{\pi} \tag{6.6}$$

Fig.6.8 shows the measured values compared to the calculated swelling coefficients. The measured values are of the same order of magnitude but lower than the theoretical ones as is the increase with increasing surfactant concentration. Comparing the form of the obtained data, the introduction of a hydration layer does not lead to a better quality of fit. In contrast, the form of the experimental data is closer to that calculated when adding slip at the surface. However, this leads also to an increase in the swelling coefficients, making them about an order of magnitude too high.

The exact comparison of the model with experimental data would require a better control of the properties of the lamellar phase in the sample. The influence of the vesicles in the lamellar phase are discussed in the next section. Furthermore, an increase of contrast in the images would be necessary to obtain better statistics. For this, a

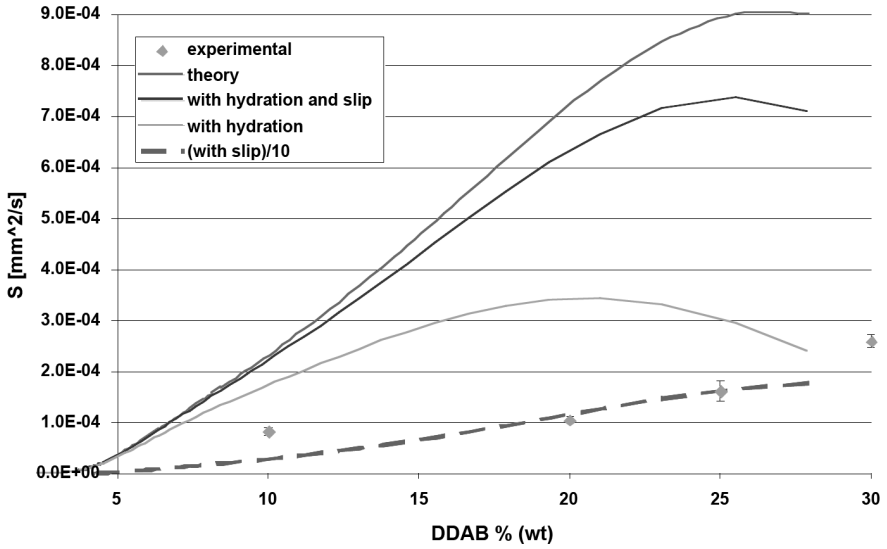

Figure 6.8: Swelling rate S versus surfactant concentration ϕ_{DDAB} for T=20°C. The solid (and dashed) lines show theoretical calculation for T=20°C.

method of introducing water to the system without disrupting the droplet interface would be of great use. In the conclusion of this chapter, a method to obtain a less disrupted interface is proposed.

6.2.1.2 The influence of vesicles on the swelling behaviour

As already mentioned, the occurrence of vesicles in the lamellar phase influences the dissolution behaviour of the droplet. The almost spontaneous formation of vesicles is well known for this system, especially at lower surfactant concentration (see section 3.2.1.1).

Preparation of samples in which no vesicles could be found has not been achieved. This might be explained by the shear induced formation of vesicles, as has been reported in [Bergmeier 97]. Just by using a pipette to place a droplet on a glass slide, the sample is exposed to an external shear. This increases the possibility of finding vesicles in the sample. A microscopic image of the typical texture of a samples in the swollen lamellar phase is shown in Fig.6.9(a).

Furthermore, the exposure of the sample to mechanical vibrations as well as to temperature changes also led to an increase in vesicle number. Especially after several transitions of the sample into its low-temperature crystalline phase vesicle formation was observed. These observations are also known for other systems [Heimburg 03].

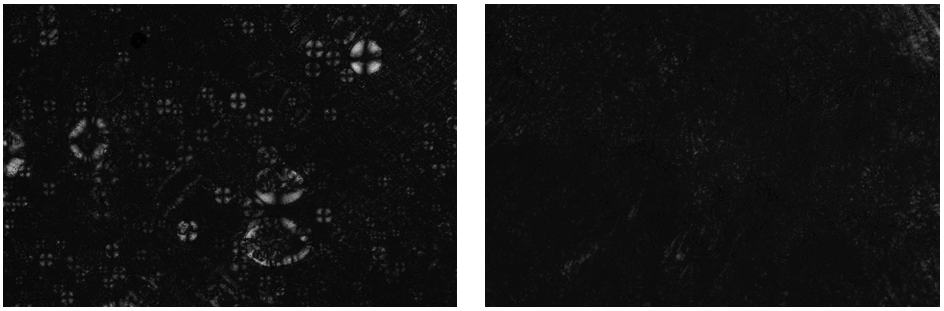

(a) (b)

Figure 6.9: Typical texture of the lamellar phase in samples exposed to temperature changes and shearing, ϕ_{DDAB}<30% (a) ϕ_{DDAB}>30% (b) observed under crossed polarisers. In the swollen lamellar phase a high number of vesicles can be found in the sample (image size 1.5x2.2mm).

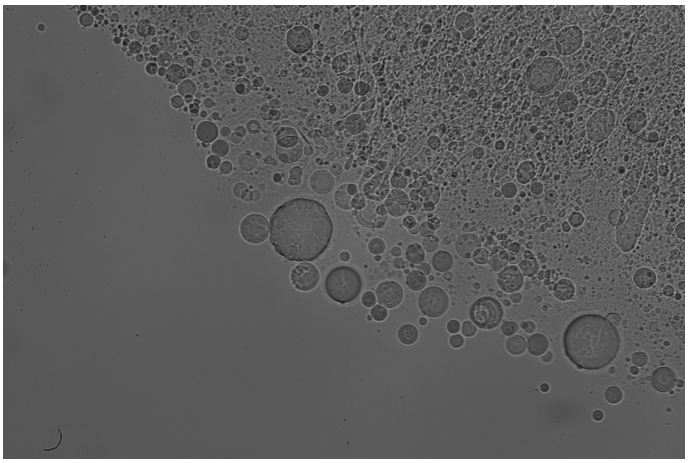

Figure 6.10: Typical image of the sample interface during the dissolution of a vesicle rich phase (image size 1.5x2.2mm).

It has already been observed that myelin formation can be suppressed by the occurrence of a great number of vesicles in the sample [Buchanan 99]. Instead of a forest of myelinic figures, the interface of a vesicle rich lamellar phase during the dissolution process is characterised by vesicles diffusing into the water (see Fig.6.10).

In the theoretical model, an ideally uniform interface consisting of a dense myelinic forest is assumed. This is mathematically expressed in the value of the concentration of the fully swollen lamellar phase leaving the sample ϕ_{fs}. The value of this concentration has been measured for the $C_{12}E_3$/water system [Buchanan 99] and is close to the value of close-packed cylinders $\phi_{fs} \approx 0.9$.

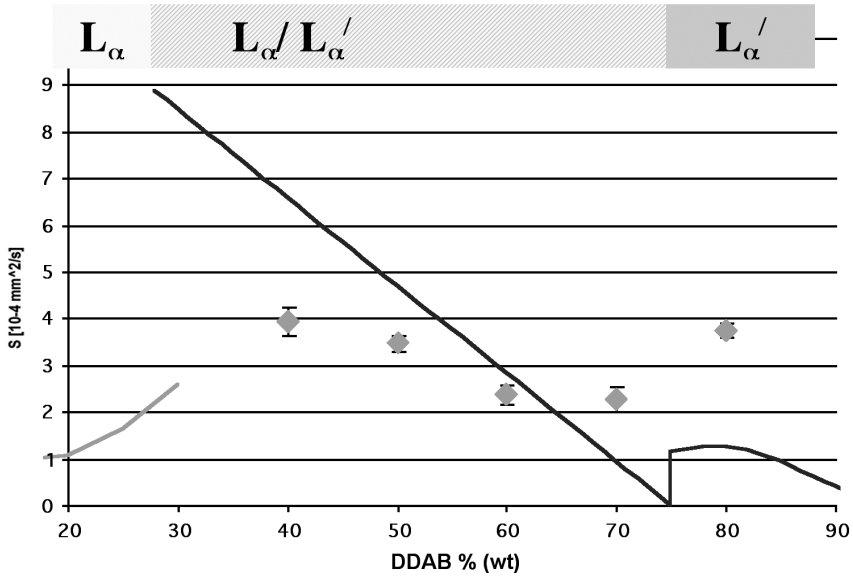

Figure 6.11: Swelling rate S for surfactant concentration ϕ_{DDAB} above ϕ_{DDAB}=28% at 20°C compared to theory (black solid line).

In the case of the more loose myelin forest, this estimation is not valid. The deviation relation from these theoretical assumptions can give a possible explanation for the low quality of the fit. However, the model still gives a reasonable estimate of dissolution rates.

6.2.1.3 Dissolution of the collapsed L'_α-phase ($\phi_{DDAB} > 28\%$)

For surfactant concentrations between ϕ_{DDAB}≈28% and ϕ_{DDAB}≈75%, two lamellar phases (L'_α and L_α) coexist (see section 3.2.1.1), which correspond to water layer thicknesses of a_w=61Åand a_w=6Å. The osmotic pressure in this region is constant and its value is $\Pi(T \approx 20°C)$=4 $10^5 Pa$ [Dubois 98]. For higher surfactant concentrations, the osmotic pressure increases exponentially. At T=20°C we obtain approximately [Dubois 98]:

$$\Pi = 10^9 \exp(-a_w/1.9\text{Å})$$

One should note that no vesicles have been observed in the collapsed lamellar phase, as previously reported by [Karukstis 03].

The measured swelling rates, along with their theoretical predictions, are presented in Fig.6.11. The swelling rate slows down with increasing surfactant concentration in this coexistence region. Two factors have to be considered: the osmotic pressure and the mobility. The osmotic pressure is constant but the mobility decreases with

increasing surfactant concentration, as the fraction of collapsed lamellae increases and thus the average mobility goes down. With this, one can calculate the average swelling rate

$$\langle S\rangle = xS(\phi_{DDAB} = 28\%) + (1-x)S(\phi_{DDAB} = 75\%) \approx xS(\phi_{DDAB} = 28\%) \quad (6.7)$$

taking into account that the swelling rate of the collapsed lamellar phase is about 1000x slower than at ϕ_{DDAB}=28%. The osmotic pressure derivative at ϕ_{DDAB}=28% surfactant concentration is approximated to the derivative on the right-hand side of the discontinuity shown in Fig.3.5 and Fig.6.6:

$$\frac{\partial \Pi}{\partial a_w} \overset{a_w \to 61\text{Å}}{\longrightarrow} 10^{4.2} Pa/\text{Å} \quad (6.8)$$

and

$$x = \frac{0.75 - \phi_{DDAB}}{0.47} \quad (6.9)$$

The presented theory depends highly on precise osmotic pressure data. Because of this, only a comparison of the shapes will be given. The almost linear decrease of the swelling rate in the coexistence region seems to be in good agreement with theory (the line in Fig.6.11). Also, the observed increase in S upon entering the region of collapsed lamellae is predicted by the theory.

The size of the error bars in the data can be explained by the following observations: in the coexistence region it is difficult to obtain a droplet of the right proportions of collapsed and swollen lamellae, as the sample has a heterogeneous appearance. Furthermore, the collapsed lamellar phase is relatively viscous, thus the properties of the lamellar phase are affected by the amount of squeezing of the sample, as has been observed by Leng et al. in [Leng 06] for the lecithin/water system.

6.2.1.4 The dependence of the swelling of pure lamellar phases on temperature

As mentioned earlier, the swelling rates depend, not only on initial surfactant concentration, but also on temperature. The temperature dependence of the swelling rate is similar for different surfactant concentration and different lamellar phases (see Fig.6.12). A slight decrease of the swelling coefficient with decreasing temperature could be observed. It is interesting that the type of lamellar phase does not greatly influence this temperature dependence, confirming that the shape of the concentration dependence discussed in the previous section is also maintained at the remaining

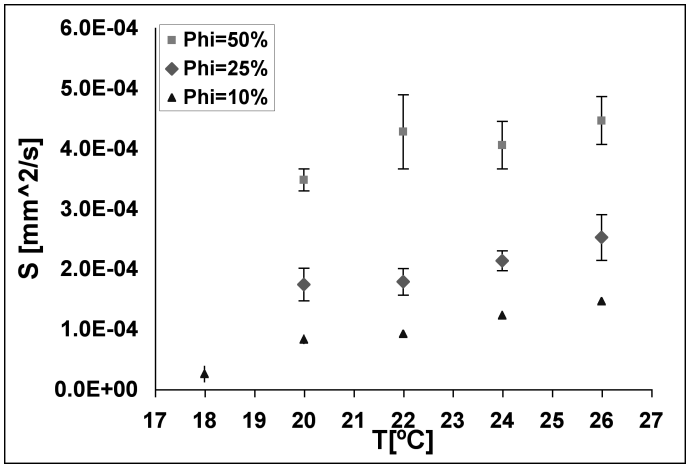

Figure 6.12: Swelling rate S for surfactant concentration ϕ_{DDAB} of 25% depending on temperature. Note the data points below 16°C have been obtained by studying overcooled L_α-phase.

temperatures in the L_α phase.

The temperature dependence, could be caused by the changes in sample morphology shown in Fig.6.13. At lower temperatures, the texture in the droplet becomes more defined. This is accompanied by a more complicated interface morphology with decreasing temperature, as shown in Fig.6.14.

The strong texture seems to suggest stable patches of bilayers, which rather tend to swell as a whole or break away from the sample than form myelin figures. Therefore a decrease in the number of myelins at the interface with decreasing temperature can be observed.

6.2.2 Properties of the myelinic figures formed during the dissolution of pure lamellar phase

The myelinic figures, which were observed during the dissolution of DDAB, were comparably unstable, especially for dilute samples, samples containing a large number of vesicles and samples at low temperatures. The influence of temperature on myelin formation has been discussed already in the previous section. As can be seen in Fig.6.14, the shape of the myelins get less defined when going to lower temperatures, often being replaced by unchanged patches of textured lamellar phase. Also for temperatures below the transition temperature to the crystalline phase, and therefore in the overcooled L_α phase region, myelins can be observed. In this respect, no differences between the L_α phase and the overcooled L_α phase can be found. This is in contrast to the L_α phase

(a) T=13°C

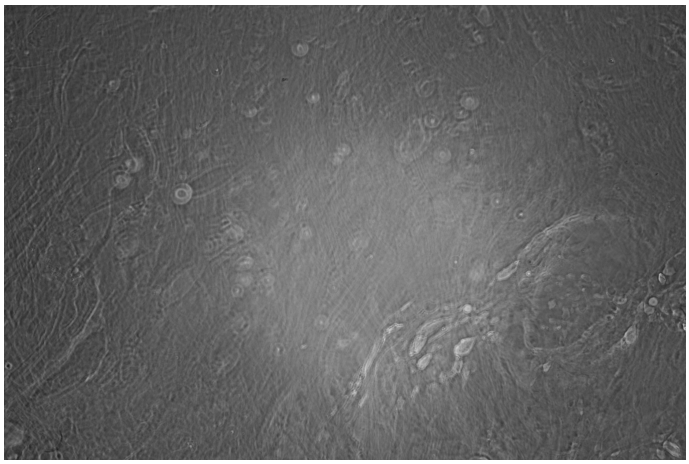

(b) T=18°C

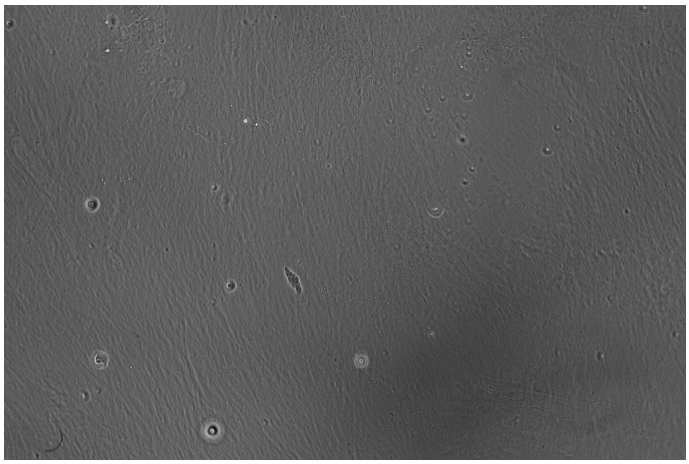

(c) T=20°C

Figure 6.13: The influence of lowering the temperature on the texture of the lamellar phase (image size 1.5x2.2mm, ϕ_{DDAB}=25%).

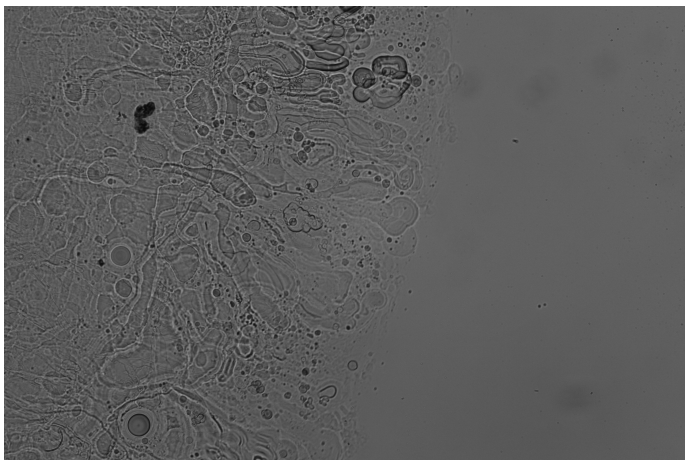

(a) T=13°C

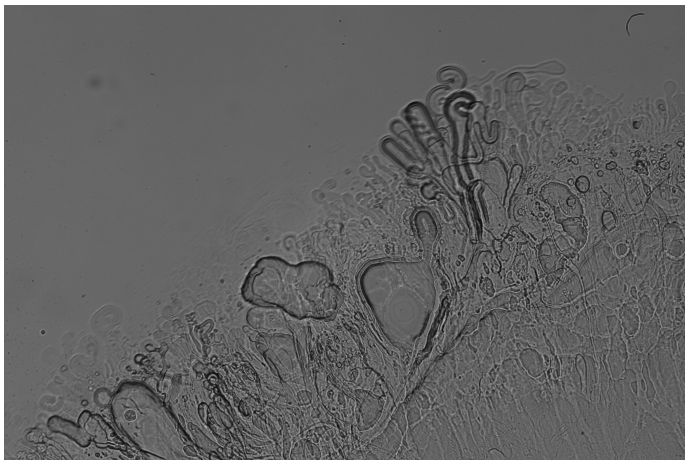

(b) T=18°C

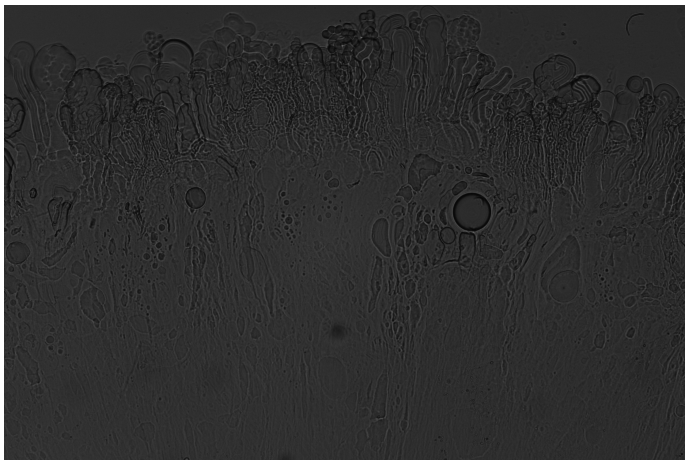

(c) T=20°C

Figure 6.14: The influence of lowering the temperature on the interface morphology of the droplet (image size 1.5x2.2mm, ϕ_{DDAB}=25%).

in coexistence with the crystalline phase, in the narrow temperature gap of 14-16°C in the equilibrium phase diagram (see Fig.4.34). The suppression of myelin formation in samples in this coexistence region will be discussed in section 6.2.3.

The appearance and stability of myelins are also affected by the initial surfactant concentration of the sample. While the myelins growing from dilute samples are, in general, thin and difficult to detect, samples in the L'_α+L_α coexistence region or pure collapsed lamellar phase form well defined myelins of greater stability (see Fig.6.15)

Furthermore, in contrast to the lecithin system, which has been studied by Leng *et al.* [Leng 06], the texture of the initial lamellar phase does not change in the region of the so-called myelin roots (see Fig.6.16). As can be seen, in case of the lecithin system, myelin texture covers almost the entire droplet with time. The myelins grow not only at their tips, but also at their roots. In case of the DDAB system, the region of the initial droplet keeps the morphology of the lamellar phase.

6.2.3 The influence of the crystalline phase at low temperatures

In the previous sections it has been discussed that myelin formation can be observed during the dissolution of all pure lamellar phases (also the non-equilibrium overcooled L_α phase). In the equilibrium phase diagram, there is a narrow gap of 2°C, in which the lamellar phase is found in equilibrium with a crystalline phase. This phase differs in its dissolution behaviour strongly from the lamellar phases discussed so far.

Fig.6.17 shows the typical morphology observed during the dissolution of a sample in the L_α+XW_n coexistence region. No myelin formation can be observed, the interface is smooth and hardly disturbed. Having a closer look, a dependence of the interface morphology on the number of crystals in the inital sample can be observed. For samples of a small concentration of lamellar phase, the texture of the lamellar phase is hard to detect. Upon dissolution, at the sample/water interface a lamellar phase forms, which quickly swells into the surrounding water, while the crystal concentration in the sample decreases. For samples in which only a few crystals are dispersed, after some time, myelinic figures can be observed to grow at the lamellar phase/water interface. However, these myelins are very short and thin. Their growing rate is very slow compared to the swelling rate of the entire sample. These myelins could not be spotted in macroscopic swelling measurements.

The swelling speed of the sample is high compared to the swelling speed of the myelin

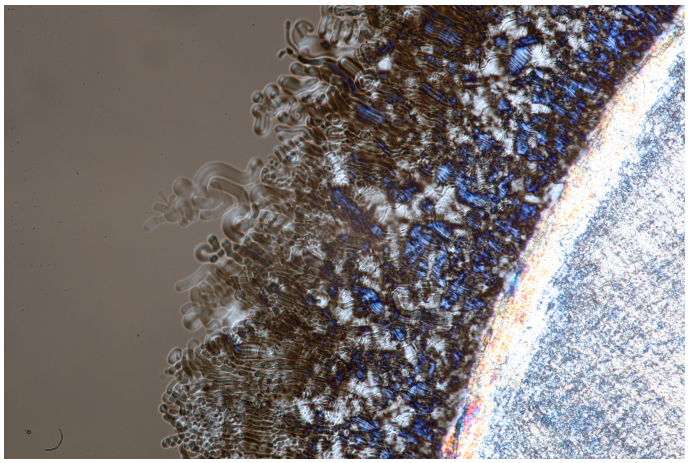

(a)

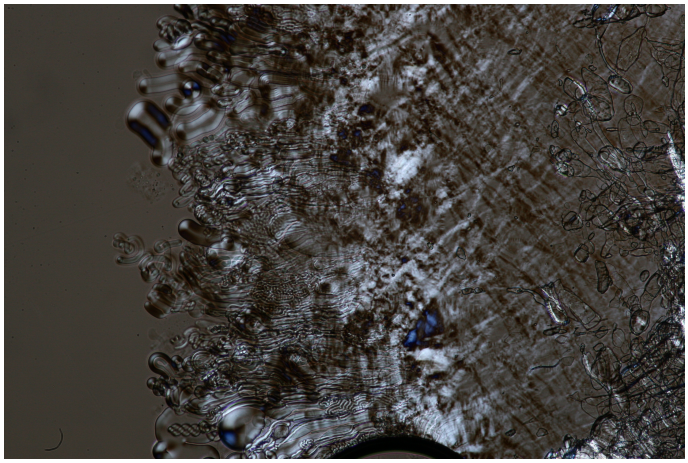

(b)

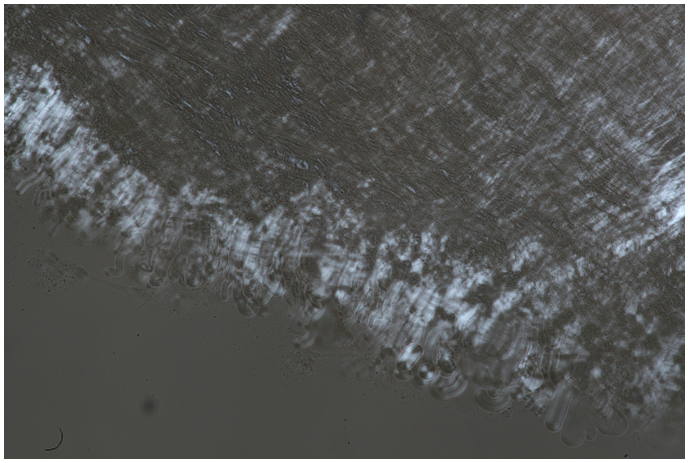

(c)

Figure 6.15: Myelins growing from the collapsed lamellar phase (a) and the L_α+L'_α coexistence region (b) are of greater stability and easier to detect than myelins obtained by the dissolution of dilute samples (c) (image size 1.5x2.2mm).

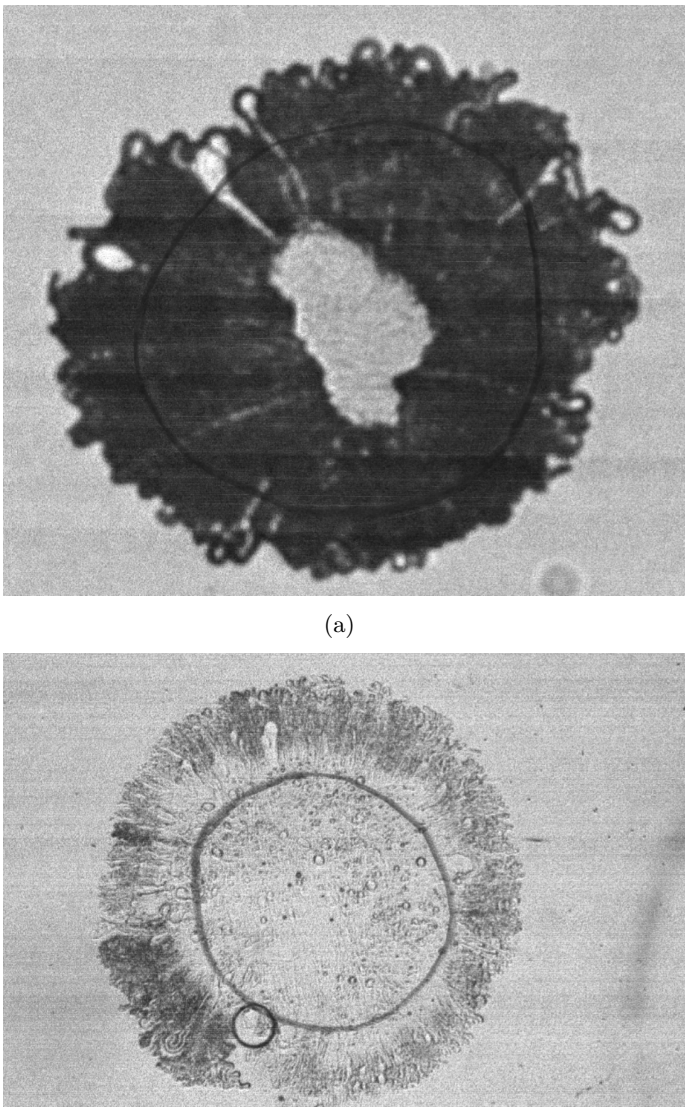

(a)

(b)

Figure 6.16: The differences in the position of the myelin roots in a sample of lecithin (a) and DDAB (b). The drawn rings show the initial interfaces.

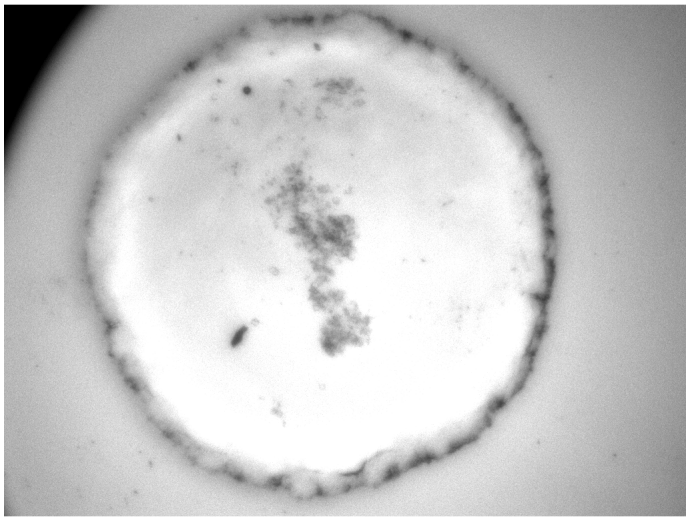

Figure 6.17: During the dissolution of a sample in L_α+XW_n coexistence region, no myelin formation can be observed.

forming lamellar phase expected for the same temperature range (see Fig.6.19). The large error bars are caused by the difficulty in defining the sample edge during the image analysis. The theoretical analysis of these swelling coefficients cannot be done with the model presented in section 2.3.2, without taking the new interface morphology into account. The model was based on the assumption that the composition is fixed at the position of the initial sample interface and that the surfactant phase which leaves this contour is fully swollen, leading to Eq.2.17. This assumption cannot be assumed to be valid in the case of the smooth interface morphology observed for the samples in the coexistence region. It can be rather expected, that a gradual swelling of the lamellar phase is observed. A gradient of the water concentration through the lamellar phase towards the droplet centre can be expected.

6.3 The influence of the crystalline phase formed by DODAB

One of the difficulties which was faced in the previous section was the poor control of the concentration of the crystalline phase within the initial sample. In this section a system is proposed, which is better suited to give insight into the influence of the crystalline phase on the dissolution behaviour of the lamellar phase and therefore on myelin formation.

The idea is to use two different surfactant systems which mix poorly, and therefore form

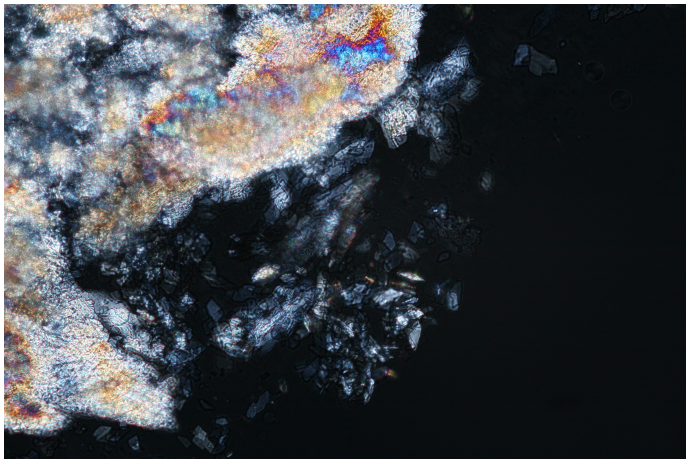

(a)

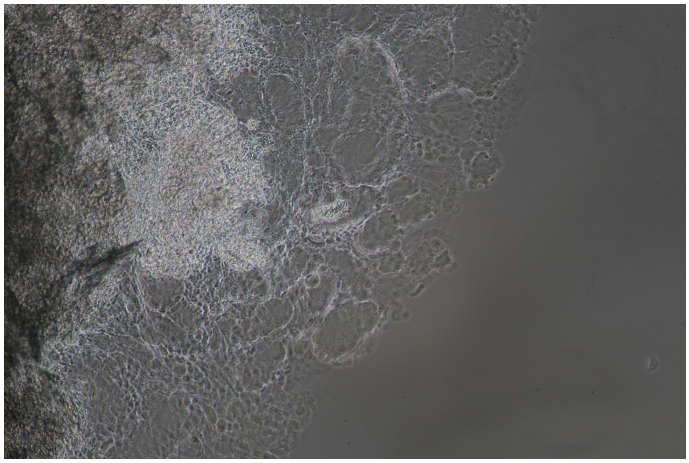

(b)

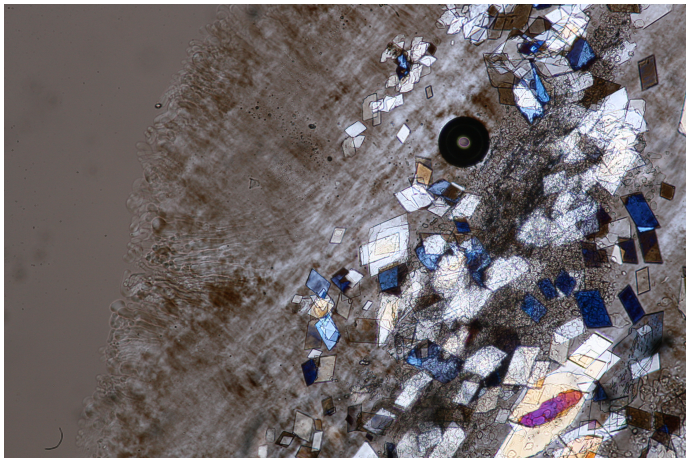

(c)

Figure 6.18: Dependence of the morphology at the sample/water interface on the number of crystals initially in coexistence with the lamellar phase. For a large number of crystals, mostly blocks of crystals are drifting away (a). Upon decrease of the crystal concentration, a lamellar phase forms at the interface (b). For samples of a low amount of crystals, short and thin myelins can be observed (c).

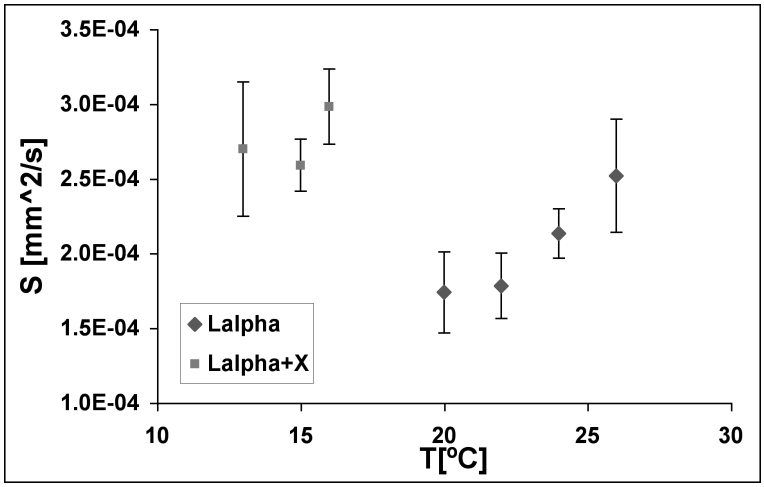

Figure 6.19: Swelling coefficients obtained during the dissolution of samples in the L_α+XW_n coexistence region.

a coexistence in the sample of phases, which are typical for each surfactant. Each of these phases would be mainly built by one of the surfactant species. In section 3.2.1.2, the mixing behaviour of DDAB with its longer analogue DODAB was presented for samples of low total surfactant concentration. This study was performed on a vesicle solution and showed the poor mixing behaviour of both surfactants.

To confirm that the system is suitable for dissolution experiments of samples of higher concentration, the thermal phase behaviour has been studied for samples of a total surfactant concentration of Φ=25%, and is presented in section 6.3.2. Furthermore it could be shown that Raman spectroscopy was suitable to distinguish between regions of the sample containing only DDAB or DODAB (see section 6.3.3).

6.3.1 Sample preparation

Samples containing a mixture of DDAB and DODAB were prepared for a total surfactant mass concentration of ϕ=25% at relative mass fractions

$$\Phi_{DODAB} = \frac{m_{DODAB}}{m_{DODAB} + m_{DDAB}} = 0 - 100\%$$

in 10% steps. The samples were equilibrated for a day at $60°C$, which is above the melting temperature of the DODAB crystals, and then stored for at least a week at $40°C$, allowing the crystals to equilibrate within the lamellar phase.

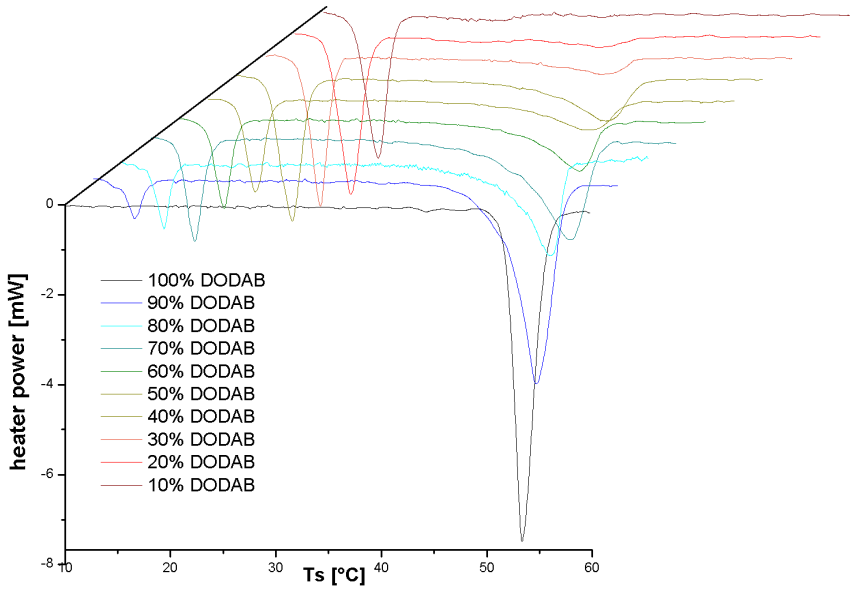

Figure 6.20: DSC plots of DDAB and DODAB solution of total surfactant concentration of Φ=25% depending on relative DODAB concentrations Φ_{DODAB}, showing two phase transition corresponding to the melting of DDAB at sample temperatures T_s of around 14°C and DODAB at sample temperatures between 30-55°C.

6.3.2 The DDAB/DODAB phase diagram

The dependence of the thermal phase transition of the concentration of DODAB in the samples of 25% total surfactant concentration has been measured by DSC (see Fig.6.20). The increase of DODAB concentration can be seen by a decrease in height in the peak at about 14°C corresponding to the melting peak of DDAB. Additionally a second peak at far higher temperatures appears. The temperature of this peak increases slightly with increasing DODAB concentration from a value of about 30°C to above 50°C for a pure DODAB solution (see Fig.6.21). Therefore the higher peaks can be assigned to the melting of the DODAB rich phase.

A phase diagram, similar to the one presented in section 3.2.1.2, can be extracted from the DSC data (see the phase boundaries on Fig.6.21). The broad shape of the coexistence region confirms the poor mixing behaviour of both surfactants, as has been already observed for vesicle solutions. The shape of the diagram is very similar to the one reported in the literature (see section 6.3), however the transition temperatures corresponding to the transition of the DODAB rich phases are shifted towards higher

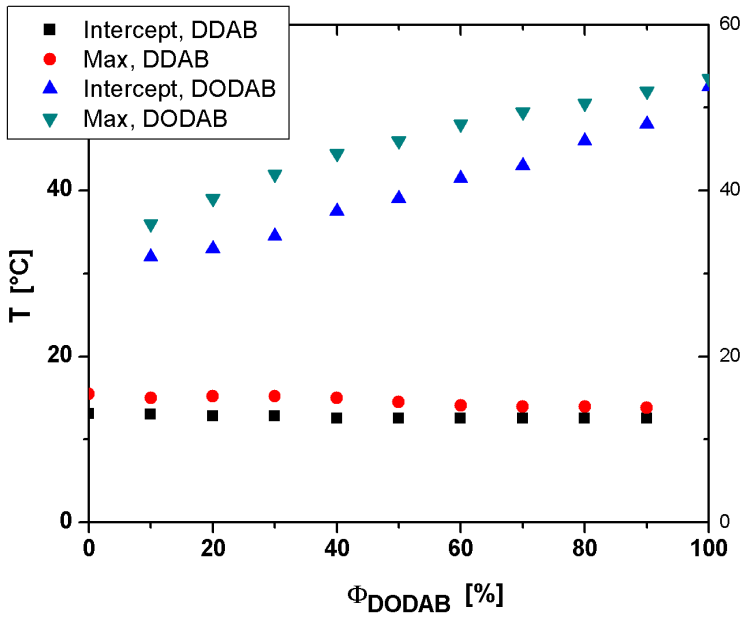

Figure 6.21: Thermal phase transition temperatures of a aqueous solution of DDAB+DODAB of total surfactant concentration of ϕ=25% depending on DODAB concentration Φ_{DODAB}.

temperatures.

It had been already mentioned that in a vesicle solution a transition to gel-phases can be observed, the transition temperature of which can be lower than the Krafft temperature of the sample. In the phase diagram reported in section 3.2.1.2 the transition to such a gel phase has been measured. In contrast, in the concentrated solutions which have been studied in this work, no gel phase was observed; the phase transitions are expected to correspond to the Krafft temperature of the surfactants.

6.3.3 The Raman spectrum of DODAB

The Raman spectrum of DODAB is, as expected, similar to the Raman spectrum of DDAB in both the lamellar phase (see Fig.6.22) as well as in the crystalline phase (see Fig.6.23). However, the slight differences spotted could be used to distinguish between pure DDAB phases and pure DODAB phases. Especially in samples within the coexistence region of DODAB crystals and the lamellar phase formed mainly by DDAB molecules, this technique can be used to get a better insight into the mixing behaviour of both surfactants and how this mixing can influence the dissolution behaviour of the

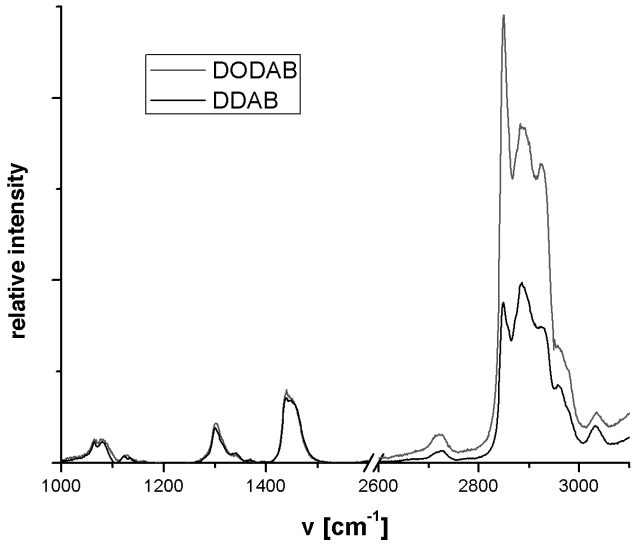

Figure 6.22: Raman spectrum of DODAB (ϕ=25%) in lamellar phase compared to DDAB ϕ_{DDAB}=10%.

lamellar phase.

In the L_α phase, the main difference in the Raman spectrum lies in the higher ratio between of the asymmetric to symmetric CH stretching peak I_{2850}/I_{2880}. The same can be observed for the crystalline phases. Furthermore, there is a marked difference in the region corresponding to the LAM vibrations in the crystalline spectras. This can be explained, by the different packing parameters for the two crystalline phases.

6.4 Conclusions and further work

The dissolution behaviour of lamellar phases formed by DDAB has been studied. The formation of myelinic figures could be observed for all pure lamellar phases. The growth kinetics of the myelins or, in other words, the swelling kinetics of the samples, could be obtained depending on initial surfactant concentration and temperature. The dependence on initial surfactant concentration was compared to the theoretical model developed to describe the myelin growth for the lecithin system. However, because of the poor data quality and the strong dependence of the kinetics on the properties of the lamellar phase (as morphology and vesicle concentration), only a rough picture of the dissolution process could be given. The theoretical model shows qualitatively similar behaviour, however the values are up to one order of magnitude above the

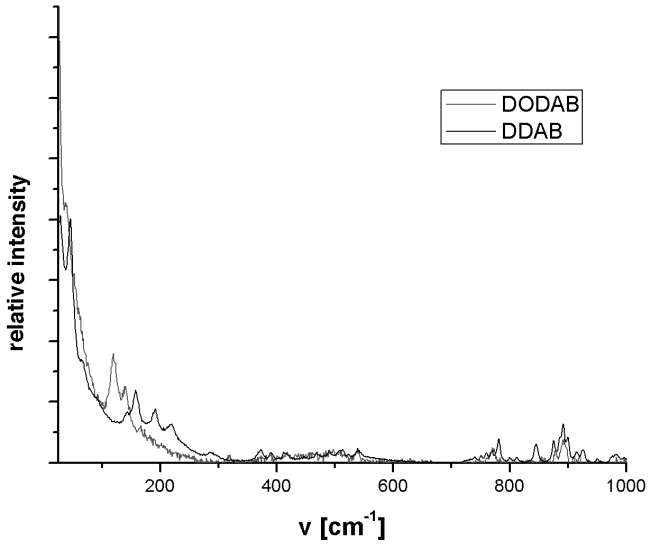

(a)

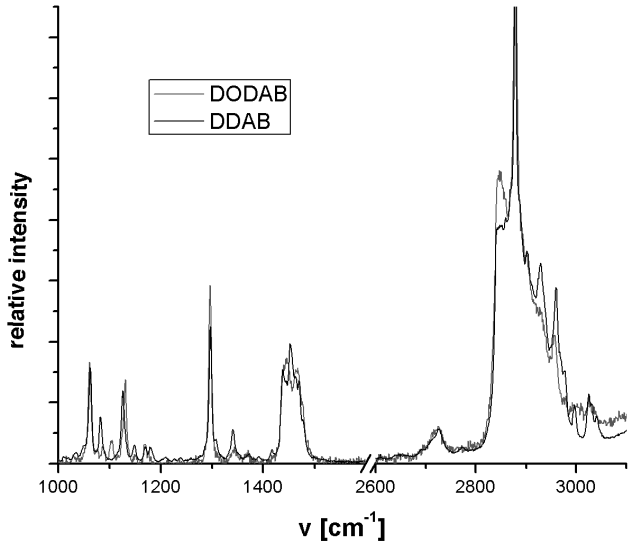

(b)

Figure 6.23: Raman spectrum of DODAB in the crystalline phase compared to DDAB.

experimentally obtained data. Therefore, the data cannot be used to confirm the quantitative validity of the theoretical model.

The low image quality is partly caused by the disruption of the droplet interface upon introduction of water, especially for dilute samples of low viscosity. In chapter 4, a phase separation of dilute DDAB samples in the XW_n+W coexistence region of the phase diagram was observed. The samples separate into a white phase, containing a crystal solution of about 10%, and a clear phase. If the sample is heated to a temperature, which is typical for the pure L_α phase, the 10% crystalline solution forms a lamellar phase, which then dissolves into the neighbouring water. No water has to be introduced into the sample, therefore the lamellar/water interface is not disrupted. This experiment would, furthermore, give the possibility to study the influence of the disruption of the interface on myelin formation and on the swelling kinetics.

In this chapter, it could be shown that the formation of myelins could be not only suppressed by changing the lamellar phase into a vesicle rich phase, as has been known already for other systems, but also by mixing the lamellar phase with a crystalline phase. In future, Raman microscopy could be used to study the changes in the lamellar phase caused by the presence of the crystalline phase. It has already been mentioned in section 2.3.3 that the lamellar phase has to be of high fluidity and low permeability to allow the formation of myelins. Therefore it is expected that the presence of the crystalline phase changes one of these properties for the bilayers.

However, there is only a narrow temperature range in the pure DDAB system, in which such experiments could be performed. Therefore, the use of a tertiary system, the DDAB/DODAB/water system, is proposed. In this system, over a broad temperature and concentration range, the lamellar phase (mainly formed of DDAB molecules) is in coexistence with the crystalline phase (mainly formed of DODAB molecules). The differences in the Raman signal of the surfactants in the lamellar and crystalline phases can be used to study their mixing behaviour and obtain greater insight into the changes in the lamellar phase suppressing myelin formation.

Chapter 7

A study of myelin formation by $C_{12}E_3$

7.1 Introduction

For a detailed study of myelinic figures, a highly stable and simple system is needed. This involves also a well characterised phase behaviour of low complexity. The study on the DDAB system, described in the previous chapter, could therefore only give limited insight into myelin formation and growth.

By comparison, the non-ionic surfactant $C_{12}E_3$ is known to form highly stable myelins upon dissolution in water at room temperatures [Kennedy 05, Buchanan 99, Buchanan 00, Chen 00a, Laughlin 98]. These myelins form at the L_α/water interface and were described as relatively long-lived metastable states. The increased stability of the myelins compared to the DDAB system (see chapter 6) made it possible to perform a more detailed investigation of their growth and shape. Furthermore this system, with its relatively slow growth rates, is ideally suited for a statistical study of the changes in the appearance (especially the thickness) of the myelinic tubules, as well as their stability.

The equilibrium phase diagram of this system is well established [Laughlin 98, Laughlin 00, Mitchell 83, Oswald 05] and has been described in section 3.2.2.1. To summarize, at room temperature (T≈20°C) concentrated $C_{12}E_3$ forms inverted micelles (region D in Fig.7.1). With dilution one enters first a coexistence region with a lamellar phase (C), then a pure lamellar phase (B), and then a coexistence region with water (A). The temperature dependence within 10°C around room temperature can be neglected, and therefore temperature control is not needed during these measurements. The simplicity of the phase diagram leads to a straight-forward interpretation of the experimental results.

To obtain a three dimensional picture of myelin growth, 2-D imaging techniques, such as microscopy and direct observation, have been combined with depth profiling using

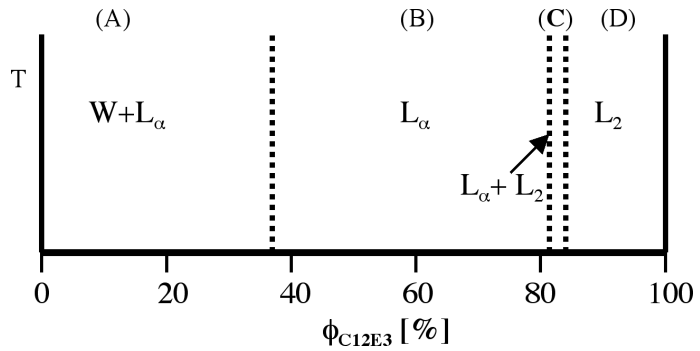

Figure 7.1: Schematic phase diagram of $C_{12}E_3$ close to room temperature (T≈20°C).

confocal microscopy. The growth of the generally cylindrical myelins of a diameter between 20-60μm (see section 7.3) can be divided into three parts (see section 7.5): a pre-diffusive, a diffusive and a sub-diffusive growth regime. The pre-diffusive and diffusive growth speed, as well as the thickness of the myelins, increases with increasing concentration of the initial lamellar phase. The growth kinetics can be compared to the DDAB system (see chapter 6) or lecithin [Leng 06] and can be explained in terms of the Leng-model (see section 2.3.2).

However, in contrast to the DDAB or lecithin system, there is a density mismatch between the phases, involving $C_{12}E_3$ molecules, and pure water. Therefore, the lower density of the myelins, compared to water, combined with the small bending modulus of the myelinic tubes in the $C_{12}E_3$ system leads to a creaming force during myelin growth (see section 7.4). The creaming of myelins has not been observed previously. The results of the 3-D evolution of the myelin/water interface with time suggests that they could be used to explain the dependence of the myelin growth speed observed with 2-D imaging techniques on sample thickness.

7.2 Sample preparation

Solutions of $C_{12}E_3$ were prepared in the range of surfactant mass fraction ϕ_{C12E3}=35% to 85% in distilled water to span region A-D (Fig.7.1). The samples were homogenised either by shaking using a mechanical shaker or by rotating the sample once per second for several hours. As the observed viscosity of these samples was typically high, particularly in the L_α region, they were then left at room temperature (T=20±2°C) for several days to equilibrate. The efficacy of this length of equilibration time has been confirmed by comparing selected results to those obtained from samples which were equilibrated for several weeks.

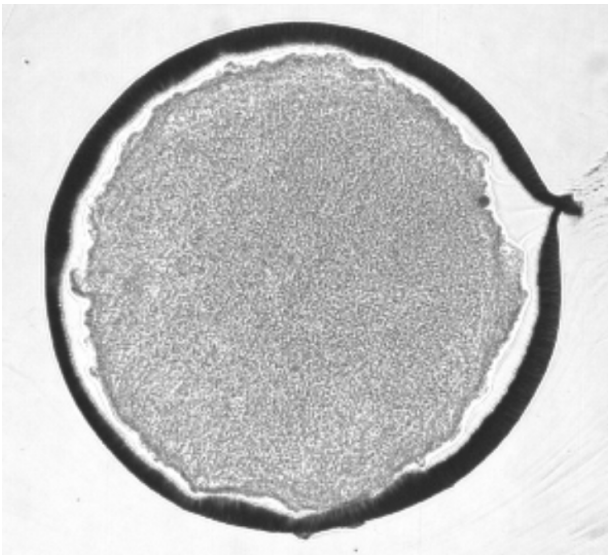

Figure 7.2: Typical sample in the coexistence region of L_α+L_2 after being contacted with water. The lamellar phase is surrounded by the water-like L_2 phase.

Once equilibrated, these samples were observed visually by eye through cross polarizers. For ϕ_{C12E3}<80% (region A-C), as expected, birefringent regions characteristic of lamellar phases were observed. At high values of ϕ_{C12E3} in region B, significant turbidity was observed, whilst clear samples were formed in region D. This enables phase separation (into the turbid L_α phase and the clear L_2 phase) to be monitored readily in region C. During the measurements, this is necessary to determine the location of the L_α/W, L_α/L_2 or L_2/W interfaces when working on samples in regions C and D (see Fig.7.2).

For confocal microscopy, samples at surfactant mass fraction ϕ_{C12E3}=65% were prepared with sufficient optical contrast by adding trace amounts of one of two lipophilic dyes (Rhodamine B (Fluka, standard Fluka grade) or $DiIC_{18}$ (Aldrich, 97%)) to pure $C_{12}E_3$. After mixing the sample for 2 hours, the samples were centrifuged to get rid of excess solid dye and the upper liquid phase was extracted into another vial. Several grams of solution of 65% (w/w) $C_{12}E_3$+Dye in water (Millipore) were mixed and left on a shaker over night. The samples were put on a roller for several days to equilibrate giving a homogenous pink colour and a viscosity similar to samples without the dye. Neither dye caused an observable change in the bulk sample properties, such as birefringence and viscosity.

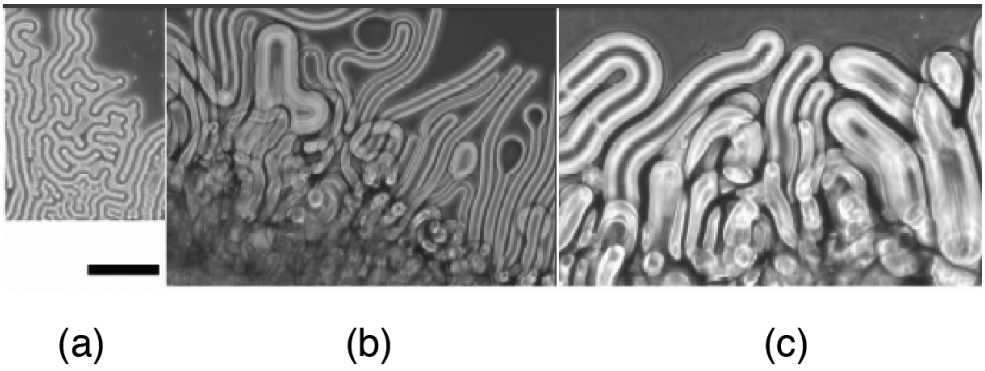

Figure 7.3: Myelins as observed by optical microscopy for sample thickness b of 13μm (a), 200μm (b) and 600μm (c) and ϕ_{C12E3}=65% (a,c) and ϕ_{C12E3}=60% (b) (scale bar=200μm).

7.3 Myelin shape and width

The formation and growth of myelins was studied using optical microscopy (see Fig.7.3). Upon contact with water, the myelins started to form after a delay time t' of a few seconds (see section 7.5). Myelins grew from the interface of the droplet into the surrounding water. In the case of droplets containing an L_2 phase (region C or D), the initial L_2/W interface changed rapidly into a L_2/L_α/W interface, from which myelins started to grow. The myelins were typically stable for hours. During this time, they grew in length, while their width remained constant with time and position along the myelins. However, the individual myelins had somewhat different lengths and widths and some were also curved or branched.

The distribution of the (projected) myelin width $N(d)$ was obtained as a function of the initial surfactant concentration ϕ_{C12E3} and sample thickness b. The width d of the myelins was measured manually, typically for about 100 myelins for each sample (see Fig. 7.4). The resulting distribution, $N(d)$, was found to fit well to a Schultz distribution

$$N(d) = \frac{(d)^z}{z!}(\frac{z+1}{\langle d\rangle})^{z+1}\exp[-\frac{d}{\langle d\rangle}(z+1)], \tag{7.1}$$

with average myelin width $\langle d\rangle$ and polydispersity σ=$\sqrt{\frac{1}{z+1}}$. The distribution $N(d)$ was followed for up to two hours and its form was found to be independent of time. The average width $\langle d\rangle$ depended, however, on ϕ_{C12E3} and b.

The dependence of the average myelin width $\langle d\rangle$ on the initial surfactant concentration ϕ_{C12E3} was investigated for a constant sample thickness b=200μm (see Fig.7.5).

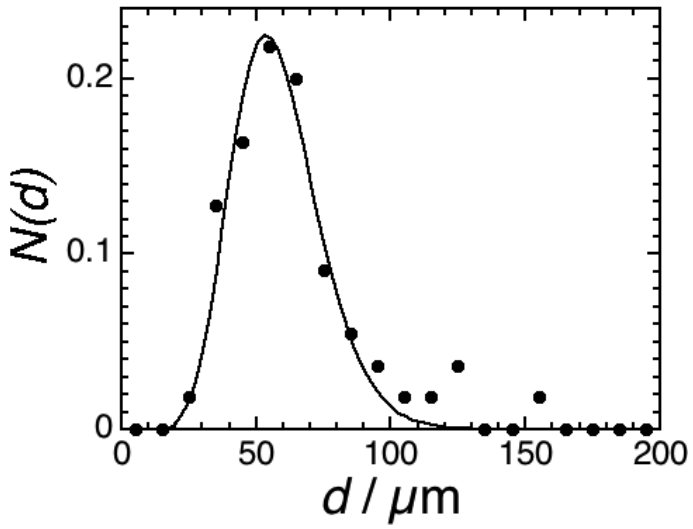

Figure 7.4: Distribution of the (projected) myelin width $N(d)$ based on the measurement of 60 individual myelins in a sample with initial surfactant concentration ϕ_{C12E3}=75% and sample thickness b=200μm. The line represents a fit by a Schultz distribution with average myelin width $\langle d\rangle$=58.3μm and polydispersity σ=0.28.

With increasing ϕ_{C12E3}, $\langle d\rangle$ starts around 20μm and then increases before remaining constant at around 60μm for ϕ_{C12E3}=70%. The width $\langle d\rangle\approx$60μm remains constant for $\phi_{C12E3}>$70%, where inverted micelles are presented in the initial droplet. This is consistent with the L_2 phase first transforming into the most concentrated L_α phase and myelins then growing out of this concentrated lamellar phase. Moreover, the myelins have a relatively low polydispersity (indicated by the bars in Fig.7.5). In all cases the myelins are stable for hours without noticeable changes in their morphology.

The average myelin width $\langle d\rangle$ also depends on the sample thickness b (see Fig.7.6). For sample thicknesses $b<$20μm, the projected average width $\langle d\rangle\approx$20μm is independent of b and hence the myelins are not cylindrical. These myelins are also relatively unstable; within minutes they dissolve behind the growing tips. With increasing sample thickness, 20μm$<b<$600μm, $\langle d\rangle$ increases. The increase of $\langle d\rangle$ is steeper for more concentrated samples. A maximum width $\langle d\rangle\approx$60μm is reached for large sample thicknesses $b>$600μm. For those samples, as well as for thin samples ($b<$20μm), the mean myelin width does not significantly depend on surfactant concentration. Upon increasing b, the morphology also changes, evolving from a tight network with a large fraction of branched myelins to a looser network of rather curved myelins (see Fig.7.3).

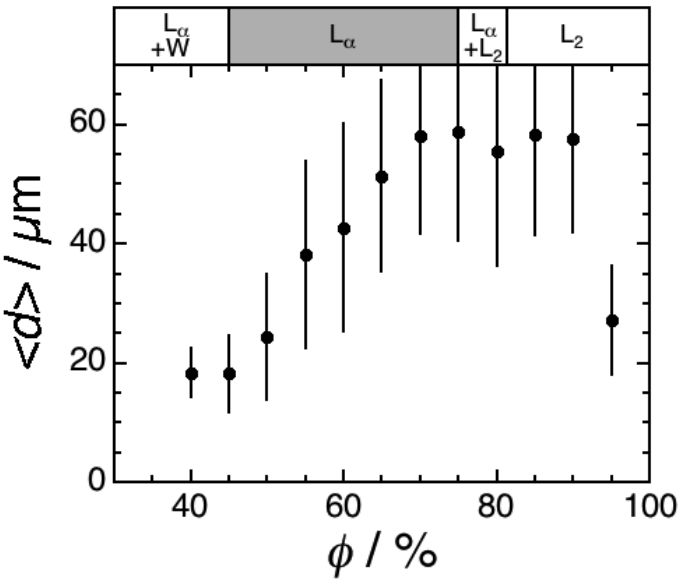

Figure 7.5: Average Myelin width $\langle d \rangle$ as a function of initial surfactant concentration ϕ for spacer thickness b= 200μm. On top of the graph, the corresponding phase diagram is indicated.

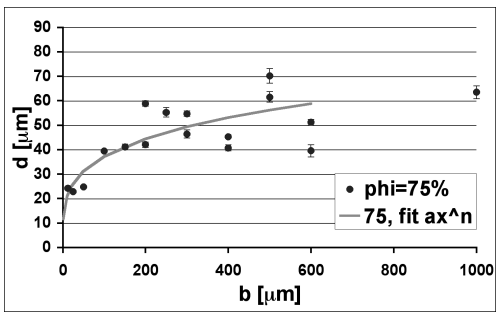

(a) ϕ_{C12E3}=75%

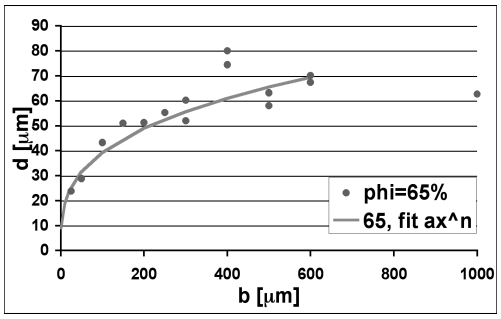

(b) ϕ_{C12E3}=65%

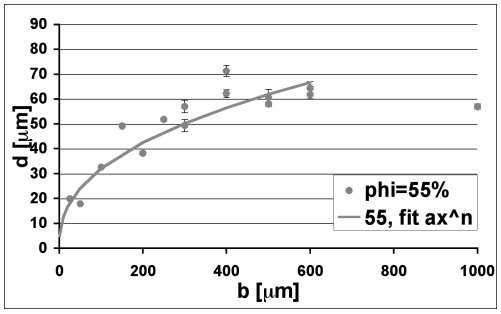

(c) ϕ_{C12E3}=55%

Figure 7.6: Average myelin width $\langle d \rangle$ as a function of spacer thickness b for different initial surfactant concentration ϕ_{C12E3}. The lines show fits of the data with the power functions, used in the section 7.6.

7.4 3-D profile of the myelinic forest

Convential microscopy only provides a projection onto an xy-plane. The experiments have been therefore complemented by confocal microscopy to obtain 3-D information on myelin growth according to the methodology presented in section 3.3.4.3.

The evolution of the sample interface during the growth of myelins in 3-D is presented in Fig.7.7. It can be seen that the nearly vertical interface, recorded at early times, changes during the myelin growth. The interface moves faster at the top of the sample. This leads to a progressive slant of the interface. This has been observed for all sample thicknesses b studied (see Fig.7.8 and Fig.7.9(a)). Furthermore, it can be seen that similar results are obtained for two different dyes (Rhodamine B and $DiIC_{18}$), indicating that the z-profiles are not significantly affected by the presence of the dyes.

As can be seen in the figures, at the top of the sample, a layer of single myelins develops. The thickness of this layer corresponds, at later times, to the myelin width $\langle d(b) \rangle$ obtained by convential microscopy (see Fig.7.6). This is consistent with a cylindrical shape of the myelins for the range $100\mu\text{m}<b<400\mu\text{m}$. A cylindrical shape seems to be more stable than the non-cylindrical shape found at $b<20\mu\text{m}$, which is in agreement with the observation for the lecithin system [Sakurai 90].

The slope of the interface can be attributed to creaming of the myelins. The density of myelins can be estimated from the surfactant density $\rho_{C12E3}(20°\text{C})=0.927\text{g/cm}^3$ and water density $\rho_{H2O}(20°\text{C})=0.998\text{g/cm}^3$ to be

$$\rho_{myelin}(20°C) = 0.966 g/cm^3$$

assuming the myelins represent a fully swollen lamellar phase [Sakurai 90, Kennedy 05] with a surfactant concentration $\phi_{C12E3}\approx 45\%$ [Laughlin 94, Laughlin 00, Mitchell 83]. The myelin density ρ_{myelin} is thus lower than the density of the surrounding water ρ_{H2O}, which can lead to creaming.

7.5 Myelin growth kinetics

For a quantitative investigation of the myelin growth kinetics, the same methodology as already presented in chapter 6 has been used. Compared to the DDAB system, the myelins appear as a dark ring, due to their more defined and less dilute structure (see Fig.7.10). It should be noted, that also in this case, no significant change within

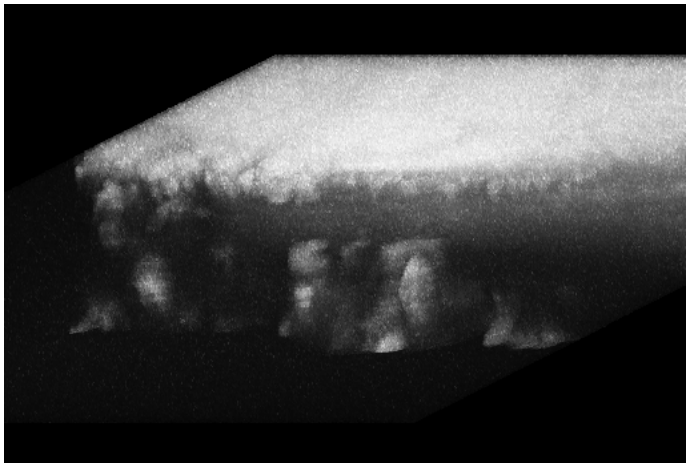

(a) t=5min

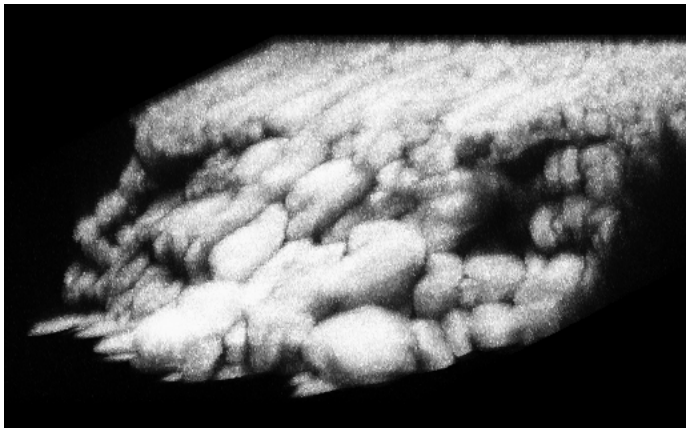

(b) t=16min

(c) t=27min

Figure 7.7: The evolution of the 3-D profile of the myelinic forest with time t for sample thicknesses b=300μm (the images are displayed upside down, image size 821x821x300μm^3).

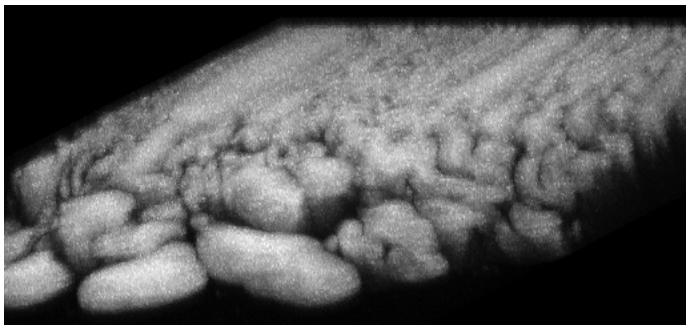

(a) b=200μm

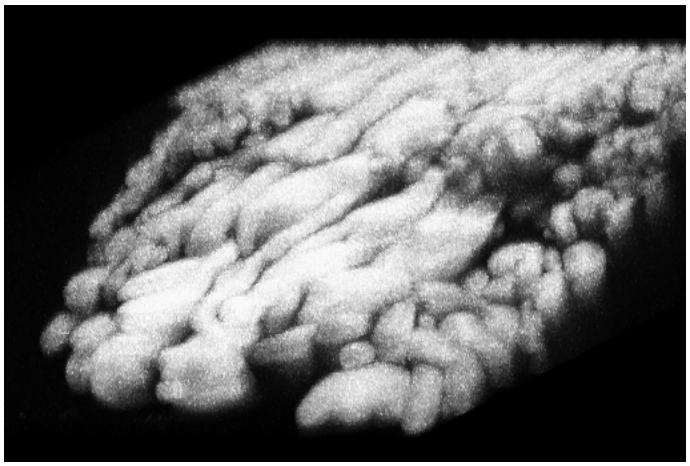

(b) b=300μm

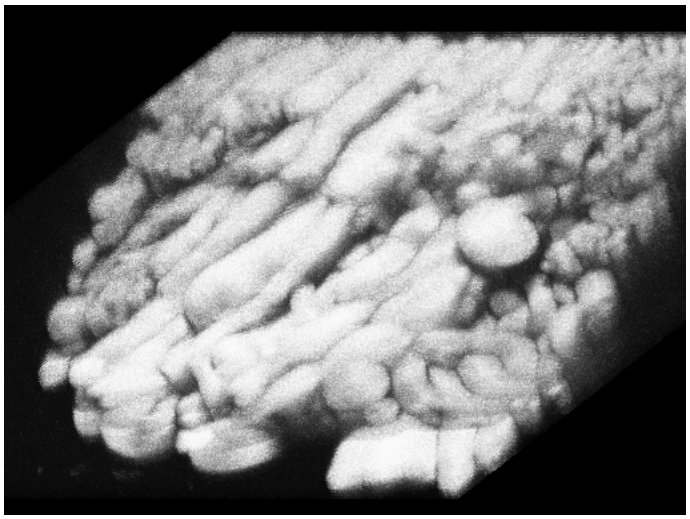

(c) b=400μm

Figure 7.8: 3-D profile of the myelinic forest after growth time of t≈30min for different sample thicknesses b (the images are displayed upside down, image size 821x821xb μm^3).

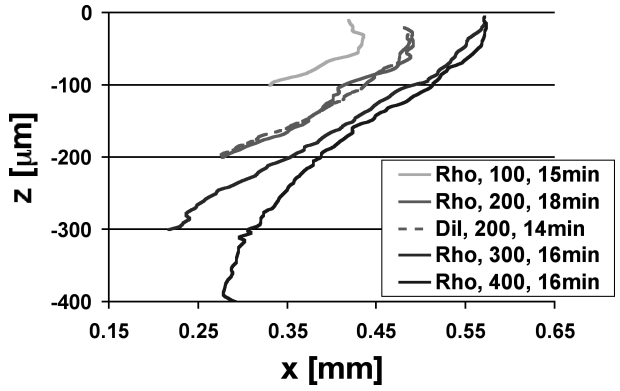

(a)

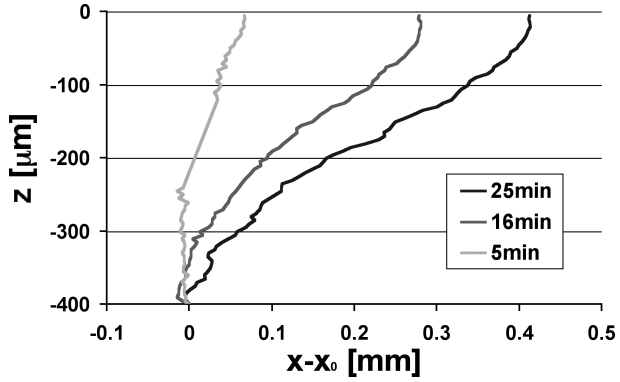

(b)

Figure 7.9: Dependence of the z-profiles with the relative lateral distance, x, on the choice of dye (a), sample thickness b (a) and time t (b).

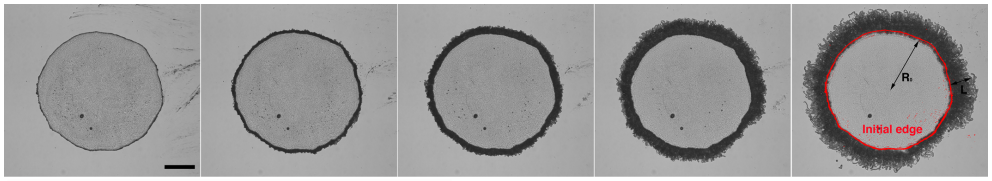

Figure 7.10: A typical time series for a dissolution experiment of a droplet of lamellar phase of $C_{12}E_3$ (ϕ_{C12E3}=70%, b=200μ) observed with the direct observation setup (scale bar=2mm).

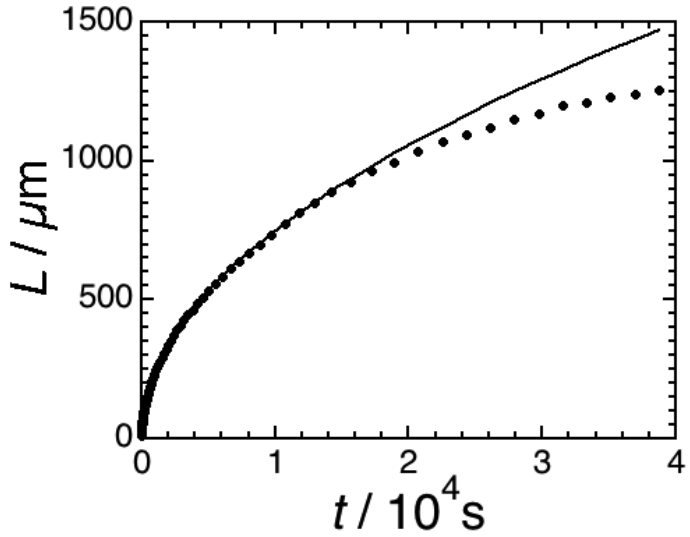

Figure 7.11: Time dependence of the average myelin length $l(t)$ (ϕ_{C12E3}=70%, b=200μm). The line represents a fit to Eq.6.1.

the initial droplet can be observed, in contrast to the observation in the lecithin system [Leng 06].

The direct observation setup, as with any conventional optical microscope, provides a projection of the sample. Due to the projection, the length $l(t)$ corresponds to the longest myelins, which grow at the top of the sample (see section 7.4). In agreement with previous studies [Buchanan 99, Buchanan 00], after t', the myelin length $l(t)$ initially shows a square root dependence on time except at long times, where there is a subdiffusive regime (see Fig.7.11)

The dependence of the swelling coefficient S on the initial surfactant concentration ϕ_{C12E3} has been investigated for a fixed sample thickness b=200μm, where stable myelins are formed (see Fig.7.12). The swelling coefficient S is very small for ϕ_{C12E3} close to the coexistence of the L_α phase and water, i.e. for the already almost maximally

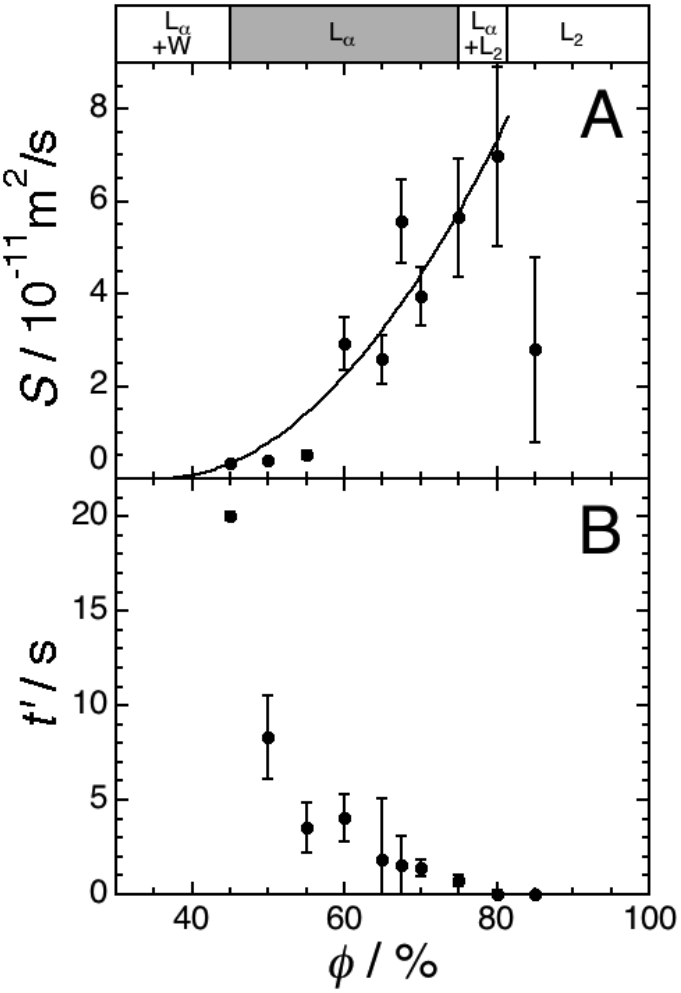

Figure 7.12: Dependence of the average swelling coefficient S (a) and delay time t' (b) on the initial surfactant concentration ϕ_{C12E3} (b=200μm). On top of the graph the corresponding phase diagram is indicated.

swollen lamellar phase. With increasing surfactant concentration, S increases to reach $S{\approx}7{\cdot}10^{-11}\mathrm{m}^2/\mathrm{s}$. For $\phi_{C12E3}{>}80\%$ where there is an initial L_2 phase, S decreases again. The delay time t' decreases with increasing surfactant concentration, but even for small ϕ_{C12E3} it reaches values ($t'{\approx}20\mathrm{s}$) which are small compared to the time scale of myelin growth (see Fig.7.11).

It is reassuring that the magnitude of the swelling coefficient S is similar to values determined earlier [Buchanan 99] and is comparable to values of the $C_{12}E_6$ analogue with a longer head group of $S{=}21.9{\cdot}10^{-11}\mathrm{mm}^2/\mathrm{s}$ [Chen 00a].

The dependence of S on ϕ_{C12E3} is consistent with osmotic pressure Π being the

driving force of myelin growth [Leng 06, Zou 06, Chen 00a]. With increasing surfactant concentration, and thus decreasing water content of the surfactant droplet, the osmotic pressure difference between the surfactant phase and bulk water, and thus the driving force, increases. This is consistent with an increasing $S(\phi)$. It is furthermore consistent with a decrease in the delay time $t'(\phi)$, i.e. the time needed to form myelins and establish a diffusive myelin growth with a $t^{1/2}$ dependence.

To compare the experimentally determined swelling coefficient with the theory presented in section 2.3.2, the osmotic pressure dependence on surfactant concentration has to be known. The osmotic pressure Π of a lamellar phase formed by a (dilute) non-ionic surfactant is dominated by undulations and given by [Bagger-Jörgensen 96]:

$$\Pi = \frac{3\pi^2}{64}\frac{(k_BT)^2}{\kappa}\frac{1}{d_b^3}\frac{\phi^3}{(1-\phi)^3}, \tag{7.2}$$

where κ is the bending modulus. We thus obtain for the swelling coefficient

$$S(\phi) = \frac{\pi(k_BT)^2}{32\phi_{cyl}^2\eta d_b\kappa}(\phi-\phi_{fs}) = \chi(\phi-\phi_{fs})^2. \tag{7.3}$$

Based on literature values for the bilayer thickness d_b=2.5nm [Bell 96, Lu 93a, Lu 93b], bending modulus κ=2.5k$_B$T (taken from a similar system, $C_{12}E_6$ [Bagger-Jörgensen 96]) and viscosity of water η=0.001Pas [Raviv 01], a value of χ^{calc}=8x10^{-11}m^2/s is expected. A fit of the $(\phi-\phi_{fs})^2$ dependence to the data (solid line in Fig.7.12(a)) results in good agreement with the data and yields χ=36x10^{-11}m^2/s which is encouraging, taking into account that χ^{calc} is based on a very simple model and involves no free parameters.

7.6 The influence of the creaming process on the observed myelin kinetics

Next, the dependence of the swelling coefficient S on the sample thickness b was investigated (see Fig.7.13). With increasing b the swelling coefficient increases and reaches a limiting value for b>300μm.

In section 7.4, the creaming of myelins during the dissolution process has been described. This has an effect on the growth kinetics observed with the direct observation setup, as only the growth of the longest myelins are recorded, i.e. the kinetics of the single myelin layer on top of the sample has been investigated. Especially for samples

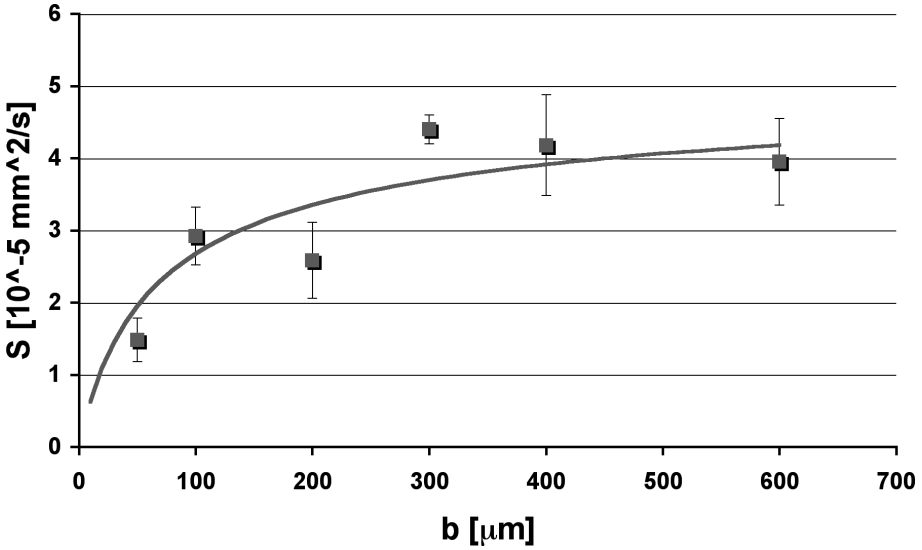

Figure 7.13: Dependence of the swelling coefficient S on sample thickness b (ϕ_{C12E3}=65%) - The line shows a fit to Eq.7.4 with fitting parameters $\overline{S}$=(1.3±0.1)10^{-5}mm^{2}s^{-1} and $x \rightarrow \infty$.

of greater thickness b, this growth rate cannot simply be compared to the growth rate of all myelins in the sample. For this, the slant in the interface has to be taken into account.

In order to model the evolution of the interface in 3-D with time, more accurate data than the ones which have been so far obtained by confocal microscopy are needed, and an influence of the dye on the growing rate needs to be further investigated and discounted. In this section, however, a highly simplified model calculating the effect of the slant in the interface on the average kinetics, based on an interface profile similar to the one observed, is presented. It has to be noted, that this model cannot be used to model the evolution of the experimentally obtained interface. It only gives an indication, that the dependence of the swelling coefficient S on sample thickness b could be caused by the creaming of the myelinic figures.

The model is based on the following assumption: The water flux into the lamellar phase is not significantly affected by the presence of the myelin phase. The amount of water entering the sample depends only on the osmotic pressure and water mobility at the myelin roots. This infers that the water flux into the lamellar phase does also not depend on the z-geometry of the myelins, but has a constant value per unit area. The validity of this assumption will be discussed later.

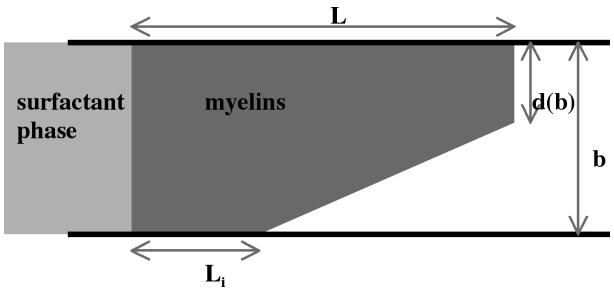

Figure 7.14: Simplified form of the interface profile obtained by confocal microscopy.

In this case the change of the spacer thickness b, which influences the z-profile of the myelin front, therefore does not change the water flux per unit area into the sample. The same amount of surfactant per unit area has to leave the sample with a mean swelling coefficient $\overline{S}$. This differs from S, the swelling coefficient measured by macroscopic observation. Results obtained by confocal microscopy show that the profile evolves at a different speed at different heights of the sample, which could be attributed to the difference in density. S then corresponds to the largest value, seen at the top of the sample. Averaging over z, we can obtain the mean swelling coefficient $\overline{S}$. In this model, a highly simplified form of the interface profile is used (see Fig.7.14).

This profile consists of a layer of single myelins growing at the top of the sample cell with the experimentally determined swelling coefficient S, resulting in a length increase with time $L(t)$. The thickness of this layer d (the myelin thickness) depends on b (see Fig.7.6). Using a power function fit

$$d = ab^n$$

to the experimental results (solid lines in Fig.7.6), the dependence of $d(b)$ can be described.

The average surfactant flux per unit area is determined by the average length $\langle L \rangle$ of the myelinic layer, which can be calculated geometrically from Fig.7.14 as

$$\langle L \rangle = \frac{(b-d)L_i + (b+d)L}{2b} \tag{7.4}$$

Using Eq.6.1 (neglecting t_0 and l_0) the relation between the macroscopic swelling coefficient S and the average swelling coefficient $\overline{S}$ can be predicted. For simplicity, the bottom layer L_i was predicted to swell with a swelling coefficient $S_i = \frac{S}{x^2}$, where x>1

is a parameter.

$$S(b) = (\frac{2b}{(b - d(b))/x + b + d(b)})^2 \overline{S} \tag{7.5}$$

Fitting the parameter $\overline{S}$ and x to the experimentally obtained results (Fig.7.13) using the least square method, we obtained $\overline{S}$ =(1.3 $\pm$ 0.1)10 $^{-1}$ mm ^{2} s^{-1} and $x \rightarrow\infty$ for sample having ϕ=65% (see line in Fig.7.13). One should note that the obtained fitting parameter $x \rightarrow\infty$ would suggest no swelling for the bottom layer, which was not observed in the experiments. However, the shape of this interface has been estimated using a straight line and neglecting the experimentally observed curvature (Fig.7.14 and Eq.7.4). This deviation could be the origin of the underestimation of the swelling of this bottom layer.

In future, confocal microscopy could be used to obtain a more detailed picture of the dependence of the observed swelling coefficients on z. So far the quality of the data is only good enough to give a qualitative insight into idea the evolution of the shape of the myelin front and the effects of creaming.

The quality of the fit to the data in Fig.7.13 supports the assumption, that the myelins do not strongly affect the water flux into the lamellar phase. The relatively loose network of myelins seems not to influence the amount of water penetrating the sample, or the mobility of the water within the lamellar phase, driven by the osmotic pressure gradient at the myelin roots.

7.7 Conclusion and future work

The morphology and growth of myelins in aqueous surfactant solutions containing the non-ionic surfactant $C_{12}E_3$ has been studied. Using a combination of the 2-D imaging techniques of microscopy or direct observation and depth profiling with confocal microscopy, a detailed 3-D picture of the shape and growth of the myelins has been obtained.

Myelins formed by the non-ionic surfactant $C_{12}E_3$ are generally characterised by their cylindrical shape. However, if the sample is very thin with a thickness b<20μm, non-cylindrical myelins form, which tend to be unstable. The width of the myelins could be modelled with a Schultz-distribution with a relatively small polydispersity. The average value of the width $\langle d \rangle$ ranges between about 20μm and 60μm and increases with the initial surfactant concentration ϕ_{C12E3} and thickness of the sample b.

Myelin growth starts after a relatively short delay time (t'<20s), which depends on the initial surfactant concentration ϕ_{C12E3}. During the first few hours, the growth follows a diffusion-like behaviour, i.e. the length $l(t)$ increases with a square-root dependence $l(t) \sim t^{1/2}$. Then, at later times, a subdiffusive growth is observed. The growth rate of the diffusive growth, characterised by the swelling coefficient S, has been investigated. It depends on the initial surfactant concentration ϕ_{C12E3} and, apparently, the sample thickness b.

We suggest, that the dependence of the observed swelling coefficient S on sample thickness b is due to a slanted, instead of vertical, interface between the myelins and the water. The slanted interface is due to a density difference between myelins and water which leads to creaming and thus faster progression of the myelin front at the top of the sample. This maximum length is determined in a projection as obtained by optical microscopy and is used to calculate S. In contrast, an average length $\langle L \rangle$ is more representative of the rate of myelin formation and should be used instead. Using confocal microscopy, the slant of the interface was investigated, which depended on sample thickness b. The low resolution of time and long acquisition times during the measurement made it not possible to obtain a precise time dependence of the interface profile, to obtain a complete 3-D reconstruction of the evolution of the interface with time. However, a highly simplified model already suggests that the creaming of myelins might explain the observed dependence of the swelling coefficient, S, on sample thickness b. In future more precise data on the time dependence of the interface could result in a complete 3-D reconstruction of the interface, which could be used to develop a more sophisticated model to quantify profile evolution and its effects on apparent and intrinsic swelling rates.

Furthermore, the initial surfactant concentration ϕ_{C12E3} was found to affect the swelling coefficient S. Using the Leng-model, S was related to the mobility of water in the surfactant phase and the osmotic pressure difference between the lamellar phase and water (see section 2.3.2). Since the dependence of the mobility and the osmotic pressure on the properties of the lamellar phase are known [Brochard 75, Bagger-Jörgensen 96], the dependence of S on ϕ_{C12E3} could be calculated

$$S(\phi) \sim (\phi - \phi_{fs})^2.$$

This dependence was found to agree with the experimental observations and also the magnitude of S is of the order of the experimental values obtained. This supports the explanation that myelin growth is indeed driven by the osmotic pressure difference and

limited by the mobility of water within the surfactant phase.

Chapter 8

Conclusion

In this thesis, a detailed study of the equilibrium and non-equilibrium behaviour of three aqueous surfactant systems is presented. The results are based on a broad range of experimental techniques, recording changes in the samples at different length scales, as well as the thermodynamic parameters of the phase transitions involved.

The equilibrium phase diagram of the cationic surfactant DDAB has been studied in great detail. The results could not been explained within the frame of the existing equilibrium phase diagram, therefore, an amended form for the low temperature region has been proposed, based on experimental results and theoretical considerations. The new phase diagram has been tested by studying a range of phase transitions along isoplethal and isothermal paths. The obtained results could not be completely explained by the previously reported phase diagram in the literature, however, they could be by the new phase diagram proposed in this thesis. This gives great support for the accuracy of this new phase diagram.

The main difference is the vanishing of the previously reported equilibrium L_β phase. It has to be noted that this phase did not appear in any phase diagram of DDAB analogues, which differ in the length of the hydrocarbon chains. Instead, a coexistence region of crystals and a dilute monomer solution was seen in the low temperature regions. For the DDAB system, the amended phase diagram explains this trend. This low temperature crystalline phase was characterised.

A range of more precisely temperature controlled experiments is proposed at different parts of this thesis, which are necessary to establish the precise positions of the phase boundaries in the diagram. These experiments are based on the knowledge which has been accumulated during the experimental work of this thesis.

It has to be noted that the strength of this work lies in the combination of different experimental techniques with theory. These broad range of data were necessary to

derive a self consistent picture, and only after the last data set were obtained, could the conclusions about the complex equilibrium phase behaviour be drawn. At this point I would like to thank again Bob Laughlin, who did never hesitate to share his expertise, to test the correctness of these conclusions and make me aware of the broad range of theoretical knowledge which is reported in the literature. Bob's experience has been invaluable in selecting from the hundreds of articles which have been read for this work, the ones with the most reliable information.

The second major part of this thesis, presents a study of the so-called myelinic figures, wormlike interface instabilities, which are observed during the dissolution of some lamellar phases. Despite their discovery at the beginning of the 18^{th} century, the reason for their formation and growth is still not fully understood.

The formation of myelins from two surfactant systems, DDAB and the non-ionic surfactant $C_{12}E_3$ were investigated. Especially the results obtained in the more stable non-ionic system, support the importance of the osmotic pressure between the surfactant phase and the surrounding water. The growth kinetics of the myelin could be shown to depend on sample concentration, proposed by a previously developed osmotically controlled model, which was based on data of the dissolution of lecithin.

The data suggest that the kinetics of the water which diffuses into the lamellar phase controls the kinetics of myelin growth, which, as a result of the water entering the sample, by osmosis, are pushed out into the surrounding solution.

Further experiments are proposed to obtain a more detailed description of this myelin growth, as well as of the conformational properties of the surfactant molecules in the surfactant phase, which are needed for myelins to form.

Appendix A

Appendix

A.1 LabView codes

LabView is a powerful programming language, which not only allows for control of external equipment, such as cameras, but also for analysis of images. This programming language is not a text-based language as e.g. C++ or FORTRAN, but a graphical one. A code consists of a front-panel, which is a user-interface for using the written program, and a block-diagram, where the steps of the program are defined. The front-panel consists of inputs and outputs. The input parameters can sometimes be changed while a program is running, but often they have to be declared before the start of the program. The block-diagram is in the style of an electronic control board in which single steps are connected by wires. In this section the concept of the codes used in this work will be explained as well as the purpose of them.

LabView was used to control a camera (IEEE 13294) during the direct observation measurements (see section A.1.1) and to manipulate (see section A.1.2) and analyse (see section A.1.3.2) images obtained by this technique as well as by conventional (see section A.1.3.3) and confocal (see A.1.3.4) microscopy. The codes require LabView 8.0 (with Vision) as well as the Vision Assistant 8.0. The programs are written for the camera IEEE 13294, the driver and controls of which have to be installed on the PC.

A.1.1 Controlling the camera for the direct observation measurements

A.1.1.1 Concept

The measurements, which were performed on a direct observation setup, required in general three basic steps.

1. The optics of the setup have to be aligned (PREVIEW.VI).

2. A calibration and a background image have to be taken (SNAP.VI).

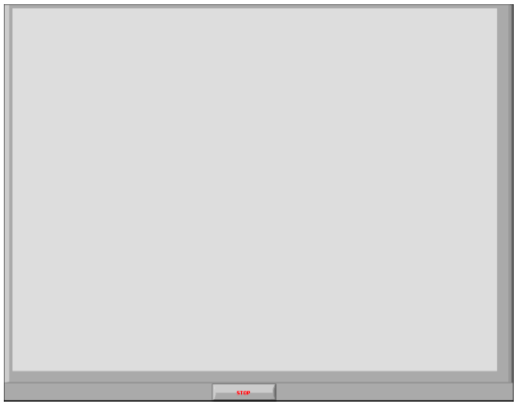

(a)

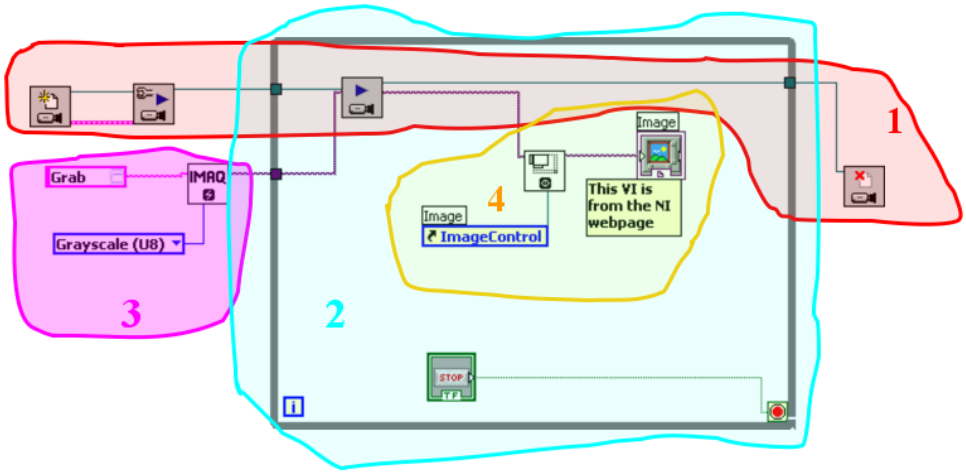

(b)

Figure A.1: Front-panel (a) and block-diagram (b) of PREVIEW.VI.

3. A time series of images with time steps adequate for the sample kinetics have to be taken (GRABBING.VI, where one can, not only control the time steps, but also change them whilst measuring in order to react to changes in the sample kinetics).

In the following, the three steps with their programs will be described in more detail.

A.1.1.2 Aligning the optics

In order to align the optics of a direct observation setup a simple *preview* program is needed. In figures A.1 the commented LabView code of the required program can be found.

The block-diagram consists, first of all, of a step which reads images taken with a camera (1). These images are displayed in the front-panel as an 8bit greyscale picture (3). The while-loop is required for renewing the display every 0.1s so that not only one static image is shown (2). The size of the display is set by the size of the read image (4).

A.1.1.3 Calibration and background correction

For the calibration of the setup, an image of a calibration ruler/grid of an appropriate length scale for the sample (mm range) is needed. Furthermore, an image of the background has to be taken for further background correction of the images (see section A.1.3.1). The program *SNAP.VI*, shown in Fig.A.2, is based on the *preview*-program with the additional option of saving images. Once the program is started, a preview is displayed. The *SNAP*-button saves the image of a given name. The program will ask where the image should be saved. The program offers the possibility of changing the filename/destination in order to save several images.

The block-diagram consists of a while-loop which checks every 1s if the *SNAP*-button is switched. This loop contains a sequence, the first part of which is the *preview*-program. The second part is only executed if the *SNAP*-button is switched. If so, the image is saved using the filename defined in the front-panel. A file-dialog appears asking about the destination folder. The file is saved as a 16bit PNG image[1]. The *SNAP*-button switches automatically off, so that another image can be chosen and saved.

A.1.1.4 Time series

Swelling measurements require a sample to be recorded over a certain period of time. It is reasonable to save only as many pictures as necessary responding to the sample kinetics and the planned analysis. The following concept is used:

- Over the first seconds, a lot of pictures are taken in order to obtain a good estimation of the starting time of the swelling process (water surround the sample).

- Knowing the $t^{1/2}$-dependent swelling behaviour, the time steps Δt between the

[1]This format has been chosen because of the possibility of storing additional information e.g. the calibration to the image.

(a)

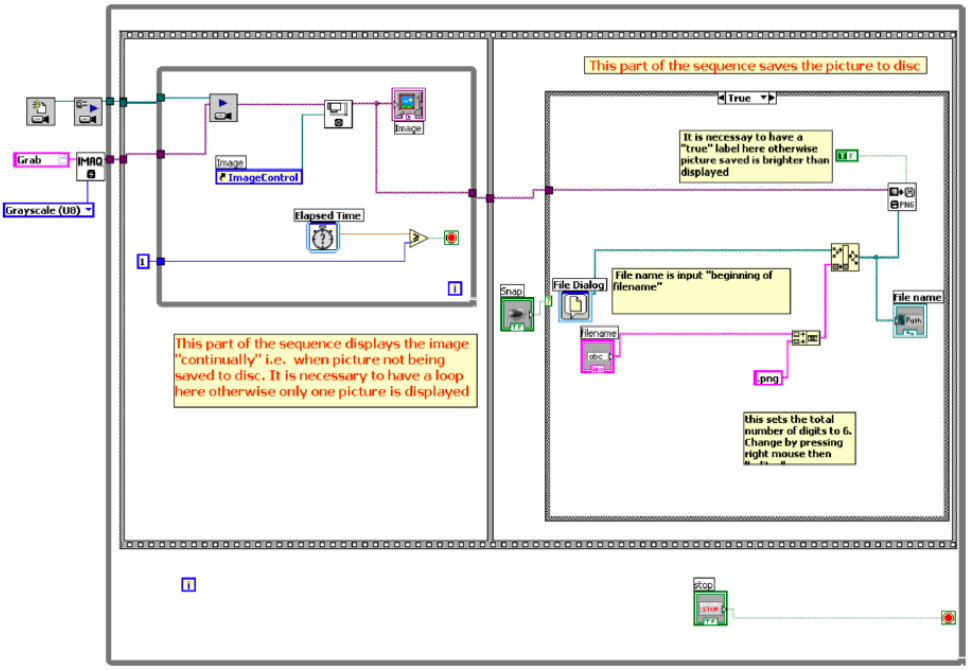

(b)

Figure A.2: Front-panel (a) and block-diagram (b) of Snap.VI.

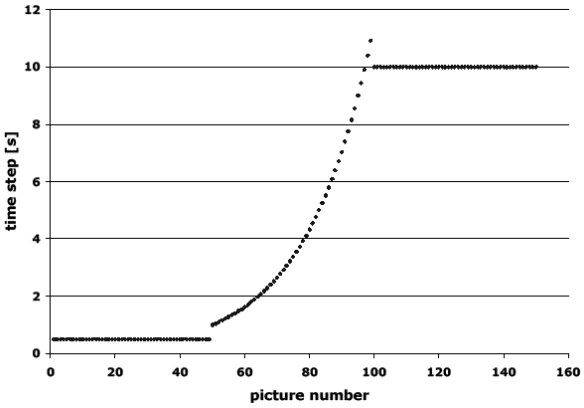

Figure A.3: Time step dependence on picture number. The whole series last over 12 min.

pictures increase with a constant factor a, having

$$\Delta t_n = \Delta t_0 a^n. \tag{A.1}$$

The factor a and the initial time steps Δt_0 have to take into account the sample kinetics, the number of pictures N to be saved and the maximal final step Δt_N. These parameters are related in the following equation

$$t_{all} = \Delta t_0 \frac{a^{N+1} - 1}{a - 1} = \frac{\Delta t_N a - \Delta t_0}{a - 1}, \tag{A.2}$$

where t_{all} is the overall time of this step.

- To obtain an accurate fit of the slope of the line to the data, the last data points are most important. Therefore the last images are taken with a constant rate $\Delta t \approx \Delta t_N$.

Fig.A.3 shows an example of the time-step dependence on image number as was predominantly used in this work.

For the swelling measurements the program *GRABBING.VI*, presented in Fig.A.4, was used. The input data for the time series should be filled before the program is started. When started, a preview is displayed. Images are taken once the *Start grabbing*-button is switched. The destination folder for the images will be chosen. If there is a need to change the input values, the *Start grabbing*-button should be switched off. Switching the button on again starts the program using the picture number, at which it has been interrupted, and using the new input values. The program stops when 'Number'='Number of pictures' or the *STOP*-button is pressed. The time count

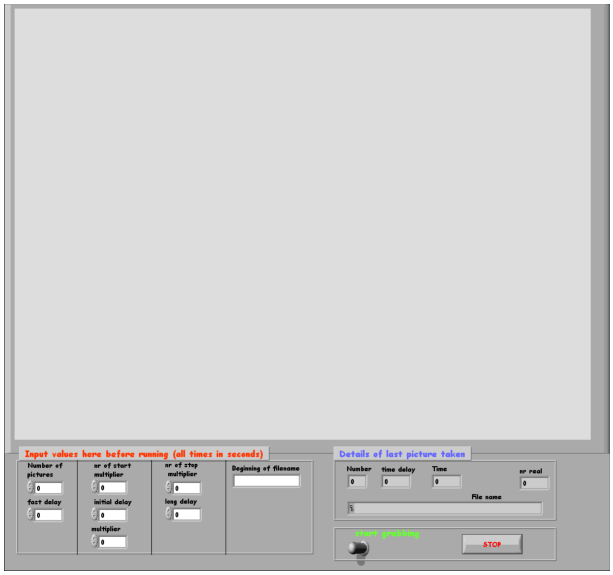

(a)

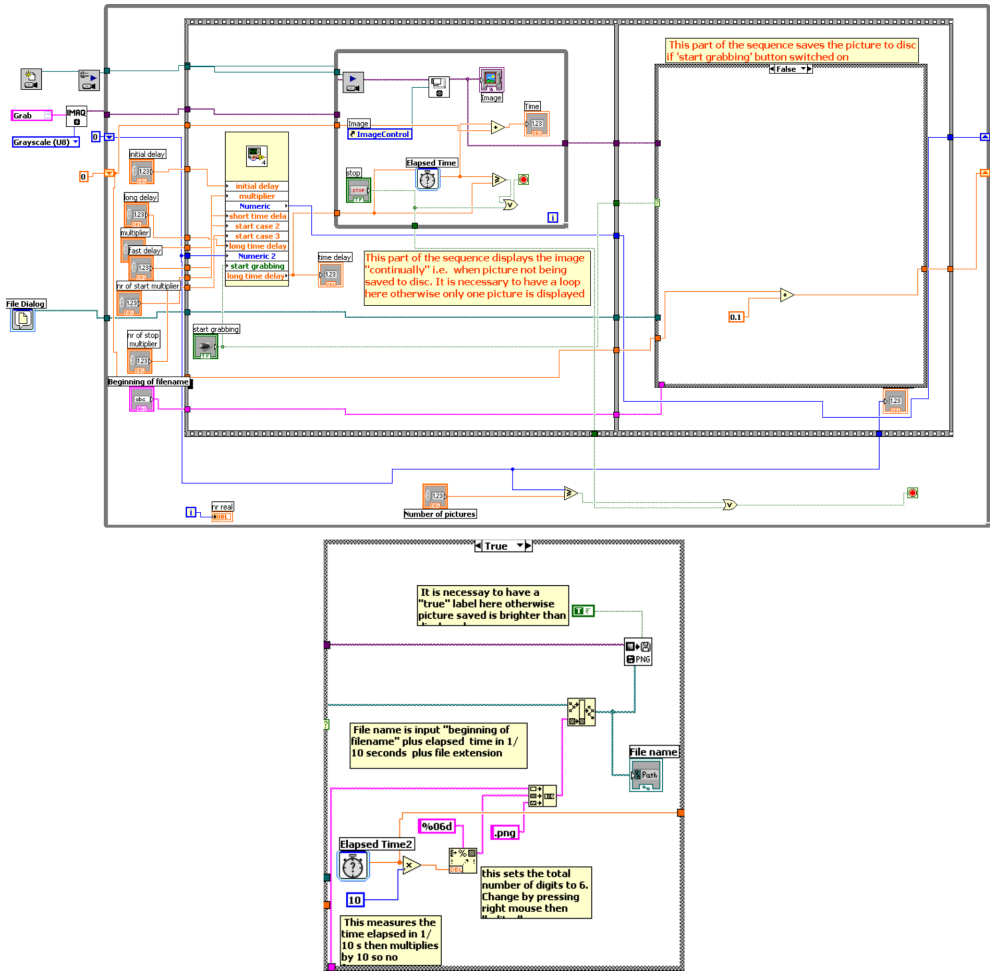

(b)

Figure A.4: Front-panel (a) and block-diagram (b) of GRABBING.VI.

starts, when the program is started. Once the *Start grabbing*-button is switched for the first time, the time count starts again.

The block-diagram follows the same principle as the program *SNAP.VI*. The difference is only that the *Timemultiplier (SubVI).VI* (see Fig.A.5) is added to calculate the correct time step between the pictures based on a case structure:

- '-2' (before the time series starts, or when stopped in between): Its function is to check every 0.1s if the *START*-button of the program has been pressed.
- '-1'(grabbing of first pictures): gives the short time delay and increases picture number by 1.
- '0' (starts when 'number picture'='start case 2'): calculates the increased delay time, using the initial delay and the multiplier and increases the picture number by 1.
- '1' (grabbing last pictures, starts when 'number picture'='start case 3'): gives the long time delay and increases the picture number by 1

Furthermore, the time (displayed in the front-panel) is added in 6 digits to the filename of the images. To give a precise time, the time format is 0.1s.

A.1.2 Manipulating images - Joining images to a movie

Having a set of recorded images, these can be joined to movie (AVI-file). The program *MakeMovie.VI* (see Fig.A.6) writes a certain number of images to a movie. One has to note that the time step (1/*'frame per second'*) between the images is constant and does therefore not correspond to the real time. Therefore, the time needs to be displayed in the movie. Before starting the program, the inputs have to be defined. Upon starting, the first picture as well as the name and destination of the AVI file have to be chosen. The program stops after writing the specified number of pictures to the AVI-file or in case the next picture cannot be found.

The block-diagram contains the following parts:

1. The time is extracted from the file name and the real time calculated, setting the time of the first picture to zero.
2. The next image is searched assuming that the name is oldname(oldtime+x).pgn, where x is increased by 1 until an image is found.
3. The information of the real time is displayed in the image.

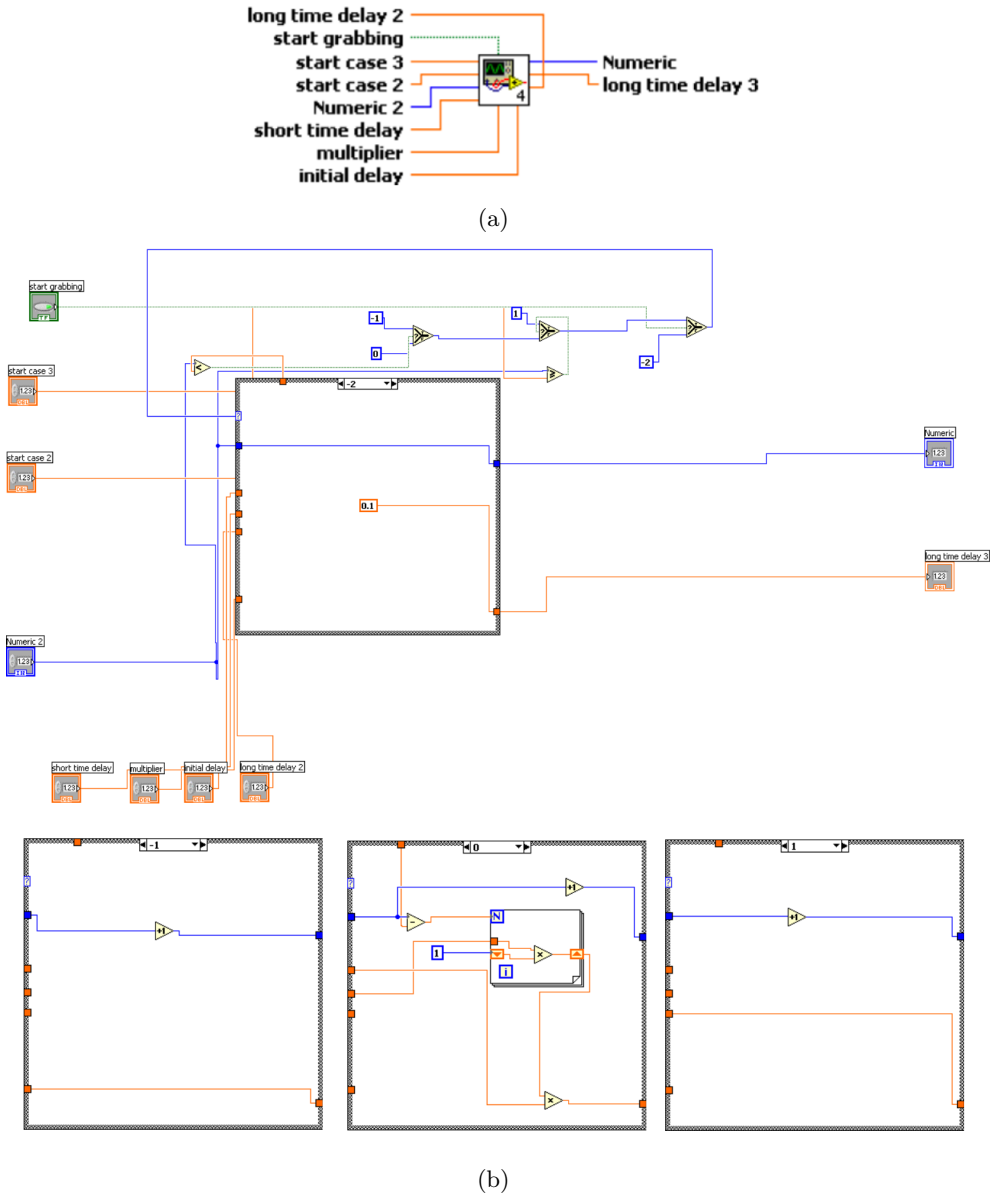

Figure A.5: Connector panel (a) and block-diagram (b) of the SubVI *Timemultiplier*, giving the time step and the actual picture number.

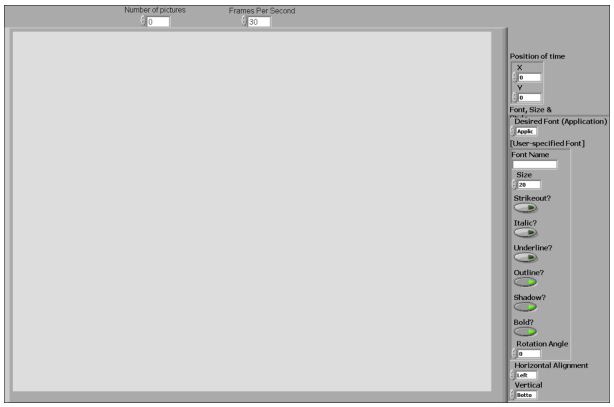

(a)

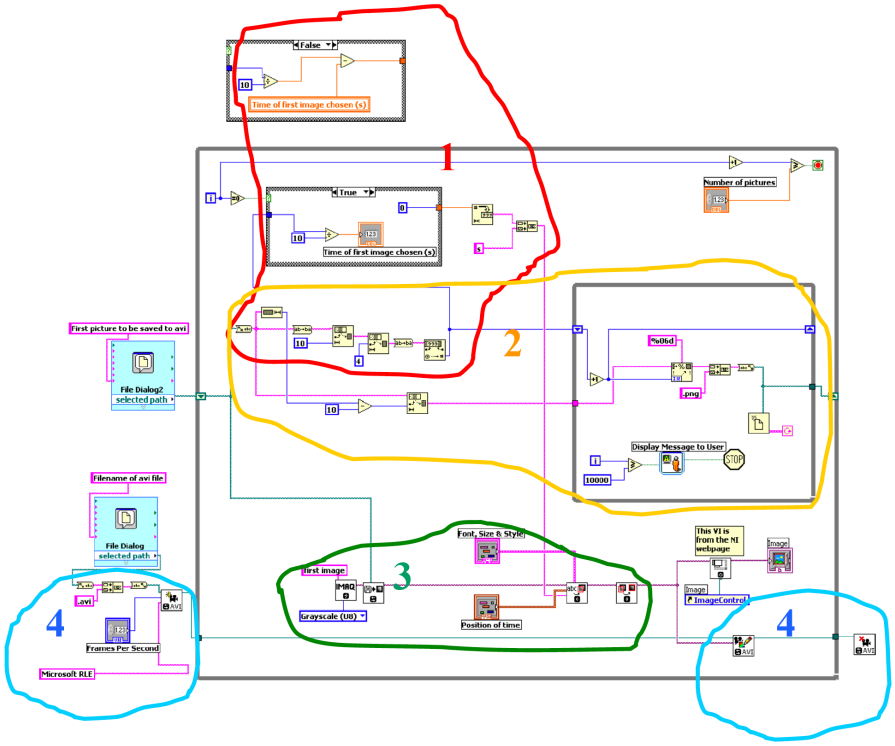

(b)

Figure A.6: Front-panel (a) and block-diagram (b) of MakeMovie.VI.

4. An AVI-file with a specified 'frames per second'-rate and using a chosen compressor is created.

A.1.3 Analysing images

LabView, in combination with Vision Assistant, provides the possibility of analysing images obtained from measurements using the direct observation setup as well as (confocal) microscopy. Most options for image manipulation require an 8-bit image type. Therefore, at the beginning, the image is always converted to this format. In the case of poor image quality, background correction was needed (see section A.1.3.1). The image analysis was based on finding a particle on the image and measuring its size and position (see section A.1.3.2-A.1.3.4). There is a wide range of options such as selecting certain objects, erasing parts of the image, modifying the darkness and contrast as well as measuring distances, areas etc. Therefore, the algorithm, presented here, could be modified if the images required slightly different treatment.

A.1.3.1 Background correction

Even after aligning the optics of e.g. a direct observation setup or microscope, the background image shows that the illumination is not uniform (see Fig.A.7). The variations in the light intensity might be caused by some optical parts not perfectly aligned or by the divergence in the sensitivity of certain pixels in the camera. For particles which are difficult to identify due to their low contrast, the images have to be corrected to maximize resolution.

The image correction contains the following steps:

1. For every pixel, the detected value of a background image $I_b(x, y)$ is set as 100% illumination and the corresponding maximal camera detection.

2. The recorded intensity of an image $I(x, y)$ will be divided by its 100% value, therefore the background intensity. This will give a value of 1 for equal intensity of the image and the background, therefore for points where no (visible) particle is detected. A smaller value corresponds to particles with a greater scattering ability, while bigger values are caused by particles which scatter less light than the background. The latter can only happen, if the background image is taken through a media (e.g. glass plate, water etc.).

3. The obtained ratios *r(x,y)* have to be changed into greyscale values for the corrected image. To obtain maximal resolution in this image, the smallest ratio

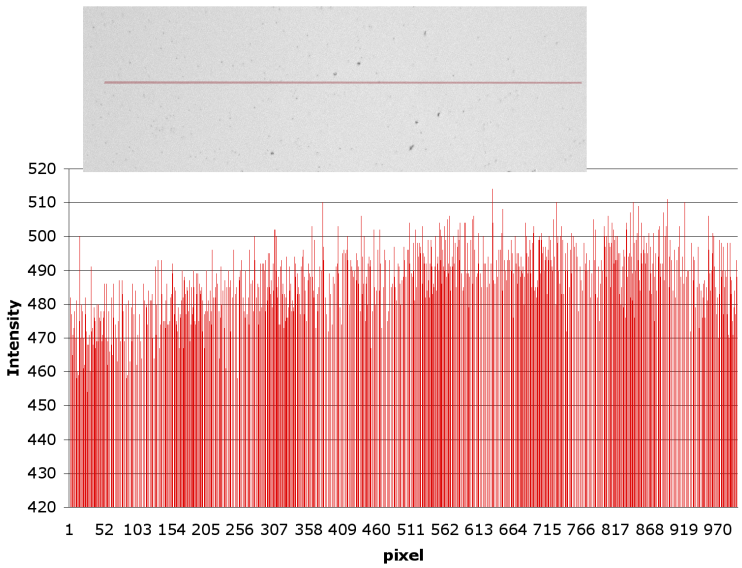

Figure A.7: Line profile of background (image shown in inset).

r_{min} is set to zero and the values are multiplied by a constant I_0.

$$I_{corr}(x,y) = \left(\frac{I(x,y)}{I_b(x,y)} - r_{min} \right) I_0 \tag{A.3}$$

The value I_0 has to be such, that the highest possible ratio is displayed as the highest greyscale value. In general, one can write[2]:

$$I_0 = \frac{`maxgreyscalevalue'}{r_{max} - r_{min}} \overset{8-bit}{=} \frac{255}{r_{max} - r_{min}} \tag{A.4}$$

One should note, that for a whole series of images, which are intended to be analysed using the same parameters, the values x_{min} and I_0 have to be the same for the whole series.

This procedure leads to a uniform background (see Fig.A.8). Furthermore, dirt in the optical path can be removed with the background correction (see Fig.A.9). Thus a more homogeneous image will be obtained, which is independent of the quality of illumination or light detection.

The code for the corresponding LabView program will be explained in more detail

[2]For example, an image showing a maximal arise of brightness of 25% and a maximal decrease of 50%, corresponds to a maximal or minimal ratio against the background of 1.25 and 0.5, respectively. Therefore r_{min}=*0.5* and the difference between the highest and lowest value is 0.75. If all values between 0 and 0.75 have to be displayed on a 8bit greyscale (values between 0-255), than the value I_0 corresponds to the divergence of 255/0.75=340.

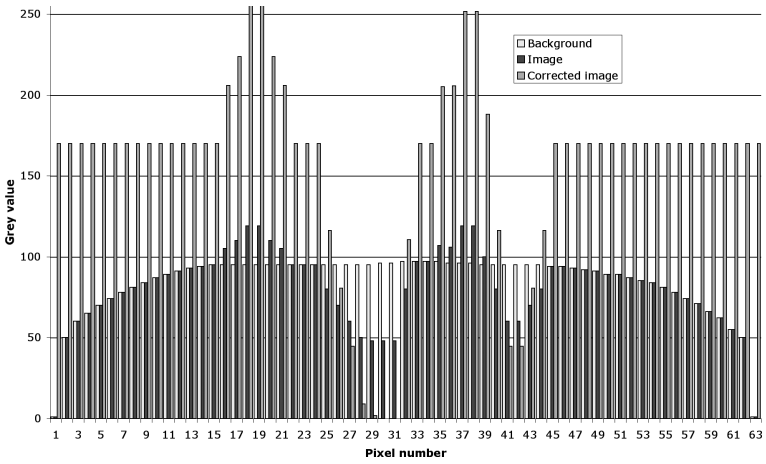

Figure A.8: Line profile of background and image before and after correction.

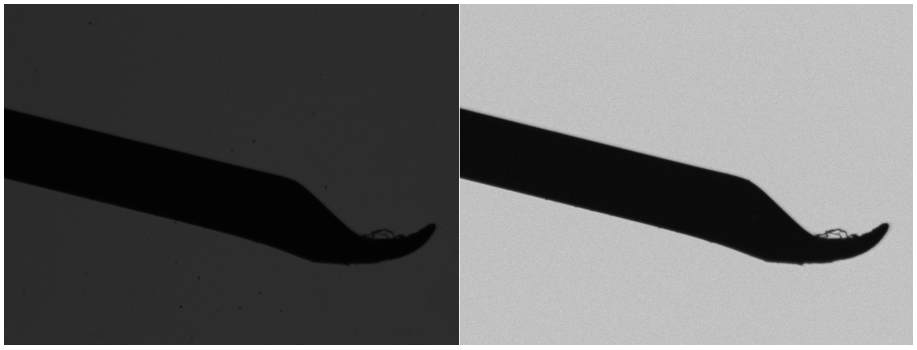

Figure A.9: Image of a needle on a glass plate before (left) and after (right) image correction.

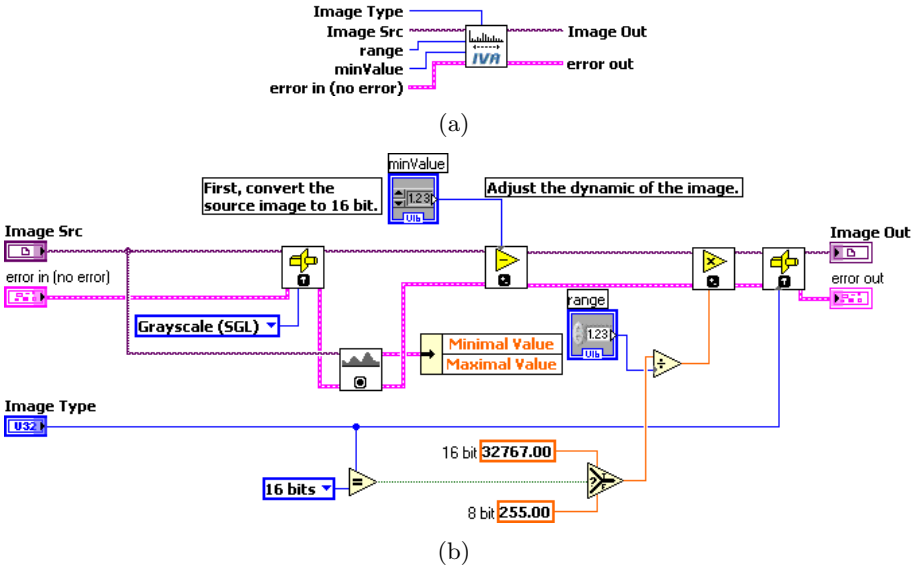

Figure A.10: Connector Pallet (a) and block-diagram (b) of *IVA Adjust Dynamic Whole Range.VI*.

in the following paragraphs. As already mentioned, most of the image processing functions are only available for 8bit greyscale pictures. Therefore the recorded 16bit PGN files have to be converted. To maintain as much information as possible, only the used region of the 16bit scale should be compressed to the much smaller 8bit scale. This has to be done in the same way for the background image and all the images of one series, to not shift the greyscale in the images against each other. This conversion is done in the subVI *IVA Adjust Dynamic Whole Range.VI* (see Fig.A.10).

The input values are the image, which has to be converted, the desired image type, the range in the 16bit scale, which should be considered (*range=(Max*(I_{max}; $I_{b,max}$) and *minValue=Min*(I_{min}; $I_{b,min}$)). After the image is read, the minimal value of interest of the greyscale is subtracted from the grey levels to shift the region of interest to the lowest values. Then the region is divided by 255, to obtain only values between 0 and 255. After this, the first 8 bits of the 16bit image are written to an 8bit image without changes.

The image correction is done according to the ideas introduced above with the *ImageCorrection.VI* (see Fig.A.11). The front-panel displays the image, before correction, as a picture and the corrected image as a matrix of the grey levels. The inputs *Min Grey Level* and *Max-Min* correspond to the image conversion, discussed above. The program converts a certain number of images (input *nb of pictures*) in

(a)

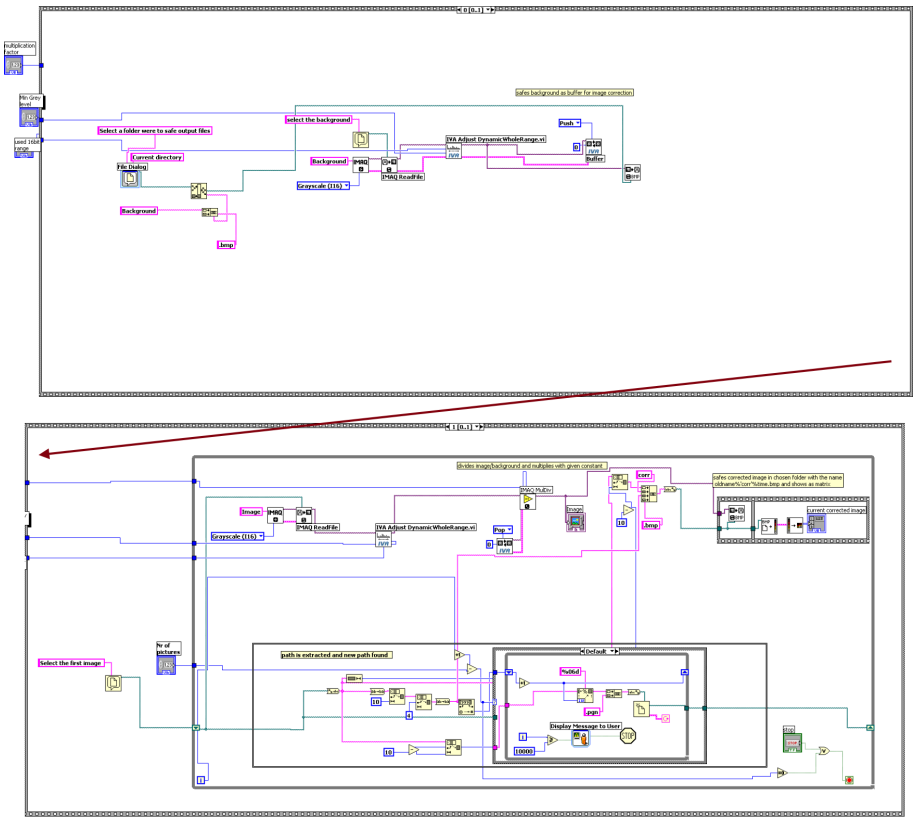

(b)

Figure A.11: Front-panel (a) and block-diagram (b) of *ImageCorrection.VI*.

a folder with the name *name'time+x'.png* and saves them as *corrname'time+x'.bmp*. The input *Multiplication-factor* corresponds to the I_0-factor in Eq.A.4.

The block-diagram consists of a sequence in the first frame, of which the background picture is converted and saved. In the second part, one picture after the next, scanning through the folder, is divided by the background image and multiplied by the multiplication factor. After this, the corrected image is saved and, for control, the image is written into a matrix on the front-panel to give the possibility of controlling the greyscale values.

It should be mentioned that optimising the quality of the images often changes crucial parts, which can lead to a wrong analysis. Therefore, the effect of the image correction was controlled for a few random images of each series.

A.1.3.2 Analysis of images taken in the direct observation setup

Before providing the details about how to analyse the images obtained during the swelling measurements, the images themselves and the ideas will be discussed shortly. The 'ideal' image contains a circular object, the size of which increases with increasing image number. In order to calculate the growing rate, the area of the object has to be measured. Assuming a perfect circle, the growing distance can be obtained from

$$l_n = \sqrt{\frac{A_n}{\pi}} - \sqrt{\frac{A_0}{\pi}}. \tag{A.5}$$

As the recorded images are in general not ideal, this section gives only an idea about the analysis for circular samples which have a sharp edge. Most of the other images were manually analysed based on the proposed concept. In the end of this section, some advice will be given, for minimizing errors in the analysis caused by the experimental setup.

The analysis of a whole time series requires two steps:

1. The threshold grey level of the sample edge is found and the proposed algorithm is tested on one image.
2. The complete series of images is analysed using the input values obtained in step 1.

Analysis of one image In order to analyse a whole time series with the best parameters, at least one image of this series was analysed using the script *FirstPicture.src*

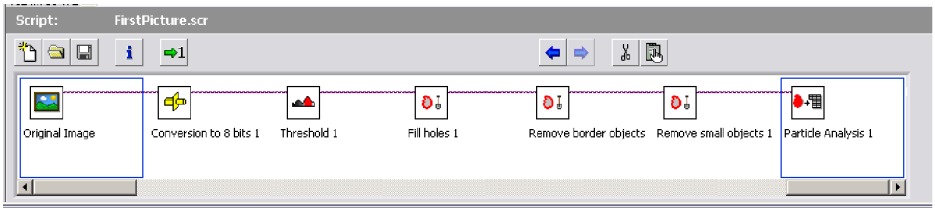

Figure A.12: The steps in the analysis script for Vision Assistant: FirstPicture.src.

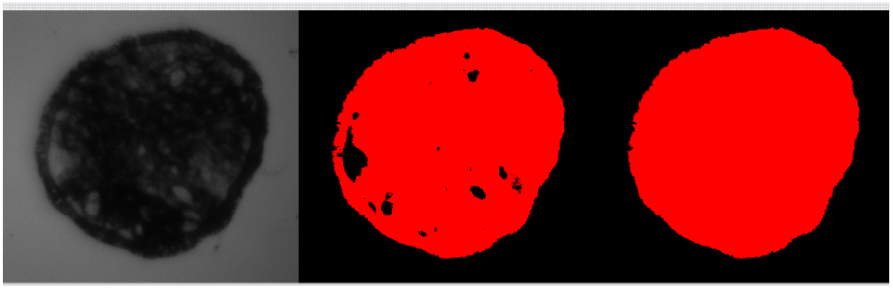

Figure A.13: Change of analysed image in step 4 and 5 of the script.

(see Fig.A.12) in Vision Assistant, which contains all steps, found later in the analysis program. In case this script was insufficient, steps were added or removed. If it was possible to find a new form of the script, which sufficiently analysed all images, this script was saved as a LabView code and the changed parts added to the program ANALYSEPICTURE.VI.

The steps of the script are:

1. The image is opened.
2. The image is converted to an 8bit-format[3].
3. Dark objects (the particles of interest) are selected (see Fig.A.13).
4. Holes within these objects are filled (see Fig.A.13).
5. Border objects are removed.
6. Small objects are removed until only the particle of interest is left.
7. The particle area and its centre of mass is measured.

Analysis of a whole time-series As already mentioned, the analysis of the whole series of images follows the concept used for the single image, only adding a step, which extracts the information of the measurement time from the image name.

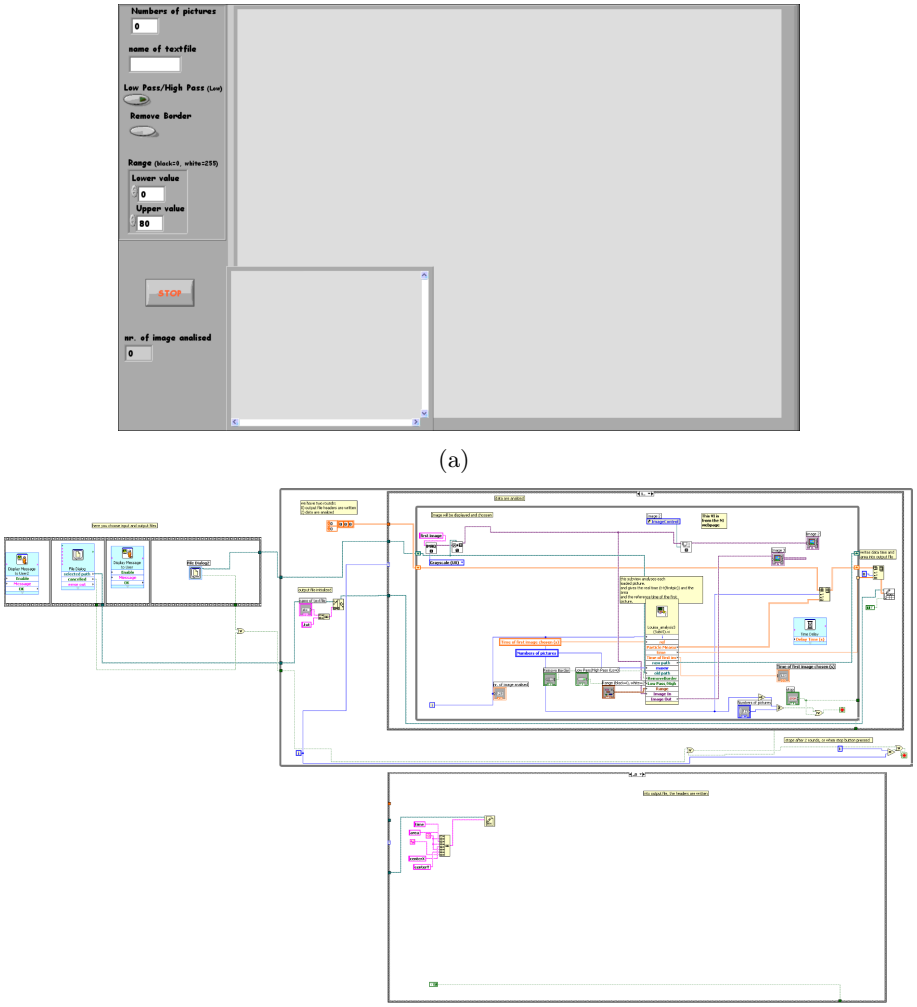

(a)

(b)

Figure A.14: Front-panel (a) and block-diagram (b) of *ANALYSEPICTURE.VI*.

The front-panel of the analysis program is shown in Fig.A.14(a). Before the program is started, the inputs have to be defined. The analysed data is saved in an external .txt file. The *remove border*-button was only switched, if the sample did not touch the border of the image. The range corresponds to the threshold value obtained in for the single image analysis. After starting the program, only the destination of the text file and the first image which should be analysed, are chosen. The program stops when the inserted *number of pictures* has been analysed, the next image cannot be found or the *STOP*-button is pressed. For technical reasons, the last line of the text file contains four zero's.

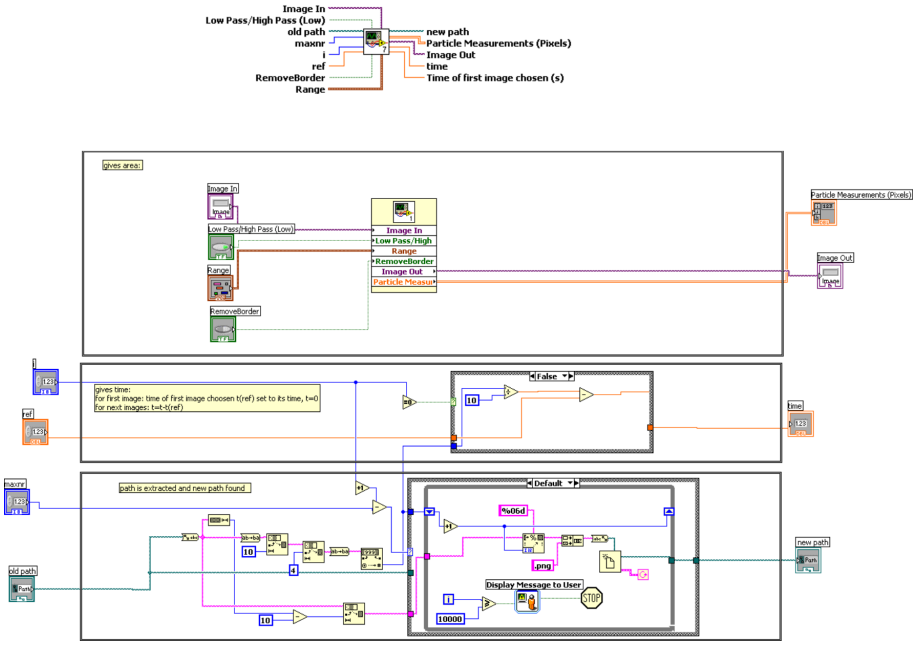

Figure A.15: Connector palette and block-diagram of *AnalysePicture(SubVI).VI*.

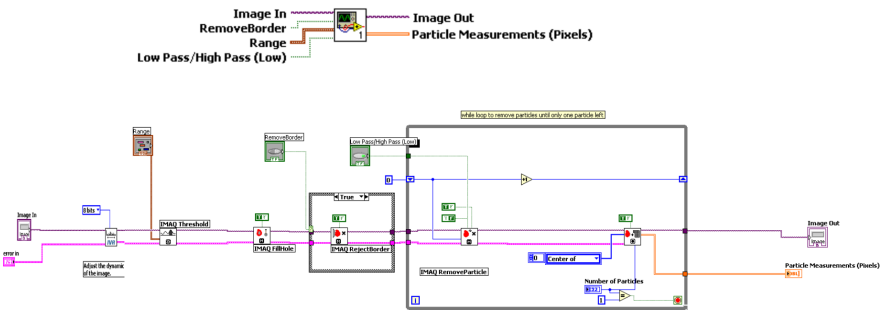

Figure A.16: Connector palette and block-diagram of *GetArea(SubVI).VI*.

The code of the program is written in three different VI's (1 VI and 2 SubVI's). The first one (see Fig.A.14(b)) contains the communication code with the user. It creates a text file and writes into the first line the description 'time area centreX centreY', before the analysis starts.

The second VI (see Fig.A.15) consists of 3 parts. The middle and the bottom ones are responsible for extracting the time from the file name and finding the path to the next image which should be analysed. Both parts have already been discussed in A.1.2. The upper part contains the third VI (see Fig.A.16).

This SubVI consists of the code which has been extracted from the Vision Assistant script (see Fig.A.12). The case structure around the *remove border*-function gives the possibility to enable it if necessary. The while loop around the *removing objects*-function makes sure, that only one particle is left, which will be analysed.

A.1.3.3 Analysis of images taken with a microscope

Images recorded by microscopy have to be analysed measuring the area on a picture occupied by the crystalline phase depending on time. The area occupied by the crystalline phase was selected according to the greyscale value of the pixels. All pixels above a certain threshold value have been counted and added to the area.

In some images, the interface of the crystalline phase is not very clear, but rather characterised by a decrease in density as shown in Fig.5.5. Therefore no sharp jump of the greyscale value on that interface can be found. In this case, a medium greyscale value has been chosen, which selects about half of this interface region. In the case of a linear decrease in density, this would correspond to an effective selection of all crystals.

A.1.3.4 Analysis of images taken with a confocal microscope

In images obtained by confocal microscopy, the image area occupied by the surfactant phase had to be selected. The images of one scan were merged into a montage (see Fig.A.17) using the Confocal Assistant 4.02. The edge of the area occupied by surfactant phase was enhanced manually (using e.g. the program Paint). The modified images were analysed with the Vision Assistant using the following steps (see Fig.A.18):

1. The RGB image is converted into an 8bit greyscale image.
2. Particles above a certain threshold are selected.
3. Holes in the particles are filled.

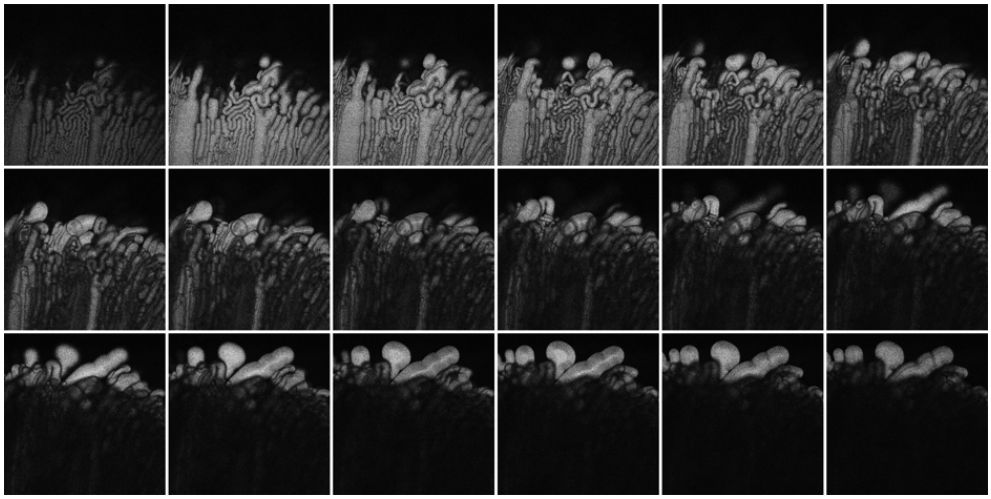

Figure A.17: Typical image obtained during the confocal measurements discussed in chapter 7.

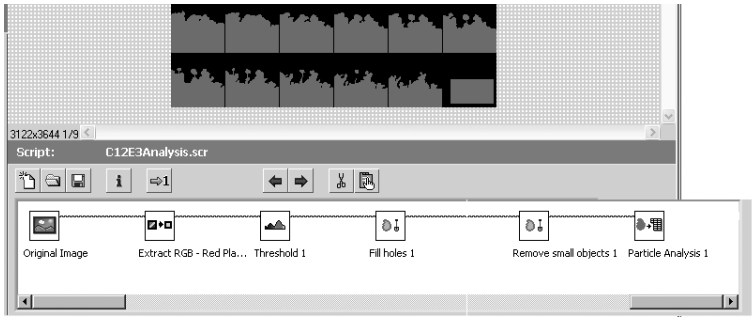

Figure A.18: Vision Assistant Script for the analysis of images obtained by confocal microscopy in chapter 7.

4. Small objects are removed.

5. The measured particle areas, positions and widths for one series are saved in an external file.

A.2 Fortran code for SAXS data

The following fortran code has been used to background correct data, which have been obtained by the SAXS measurements (see section 3.3.3.1). The program has been initially programmed by Wim Pyckhout-Hintzen.

```
program reduceXdata
implicit real*8 (a-h,o-z)
```

```
double precision sample(900),back(900),dark(900),reduced(900)
double precision dreduced(900),dsample(900),dback(900),ddark(900)
double precision theta(900),q(900)
character*30 dummy,answer,file_sample,file_back,file_dark,file_out

print*,'input of 2 plotso(.plt) files:first data, then background'
print*,'data will be normalized by time in seconds (input)'
print*,'and corrected for background'
print*,'output is q,I and deltaI'

write(6,*)'will darkcurrent data also be read in? (y/n/Y/N)'
read(5,'(A)')answer

write(6,*)'input sample-data filename'
read(5,'(A)')file_sample
open(unit=10,name=file_sample,type='old')

write(6,*)'input background-data filename'
read(5,'(A)')file_back
open(unit=11,name=file_back,type='old')

if ((answer.eq.'Y').or.(answer.eq.'y')) then

write(6,*)'input darkcurrent-data filename'
read(5,'(A)')file_dark
open(unit=12,name=file_dark,type='old')

else
endif

write(6,*)'output reduced-data filename'
read(5,'(A)')file_out
open(unit=13,name=file_out,type='unknown')

write(6,*)'sample was measured for time (in seconds):...?'
read(5,*)time_sample
write(6,*)'background was measured for time (in seconds):...?'
read(5,*)time_back

if ((answer.eq.'Y').or.(answer.eq.'y')) then
write(6,*)'dark current was measured for time (in seconds):...?'
read(5,*)time_dark
else
```

```
time_dark=1.
endif

write(6,*)'PURE transmissions of sample and of background'
read(5,*)trans_sample, trans_back
write(6,*)'sample thickness in cm'
read(5,*)thick_sample

write(6,*)'RAW counting rate of standard FEP1400 in cps'
read(5,*)sumfepcps

c FEP1400 characterized at ERSRF: dSigma/dOmega=(6.657+/- 0.002)mm-1
c transmission at NANOSTAR Cu Kalpha=0.382, thickness=0.35mm
c so: D*T*dSigma/dOmega=0.89 dimensionless!

c scaling formula for relation of binned peak-intensity and integral sum
c I-standard=0.00177*sumfepcps-0.00563)

scattfep=0.00177*sumfepcps-0.00563
number=0

do i=1,15
read(10,'(A1)')dummy
read(11,'(A1)')dummy
if ((answer.eq.'Y').or.(answer.eq.'y')) then
read(12,'(A1)')dummy
endif
enddo

do i=1,900
number=number+1
c print*,'number=',number
read(10,*,end=99)theta(i),sample(i),dsample(i),q(i)
c print*,'i,q=',i,q(i)
read(11,*)theta(i),back(i),dback(i),q(i)

if ((answer.eq.'Y').or.(answer.eq.'y')) then
read(12,*)theta(i),dark(i),ddark(i),q(i)
else
dark(i)=0.
ddark(i)=0.
endif
```

Glass Name	**Index of Refraction (nd)**	**Abbe Number (vd)**	**Density** (g/cm^3)	**Coefficient of linear expansion**	**Max. operating T** (°C)	**Lense**
BaK4	1.569	56.10	3.10	7.00	55	Achromat 2/3
BaFN10	1.670	47.10	3.76	6.80	649	Achromat 1
SF10	1.728	28.40	4.28	7.50	454	Achromat 1-3
B270/S1	1.523	58.50	2.55	8.20	533	condenser

Coating	**Coating Description**	**Specifications**
antireflection	Wave MgF_2 at 550nm	Rave≤1.75%, 400-700nm (BK7)
mirror	protected aluminium, wave SiO overcoat	Rave>90%, 400-650nm
first-front mirror	VIS enhanced aluminium, multilayer film of dielectrics wave	Rave>95%, 450-650nm

Table A.1: Characteristics of the glasses and coatings used in the direct observation setup.

```
reduced(i)=(sample(i)/time_sample-dark(i)/time_dark)-
1 trans_sample*(back(i)/time_back-dark(i)/time_dark)
reduced(i)=reduced(i)*0.89/(trans_sample*trans_back*thick_sample
1 *scattfep)

err=(dsample(i)/time_sample)**2+(dback(i)/time_back)**2
dreduced(i)=dsqrt(err)*0.89/(trans_sample*trans_back*thick_sample
1 *scattfep)

write(13,*)q(i),reduced(i),dreduced(i)

enddo
99 print*,'number of data points treated=',number-1
stop
end
```

A.3 Technical specifications of the optics used in the direct observation setup

The glass characteristics of the lenses as well as the coatings of the lenses and the mirrors are summarized in Tab.A.1.

The index of refraction refers to the ratio of the speed of light in a vacuum to the speed of light through a given material at a given wavelength. For lenses of a higher index of refraction, light is bent more efficiently, decreasing the need for curvature in the lense. Thus spherical aberration is less present in lenses with higher indices of

refraction.

The Abbe number of a material quantifies the amount of dispersion (variations in refractive index) for a specific spectral range. A high Abbe number generally gives less colour dispersion and reduces colour aberration.

When dealing with applications involving extreme temperatures and quick temperature differentials, a glass' coefficient of expansion becomes a key factor.

Optical coatings are used to either increase the transmission of light by reducing back reflections (as in the case of lenses, windows, etc.) or to increase the reflection of light (as in the case of mirrors).

A.4 List of abbreviations

Symbol	Quantity
P	Packing parameter Number of phases
v	Volume of surfactant chain Velocity
l	Length of surfactant chain
a_0	Optimal surface area occupied by the surfactant head
F	Degrees of freedom
C	Number of components
c_i	Composition
x_i	Ratio of phases
G	(Gibbs) free energy
H	Enthalpy
S	Entropy
T	Temperature
Z	Number of bonds
N	Number of molecules
E_{ij}	Interaction energy
$\Delta \mathrm{U}_m ix$	Energy of mixing
χ	Interaction parameter
k_B or k	Boltzmann constant
S_{mix}	Entropy of mixing
F	(Elastic) free energy Force
R_i	Principal radius of curvature
κ	mean bending modulus
$\overline{\kappa}$	Gaussian bending modulus
Φ	$\frac{\delta}{d}$
δ	Bilayer thickness
d	Bilayer repeating distance Myelin width
V	Volume of interacting bilayer patches
U_V	Van der Waals interaction
L	Growth rate of nuclei
ϕ_s^0	Initial surfactant concentration
ϕ_w^c	Water concentration of the fully swollen lamellar phase

Symbol	**Quantity**
R	Radius
ϕ_i	Concentration [V/V]: i=w: water i=2 or without i: surfactant i=fs: fully swollen lamellar phase i=t: defects Concentration [w/w]: i=DDAB, C12E3 or DODAB
L_s or l	Growing length
j_i	Volumetric flux of: i=fs: fully swollen lamellar phase i=w: water
t	Time
D_i	Interdiffusion coefficient of : i=fs: fully swollen lamellar phase i=w: water
S	Swelling rate
Π	Osmotic pressure
λ_w	Mobility of water
ζ_w	Slip coefficient of water flow between bilayers
a_w	Water layer thickness
ρ_i	Density Electron density
η	Viscosity of water
b	Thickness of the hydration layer Spacer (sample) thickness
ϵ	Distance between the water-hydration layer interface and the position at which the velocity is zero
a	Radius of defects
T_M	Main transition temperature
m	Molecular mass
s	Area per headgroup
V_m	molecular volume
Σ	Charge denisty
Δ^*	Maximum swelling
δ, a_b^c	Bilayer thickness
a_{Br}	Ion layer thickness
s	Spin

Symbol	Quantity
ν	Frequency
δ	Chemical shift
ΔU	Potential difference
B	Magnetic field strength
ΔE	Energy
h	Planck's constant
$\overline{\nu}$	Wavenumber
c	Velocity of light
Θ_c	Critical angle
P	Induced dipole moment
$\vec{E}$	Electric field
α	Polarizability
I	Intensity
Ψ	Wavefunction
k	Spring constant
m_r	Reduced mass
T_i	Kinetic energy
V_i	Potential energy
F_i	Fock operator
h_i	One-electron hamiltonian
J_{ij}	Coulomb operator
K_{ij}	Exchange operator
E_{EC}	Exchange and correlation energy
Φ	Basis function
Φ_{DODAB}	relative mass fraction of surfactant concentration
c_i and d_i	Coefficient
μ	Electric dipole moment
λ	wavelength
d	Resolution
Q	Quantum yield
τ	life time
A	Area
D^*	Repeating distance
q	$\frac{2sin\Theta}{\lambda}$
σ	Polydispersity

Abbrevation	**Surfactant name**
DDAB	Didodecyl-dimethyl-ammonium bromide
DODAB	Dioctadecyl-dimethyl-ammonium bromide
C_12E_3	Triethylene glycol monododecyl ether

Symbol	**Phase**
L_α	(Swollen) lamellar phase
$L_\alpha^/$	Collapsed L_α phase
$[L_\alpha]$	L_1+L_α
L_β	Gel phase
L_3	Sponge phase
L_1/Iso	Micellar phase
L_2	Inverted micelles
W	Water Dilute monomer solution
X	Crystalline phase
XW_n	Crystal hydrate

Bibliography

[Adkins 83] C.J. Adkins. Equilibrium thermodynamics. Cambridge University Press, Cambridge, 1983.

[Aldrich 09] Sigma Aldrich. *Catalogue.* website, 2009.

[Anderson 95] M. Anderson, L. Hammerstrom & K. Edwards. *Effect of bilayer phase-transitions on vesicle structure and its influence on the kinetics of viologen reduction.* J. Chemical Physics, vol. 99, no. 39, pages 14531–14538, 1995.

[Angelova 86] M.I. Angelova & D.S. Dimitrov. *Liposome Electroformation.* Faraday Discussions Chem. Soc., vol. 81, pages 303–311, 1986.

[Aratono 07] M. Aratono, N. Onimaru, Y. Yoshikai, M. Shigehisa, I. Koga, K. Wongwailikhit, A. Ohta, T. Takiue, B. Lhoussaine, R. Strey, Y. Takata, M. Villeneuve & H. Matsubara. *Spontaneous vesicle formation of single chain and double chain cationic surfactant mixtures.* J. Physical Chemistry B, vol. 111, pages 107–115, 2007.

[Arunagirinathan 04] M.A. Arunagirinathan, M. Roy, A.K. Dua, C. Manohar & J.R. Bellare. *Micro-raman investigation of myelins in Aerosol-OT/water system.* Langmuir, vol. 20, pages 4816–4822, 2004.

[Atkins 05] P. Atkins & R. Friedman. Molecular quantum mechanics. Oxford University Press, Oxford, 2005.

[Bagger-Jörgensen 96] H. Bagger-Jörgensen & U. Olsson. *Experimental study of undulation forces in a nonionic lamellar phase.* Langmuir, vol. 12, page 4057, 1996.

[Bai 01] G. Bai, J. Wang, H. Yan, Z. Li & R.K. Thomas. *Thermodynamics of molecular self-assembly of two series of double-chain singly charged cationic surfactants.* J. Physical Chemistry B, vol. 105, pages 9576–9580, 2001.

[Banwell 94] C.N. Banwell & E.M. McCash. Fundamentals of molecular spectroscopy. McGraw-Hill Book Company, INC, London, 1994.

[Barnhart 82] D.M. Barnhart & D.A. Netzel. *Paramagnetically reduced carbon-13 relaxation times of hydrocarbon types: an aid to the quantitative analyses of shale oil-derived jet fuels.* In Symposium on processung of oil shale tar sands and heavy oils joint with division of petroleum chemistry and industrial and engineering chemistry, pages 233–241, 1982.

[Baryla 01] N.E. Baryla, J.E. Melanson, M.T. McDermott & Ch.A. Lucy. *Characterization of surfactant coatings in capillary electrophoresis by atomic force microscopy.* Analytical Chemistry, vol. 73, pages 4558–4565, 2001.

[Battaglia 06] G. Battaglia & A.J. Ryan. *Pathways of polymeric vesicle formation.* J. Physical Chemistry B, vol. 110, pages 10272–10279, 2006.

[Battaglia 07] G. Battaglia, S. Tomas & A.J. Ryan. *Lamellarsomes: metastable polymeric multilamellar aggregates.* Soft Matter, vol. 3, pages 470–475, 2007.

[Beales 05] P. Beales. Phase separation in binary phopholipids vesicles studied using fluorescence microscopic techniques. Edinburgh University, 2005. PhD Thesis.

[Begum 97] R. Begum & H. Matsuura. *Conformational properties of short poly(oxyethylene) chains in water studied by IR spectroscopy.* J. Chem. Soc. Faraday Trans., vol. 93, pages 3839–3848, 1997.

[Bell 96] G.R. Bell, C.D. Bain & R.N. Ward. *Sum-frequency vibrational spectroscopy of soluble surfactants at the air water interface.* J. Chem. Soc. Faraday Trans., vol. 92, pages 515–523, 1996.

[Benton 86] W.J. Benton, K.H. Raney & C.A. Miller. *Enhanced videomicroscopy of phase transitions and diffusional phenomena in oil-water-nonionic surfactant systems.* J. Colloid and Interface Science, vol. 110, no. 2, pages 363–388, 1986.

[Bergmeier 97] M. Bergmeier, H. Hoffmann & C. Thunig. *Preparation and porperties of ionically charged lamellar phases that are produced without shearing.* J. Physical Chemistry B, vol. 101, 1997.

[Bergstroem 01] M. Bergstroem. *Thermodynamics of unilamellar vesicles: influence of mixing on the curvature free energy of a vesicle bilayer.* J. Colloid and Interface Science, vol. 240, pages 294–306, 2001.

[Biltonen 90] R.L. Biltonen. *A statistical-thermodynamic view of cooperative structural changes in phospholipid bilayer membranes: their potential role in biological function.* J. Chemical Thermodynamics, vol. 22, pages 1–19, 1990.

[Blandamer 97] M.J. Blandamer, B. Briggs, P.M. Cullis, St.D. Kirby & J.B.F.N. Engberts. *Reorganisation of alkyl chains in vesicles formed in aqueous solution by dialkyldimethylammonium bromide, $R_2N^+Me_2Br^-$ where R=$C_{12}H_{25}$, $C_{14}H_{29}$, $C_{16}H_{33}$, $C_{18}H_{37}$.* J. Chem. Soc. Faraday Trans., vol. 93, pages 453–455, 1997.

[Blume 91] A. Blume. *Biological calorimetry.* Thermochimica Acta, vol. 193, pages 299–347, 1991.

[Boroudjerdi 05] H. Boroudjerdi, Y.-W. Kim, A. Naji, R.R. Netz, X. Schlagberger & A. Serr. *Statics and dynamics of strongly charged soft matter.* Physics Reports, vol. 416, pages 129–199, 2005.

[Brochard-Wyart 74] F. Brochard-Wyart. *Proprietes dynamiques des mesomorphes.* PhD thesis, Universite de Paris Sud - Centre d'Orsay, 1974.

[Brochard 75] F. Brochard & P.G. deGennes. *Hydrodynamic properties of fluid lamellar phases of lipid/water.* Pramana Suppl., vol. 1, pages 1–21, 1975.

[Buchanan 99] M. Buchanan. *Dynamics of interfaces in surfactant lamellar phases.* PhD thesis, Edinburgh University, 1999.

[Buchanan 00] M. Buchanan, S.U. Egelhaaf & M.E. Cates. *Dynamics of interface instabilities in nonionic lamellar phases.* Langmuir, vol. 16, pages 3718–3726, 2000.

[Bumajdad 04] A. Bumajdad, M.I. Zaki, J. Eastoe & L. Pasupulety. *Microemulsion-based synthesis of CeO_2 powders with high surface area and high-temperature stabilities.* Langmuir, vol. 20, pages 11223–11233, 2004.

[Caboi 96] F. Caboi & M. Monduzzi. *Didodecyldimethylammonium bromide vesicles and lamellar liquid crystals. A multinuclear NMR and optical microscopy study.* Langmuir, vol. 12, pages 3548–3556, 1996.

[Callow 09] P. Callow, G. Fragneto, R. Cubitt, D.J. Barlow & M.J. Lawrence. *Interaction of cationic lipid/DNA complexes with model membranes as determined by neutron reflectivity.* Langmuir, vol. 25, pages 4184–4189, 2009.

[Caria 96] A. Caria & A. Khan. *Phase behavior of catanionic surfactant mixtures: sodium bis(2-ethylexyl)sulfosuccinate - didodecyldimethylammonium bromide - water system.* Langmuir, vol. 12, pages 6282–6290, 1996.

[Castelli 08] F. Castelli, D. Micieli, S. Ottimo, Z. Minniti, M.G. Sarpietro & V. Librando. *Absorption of nitro-polycyclic aromatic hydrocarbons by biomembrane models: effect of the medium lipophilicity.* Chemospere, vol. 73, pages 1108–1114, 2008.

[CCCBDB 06] CCCBDB. *Computational chemistry comparison and benchmark database.* website, 2006. `http://cccbdb.nist.gov/`.

[Chaplin 09a] M. Chaplin. *Water structure and science: methods.* website, 2009. `http://www1.lsbu.ac.uk/water/methods.html#vib`.

[Chaplin 09b] M. Chaplin. *Water structure and science: water absorption spectrum.* website, 2009. `http://www1.lsbu.ac.uk/water/vibrat.html`.

[Chapman 66] D. Chapman & N.J. Salsbury. *Physical studies of phospholipids Part 5.-proton magnetic resonance studies of molecular motion in some 2,3-dialcyl-DL-phosphatidylethanolamines.* Trans. Faraday Society, vol. 62, pages 2607–2621, 1966.

[Chen 97] F.Y. Chen, W.C. Hung & H.W. Huang. *Critical swelling of phospholipid bilayers.* Physcial Review Letters, vol. 79, pages 4026–4029, 1997.

[Chen 00a] B.H. Chen, C.A. Miller, J.M. Walsh, P.B. Warren, J.N. Ruddock, P.R. Garrett, F. Argoul & C. Leger. *Dissolution rates of pure nonionic surfactants.* Langmuir, vol. 16, pages 5276–5283, 2000.

[Chen 00b] X. Chen, X. Peng, J. Kong & J. Deng. *Facilitated electron transfer from an electrode to horseradish peroxidase in a biomembrane-like surfactant film.* J. Electroanalytical Chemistry, vol. 480, pages 26–33, 2000.

[Chen 01] B.-H. Chen, C.A. Miller & P.R. Garrett. *Dissolution of nonionic surfactant mixtures.* Colloids and Surfaces A, vol. 183-185, pages 191–202, 2001.

[Chen 04] S.-M. Chen & Ch.-Ch. Tseng. *The characterization and bioelectrocatalytic properties of hemoglobin by direct electrochemistry of DDAB film modified electrodes.* Electrochimica Acta, vol. 49, pages 1903–1914, 2004.

[Chizhikov 06] V.A. Chizhikov. *Computer simulation of the 2D crystallization of a lipid membrane: dynamical parquet method.* Crystallography reports, vol. 51, pages 81–86, 2006.

[Chowdhry 84] B.Z. Chowdhry, L. Gert, A.W. Dalziel & J.M. Sturtevant. *Multicomponent phase transitions of diacylphosphatidylethanolamine dispersions.* Biophysical Journal, vol. 45, pages 901–904, 1984.

[Clint 92] J.H. Clint. Surfactant aggregation. Chapmann and Hall LTD, London, 1992.

[Cocquyt 5] J. Cocquyt, U. Olsson, G. Ofsson & P. Van der Meeren. *Thermal transitions of DODAB vesicular dispersions.* Colloid and Polymer Science, vol. 283, no. 12, pages 1376–1381, 2005.

[Connolly 02] D. Connolly & B. Paull. *Fast ion chromatography of common inorganic anions on a short ODS column permanently coated with didodecyldimethylammonium bromide.* J. Chromatography A, vol. 953, pages 299–303, 2002.

[Connolly 04] D. Connolly, D. Victory & B. Paull. *Rapid, low pressure and simultaneous ion chromatography of common inorganic anions and cations on short permanently coated monolithic columns.* J. Separation Science, vol. 27, pages 912–920, 2004.

[D'Angelo 08] G. D'Angelo, U. Wanderlingh, V.C. Nibali, C. Crupi, C. Corsaro & G. Di Marco. *Physical study of dynamics in fully hydrated phospholipid bilayers.* Philosophical magazine, vol. 88, pages 4033–4046, 2008.

[Dave 03] H. Dave, M. Surve, C. Manohar & J. Bellare. *Myelin growth and initial dynamics.* J. Colloid and Interface Science, vol. 264, pages 76–81, 2003.

[De Felici 08] M. De Felici, R. Relici, C. Ferrero, A. Tartari, M. Gambaccini & S. Finet. *Structural characterization of the human cerebral myelin sheath by small angle x-ray scattering.* Physics in medizin and biology, vol. 53, pages 5675–5688, 2008.

[De Gaetani 07] L. De Gaetani & A. Tani. *Sixfold bond orientational properties of a model liquid crystal in the dimensional crossover of B phases: a computer simulation study.* J. Chemical Physics, vol. 126, page 064909, 2007.

[De Meyer 09] F. De Meyer & B. Smit. *Effect of cholesterol on the structure of a phospholipid bilayer.* Proc. Nat. Acad. Sci. USA, vol. 106, pages 3654–3658, 2009.

[Degkwitz 38] R. Degkwitz. *Myelinfiguren und die bei ihrer Entstehung auftretenden Drucke.* Protoplasma, pages 180–183, 1938.

[DeHoff 06] R. DeHoff. Thermodynamics in materials science. Taylor & Francis Group, Boca Raton, 2006.

[Diress 04] A.G. Diress & Ch.A. Lucy. *Electroosmotic flow reversal for the determination of inorganic anions by capillary electrophoresis with methanol-water buffers.* J. Chromatography A, vol. 1027, pages 185–191, 2004.

[Du 98] H. Du, R.A. Fuh, J. Li, A. Corkan & J.S. Lindsey. *Photochem-CAD: A computer-aided design and research tool in photochemistry.* Photochemistry and Photobiology, vol. 68, pages 141–142, 1998.

[Dubois 91] M. Dubois & Th. Zemb. *Phase behavior and scattering of double-chain surfactants in diluted aqueous solutions.* Langmuir, vol. 7, pages 1352–1360, 1991.

[Dubois 92] M. Dubois, Th. Zemb, L. Belloni, A. Delville, P. Levitz & R. Setton. *Osmotic pressure and salt exclusion in electrostatically swollen lamellar phases.* J. Chemical Physics, vol. 96, pages 2278–2286, 1992.

[Dubois 98] M. Dubois, Th. Zemb, N. Fuller, R.P. Rand & V.A. Parsegian. *Equation of state of a charged bilayer system: measure of the entropy of the lamellar-lamellar transition in DDABr.* J. Chemical Physics, vol. 108, pages 7855–7869, 1998.

[Dubois 00] M. Dubois & Th. Zemb. *Swelling limits for bilayer microstructures: the implosion of lamellar structure versus disordered lamellae.* Current Opinion in Colloid & Interface Science, vol. 5, pages 27–37, 2000.

[Dynarowicz 97] P. Dynarowicz, M. Godlewska & W. Witko. *Thermal and optical properties of some dialkyldimethylammonium bromides.* Molecular Crystals and Liquid Crystals Science and Technology C, vol. 8, pages 309–317, 1997.

[Edwards 05] H. Edwards & J. Chalmers, editeurs. Raman spectroscopy in archeology and art history. RSC, Cambridge, 2005.

[Evans 94] D.F. Evans & H Wennerstrom. The colloidal domain: where physics, chemistry, biology and technology meet. Wiley VCH, New York, 1994.

[Everett 88] D.H. Everett. Basic principles of colloidal science. RSC, Cambridge, 1988.

[Feitosa 97] E. Feitosa & W. Brown. *Fragment and vesicle structures in sonicated dispersions of dioctadecyldimethylammonium bromide.* Langmuir, vol. 13, no. 18, pages 4810–4816, 1997.

[Feitosa 00] E. Feitosa, P.C.A. Barreleiro & G. Olofsson. *Phase transition in dioctadecyldimethylammonium bromide and chloride vesicles prepared by different methods.* Chemistry and Physics of Lipids, vol. 105, pages 201–213, 2000.

[Feitosa 06a] E. Feitosa, F.R. Alves, A. Niemiec, M.E. Oliveira, E.M.S. Castanheira & A.L.F. Baptista. *Cationic liposomes in mixed didodecyldimethylammonium bromide and dioctadecyldimethylammonium bromide aqueous dispersions studied by differential scanning calorimetry, nile red fluorescence and turbidity.* Langmuir, vol. 22, pages 3579–3585, 2006.

[Feitosa 06b] E. Feitosa, J. Jansson & B. Lindman. *The effect of chain length on the melting temperature and size of dialkyldimethylammonium bromide vesicles.* Chemistry and Physics of Lipids, vol. 142, pages 128–132, 2006.

[Feitosa 08] E. Feitosa & F. R. Alves. *The role of counterion on the thermotropic phase behavior of DODAB and DODAC vesicles.* Chemistry and Physics of Lipids, vol. 156, pages 13–16, 2008.

[Ferraro 03] J.R. Ferraro, K. Nakamoto & C.W. Brown. Introductory raman spectroscopy. Academic Press, London, 2003.

[Finean 57] J.B. Finean. *The role of water in the structure of peripheral nerve myelin.* J. Biophysics and Biochemistry, vol. 3, page 95102, 1957.

[Fontana 03] A. Fontana, P. Maria, G Siani & B.H. Robinson. *Kinetics of breakdown of vesicles from didodecyldimethylammonium bromide induced by single chain surfactants and by osmotic stress in aqueous solution.* Colloids and Surfaces B, vol. 32, pages 365–374, 2003.

[Fonteijn 92] T.A.A. Fonteijn, D. Hoekstra & J.B.F.N. Engberts. *Vesicle formation of di-n-alkyl phosphates: liquid crystalline behavior, myelinization, counterion influence and stability.* Langmuir, vol. 8, pages 2437–2447, 1992.

[Foucault 03] R. Foucault, R.L. Birke & J.R. Lombardi. *SERS of surfactants in monolayer and multibilayer forms on an electrified Ag surface.* Langmuir, vol. 19, pages 8818–8827, 2003.

[Frohmann 06] E.M. Frohmann, M.K. Racke & C.S. Raine. *Multiple Sclerosis - the plaque and its pathogenesis.* The New England Journal of Medicin, vol. 354, pages 942–955, 2006.

[Fu 02] Y. Fu, T. Zhang & Ch. Sun. *Multilayer films of cationic surfactants incorporating polyoxometalrate on electrodes.* J. Solid State Electrochemistry, vol. 7, pages 25–29, 2002.

[Gans 71] P. Gans. Vibrating molecules: An introduction to the interpretation of infrared and raman spectra. Chapmann and Hall LTD, London, 1971.

[Garidel 01] P. Garidel, W. Richter, G. Rapp & A. Blume. *Structural and morphological investigations of the formation of quasi-crystalline phases of 1,2-dimyristoyl-sn-glycero-3-phosphoglycerol (DMPG).* Physical Chemistry Chemical Physics, vol. 3, pages 1504–1513, 2001.

[Gaussian03 09] Gaussian03. *Online Manual*, 2009. `http://www.gaussian.com`.

[Gedig 08] M. Gedig, S. Faiss & A. Janshoff. *Melting and interdigitation of microstructured solid supported membranes quantified by imaging ellipsometry.* Biointerphases, vol. 3, pages FA51–FA58, 2008.

[Godlewska 97] M. Godlewska, S. Wrobel, B. Borzecka-Prokop, M. Michalec & P. Dynarowicz. *Phase Behavior of Didodecyldimethylammonium bromide.* Molecular Crystals and Liquid Crystals Science and Technology A, vol. 300, pages 113–126, 1997.

[Godlewska 98] M. Godlewska, B. Borzecka-Prokop, P. Dynarowicz-Latka & J. Przedmojski. *Phase Behaviour of a series of dialkyldimethylammonium-bromides studied by powder X-ray diffraction method.* Molecular Materials, vol. 9, pages 217–225, 1998.

[Gordon 08] V.D. Gordon, M. Deserno, C.M.J. Andrew, S.U. Egelhaaf & W.C.K. Poon. *Adhesion promotes phase separation in mixed-lipid membranes.* EPL, vol. 84, page 48003, 2008.

[Gottlieb 97] H.E. Gottlieb, V. Kotlyar & A. Nudelman. *NMR Chemical Shifts of Common Laboratory Solvents as trace impurities.* J. Organic Chemistry, vol. 62, no. 7512-7515, 1997.

[Griffiths 75] P.R. Griffiths. Chemical infrared fourier transformed spectroscopy. John Wiley and Sons, New York, 1975.

[Groth 03] C. Groth, J. Bender & M. Nyden. *Diffusion of water in multilamellar vesicles of dialkyl and dialkyl ester ammonium surfactants.* Colloids and Surfaces A, vol. 228, pages 64–73, 2003.

[Gruger 94] A. Gruger & C. Vogel-Weill. *Raman and infrared microspectrometric structural-analysis of myelin forms from the system 2-g-octadecenoic acid plus hydrazine 5M solution and the system cholesterol monohydrate plus sodium oleate saturated solution.* Molecular Crystals and Liquid Crystals Science and Technology A, vol. 238, pages 227–239, 1994.

[Guo 08] Zh. Guo, J. Chen, H. Liu & Ch. Cha. *Direct electrochemistry of hemoglobin and myoglobin at didodecyldimethylammonium bromide-modified powder microelectrode and application for electrochemical detection of nitric oxide.* Analytica chimica acta, vol. 607, pages 30–36, 2008.

[Guto 06] P.M. Guto & J.F. Rusling. *Myoglobin retains iron heme and near-native conformation in DDAB films prepared from pH 5 to 7 dispersions.* Electrochemistry Communications, vol. 8, pages 455–459, 2006.

[Haas 98] S. Haas. *Phasen- und Aggregationsverhalten zweikettiger, kationischer Tenside aus der homologen Reihe der N-alkyl, N-alkyl', N, N-dimethylammoniumbromide.* PhD thesis, University of Bayreuth, Bayreuth, 1998.

[Haas 99] S. Haas, H. Hoffmann, C. Thuning & E. Hoinkis. *Phase and aggregation behaviour of double-chain cationic surfactants from the class of N-alkyl-N-alkyl'-N,N-dimethylammonium bromide surfactants.* Colloid and Polymer Science, vol. 277, pages 856–867, 1999.

[Han 09] J.J. Han & D.W. Boo. *Reversible immobilization of diffusive membrane-associated proteins using a liquid-gel bilayer phase transition: a case study of annexin V monomers.* Langmuir, vol. 25, pages 3083–3088, 2009.

[Harada 01] M. Harada, S. Itakura, A. Shioi & M. Adachi. *Processes of silica network structure formation in reverse micellar systems.* Langmuir, vol. 17, pages 4189–4195, 2001.

[Haran 02] M. Haran, A. Chowdhury, C. Manohar & J. Bellare. *Myelin growth and coiling.* Colloids and Surfaces A, vol. 205, pages 21–30, 2002.

[Harwood 97] L.M. Harwood & T.D.W. Claridge. Introduction to organic spectroscopy. Oxford University Press, Oxford, 1997.

[Hatsis 03] P. Hatsis & Ch.A. Lucy. *Improved sensitivity and characterization of high-speed ion chromatography of inorganic anions.* Analytical Chemistry, vol. 75, pages 995–1001, 2003.

[Heimburg 03] T. Heimburg. *Coupling of chain melting and bilayer structure: domains, rafts, elasticity and fusion.* In H.T. Tien & A. Ottova-Leitmannova, editeurs, Planar lipid bilayers (BLMs) and their applications, chapitre 8, pages 269–293. Elsevier, Amsterdam, 2003.

[Helfrich 78] W.Z. Helfrich. *Steric interaction of fluid membranes in multilamellar systems.* Naturforsch, vol. 33a, 1978.

[Hemminger 89] W.F. Hemminger & Cammenga H.K. Methoden der thermischen Analyse. Springer Verlag, Berlin, 1989.

[Hendra 75] P.J. Hendra & H.A. Majid. *The structure of crystalline polyethylene sulphide - a laser Raman study.* J. Material Science, vol. 10, pages 1871–1873, 1975.

[Hess 98] M.W. Hess, E. Kirschning, K. Pfaller, P.L. Debbage, H. Hohenberg & G. Klima. *5000-year-old myelin: uniquely intact in molecular configuration and fine structure.* Current Biology, vol. 8, pages R512–R513, 1998.

[Horinek 09] D. Horinek, S.I. Mamatkulov & R.R. Netz. *Rational design of ion force fields based on thermodynamic solvation properties.* J. Chemical Physics, vol. 130, page 124507, 2009.

[Howe 08] J. Howe, P. Garidel, M. Wulf, S. Gerber, G. Milkereit, V. Vill, M. Roessle & K. Brandenburg. *Structural polymorphism of hydrated monoacylated maltose glycolipids.* Chemistry and Physics of Lipids, vol. 155, pages 31–37, 2008.

[Hu 07] Y. Hu, H. Sun & N. Hu. *Assembly of layer-by-layer films of electroactive hemoglobin and surfactant didodecyldimethylammonium bromide.* J. Colloid and Interface Science, vol. 314, pages 131–140, 2007.

[Ignaszak 09] A. Ignaszak, N. Hendricks, T. Waryo, E. Sogna, N. Iahed, R. Ngece, A. Al-Ahmed, B. Kgarebe, P. Baker & E.I. Iwuoha. *Novel therapeutic biosensor for indinavir - A protease inhibitor antiretroviral.* J. Pharmaceutical and Biomedical Analysis, vol. 49, pages 498–501, 2009.

[Israelachvili 98] J.N. Israelachvili. Intermolecular and surface forces. Academic Press, London, 1998.

[Jones 05] J.W. Jones, L. Lue, A. Saiani & G.J.T Tiddy. *Density measurements through the gel and lamellar phase transition of di-tetradecanoyl- and di-hexadecanoyl-phosphatidylcholines: observation of slow relaxation processes mechanisms of phase transitions.* Liquid Crystals, vol. 32, pages 1465–1481, 2005.

[Jönsson 01] B. Jönsson, B. Lindman, K. Holmberg & B. Kronberg. Surfactants and polymers in aqueous solution. John Wiley and Sons, Chichester, 2001.

[Kacperska 00] A. Kacperska. *DSC investigations of DDAB, DTAB and DHAB vesicle aqueous solutions in presence of SDS.* J. Thermal Analysis and Calorimetry, vol. 61, pages 63–73, 2000.

[Kajiyama 79] T. Kajiyama, A. Kumano, M. Takayanagi, Y. Okahata & T. Kunitake. *Crystal-liquid crystal phase transformation and water permeability of artificial amphiphiles as biomembrane model.* Chemistry Letters, pages 645–648, 1979.

[Karukstis 03] K.K. Karukstis, C.A. Zieleniuk & M.J. Fox. *Fluorescence characterization of DDAB-AOT catanionic vesicles.* Langmuir, vol. 19, pages 10054–10060, 2003.

[Kawabata 09] Y. Kawabata, A. Matsuno, T. Shinoda & T. Kato. *Formation process of bilayer gel structure in a nonionic surfactant solution.* J. Physical Chemistry B, vol. 113, pages 5686–5689, 2009.

[Kelly 06] D. Kelly. Confocal microscopy. Talk, University of Edinburgh, 2006.

[Kennedy 05] A.P. Kennedy, J. Sutcliffe & J.-X. Cheng. *Molecular composition and orientation in myelin figures characterized by coherent anti-stokes raman scattering microscopy.* Langmuir, vol. 21, pages 6478–6486, 2005.

[Kharakoz 00] D.P. Kharakoz & E.A. Shlyapnikova. *Thermodynamics and kinetics of the early steps of solid-state nucleation in the fluid lipid bilayer.* J. Physical Chemistry B, vol. 104, pages 10368–10378, 2000.

[Kharakoz 07] D.P. Kharakoz, M.S. Panchelyuga, E.I. Tiktopulo & E.A. Shlyapnikova. *Critical temperatures and critical chain length in saturated diacylphosphatidylcholines: calorimetric, ultrasonic and Monte Carlo simulation study of chain-melting/ordering in aqueous lipid dispersions.* Chemistry and Physics of Lipids, vol. 150, pages 217–228, 2007.

[Kiefer 95] W. Kiefer. *Raman Spektroskopie.* In D. Haarer & H.W. Spiess, editeurs, Spektroskopie amorpher und kristalliner Festk´orper, chapitre 5, pages 118–147. Steinkopff Verlag, Darmstadt, 1995.

[Kodama 90] M. Kodama, T. Kunitake & S. Seki. *Thermal characterization of the mode of phase transition in the dioctadecyldimethylammonium bromide-water system in relation to the stability of its gel phase.* J. Physical Chemistry, vol. 94, pages 1550–1554, 1990.

[Kodama 06] T. Kodama, A. Ohta, K. Toda, T. Katada, T. Asakawa & S. Miyagishi. *Fluorescence-probe study of vesicle and micelle formations in a binary cationic surfactant system.* Colloids and Surfaces A, vol. 277, pages 20–26, 2006.

[Koynova 98] R. Koynova & M. Caffrey. *Phases and phase transitions of the phosphatidylcholines.* Biochimica et Biophysica Acta, vol. 1376, pages 91–145, 1998.

[Kumano 84] A. Kumano, T. Kajiyama, M. Takayanagi, T. Kunitake & Y. Okahata. *Phase transition behavior and permeation properties of cationic and anionic artificial lipids with two alkyl chains.* Berichte der Bunsengesellschaft Phys. Chem., vol. 88, pages 1216–1222, 1984.

[Kunitake 77] T. Kunitake, Y. Okahata, K. Tamaki, F. Kumamaru & M. Takayanagi. *Formation of the bilayer membrane from a series of quaternary ammonium salts.* Chemistry Letters, pages 387–390, 1977.

[Kunitake 84] T. Kunitake, A. Tsuge & N. Nakashima. *Immobilization of ammonium bilayer membrane by complexation with anionic polymers.* Chemistry letters, pages 1783–1786, 1984.

[Langlois 95] V. Langlois & J.M. Williams. *Synthesis and lyotropic phase behaviour of methyl 3',4'-di-O-hexyl and -di-O-octyl-β-lactoside and partial O-acetylation of methyl 3',4'-di-O-octyl-β-lactoside.* J. Chem. Soc. Perkin Trans., vol. 1, pages 1611–1614, 1995.

[Laughlin 90] R.G. Laughlin, R.L. Munyon, Y.-C. Fu & A.J. Fehl. *Physical science of the dioctadedyldimethylammonium chloride-water system. 1.Equilibruim phase behavior.* J. Physical Chemistry, vol. 94, pages 2546–2552, 1990.

[Laughlin 91] R.G. Laughlin, R.L. Munyon, Y.-C. Fu & T.J. Emge. *Physical science of the dioctadedyldimethylammonium chloride-water system. 2. Kinetic and mechanistic aspects.* J. Physical Chemistry, vol. 95, pages 3852–3856, 1991.

[Laughlin 92] R.G. Laughlin, R.L. Munyon, J.L. Burns, T.W. Coffindaffer & Y. Talmon. *Physical science of the dioctadedyldimethylammonium chloride-water system. 3. Colloidal aspects.* J. Physical Chemistry, vol. 96, pages 374–383, 1992.

[Laughlin 94] R.G. Laughlin. The aqueous phase behaviour of surfactants. Academic Press, London, 1994.

[Laughlin 97] R.G. Laughlin. *Equilibrium vesicles: fact or fiction?* Colloids and Surfaces A, vol. 128, pages 27–38, 1997.

[Laughlin 98] R.G. Laughlin. *Recent advances in aqueous surfactant phase science: coexistence relationships of the "Sponge" phase.* In D.O. Shah, editeur, Micelles, Microemulsions, and Monolayers, pages 73–100. Marcel Dekker, New York, 1998.

[Laughlin 00] R.G. Laughlin, M.L. Lynch, C. Marcott, R.L. Munyon, A.M. Marrer & K.A. Kochvar. *Phase studies by diffusive interfacial transport using near-infrared analysis for water (DIT-NIR).* J. Physical Chemistry B, vol. 104, pages 7354–7362, 2000.

[Laughlin 09] R. G. Laughlin, 2009. private conversation.

[Lawrence 51] A.S.C Lawrence & Mills O.S. *5. Colloids and surface chemistry.* Annual reports, pages 78–86, 1951.

[Leekumjorn 07] S. Leekumjorn & A.K. Sum. *Molecular studies of the gel to liquid-crystalline phase transition for fully hydrated DPPC and DPPE bilayers.* Biochimica et Biophysica Acta, vol. 1768, pages 354–365, 2007.

[Lemmich 96] J. Lemmich, K. Mortensen, J.H. Ipsen, Th. Honger, R. Bauer & O.G. Mouritsen. *Small-angle neutron scattering from multilamellar lipid bilayers: theory, model and experiment.* Physical Review E, vol. 53, pages 5169–5180, 1996.

[Leng 06] J. Leng, M.E. Cates & S.U. Egelhaaf. A simple model for myelin growth. to be published, 2006.

[Lentz 76] B.R. Lentz, Y. Barenholz & T.E. Thompson. *Fluorescence depolarization studies of phase transitions and fluidity in phospholipid bilayers. 1. Single component phosphatidylcholine liposomes.* Biochemistry, vol. 15, pages 4521–4528, 1976.

[Levine 72] Y.K. Levine. *Physical Studies of membrane structure.* Progress in Biophysics and Molecular Biology, vol. 24, pages 1–74, 1972.

[Li 02] X. Li, T. Imae, D. Leisner & M.A. Lopez-Quintela. *Lamellar structures of anionic poly(amido amine) dendrimers with oppositely charged didodecyldimethylammonium bromide.* J. Physical Chemistry B, vol. 106, pages 12170–12177, 2002.

[Li 08] Y. Li, Q. Liu & Sh. Yao. *Cationic double-chained surfactant as pseudo-stationary phase in micellar electrokinetic capillary chromatography for drug separations.* Talanta, vol. 75, pages 677–683, 2008.

[Li 09] D. Li, P. Li, G. Li, J. Wang & E. Wang. *The effect of nocodazole on the transfection efficiency of lipid-bilayer coated gold nanoparticles.* Biomaterials, vol. 30, pages 1382–1388, 2009.

[Liang 03] J.Y. Liang, G. Lin, X. Bin, L. Jing, L.X. Dong, W.Z. Hua, W.Z. Yu & J. Weber. *A novel synthesis route and phase transformation of Zno nanoparticles modified by DDAB.* J. Crystal Growth, vol. 252, pages 226–229, 2003.

[Lin 82] K.-C. Lin, R.M. Weis & H.M. McConnell. *Induction of helical liposomes by Ca^{2+}-mediated intermembrane binding.* Nature, vol. 296, pages 164–165, 1982.

[Lincopan 09] N. Lincopan, M.R.A. Santana, E. Faquim-Mauro, M.H.B. Da Costa & A.M. Carmona-Ribeiro. *Silica-based cationic bilayers as immunoadjuvants.* BMC Biotechnology, vol. 9, 2009.

[Lindström 02] F. Lindström, M. Bokvist, T. Sparrman & G. Gröbner. *Association of amyloid-beta peptide with membrane surfaces monitored by solid state NMR.* Physical Chemistry Chemical Physics, vol. 4, pages 5524–5530, 2002.

[Lindström 06] F. Lindström, S. Thurnhofer, W. Vetter & G. Gröbner. *Impact on lipid membrane organization by free branched-chain fatty acids.* Physcial Chemistry Chemical Physics, vol. 8, pages 4792–4797, 2006.

[Liu 08] Q. Liu, Y. Yang & Sh. Yao. *Enhanced stability of surfactant-based semipermanent wall coatings in capillary electrophoresis using oppositely charged surfactant.* J. Chromatography A, vol. 1187, pages 260–266, 2008.

[Lopes 08] A. Lopes, K. Edwards & E. Feitosa. *Extruded vesicles of dioctadecyldimethylammonium bromide and chloride investigated by light scattering and cryogenic transmission electron microscopy.* J. Colloid and Interface Science, vol. 322, no. 2, pages 582–588, 2008.

[Lu 93a] J.R. Lu, M. Hromadova, R.K. Thomas & J. Penfold. *Neutron relection from triethylene glycol monododecyl ether adsorbed at the air-liquid interface: the variation of the hydrocarbon chain distribution with surface concentration.* Langmuir, vol. 9, pages 2417–2425, 1993.

[Lu 93b] J.R. Lu, E.M. Lee, R.K. Thomas, J. Penfold & S.L. Flitsch. *Direct determination by neutron relection of teh structure of triethylene glycol monododecyl ether layers at the air water interface.* Langmuir, vol. 9, pages 1352–1360, 1993.

[Mark 03] Buchanan Mark. Nonlinear dynamics in surfactant systems, pages 226–235. American Chemical Society, Washington, DC, 11 2003.

[Marques 99] E.F. Marques, O. Regev, A. Khan, M.G. Miguel & Lindman B. *Vesicle formation and general phase behavior in the catanionic mixture SDS-DDAB-Water. The cationic-rich side.* J. Physical Chemistry B, vol. 103, pages 8353–8363, 1999.

[Marques 00] E.F. Marques, O. Regev, H. Edlund & A. Khan. *Micelles, dispersions and liquid crystals in the catanionic mixture bile salt-double-chained surfactant. The bile salt-rich area.* Langmuir, vol. 16, pages 8255–8262, 2000.

[Marques 02] E.F. Marques, A. Khan & B. Lindman. *A calorimetric study of the gel-to-liquid crystal transition in catanionic surfactant vesicles.* Thermochimica Acta, vol. 394, pages 31–37, 2002.

[Marques 03] E.F. Marques, O. Regev, A. Khan & B. Lindman. *Self-organization of double-chained and pseudodouble-chained surfactants: counterion and geometry effects.* Advances in Colloid and Interface Science, vol. 100-102, pages 83–104, 2003.

[Masatoki 96a] S. Masatoki, K. Ohno, H. Yoshida & H. Matsuura. *Conformational analysis of nonionic surfactants in water by a selective monodeuteration method. C-D stretching infrared spectroscopy of alpha -Monodeuterododecyl-omega -hydroxytris(oxyethylene)s.* J. Physical Chemistry, vol. 100, pages 8487–8498, 1996.

[Masatoki 96b] S. Masatoki, K. Ohno, H. Yoshida & H. Matsuura. *Conformational order of the alkyl chain in a nonionic surfactant alpha -Dodecyl-omega -hydroxytris(oxyethylene) (C12E3) in water.* Chemistry Letters, pages 149–150, 1996.

[Mason 00] P.C. Mason, B.D. Gaulin, R.M. Epand & J. Katsaras. *Critical swelling in single phospholipid bilayers.* Physical Review E, vol. 61, pages 5634–5639, 2000.

[Matsumoto 89] T. Matsumoto, T. Heiuchi & K. Horie. *Morphology and viscoelasticity of bilayer aqueous colloids of low-molecular and macromolecular amphiphiles.* Colloid and Polymer Science, vol. 267, pages 71–79, 1989.

[Matsumoto 92] T. Matsumoto. *Internal and interfacial structure of small vesicle in aqueous colloid of didodecyldimethylammonium bromide.* Colloid and Polymer Science, vol. 270, pages 492–497, 1992.

[Matsuura 97] H. Matsuura. *Conformational behavior of nonionic surfactants in the organized phases studied by vibrational spectroscopy.* Progress in Colloid and Polymer Science, vol. 106, pages 42–48, 1997.

[Melanson 00] J.E. Melanson, N.E. Baryla & Ch.A. Lucy. *Double-chained surfactants for semipermanent wall coatings in capillary electrophoresis.* Analytical Chemistry, vol. 72, pages 4110–4114, 2000.

[Miller 93] C.A. Miller & K.H. Raney. *Solubilization-emulsificatin mechanisms of detergency.* Colloids and Surfaces A, vol. 74, pages 169–215, 1993.

[Milner 92] S.T. Milner & D. Roux. *Flory theory of the unbinding transition.* J. Physics France, vol. 2, pages 1741–1754, 1992.

[Mimica 04] D. Mimica, A. Ringuede, C. Agurto, F. Bedioui & J. Zagal. *Biomimetic electroreduction of O_2 by hemoglobin in a surfactant film: preliminary electrochemical impedance spectroscopy insight.* Electroanalysis, vol. 16, pages 1632–1636, 2004.

[Mishima 87] K. Mishima & K. Yoshiyama. *Growth rate of myelin figures of egg-yolk phophatidylcholine.* Biochimica et Biophysica Acta, vol. 904, pages 149–153, 1987.

[Mishima 89] K. Mishima & T. Morimoto. *Electric field-induced orientation of myelin figures of phophatidylcholine.* Biochimica et Biophysica Acta, vol. 985, pages 351–354, 1989.

[Mishima 92] K. Mishima, K. Fukuda & K. Suzuki. *Double helix formation of phosphatidylcholine myelin figures.* Biochimica et Biophysica Acta, vol. 1108, pages 115–118, 1992.

[Mitchell 83] D.J. Mitchell, G.J.T. Tiddy, L. Waring, T. Bostock & M.P. McDonald. *Phase behaviour of polyoxyethylene surfactants with water.* J. Chem. Soc. Faraday Trans. I., vol. 79, pages 975–1000, 1983.

[Mohabbati 08] S. Mohabbati, S. Hjerten & D. Westerlund. *Studies on the analytical performance of a non-covalent coating with N,N-didodecyl-N,N-dimethylammonium bromide for separation of basic proteins by capillary electrophoresis in acidic buffers in 25-and 50-µm capillaries.* Analytical and Bioanalytical Chemistry, vol. 390, pages 667–678, 2008.

[Monduzzi 01] M. Monduzzi & St. Mele. *A novel NMR apporach to model percolation in W/O microemulsions.* J. Physical Chemistry B, vol. 105, pages 12579–12582, 2001.

[Montalvo 02] G. Montalvo & A. Khan. *Self-assembly of mixed ionic and zwitterionic amphiphiles: associative and dissociative interactions between lamellar phases.* Langmuir, vol. 18, pages 8330–8339, 2002.

[Moon 09] S.Y. Moon, T. Sekino, T. Kusunose & S.-I. Tanaka. *Simple one-step synthesis of water and organic media soluble gold nanoparticles with various shapes and sizes.* J. Crystal Growth, vol. 311, pages 651–656, 2009.

[Morell 77] P. Morell, editeur. Myelin. Plenum Press, New York, 1977.

[Mullin 01] J.W. Mullin. Crystallization. Butterworths-Heinemann, Oxford, 2001.

[Muthukumar 07] N. Muthukumar, S. Maruthamuthu & N. Palaniswamy. *Role of cationic and nonionic surfactants on biocidal efficiency in diesel-water interface.* Colloids and Surfaces B, vol. 57, pages 152–160, 2007.

[Nageotte 36] J. Nageotte. Morphologie des gels lipoides. Hermann & C, Paris, 1936.

[Nagle 98] J.F. Nagle, H.I. Petrache, N. Gouliaev, S. Tristam-Nagle, Y. Liu, R.M. Suter & K. Gawrisch. *Multiple mechanisms for critical behavior in the biologically relevant phase of lecithin bilayers.* Physical Review E, vol. 58, pages 7769–7776, 1998.

[Nassar 97] A.-E. F. Nassar, Z. Zhang, N. Hu, J.F. Rusling & Th.F. Kumosinski. *Proton-coupled electron transfer from electrodes to myoglobin in ordered biomembrane-like films.* J. Physical Chemistry B., vol. 101, pages 2224–2231, 1997.

[Nat 05] National Instruments, Austin. *NI Vision for LabVIEW User Manual*, 2005.

[Neubauer 67] C. Neubauer. *Über das Myelin.* Fresenius' Journal of Analytical Chemistry, vol. 6, pages 189–195, 1867.

[Neuzil 81] E. Neuzil, J. Fourche, R. Jensen, H. Jensen & G. Morin. *Structural requirements of sterols for myelin tube formation with sodium oleate.* Biochimica et Biophysica Acta, vol. 641, pages 11–19, 1981.

[Ninham 83] B.W. Ninham, D.F. Evans & G.J. Wei. *The curious world of hydroxide surfactants. spontaneous vesicle and anomalous micelles.* J. Physical Chemistry, vol. 87, pages 5020–5025, 1983.

[Nyvlt 71] J. Nyvlt. Industrial crystallization from solutions. Butterworths, London, 1971.

[Oberdisse 07] J. Oberdisse, W. Pyckhout-Hintzen & E. Straube. *Structure determination of polymer nanocomposites by small angle scattering*, 2007. manuscript.

[Ochs 97] S. Ochs, R. Pourmand, R.A. Jersild & R.N. Friedman. *The origin and nature of beading: a reversible transformation of the shape of nerve fibres.* Progress in Neurobiology, vol. 52, pages 391–426, 1997.

[Ockelford 93] J. Ockelford, B.A. Timimi, K.S. Narayan & G.J.T. Tiddy. *An upper critical point in a lamellar liquid crystalline phase.* J. Physical Chemistry, vol. 97, pages 6767–6769, 1993.

[Ohno 05] K. Ohno, H. Takao, T. Masuda & Katxumoto Y. *Two characteristic H-bonded O-H stretching bands for the compounds containing ether oxygen and hydroxyl oxygen.* Chemistry Letters, vol. 34, pages 250–251, 2005.

[Ohno 06] K. Ohno, H. Takao & Y. Katsumoto. *Geometrical behavior of hydrogen bonding patterns in the alpha-dodecyl-omega-hydroxy-tris(oxyethylene)-water system monitored by near infrared spectroscopy.* Spectrochimica Acta Part A, vol. 63, pages 690–693, 2006.

[Okuyama 84] K. Okuyama, Y. Soboi, K. Hirabayashi, A. Harada, A. Kumano, T. Kaziyama, M. Takayanagi & T. Kunitake. *Single crystals of totally synthetic amphiphiles, dialkyldimethylammonium bromides.* Chemistry Letters, pages 2117–2120, 1984.

[Okuyama 88] K. Okuyama, Y. Soboi, N. Iijima, K. Hirabayashi, T. Kunitake & T. Kajiyama. *Molecular and Crystal structure of the lipid-model amphiphile, dioctadecyldimethylammonium bromide monohydrate.* Bull. Chem. Soc. Jpn, vol. 61, pages 1485–1490, 1988.

[Olla 04] M. Olla, A. Semmler, M. Monduzzi & St.T. Hyde. *From monolayer to bilayers: mesostructural evolution in DDAB/Water/Tetradecane microemulsions.* J. Physical Chemistry B, vol. 108, pages 12833–12841, 2004.

[Ono 05] Y. Ono, H. Kawasaki, M. Annaka & H. Maeda. *Effects of micelle-to-vesicle transitions on the degree of counterion binding.* J. Colloid and Interface Science, vol. 287, pages 685–693, 2005.

[Oswald 05] P. Oswald & P. Pieranski. Nematic and cholesteric liquid crystals: concepts and physical properties illustrated by experiments. Taylor & Francis Group, Boca Raton, 2005.

[Pabst 04] G. Pabst, H. Amenitsch, D.P. Kharakoz, P. Laggner & M. Rappolt. *Structure and fluctuations of phosphatidylcholines in the vicinity of the main phase transition.* Physical Review E, vol. 70, page 021908, 2004.

[Palffy-Muhoray 07] P. Palffy-Muhoray. *The diverse World of liquid crystals.* Physics Today, pages 54–60, 2007.

[Patrick 96] H.N. Patrick & G.G. Warr. *Counterion binding and regulation of interactions between charged bilayers.* J. Physical Chemistry, vol. 100, pages 16268–16274, 1996.

[Pelletier 06] S. Pelletier & Ch.A. Lucy. *Fast and high-resolution ion chromatography at high pH on short columns packed with 1.8 µm surfactant coated silica reverse-phase particles.* J. Chromatography A, vol. 1125, pages 189–194, 2006.

[Peng 09] Y. Peng, Y. Ji, D. Zheng & S. Hu. *In situ monitoring of nitric oxide release from rat kidney at poly(eosin b)-ionic composite-based electrochemical sensors.* Sensors and Actuators B, vol. 137, pages 656–661, 2009.

[Pereira 8] E. M. A. Pereira, P. M. Kosaka, H. Rosa, D. B. Vieira, Y. Kawano, D. F. S. Petri & A. M. Carmona-Ribeiro. *Hybrid materials from intermolecular associations between cationic lipid and polymers.* J. Physical Chemistry B, vol. 112, no. 31, pages 9301–9310, 2008.

[Petrache 98] H.I. Petrache, N. Gouliaev, St. Tristam-Nagle, R. Zhang, R.M. Suter & J.F. Nagle. *Interbilayer interactions from high-resolution x-ray scattering.* Physical Review E, vol. 57, no. 6, pages 7014–7024, 1998.

[Poynor 06] A. Poynor, L. Hong, I.K. Robinson, St. Granick, Z. Zhang & P.A. Fenter. *How water meets a hydrophobic surface.* Physical Review Letters, vol. 97, page 266101, 2006.

[Proverbio 02] Z.E. Proverbio, P.C. Schulz & J.E. Puig. *Aggregation of the aqueous dodecyltrimethylammonium bromide-didodecyldimethylammonium bromide system at low concentration.* Colloid and Polymer Science, vol. 280, pages 1045–1052, 2002.

[Qin 09] S.-S. Qin, Z.-W. Yu & Y.-X. Yu. *Structural Characterization on the gel to liquid-crystal phase transition of fully hydrated DSPC and DSPE bilayers.* J. Physical Chemistry B, vol. 113, pages 8114–8123, 2009.

[Raviv 01] U. Raviv, P. Laurat & J. Klein. *Water confined down to subnanometer films.* Nature, vol. 413, pages 51–54, 2001.

[Raviv 02] U. Raviv, S. Giasson, J. Frey & J. Klein. *Viscosity of ultra-thin water films confined between hydrophobic or hydrophilic surfaces.* J. Physics: Condensed Matter, vol. 14, pages 9275–9283, 2002.

[Raviv 04] U. Raviv, S. Perkin, P. Laurat & J. Klein. *Fluidity in water confined down to subnanometer films.* Langmuir, vol. 20, pages 5322–5332, 2004.

[Rheinstädter 06] M.C. Rheinstädter, W. Häußler & T. Salditt. *Dispersion relation of lipid membrane shape fluctuations by neutron spin-echo spectrometry.* Physical Review Letters, vol. 97, page 048103, 2006.

[Rhinne 56] F.N. Rhinne. Phase diagrams in metallurgy. McGraW-Hill Book Company, INC, New York, 1956.

[Richardson 01] P.R. Richardson. *Spectroscopic and computational studies on a number of conformationally flexible molecules.* PhD thesis, University of Edinburgh, 2001.

[Richter 99] F. Richter, L. Finegold & G. Rapp. *Sterols sense swelling in lipid bilayers.* Physical Review E, vol. 59, pages 3483–3491, 1999.

[Rinne 33] F. Rinne. *Investigations and considerations concerning paracrystallinity.* Trans. Faraday Society, vol. 29, pages 1016–1032, 1933.

[Riske 09] K.A. Riske, R.P. Barroso, C.C. Vequi-Suplicy, R. Germano, V.B. Henriques & M.T. Lamy. *Lipid bilayer pre-transition as the beginning of the melting process.* Biochimica et Biophysica Acta, vol. 1788, pages 954–963, 2009.

[Roach 09] B. Roach, 2009. private conversation.

[Rosa 08] H. Rosa, D.F.S. Petri & A.M. Carmona-Ribeiro. *Interactions between bacteriophage DNA and cationic biomimetic particles.* J. Physical Chemistry B, vol. 112, pages 16422–16430, 2008.

[Roux 92] D. Roux, C. Coulon & M.E. Cates. *Sponge phases in surfactant solutions.* J. Physical Chemistry, vol. 96, 1992.

[Rubingh 91] D.N. Rubingh & P.M. Holland, editeurs. Cationic surfactants: Physical chemistry, volume 37 of *Surfactant Science Series.* Marcel Dekker, Inc., New York, 1991.

[Rusling 93] J.F. Rusling & A.-E. F. Nassar. *Enhanced electron transfer for myoglobin in surfactant films on electrodes.* J. American Chemistry Society, vol. 115, pages 11891–11897, 1993.

[Sakurai 77] I. Sakurai, S. Iwayanagi, T. Sakurai & T. Seto. *X-ray study on egg-yolk lecithin: unit cell data and electron density profile.* J. Molecular Biology, vol. 117, pages 285–291, 1977.

[Sakurai 83] I. Sakurai & Y. Kawamura. *Magnetic-field-induced orientation and bending of the myelin figures of phosphatidylcholine.* Biochimica et Biophysica Acta, vol. 735, pages 189–192, 1983.

[Sakurai 84] I. Sakurai & Y. Kawamura. *Growth mechanism of myelin figures of phophatidylcholine.* Biochimica et Biophysica Acta, vol. 777, pages 347–351, 1984.

[Sakurai 85] I. Sakurai. *Concentration gradient along the long axis of myelin figures of phosphatidylcholine.* Biochimica et Biophysica Acta, vol. 815, pages 149–152, 1985.

[Sakurai 90] I. Sakurai, T. Suzuki & S. Sakurai. *Structure and growth behavior of myelin figures.* Molecular Crystals Liquid Crystals, vol. 180B, pages 305–311, 1990.

[Salzer 08] J. Salzer. *Switching myelination on and off.* J. Cell Biology, vol. 181, pages 575–577, 2008.

[Sandermann 77] H. Sandermann, H. Falk & G. Schumacher. *Rapid and sensitive determination of phopholipid thermal-phase transition temperatures by microscopy.* Analytical Biochemistry, vol. 82, pages 583–585, 1977.

[Sanders 46] F.K. Sanders & D. Whitteridge. *Conduction velocity and myelin thickness in regenerating nerve fibres.* J. Physiology, vol. 105, pages 152–174, 1946.

[Saveyn 09] P. Saveyn, P. Van der Meeren, M. Zackrisson, T. Narayanan & U. Olsson. *Subgel transition in dilute vesicular DODAB dispersions.* Soft Matter, vol. 5, pages 1735–1742, 2009.

[Schulz 93] P.C. Schulz & J.E. Puig. *The state of water in lyotropic liquid crystals.* Colloids and Surfaces A, vol. 71, pages 83–90, 1993.

[Schulz 98] P.C. Schulz, J.L. Rodriguez, F.A. Soltero-Martinez, J.E. Puig & Z.E. Proverbio. *Phase behaviour of the dioctadecyldimethylammonium bromide-water system.* J. Thermal Analysis, vol. 51, pages 49–62, 1998.

[Seddon 83] J.M. Seddon, K. Harlos & D. Marsh. *Metastability and polymorphism in the gel and fluid bilayer phases of dilauroyl-phosphatidylethanolamine.* J. Biological Chemistry, vol. 258, pages 3850–3854, 1983.

[Shao 05] Y. Shao, Y. Jin, J. Wang, L. Wang, F. Zhao & S. Dong. *Conducting polymer polypyrrole supported bilayer lipid membranes.* Biosensors and Bioelectronics, vol. 20, pages 1373–1379, 2005.

[Shumyantseva 09] V. Shumyantseva, E. Suprun, T. Bulko & A. Archakov. *Electrochemical methods for the investigation of bioaffinity interactions based on gold nanoparticles modified sensors.* Electroanalysis, vol. 21, pages 530–535, 2009.

[Silas 01] J.A. Silas & E.W. Kaler. *The phase behavior and microstructure of efficient cationic-nonionic microemulsions.* J. Colloid and Interface Science, vol. 243, pages 248–254, 2001.

[Silva 8] J. P. N. Silva, P. J. G. Coutinho & M. E. C. D. R. Oliveira. *Characterization of monoolein-based lipoplexes using fluorescence spectroscopy.* J. Fluorescence, vol. 18, no. 2, pages 555–562, 2008.

[Silver 86] B.L. Silver. The physical chemistry of membranes. Allen & Unwin and The Solomon Press, 1986.

[Sobral 8] C. N. C. Sobral, M. A. Soto & A. M. Carmona-Ribeiro. *Characterization of DODAB/DPPC vesicles.* Chemistry and Physics of Lipids, vol. 152, no. 1, pages 38–45, 2008.

[Soltero 00] J.F.A. Soltero, F. Bautista, E. Pecina, J.E. Puig, O. Manero, Z. Proverbio & P.C. Schulz. *Rheological behavior in the didodecyldimethylammonium bromide/water system.* Colloid and Polymer Science, vol. 278, pages 37–47, 2000.

[Soutzidou 02] M. Soutzidou, V.-A. Glezakou, K. Viras, M. Helliwell, A.J. Masters & M.A. Vincent. *Low-frequency raman spectroscopy of n-alkohols. LAM vibration and crystal structure.* J. Physical Chemistry B, vol. 106, no. 17, pages 4405–4411, 2002.

[Starrs 99] L. Starrs. *Collapse of transient gels in colloid-polymer mixtures.* PhD thesis, University of Edinburgh, 1999.

[Steinman 96] L. Steinman. *Multiple Sclerosis: A coordinated immunological attack against myelin in the central nervous system.* Cell, vol. 85, pages 299–302, 1996.

[Stenstam 03] A. Stenstam, G. Montalvo, I. Grillo & M. Gradzielski. *Small angle neutron scattering study of Lysozyme-Sodium Dodecyl Sulfate Aggregates.* J. Physical Chemistry B, vol. 107, pages 12331–12338, 2003.

[Stoeckenius 59] W. Stoeckenius. *An electron microscope study of myelin figures.* J. Biophysic. and Biochem. Cytol., vol. 5, pages 491–500, 1959.

[Suga 93] K. Suga, M. Bradley & J.F. Rusling. *Probing the interface of cast surfactant films and an underlying metal by surface-enhanced raman scattering spectroscopy.* Langmuir, vol. 9, pages 3063–3066, 1993.

[Svitova 01] T.F. Svitova, R.M. Hill & C.J. Radke. *Spreading of aqueous trisiloxane surfactant solutions over liquid hydrophobic substrates.* Langmuir, vol. 17, pages 335–348, 2001.

[Tarazona 97] A. Tarazona, E. Koglin, B.B. Coussens & R.J. Meier. *Conformational dependence of Raman frequencies and intensities in alkanes and polyethylene.* Vibrational Spectroscopy, vol. 14, pages 159–170, 1997.

[Taribagil 05] R. Taribagil, M.A. Arunagiritnathan, C. Manohar & J.R. Bellare. *Extended time range modeling of myelin growth.* J. Colloid and Interface Science, vol. 289, pages 242–248, 2005.

[Tasaki 96] K. Tasaki. *Poly(oxyethylene)-water interactins: a molecular dynamic study.* J. Am. Chem. Soc., vol. 118, pages 8459–8469, 1996.

[Tenchov 01] B. Tenchov, R. Koynova & G. Rapp. *New Ordered Metastable phases between the gel and subgel phases in hydrated phospholipids.* Biophysical Journal, vol. 80, pages 1873–1890, 2001.

[Tiddy 82] G.J.T. Tiddy, K. Rendall & P. Galsworthy. *Lyotropic mesophase behaviour of n-$C_{16}H_{33}EO_3$ - evidence for two V_2 phases.* Molecular Crystals and Liquid Crystals, vol. 72, pages 147–152, 1982.

[Tonegawa 00] A. Tonegawa, K. Ohno, H. Matsuura, K. Yamada & T. Okuda. *Conformational dynamics of alkyl chains in the lamellar phase of a nonionic surfactant C12E3 studied by deuterium nuclear magnetic resonance.* Chemistry Letters, pages 324–325, 2000.

[Undabeytia 04] T. Undabeytia, S. Nir & M.J. Gomara. *Clay-vesicle interactions: fluorescence measurements and structural implications for slow release formulations of herbicides.* Langmuir, vol. 20, pages 6605–6610, 2004.

[University 09] The Open University. *Introduction to polymers.* website, 2009. `http://openlearn.open.ac.uk/mod/resource/view.php?id=196633`.

[Urban 07] K. Urban, C.M. Schneider, Th. Brückel, St. Blügel, K. Tillmann, W. Schweika, M. Lentzen & L. Baumgarten, editeurs. Probing the nanoworld: microscopies, scattering and spectroscopies of the solid state. Forschungszentrum Jülich GmbH, 2007.

[Vanderbilt 09] Vanderbilt. website, 2009. `http://www.mc.vanderbilt.edu/histology/slide.php?image_name=myelin&slide_file=images/histology/nervous_tissue/display/schwann3.jpg&image_id=1058`.

[Vavasour 09] I.M. Vavasour, C. Laule, D.K.B. Li, J. Oger, G.R.W. Moore, A. Traboulsee & A.L. MacKay. *Longitudinal changes in myelin water fraction in two MS patients with active disease.* J. Neurological Sciences, vol. 276, pages 49–53, 2009.

[Virchow 54] R. Virchow. *On the general appearance of the nerve-like structures from animal substances.* Virchow's Archive, vol. 6, page 562, 1854.

[Viseu 00a] M.I. Viseu, K. Edwards, C.S. Campos & S.M.B. Costa. *Spontaneous vesicle formed in aqueous mixtures of two cationic amphiphiles.* Langmuir, vol. 16, pages 2105–2114, 2000.

[Viseu 00b] M.I. Viseu, M.M. Velázeuez, C.S. Campos, I. García-Mateos & S.M.B. Costa. *Structural transitions in a bicationic amphiphile system studied by light-scattering, conductivity, and surface tension measurements.* Langmuir, vol. 16, pages 4882–4889, 2000.

[Viseu 04] M.I. Viseu, T.I. Carvalho & S.M.B. Costa. *Conformational transitions in beta-lactoglobulin induced by cationic amphipiles: equilibrium studies.* Biophysical Journal, vol. 86, pages 2392–2402, 2004.

[Vogel-Weill 91] C. Vogel-Weill, Gruger A. & E. Neuzil. *Raman and infrared microspectrophotometric investigation of myelin forms.* Comptes Rendus de l Academie des Sciences, vol. 312, pages 1077–1082, 1991.

[Volodkin 08] D. Volodkin, Y. Arntz, P. Schaaf, H. Moehwald, J.-C. Voegel & V. Ball. *Composite multilayer biocompatible polyelectrolyte films with intact liposomes: stability and temperature triggered dye release.* Soft Matter, vol. 4, pages 122–130, 2008.

[Waggett 08] R.J. Waggett & E.J. Buskey. *Escape reaction performance of myelinated and non-myelinated calanoid copepods.* J. Experimental Marine Biology and Ecology, vol. 361, pages 111–118, 2008.

[Warr 88] G.G. Warr, R. Sen, D.F. Evans & J.E. Trend. *Microemulsion formation and phase behavior of dialkyldimethylammonium bromide surfactants.* J. Physical Chemistry, vol. 92, pages 774–783, 1988.

[Wilkinson 84] D.A. Wilkinson & J.F. Nagle. *Metastability in the phase behaviour of dimyristoylphosphatidylethanolamine.* Biochemistry, vol. 23, pages 1538–1541, 1984.

[Wu 09] G. Wu, H.A. Khant, W. Chiu & K.Y.C. Lee. *Effects of bilayer phases on phospholipid-poloxamer interactions.* Soft Matter, vol. 5, pages 1496–1503, 2009.

[Wunderlich 78] F. Wunderlich, W. Kreutz, P. Mahler, A. Ronai & G. Heppeler. *Thermotropic fluid → ordered 'discontinuous' phase separation in microsomal lipids of tetrahymena. An x-ray diffraction study.* Biochemistry, vol. 17, pages 2005–2010, 1978.

[Yassine 04] M.M. Yassine & Ch.A. Lucy. *Factors affecting the temporal stability of semipermanent bilayer coatings in capillary electrophoresis prepared using double-chained surfactants.* Analytical Chemistry, vol. 76, pages 2983–2990, 2004.

[Youssry 08] M. Youssry, L. Coppola, I. Nicotera & C. Moran. *Swollen and collapsed lyotropic lamellar rheology.* J. Colloid and Interface Science, vol. 321, pages 459–467, 2008.

[Zana 05] R. Zana, editeur. Dynamics of surfactant self-assemblies: micelles, microemulsions, vesicles and lyotropic phases, volume 125 of *Surfactant Science Series*. Taylor & Francis Group, Boca Raton, 2005.

[Zemb 93] Th. Zemb, D. Gazeau, M. Dubois & T. Gulik-Krzywicki. *Critical behaviour of lyotropic liquid crystals.* Europhysics Letters, vol. 21, pages 759–766, 1993.

[Zhao 09] M. Zhao, L. Zhang, N. Chen, Ch. Wang, L. Fan & Sh. Yang. *Electrochemistry of $Sc_3N/MVAt\ C_{78}$ embedded in didodecyldimethylammonium bromide films in aqueous solution.* Microchimica Acta, vol. 165, pages 45–52, 2009.

[Zhu 01] Y. Zhu & St. Granick. *Viscosity of interfacial water.* Physical Review Letters, vol. 87, page 096104, 2001.

[Zou 06] L.-N. Zou & S.R. Nagel. *Stability and growth of single myelin figures.* Physical Review Letters, vol. 96, page 138301, 2006.